
**DESIGN, FABRICATION AND
CHARACTERIZATION OF
NANOSTRUCTURED HYBRID
BIO/NON-BIO INTERFACES FOR
BIOMOLECULAR INTERACTIONS
STUDY AND INDUSTRIAL
APPLICATIONS**

Rosalba Moretta

Dottorato in Biotecnologie – XXXII ciclo

Università di Napoli Federico II



Dottorato in Biotecnologie – XXXII ciclo

Università di Napoli Federico II



**DESIGN, FABRICATION AND
CHARACTERIZATION OF
NANOSTRUCTURED HYBRID
BIO/NON-BIO INTERFACES FOR
BIOMOLECULAR INTERACTIONS
STUDY AND INDUSTRIAL
APPLICATIONS**

Rosalba Moretta

Dottorando: Rosalba Moretta

Relatore: Paola Giardina, Luca De Stefano

Coordinatore: Prof. Marco Moracci

Settore Scientifico Disciplinare: BIO/10 - FIS/07

INDICE

RIASSUNTO	1
SUMMARY	6
Abbreviations	7
1. Nanostructured materials: production and properties	8
1.1 Aim of the project	9
1.2 Porous silicon: from formation to biological applications	9
1.3 Synthesis, characterization and biomedical applications of gold nanoparticles	12
1.4 Nanostructured zinc oxide: properties and applications	15
2. Engineering nanostructured semiconductors for biosensing and biomedical applications	18
2.1 A hybrid porous silicon-based biosensor	18
2.1.1 Design of a stable hybrid device based on porous silicon for biosensing purpose	18
2.1.2 Early detection of Brugada Syndrome	30
2.2 Porous silicon Quantum Dots for bioimaging	43
2.2.1 Characterization of chemically modified PSiNPs	44
2.2.2 PSiNPs for <i>in vivo</i> imaging	50
2.3 ZnO-based nanostructured platform for label free optical biosensor	59
3. Gold nanoparticles for biomolecular and industrial applications	71
3.1 Design and synthesis of hybrid gold nanoparticles for biomedical applications	71
3.2 The antibacterial activity of gold nanoparticles-antimicrobial peptide complex	82
4. Conclusions	93
5. References	98

APPENDIX I. Publications, communications, experience in foreign laboratory, courses and workshops	108
APPENDIX II. Research articles	115

Riassunto

Introduzione

Il costante avanzamento delle nanotecnologie ha portato allo sviluppo di dispositivi ibridi, costituiti da nanomateriali caratterizzati da superfici funzionalizzate con elementi biologici. L'interesse verso la realizzazione di materiali ibridi scaturisce dalla possibilità di combinare proprietà funzionali di diversi composti in un singolo sistema. In questo modo, il dispositivo risultante avrà proprietà incrementate rispetto ai materiali di partenza, permettendo applicazioni diversificate in svariati campi di ricerca, che vanno dalla biosensoristica all'ambito biomedico.

Materiali nanostrutturati adoperati

Negli ultimi anni, i materiali nanostrutturati, grazie alle loro peculiari proprietà fisico-chimiche, sono stati ampiamente utilizzati per applicazioni biotecnologiche. Nel seguente lavoro di tesi, verranno presentati tre diverse tipologie di nanomateriali:

- Silicio poroso (PSi)
- Nanoparticelle d'oro (AuNPs)
- Ossido di zinco (ZnO)

Il PSi è un materiale nanostrutturato che ha suscitato grande interesse nel corso degli anni. Le sue proprietà ottiche, la sua morfologia simile ad una spugna, caratterizzata da un'ampia area superficiale, lo rende particolarmente utile per l'immobilizzazione di biomolecole [1]. Il silicio poroso è ottenuto mediante attacco elettrochimico di silicio cristallino drogato, in una soluzione di acido fluoridrico (HF). Il PSi può essere definito come un network di vuoti, da cui dipendono le proprietà ottiche, che possono essere controllate modificando i parametri di processo (drogaggio del silicio cristallino, tempo di attacco, concentrazione di elettrolita, etc.), ottenendo diverse strutture fotoniche (Fabry-Perot, specchio di Bragg, microcavità ottica, sequenza multistrato aperiodica, etc.), mostrate in Figura 1 [2].

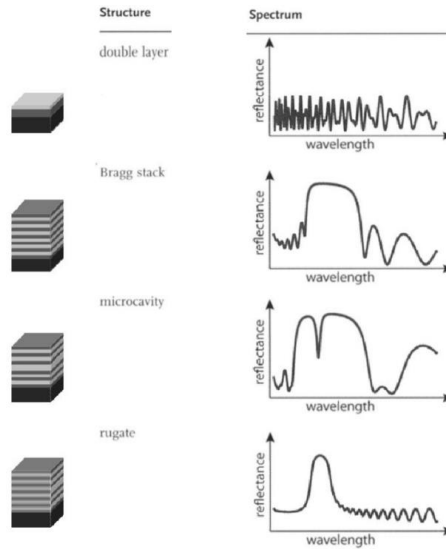


Figura 1 - Esempi di strutture fotoniche del PSi [2]

Il principale inconveniente nell'utilizzo del PSi è la sua instabilità chimica quando esposto all'aria o ad un mezzo acquoso: infatti, in tali condizioni si verifica la formazione di uno strato di ossido superficiale dovuto alla sostituzione dei legami nativi Si-H, termodinamicamente instabili, con quelli Si-O-Si, dovuti all'interazione della superficie del materiale con l'ossigeno. Per queste ragioni, al fine di avere un dispositivo che sia stabile, è fondamentale un processo di passivazione della sua superficie [1]. Tale materiale trova impiego non solo nelle applicazioni bio-sensoristiche ma anche in ambito biomedico come potenziali nanovettori o come sonde per l'imaging diagnostico, in particolare senza ausilio di sonde fluorescenti o radiometriche (e perciò definite label-free).

Tra le nanoparticelle metalliche, quelle d'oro rappresentano le più comunemente utilizzate in vari campi di ricerca grazie alle loro proprietà chimico-fisiche. Le nanoparticelle d'oro possono essere ottenute mediante svariate tipologie di sintesi, tra cui la più comune è quella proposta da Turkevich, in cui la riduzione di acido cloroaurico (HAuCl_4) avviene in condizioni di ebollizione e mediante aggiunta di citrato [3]. Al fine di poter utilizzare tale materiale per applicazioni biotecnologiche, è importante poterne controllare la stabilità, evitando l'aggregazione delle singole particelle. Il controllo fine del processo di condensazione è ottenuto mediante l'utilizzo di agenti stabilizzanti, molti dei quali

presentano caratteristiche di tossicità e quindi non utilizzabili per applicazioni biomedicali [4]. A tale scopo, molecole organiche tossiche possono essere sostituite da molecole anfifiliche come il polietilene glicole (PEG), con lo scopo di ottenere nanoparticelle biocompatibili e con aumentata solubilità in acqua [5], [6]. Inoltre, sfruttando la presenza di particolari gruppi funzionali presenti sulle AuNPs, è possibile funzionalizzarle mediante l'aggiunta di varie molecole biologiche quali peptidi, enzimi o DNA. La loro stabilità, biocompatibilità, reattività chimica rendono tali NPs applicabili in svariati campi, da quello biomedico a quello industriale (come marcatori o veicoli per il rilascio dei farmaci, prodotti cosmetici, biosensori) (Figura 2) [7], [8].

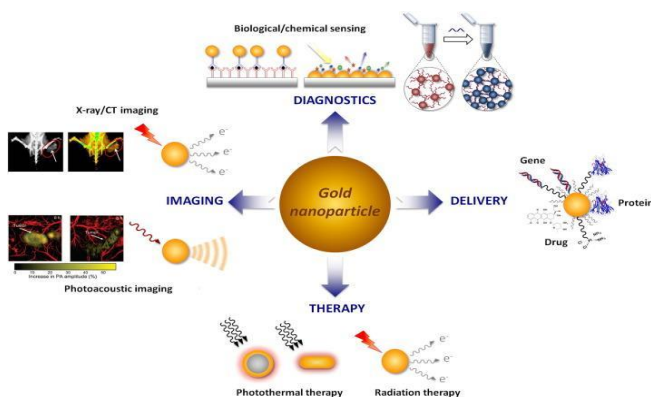


Figura 2 - Schema delle principali applicazioni delle AuNPs [8]

Lo ZnO rappresenta un'altra tipologia di materiale nanostrutturato e multifunzionale, avente notevoli proprietà fisico-chimiche quali alta stabilità chimica, termica, meccanica e biocompatibilità. Le proprietà piezo- e piroelettriche lo rendono idoneo per lo sviluppo di sensori. Inoltre, grazie alla sua biocompatibilità e biodegradabilità, è stato identificato come un materiale riconosciuto sicuro dalla Food and Drug Administration (FDA). Le diverse morfologie ad elevata area superficiale, ottenute sfruttando varie tecniche di sintesi, rendono tale materiale ampiamente versatile in vari campi della nanotecnologia [9]–[11].

Dispositivi ibridi nanostrutturati sviluppati

L'opportuna passivazione/funzionalizzazione dei materiali sopra elencati, ha portato allo sviluppo di dispositivi nanostrutturati e nanoparticelle aventi impiego in ambito biomedico e ambientale.

a. Monitoraggio ottico dell'interazione molecolare PNA/DNA

Il PSi è stato utilizzato come trasduttore ottico per la realizzazione di un biosensore capace di diagnosticare la sindrome di Brugada in fase precoce. Al fine di realizzare un dispositivo multiparametrico, l'ossido di grafene, dotato di una propria fotoluminescenza, è stato infiltrato e immobilizzato all'interno della matrice porosa mediante l'impiego di chimica covalente. Un acido peptidico nucleico (PNA), agganciato covalentemente al supporto, è stato scelto come biosonda. La natura neutra dello scheletro del PNA ha come conseguenza un'affinità di legame PNA/DNA più forte di quella tra due filamenti di DNA. Inoltre, il complesso formato tra PNA/DNA è più sensibile alla presenza del singolo mismatch rispetto al complesso DNA/DNA. Ne consegue che tale biosonda è ideale per la realizzazione di biosensori altamente sensibili e specifici, utili per le identificazioni di mutazioni geniche. In conclusione, l'utilizzo di un tale dispositivo, ha permesso l'identificazione selettiva del DNA target. L'ibridazione è stata confermata mediante l'utilizzo di differenti tecniche di analisi.

b. Nanoparticelle di silicio poroso (PSiNPs) modificate per applicazioni *in vivo*

Le PSiNPs, grazie alla loro biocompatibilità, insieme con l'intrinseca natura fotoluminescente e la morfologia porosa hanno suscitato grande interesse per applicazioni nell'ambito della nanomedicina. In questo lavoro di tesi, esse sono state utilizzate come possibili sonde label-free per imaging *in vivo* in *Hydra vulgaris*. Al fine di mediare l'internalizzazione delle NPs nell'animale, esse sono state opportunamente passivate mediante idrosililazione, in modo da garantire una maggiore stabilità in soluzione acquosa, e successivamente modificate con poly-L-lisina, tale da conferire una carica positiva superficiale, facilitandone l'internalizzazione nell'organismo di *Hydra*. L'uptake e la citotossicità del materiale sono stati monitorati mediante l'utilizzo della microscopia a fluorescenza risolta in tempo.

c. ZnO·F come trasduttore per biosensori label-free

L'ossido di zinco nanostrutturato (nZnO) e la sua forma drogata con fluoro (nZnO·F), ottenuti mediante sintesi idrotermica, sono stati opportunamente funzionalizzati, al fine di immobilizzare sulla loro superficie una proteina modello, la proteina A, estratta da *Staphylococcus aureus*. Lo scopo di tale lavoro è stato quello di valutare la possibilità di utilizzo di tali materiali come biosensori. In particolare, i risultati rivelano che nZnO·F è suscettibile di una

funzionalizzazione più efficace rispetto allo nZnO. Tale effetto potrebbe essere attribuito alla sua natura rugosa che permette una maggiore immobilizzazione di biomolecole. Ciò apre la strada all'utilizzo di tale piattaforma nanotecnologica per applicazioni biosensoristiche label-free.

d. Realizzazione di AuNPs ibride per applicazioni biomediche

Le nanoparticelle ibride sono state ampiamente utilizzate per applicazioni in ambito biomedico, sia nell'ambito diagnostico che terapeutico. Principalmente, quelle metalliche potrebbero essere utilizzabili come possibile agente di contrasto, capace di aumentare l'intensità di segnale in MRI e PET, o come nanovettori per veicolare farmaci all'interno delle cellule. Lo scopo di questo lavoro era quello di proporre la sintesi di due nanocomplessi che differissero sostanzialmente solo per la chelazione o meno del rame durante il processo di sintesi. Una volta studiata e valutata la stabilità morfologica e chimica delle nanoparticelle ibride realizzate, si è passati all'analisi in cellula, al fine di valutarne l'internalizzazione, la loro distribuzione e la citotossicità. I risultati ottenuti hanno mostrato che le NPs, aventi il rame in forma chelata, erano quelle che meglio si prestavano per le future applicazioni biologiche.

e. Realizzazione del complesso AuNPs-TL48 e monitoraggio dell'attività antibatterica

L'utilizzo massivo di antibiotici ha comportato l'inevitabile insorgenza di patogeni antibiotico-resistenti, che rappresentano un serio rischio di salute pubblica. A tal proposito, è in continua evoluzione lo sviluppo di molecole in grado di difendere l'uomo da agenti patogeni. In questo contesto, negli ultimi anni l'attenzione è stata focalizzata sui peptidi antimicrobici, presenti già in diverse specie, sia animali che vegetali. Pertanto, essendo le nanoparticelle d'oro dotate esse stesse di un'attività antibatterica intrinseca, in questo lavoro sono stati sviluppati due nanocomplessi, caratterizzati dall'interazione delle AuNPs con la temporina TL48, un peptide antimicrobico derivante dalla *Rana Temporaria*, attivo su batteri Gram-negativi, Gram-positivi e lieviti. Dopo aver valutato la stabilità dei nanocomplessi ottenuti, resta da monitorare se l'attività antibatterica dei complessi ibridi sviluppati possa essere incrementata rispetto all'attività del peptide non legato alla superficie d'oro.

Summary

Hybrid devices have one or more biological components bioconjugated with functional support surfaces preserving their specific activity and properties. They are extremely interesting from the biotechnological point of view since: 1) They provide a creative way to combine functional properties of different substances into a singular molecular composite; 2) They could show enhanced properties due to the coupling of different elements; 3) Their properties open innovative ways to applications in different fields, such as food, agriculture, medicine and so on.

The goal of this PhD thesis is the development of some hybrid-nanocomposites, made of nanostructured materials and biological elements, in which the key issue is the interface between the bio and non-bio components of the systems.

Bioconjugated nanostructured materials reveal peculiar physical and chemical properties that can boost their use in biotechnological applications. Inorganic nanoparticles, in particular those based on noble metals and semiconductors in native form or oxide, are becoming common tools in many popular fields of investigation such as nanomedicine, imaging, environmental monitoring and biomolecular sensing. Porous silicon (PSi), Gold nanoparticles (AuNPs) and Zinc Oxide (ZnO) are three highly-performing nanostructured systems whose features have been exploited in this thesis.

The research approach used in this work thesis is focused on the synthesis and fabrication of nanostructured support materials, in planar or in nanoparticle shapes, followed by the functionalization and passivation of the material surfaces. Finally, biological elements are immobilized on the solid supports for specific studies and applications. Different hybrid devices have been developed in this work for applications in several research areas, in particular:

- Hybrid silicon-based device for the detection of Brugada Syndrome for diagnostic purposes;
- Luminescent silicon nanoparticles as label-free bioprobes for fluorescent bioimaging applications;
- Hybrid gold-copper nanoparticles as promising contrast agent in nuclear magnetic resonance;
- Gold nanoparticles complexed to an antimicrobial peptide to enhance the antibacterial activity of the peptide.

The results obtained in each case highlighted the innovative potentialities of these nano-complexes in solving problems and breaking barriers in different ambits, spanning from diagnostic to healthcare.

Abbreviations

AMPs	Antimicrobial peptide
AFM	Atomic force microscopy
APTES	(3-Aminopropyl)-triethoxysilane
AuNPs	Gold Nanoparticles
BOC	<i>t</i> -butyloxycarbonyl
BS	Brugada Syndrome
c-AuNPs	Citrate gold nanoparticles
DLS	Dynamic Light Scattering
DPEG	Polyethylene glycol diacid
FFT	Fast Fourier Transform
FT-IR	Fourier Transform Infrared Spectroscopy
GO	Graphene Oxide
h-PSiNPs	Hydrosilylated porous silicon nanoparticles
LSP	Localized Surface Plasmon
LSPR	Localized Surface Plasmon Resonance
NMs	Nanostructured materials
nZnO	Nanostructured Zinc oxide
nZnO-F	Fluorine-doped Zinc oxide
PL	Steady-state photoluminescence
PLL	Poly-L-Lysine
PNA	Peptide nucleic acid
PrA	Protein A
PSi	Porous Silicon
PSiNPs	Porous silicon nanoparticles
RT-HPLC	Reverse-phase high-performance liquid chromatography
TEM	Transmission electron microscopy
QDs	Quantum dots
QY	Quantum yield
SEM	Scanning electron microscopy
SPR	Surface Plasmon Resonance
TFA	Trifluoroacetic acid
UDA	Undecylenic acid
Uv-vis	Ultraviolet -visible spectroscopy
WCA	Water contact angle

1. Nanostructured materials: production and properties

The research work supporting the PhD thesis entitled “DESIGN, FABRICATION AND CHARACTERIZATION OF NANOSTRUCTURED HYBRID BIO/NON-BIO INTERFACES FOR BIOMOLECULAR INTERACTIONS STUDY AND INDUSTRIAL APPLICATIONS” has been done in the frame of a collaboration between the National Research Council – Institute for Microelectronics and Microsystems and the Department of Chemical Sciences, University of Naples “Federico II”, under the co-tutoring of Dr. Luca De Stefano and Prof. Paola Gardina.

Any material with a fine structure of small size, i.e. in the range between 1 to 100 nm, can be considered “nanostructured”. Nanostructured materials (NMs) exhibit innovative chemical-physics properties related to the “size effect” [12]. These properties, such as photoluminescence, reflectivity, high surface area, absorption and so on, make these compounds attractive for biotechnological uses. The rapid advances of these materials have received great attention in almost every research fields. This is essentially due to their physicochemical properties because they offer several advantages compared with their corresponding bulky counterparts [13]. Implant engineering, site-specific drug delivery, non-invasive imaging, clinical biosensors and diagnostics are only few examples of the principal applications of these materials. On the other hand, nanostructured materials are largely used in waste-water or air purification, environmental monitoring and precision agriculture.

There are two possible approaches to the fabrication of NMs: the top-down methods are those in which a macroscopic material is reduced or defined down to nanometric scale by removing matter essentially; the other way is defined as the bottom-up approach and in this case nano-objects are built by adding atoms together, just it happens in the self-assembling of natural structures like marine shells.

Currently, there is the interest in mixing properties of several compounds (i.e., biological elements with functional support surface) into a singular macromolecular element. This is the base for the development of hybrid devices, with enhanced functional properties.

In this section, the main characteristics of three nanostructured materials will be discussed: porous silicon, zinc oxide and gold

nanoparticles. All these materials were chemically modified using several approaches that will be discussed in section 2 and 3.

1.1 Aim of the project

When a biological element (such as protein, enzyme, peptide, nucleic acid and so on) is conjugated to a functional support surface, the key issue is the bio/non-bio interface that exists between them. Biological molecules can be simply absorbed on a solid surface or covalently bound on it. Even if absorption could seem a straightforward process, the resulting bioconjugated surface is not ordered and cannot be properly designed. The covalent approach gives finely tunable multilayers but it requires complex chemistry procedures.

The activity of my PhD thesis project has been focused on the development of hybrid-nanocomposites made of biological elements and nanostructured materials, in which the interface between the bio and non-bio components of the system have been properly designed. Porous Silicon (PSi), gold nanoparticles (AuNPs) and Zinc oxide (ZnO) are bright examples among the huge community of nanostructured materials, and they have been used for the realization of this work of thesis. Once properly modified, these materials have been applied in biomedical and industrial fields, from the development of biosensors to antimicrobial activity.

1.2 Porous silicon: from formation to biological applications

Porous silicon was accidentally discovered in 1950 by Dr. Arthur Uhlir at Bell Laboratories while performing electropolishing of crystalline silicon study in a HF-based solution. He noticed that, under appropriate electrochemical conditions, there was the formation of a matt dark layer on the silicon surface, which it was believed to be a subfluoride $(\text{SiF}_2)_x$, grown during the anodic dissolution [14]. Only in 1969 it was discovered that a porous matrix was formed by electrochemical process of silicon wafer [15]. This material was forgotten until 1990, when Leigh Canham studied bright, red-orange photoluminescence from the material [16]. Since then, the scientific community showed a great interest in this new material, publishing thousands of papers concerning the properties and applications of porous silicon. PSi is a very promising material due to its excellent mechanical and thermal properties, its compatibility with silicon-based microelectronics and its low cost. It shows a sponge-like morphology, characterized by high surface area of about $500 \text{ m}^2 \text{ cm}^{-3}$, a controllable pore size and there is the possibility to modify the surface

chemistry. All these features make this material useful for several kind of applications.

Electrochemical etching has been the most common method for the fabrication of porous silicon over the last 60 years. The cell used for the process is schematized in Figure 1.1. The silicon wafer is the anode, placed in back-side contact on an aluminium plate while the front side is sealed with an O-ring and exposed to the HF solution. The cathode used in porous silicon etching cells is platinum or any other HF resistant and conducting material. The cell body is made of an acid resist polymer such as polyvinylidene fluoride (PVDF) or polytetrafluoroethylene (PTFE). The passing of electrical current through the silicon wafer leads to the dissolution of silicon atoms and the removal of surface roughness. A mix of electronic and chemical factors are involved in the process controlling pore formation. Modulating electrolyte composition, type of silicon wafer, dopant type and concentration, temperature, applied voltage, light intensity makes it possible to engineer porous silicon structures with specific morphological and optical properties [17].

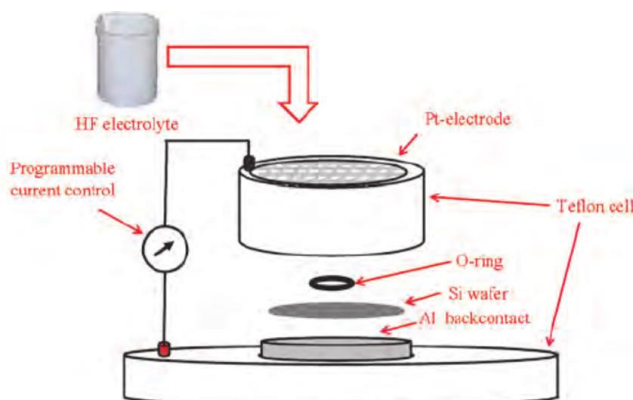


Figure 1.1 - Electrochemical etching set-up

The chemistry dissolution of silicon is explained in Figure 1.2, in which the mechanism proposed by Lehmann and Gösele is schematized, receiving great attention [18]. It is generally accepted that holes are required in the initial step of electropolishing and pore formation. The surface of as-etched PSi is passivated by Si-H bonds. The dissolution of a surface atom begins when a hole has sufficient energy to reach the

interface of silicon and electrolyte. At this step, fluoride ion from the solution could attach Si-H bond and a Si-F bond is formed (step 1 in Figure 1.2). Because of the polarizing effect of Si-F bond, another F⁻ ion can attach, releasing hydrogen molecule (steps 2 and 3). The polarization induced by Si-F bonds reduces the electron density of the Si-Si backbonds; these weakened bonds will be now attached by HF or H₂O (step 4) leaving the surface passivated by hydrides again (step 5).

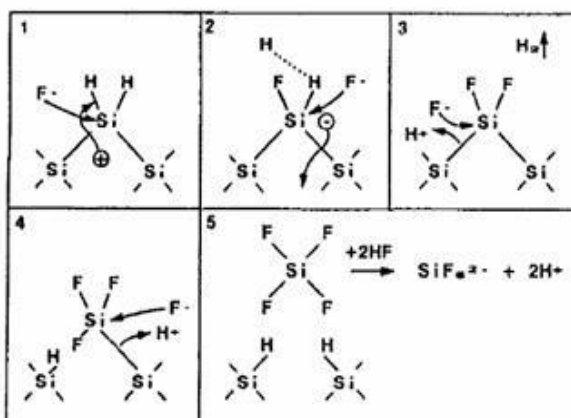


Figure 1.2 – Dissolution mechanism of silicon in HF solution

The main problem of porous silicon is its instability at ambient air or aqueous solutions due to the formation of an oxide layer. The oxidation of the material and the subsequent dissolution of matrix influence the physicochemical, optical and electronic properties of porous silicon. This leads to instability of porous silicon layer that is unacceptable for many applications. To stabilize the as-etched PSi, several treatments have been developed, avoiding the formation of the oxide layer. One of this is the intentional growth of an oxide layer on the surface *via* thermal oxidation, a process developed in a tube furnace, from several minutes to hours. In this case, SiO₂ bonds completely replace Si-H bonds from the entire skeleton [19]. After the oxidation step, silanol chemistry could be employed to modify silica surface thanks to the possibility to form a dense monolayer on PSi surface through Si-O-Si bonds, able to stabilize and protect the surface [20]. Thermal hydrosilylation reaction is an alternative passivation process, involving the formation of Si-C bonds to hydrogen-terminated porous silicon. This reaction, first demonstrated by Buriak [21], [22] and elaborated by Boukherroub and

others, involves the grafting of alkenes or alkynes to hydrogen-terminal PSi [23]. The reaction, which can be promoted by heat, Lewis acid catalysis, light and so on, in inert atmosphere and completely deoxygenated/dried reagents, involves the formation of alkyl chains covalently attached to the surface by Si-C bonds. Using this passivation strategy, several functional groups could be added to the porous silicon surface, useful for the subsequent conjugation with biomolecules (i.e., enzyme, DNA, aptamer).

Even if optoelectronic is the main research area of porous silicon, over the last decade the material has found applications in different fields such as medicine, diagnostics, cosmetics and so on. PSi has exhibited extraordinary qualities for applications in biological field as drug delivery system and imaging agent, thanks to its biocompatibility and biodegradability [24]. The porous nature of the material gives the possibility to confine a molecular or nanosized payload, typically a drug but also enzyme, gene and so on, inside the pore [25]. A nanovector like this, has the potential to deliver drugs to the appropriate location, minimizing side effects. PSi nanovectors can also be used for theranostic applications, in which therapeutic and diagnostic properties coexist in the same system. Photoluminescent PSi nanoparticles (NPs) can also be used as label free probe for bioimaging application and this property will be discussed in the section 2.

Moreover, its application has been explored as a biosensing platform taking advantage of its sensitivity, biocompatibility and its high surface area. Several bioprobes could be immobilized on porous silicon (i.e., enzyme, proteins, antibody, DNA, aptamer) [26], [27]. The optical, electronic and electrochemical properties of PSi give the possibility to design novel biosensors in which the biological recognition event is detected as a quantifiable signal. A biosensing platform based on PSi will be discussed in section 2.

1.3 Synthesis, characterization and biomedical applications of gold nanoparticles

Gold nanoparticles (AuNPs) have aroused great interest in the field of nanotechnology. Thanks to their physical and chemical properties, AuNPs find applications in several fields of research, from sensing to imaging.

Their large surface-to-volume ratio, biocompatibility, low toxicity, size and shape-related optoelectronic properties make AuNPs important tools in biotechnology. As any other noble metal, they present an optical phenomenon known as surface plasmon resonance (SPR) due to the

collective oscillation of nanoparticles free electrons induced by electromagnetic frequency: this happens only when the particle size is smaller than the excitation light wavelength. This phenomenon was theoretically described by Mie, solving Maxwell's equations [28]–[30]. The SPR band intensity and wavelength are influenced by the factors affecting the electron charge density on the particle surface such as particle size and shape, surface ligand, composition and dielectric constant of surrounding medium. SPR band could be indicative of the stability of AuNPs because their aggregation can be monitored via a colour change (from red to blue due to the interparticle plasmon coupling) of the solution and as a variation in peak position and shape (Figure 1.3) [29].

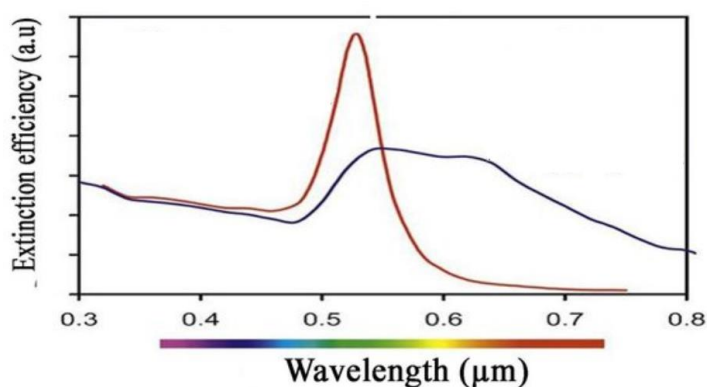


Figure 1.3 – Uv-spectra of monodisperse (red line) and agglomerated (blue line) AuNPs

Particles of different size and shape show different optical properties, so, in recent time, researchers have focused their attention on the developing of different methods of synthesis. There are many approaches to synthesize AuNPs divided in physical, chemical and biological but the chemical processes are the most common. The first chemical approach to obtain AuNPs was performed by Faraday in 1857 in which the dispersion of AuNPs was obtained using a two-phase system consisting of an aqueous solution of chloroaurate (AuCl_4^-) and phosphorus in carbon disulphide as reducing agent [31]. Later, Turkevitch, in 1951, performed a new method in which the boiling solution of AuCl_3^- was both reduced and stabilized by citrate, yielding nanoparticles of 15 nm in diameter [3]. Varying the ratio citrate/gold it is possible to obtain nanoparticles up to 150 nm in diameter. Synthesis in

organic phase represents another method commonly used to obtain AuNPs, generally characterized by the use of a phase transfer agent (i.e., tetraoctylammonium bromide) and sodium borohydride as reducing agent. This methodology produces low dispersity of AuNPs from 1.5 to 5 nm [32]. Recently, green chemistry is arising much interest thanks to the possibility to produce a biocompatible and environmentally friendly product. Plant extracts, but also bacteria and fungi, are used as reducing and stabilizing agents [33]–[36].

One of the main problem of nanoparticles in a colloidal system is the aggregation. Stabilizers, usually surfactant molecules, were commonly used to overcome this problem but, their toxic nature, make them not suitable for biomedical applications. Polymers, such as polypeptide, polyethylene glycol (PEG) or proteins, represent some valid alternative to avoid the agglomeration in various extreme conditions. They are also able to increase the biocompatibility and the water solubility of nanoparticles, properties useful for the applications in biomedical field [37].

Biomolecules can be attached to AuNPs in two different ways, physical or chemical interactions, depending on the application. Physical interactions, such as hydrophobic and electrostatic interactions, represent a simpler way for binding molecules to AuNPs surface, commonly used in delivery and sensing applications thanks to their reversible nature. On the other hand, the covalent approach is used to obtain stable constructs by attachment of thiolate groups to AuNPs surface or by carbodiimide chemistry.

The optical properties of AuNPs make them suitable for a broad range of applications in biomedical field. In the last years, AuNPs have been emerged as a valid candidate in drug delivery of small and large molecules like proteins, DNA or RNA but also drugs can be easily carried by AuNPs because of its high surface/volume ratio. Few examples are offered by PEGylated-AuNPs, used to deliver some of tumour therapeutic agents like doxorubicin [38], anthracycline while AuNRs were used to inhibit H1N1 influenza virus after functionalization with innate immune response activators [39]. Moreover, AuNPs have been explored as transfection agent in gene therapy to cure cancer and genetic disorders. Photothermal therapy (PTT) is a highly applied method for cancer treatment and AuNPs, having maximum absorption in the visible or near IR, are able to damage cancer cells based on the effect of heat under laser irradiation [40]. To increase the dosage of AuNPs in the interest site and to minimize the side effects, the surface of AuNPs can be opportunely modified using targets for cancer cells (i.e., antibody). Furthermore, the optical and electric properties of

AuNPs make them employed for cell imaging: they can be used as contrast agent or to prepare surface-enhanced Raman scattering (SERS) nanoparticles.

In recent years, AuNPs complexed with antimicrobial peptide (AMP) have represented an alternative solution in the fight against drug-resistant pathogens. AuNPs have an own bactericidal effect on a several range of microorganisms. As a consequence, AuNPs complexed to the AMPs give, as a result, an enhancement of the antimicrobial activity [41].

Not least important, is the use of AuNPs as biological and chemical sensors to detect the presence of specific analytes and their concentrations. They are widely used in diagnostics or in environmental monitoring [42], [43]. The most common sensors based on AuNPs are colorimetric, whose functional mechanism derives from the aggregation behaviours of AuNPs after the interaction with the analyte of interest. Moreover, the colorimetric response is easy to monitor at naked-eye, without the use of sophisticated instrumentation.

1.4 Nanostructured zinc oxide: properties and applications

Nanostructured zinc oxide (ZnO) has received great attention in the last decade thanks their remarkable physical properties and potential applications in various emerging area. It was defined a multifunctional material due to its intrinsic characteristics, such as high chemical, thermic and mechanic stability, photostability, biocompatibility and nontoxicity. It is an inorganic material, n-type semiconductor in group II-IV with a wide band-gap of 3.37 eV, useful for short wavelength optoelectronic applications. Moreover, it shows a high excitonic band energy of 60 meV, which ensures an excitonic emission at room temperature and makes this material a possible candidate for fabricating UV and blue LEDs [44]–[46].

ZnO presents three crystal structures: rocksalt, zinc blende and wurtzide, as shown in Figure 1.4. The wurtzide structure is the most stable one in ambient conditions. It is a hexagonal structure characterized by alternating planes composed of tetrahedrally coordinated O^{2-} and Zn^{2+} , stacked alternatively along c-axis and showing a non-central symmetric structure with a consequent piezoelectricity and pyroelectricity.

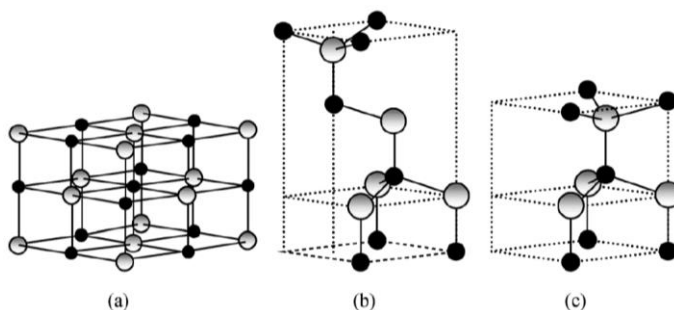


Figure 1.4 – Stick and ball representation of ZnO crystal structures: (a) cubic rocksalt, (b) cubic zinc blende, (c) hexagonal wurtzite. Gray and black spheres denote Zn and O atoms respectively [47].

The growth of ZnO can be obtained by different techniques, giving the possibility to obtain products whose particles are different in size, shape and spatial structure. Among the different methods, vapour transport process is a technique commonly used to synthesize ZnO nanostructures. In this process, Zn and oxygen react with each other, forming ZnO nanostructures. This method can be splitted in catalyst free vapor-solid (VS) process, in which the nanostructures are produced by condensing directly from vapor phase, and vapour liquid-solid (VLS) process, in which nanoparticles or nanoclusters of Au, Co, Cu and Sn have been used as catalysts. While the first method provides less control on the geometry, alignment and precise location of ZnO nanostructures, the latter method provides a controlled growth of nanostructures [44]. ZnO nanostructured could be also synthesized by electrodeposition, sol-gel, hydrothermal process and so on. In particular, hydrothermal growth has many advantages because it does not require the use of organic reagents, making the process environmentally friendly, the reaction conditions are mild, for example the temperature of process is low, and it could be used on different surface [48].

Controlling several synthesis parameters, such as deposition temperature, pressure, carrier gas flux, various ZnO nanostructures can be obtained. ZnO can be in one -(1D) (i.e., nanorods, nanoneedles, nanorings, nanowires), two (2D) (i.e., nanoplate, nanosheet) and three dimensional (3D) structures (i.e., flower, snowflakes).

The interest in ZnO is due to its uncountable physical properties, including optical, electrical, piezoelectric and magnetic properties. ZnO shows a high photoluminescence (PL) after UV exposition, whose spectrum is characterized by a peak at 380 nm [49]. This optical

property has been widely used in optoelectronic characterizations, giving information about band-gap, defects and crystal quality of the material. Therefore, as semiconductor material, undoped ZnO shows a n-type conductivity due to native defects such as oxygen vacancies and zinc interstitials electrical properties, useful for potential applications of this material in the development of devices. Moreover, its piezoelectric properties have been studied for applications in piezoelectric sensors. Thanks to its multifunctional properties, ZnO is considered a transducer material useful for biosensor development in which a probe needs to be opportunely immobilized on the surface. The immobilization process can be obtained *via* covalent chemistry or *via* physical absorption. In the covalent process, the organic cross-linkers are characterized by a reactive head group able to interact covalently with the sensing surface [50], [51]. Moreover, they allow to obtain a highly oriented, ordered and packed organic layer on the ZnO surface showing selective site for binding of bioelements. Silanization of ZnO surface is a covalent method commonly studied by several research groups. Studies conducted on ZnO nanostructures have shown that their inhomogeneous nature (i.e., the oxygen vacancies) is responsible of the different binding affinities [52].

Because of its interesting properties, ZnO is used in several fields, playing an important role in a wide range of applications, from pharmaceuticals to agriculture, from paints to chemicals.

2. Engineering nanostructured semiconductors for biosensing and biomedical applications

Semiconductors dominate the telecom and electronic market for over seventy years, from the discovery of the solid-state transistor in 1943 by Bardeen, Brattain and Shockley. Nowadays, semiconductors are becoming more and more important in very different fields, ranging from optoelectronics to biosensors and biomedicine. In particular, in the last years, there has been a strong demand for the use of devices based on nanostructured semiconductors for the development of low-cost, efficient and portable biosensors, able to analyse the samples in real-time. The biosensor is a hybrid device characterized by a bioprobe, i.e. a biological active element, employed to selectively recognize a biomolecular target, immobilized on a transducer material which converts the biomolecular interaction into an analytical signal. Semiconductors such as the PSi and ZnO, due to their chemical-physical properties, are widely used for this purpose. Moreover, the intrinsic photoluminescent nature, the biodegradability and the favourable mesoporous structure of PSi nanoparticles (NPs), make them applicable as a label-free probe for *in vivo* imaging.

PSi and ZnO are the two nanostructured semiconductors that will be presented in this section. In particular, the role of PSi as a transducer material, for the development of a biosensor, and PSiNPs, for *in vivo* imaging, will be discussed in sections 2.1 and 2.2. A ZnO-based transducer material for biosensing purpose will be discussed in section 2.3.

2.1 A hybrid porous silicon-based biosensor

2.1.1 Design of a stable hybrid device based on porous silicon for biosensing purpose

The combination of biological elements with support surface is the key for the development of hybrid devices, in which, mixing the functional properties of several compounds, results an enhancement of device properties. Recently, PSi has been used, as transducer material, complexed with nanosheets of graphene oxide (GO), electrostatically immobilized on amino-modified mesoporous silicon [53], [54]. The idea to combine both these materials in a single platform is due to the possibility to analyse two different characteristics of the material: the reflectance of PSi and the photoluminescence (PL) of GO. GO is a two-dimensional material that has attracted great attention because of its electrical, mechanical and optical properties. Moreover, a broad PL

from 500 to 800 nm has been reported [55]. Unfortunately, the PL of GO is very weak, limiting its use in optoelectronic devices but, the infiltration of the material into large specific surface as PSi is an approach able to tune the PL emission from GO.

In the following study, the attention is focused on the covalent grafting of GO into PSi surface with the goal to obtain a robust system for biosensing purpose. In this section is reported the design and the possible application of the multiparametric device, using a covalent approach.



Toward Multi-Parametric Porous Silicon Transducers Based on Covalent Grafting of Graphene Oxide for Biosensing Applications

Rosalba Moretta^{1,2}, Monica Terracciano¹, Principia Dardano¹, Maurizio Casalino¹, Luca De Stefano^{1*}, Chiara Schiattarella^{1,3} and Ilaria Rea¹

¹ Institute for Microelectronics and Microsystems, Unit of Naples, Naples, Italy, ² Department of Chemical Sciences, "Federico II" University of Naples, Naples, Italy, ³ Department of Physics, "Federico II" University of Naples, Naples, Italy

OPEN ACCESS

Edited by:

Thierry Djenizian,
École des Mines de
Saint-Étienne–Campus Georges
Charpak Provence, France

Reviewed by:

Rabah Boukherroub,
UMR8520 Institut D'électronique, de
Microélectronique et de
Nanotechnologie (IEMN), France
Ciro Chiappini,
King's College London,
United Kingdom

*Correspondence:

Luca De Stefano
luca.destefano@na.imm.cnr.it

Specialty section:

This article was submitted to
Chemical Engineering,
a section of the journal
Frontiers in Chemistry

Received: 10 September 2018

Accepted: 08 November 2018

Published: 22 November 2018

Citation:

Moretta R, Terracciano M, Dardano P,
Casalino M, De Stefano L,
Schiattarella C and Rea I (2018)
Toward Multi-Parametric Porous
Silicon Transducers Based on
Covalent Grafting of Graphene Oxide
for Biosensing Applications.
Front. Chem. 6:583.
doi: 10.3389/fchem.2018.00583

Graphene oxide (GO) is a two-dimensional material with peculiar photoluminescence emission and good dispersion in water, that make it an useful platform for the development of label-free optical biosensors. In this study, a GO-porous silicon (PSi) hybrid device is realized using a covalent chemical approach in order to obtain a stable support for biosensing applications. Protein A, used as bioprobe for biosensing purposes, is covalently linked to the GO, using the functional groups on its surface, by carbodiimide chemistry. Protein A bioconjugation to GO-PSi hybrid device is investigated by atomic force microscopy (AFM), scanning electron microscopy (SEM), water contact angle (WCA) measurements, Fourier transform infrared (FTIR) spectroscopy, steady-state photoluminescence (PL), and fluorescence confocal microscopy. PSi reflectance and GO photoluminescence changes can thus be simultaneously exploited for monitoring biomolecule interactions as in a multi-parametric hybrid biosensing device.

Keywords: porous silicon, graphene oxide, covalent grafting, photoluminescence, optical device

INTRODUCTION

Graphene oxide (GO) is the oxidized counterpart of graphene, characterized by oxygen-bearing functional groups in the form of epoxy, hydroxyl, and carboxyl acids groups on both the basal plane and edges (Dreyer et al., 2010). The oxygen-containing functional groups on the GO sheets make this material more hydrophilic than graphene. In the last decade, GO has attracted great attention because of its unique electronic, mechanical, thermal, and optical properties (Park and Ruoff, 2009; Loh et al., 2010). Moreover, GO can be functionalized with biomolecules without using cross-linkers in aqueous solution, so that this material is particularly interesting for biosensing applications (Jung et al., 2010; Loh et al., 2010; Liu et al., 2012; Zhang et al., 2013).

Several strategies have been published to functionalize GO. In particular, carboxylic acid groups on the GO sheets can be used as reactant sites for immobilization or conjugation of several biological molecules such as proteins, peptides, antibodies, DNA, and so on (Zhang et al., 2010; Wu et al., 2011). Furthermore, GO exhibits steady-state photoluminescence (PL) particular features, such as a broad PL emission from 500 to 900 nm on exposure to near UV radiation, that have been proposed for the development of a new class of optoelectronic devices (Chien et al., 2012). Unfortunately, the PL of a thin layer of GO nanosheets is too weak, mainly due to the oxygen-functional groups producing non-radiative recombination between their electrons

and holes present in sp^2 clusters (Gupta et al., 2014). Oxygen plasma treatment can be used to get higher PL emission from GO (Gokus et al., 2009; Eda et al., 2010). An alternative approach based on the infiltration of GO into large surface area substrate is a valid strategy to enhance the light generation from the resulting composite material, and porous silicon (PSi) is optimal candidate for this task. PSi is a nanostructured material produced by electrochemical anodization of doped crystalline silicon in hydrofluoric acid (HF)-based solution. Pores size and morphology of PSi samples can be properly tuned changing the etching parameters (HF concentration, current density) and the characteristics of the silicon substrate (dopant type, resistivity, crystal orientation). Due to its sponge-like morphology, characterized by a specific surface area of hundreds of $m^2\text{ cm}^{-3}$, PSi is definitely an ideal transducer for the development of several kinds of biosensors (Sailor, 2012; Canham, 2017). In recent papers, hybrid devices constituted by GO electrostatically immobilized on amino-modified mesoporous silicon (i.e., PSi with a pores size <50 nm) were described. In particular, homogeneous monolayer and aperiodic Thue-Morse multi-layered structure made of 64 layers were used in order to infiltrate GO nanosheets by spin-coating. The enhancement and the modulation of the PL signal emitted from GO adsorbed on both the hybrid structures were highlighted, while these phenomena were not observed in the case of GO on crystalline flat silicon (Rea et al., 2014, 2016).

In this work, a chemical procedure to covalently bind GO to PSi surface has been developed in order to realize a stable hybrid device for biosensing purposes. Macroporous silicon, characterized by pores size >50 nm, has been used in infiltrating the GO sheets inside the pores of material. The GO-PSi hybrid device has been covalently conjugated to FITC-labeled protein A (PrA*) derived from *Staphylococcus aureus* as a model bioprobe. The effective covalent interaction between GO-PSi and PrA* demonstrates the possibility to realize a robust system for biosensing whose operating mechanism is based on the changes of PSi reflectance and GO photoluminescence.

The development of GO-PSi hybrid device and its interaction with the PrA* have been investigated by Fourier transform infrared spectroscopy (FTIR), spectroscopic reflectometry, steady-state photoluminescence (PL), atomic force microscopy (AFM), scanning electron microscopy (SEM), water contact angle (WCA) measurements, and fluorescence confocal microscopy.

MATERIALS AND METHODS

Chemicals

Hydrofluoric acid (HF), undecylenic acid (UDA), N-(3-Dimethylaminopropyl)-N'-ethylcarbodiimide hydrochloride (EDC), N-hydroxysuccinimide (NHS), MES hydrate, tert-Butyloxycarbonyl-NH-PEG-Amine (BOC-NH-PEG-NH₂), trifluoroacetic acid (TFA), chloroform, tetrahydrofuran, FITC-labeled Protein A (PrA*) from *S. aureus* were purchased from Sigma Aldrich (St. Louis, MO, USA). Graphene oxide (GO) nanosheets were purchased from Biotool.com (Houston, TX,

USA) as a batch of 2 mg/mL in water with a nominal sheets size between 50 and 200 nm.

Preparation of Graphene Oxide

Graphene oxide (GO), 1 mg ml⁻¹, was sonicated using an ultrasonic processor for 1 h in ice at 50% of available power amplitude.

Porous Silicon (PSi) Layer Fabrication and Hydrosilylation Process

PSi was fabricated by electrochemical etching of *n*-type crystalline silicon (0.01–0.02 $\Omega\text{ cm}$ resistivity, (100) oriented and 500 μm thick) in HF (5% in weight)/ethanol solution at room temperature (RT). Before the etching process, the silicon substrate was immersed in HF solution for 2 min to remove the oxide native layer. A current density of 20 mA cm⁻² for 90 s, was applied to obtain a single layer of PSi with a porosity of 61% ($n_{\text{PSi}} = 1.83$ at $\lambda = 1.2\mu\text{m}$), a thickness *L* of 2.1 μm and a pores dimension between 50 and 250 nm, determined by ellipsometry and SEM imaging (Terracciano et al., 2016). The as-etched PSi was placed in a Schlenk tube containing deoxygenated neat UDA (99% v/v) and allowed to react at 110°C for 18 h under a stream of argon. The treated chip was extensively washed in tetrahydrofuran and chloroform in order to remove the excess of reagent (Shabir et al., 2017).

Pegylation of PSi Layer and Covalent Grafting of GO

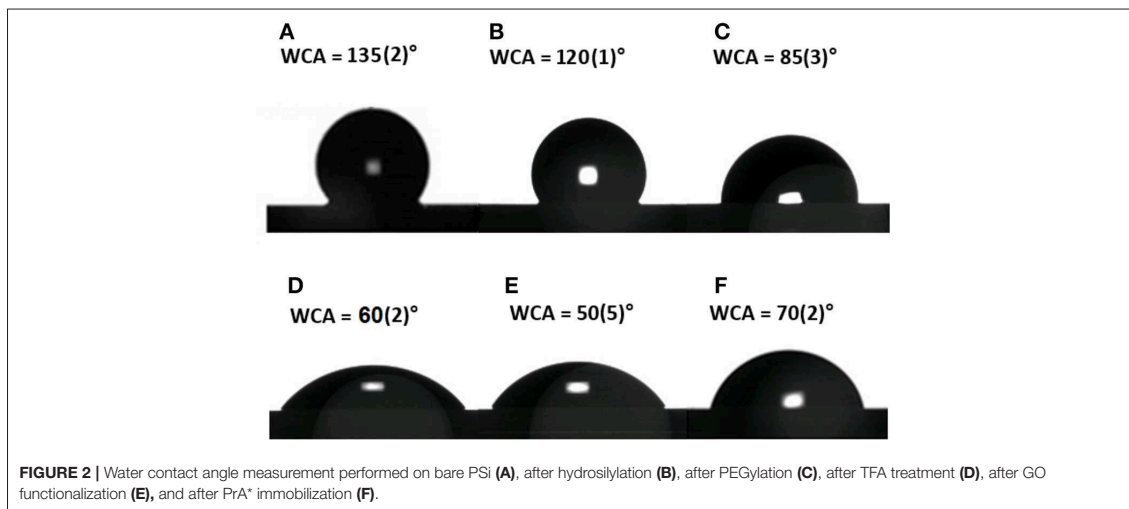
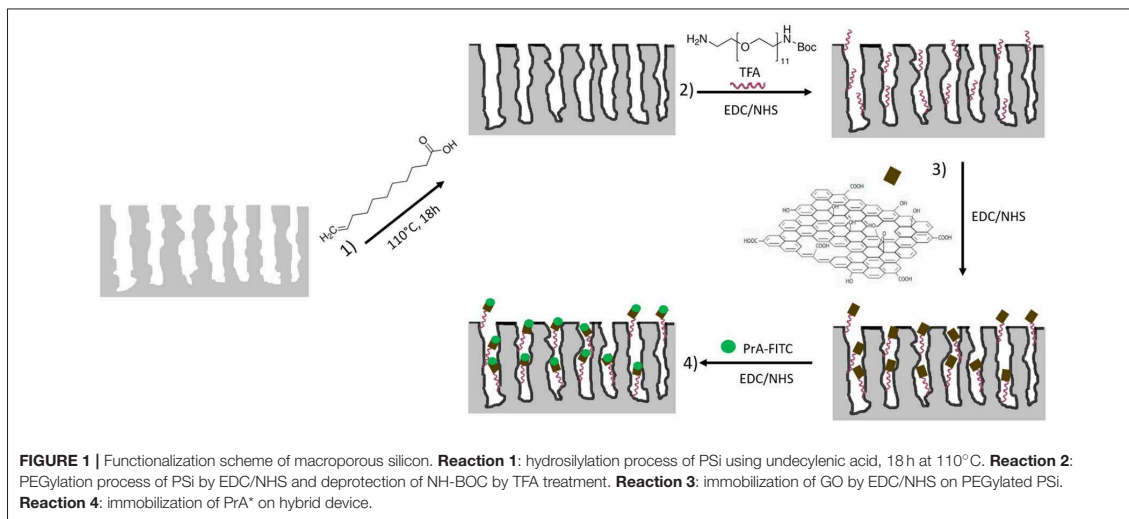
UDA-modified PSi sample was placed in a Schlenk tube containing freshly prepared EDC/NHS aqueous mixture (0.005 M in MES 0.1 M) for 90 min at RT. Sample was rinsed in deionized water three times and dried under nitrogen stream. PEGylation was performed dipping the sample in BOC-NH-PEG-NH₂ solution (0.4 M, overnight, at 4°C) (Harris et al., 1992; Sam et al., 2010); the excess of reagent was removed rinsing the sample in MES buffer and in deionized water. The *t*-butyloxycarbonyl (BOC) protecting group of amine portion was removed from the PEG covalently bound to PSi surface incubating the sample in a solution of TFA (95% v/v, 90 min, at RT): sample was then washed in deionized water so as to remove the excess of TFA. GO was covalently bound to the PSi surface incubating the sample in sonicated GO (1 mg/ml) in presence of EDC/NHS (0.020 M EDC and 0.016 M NHS in MES 0.1 M, overnight, at RT).

Covalent Grafting of FITC-Labeled Protein a on PSi Layer

GO-modified PSi was incubated in 0.33 mg/ml of FITC-labeled Protein A (PrA*) in presence of EDC/NHS (0.020 M EDC and 0.016 M NHS in MES 0.1 M, overnight, at RT). The reaction was conducted over-night at RT.

Atomic Force Microscopy

A XE-100 AFM (Park Systems) was used for the imaging of PSi sample before and after functionalization with GO. Surface imaging was obtained in non-contact mode using silicon/aluminum coated cantilevers (PPP-NCHR 10 M; Park



Systems) 125 μm long with resonance frequency of 200 to 400 kHz and nominal force constant of 42 N/m. The scan frequency was typically 1 Hz per line. AFM images were analyzed by the program XEI 1.8.1.build214 (Park Systems).

Scanning Electron Microscopy

SEM characterization of PSi sample was performed before and after GO functionalization. Images were acquired at 5 kV accelerating voltage and 30 μm wide aperture by a Field Emission Scanning Electron Microscope (Carl Zeiss NTS GmbH 1500 Raith FESEM). InLens detector was used. Samples were tilted at 90° in order to perform SEM analysis in lateral view.

Water Contact Angle Measurements

Sessile drop technique was used for WCA measurements on a First Ten Angstroms FTA 1000 C Class coupled with drop shape analysis software. Results of WCA are expressed as mean \pm standard deviation (s.d.) of at least three measurements on the same sample of three independent experiments (i.e., at least nine measurements for each result).

Fourier Transform Infrared Spectroscopy

The FTIR spectra of all samples were obtained using a Nicolet Continuum XL (Thermo Scientific) microscope in the wavenumber region of 4,000–650 cm^{-1} with a resolution of 4 cm^{-1} .

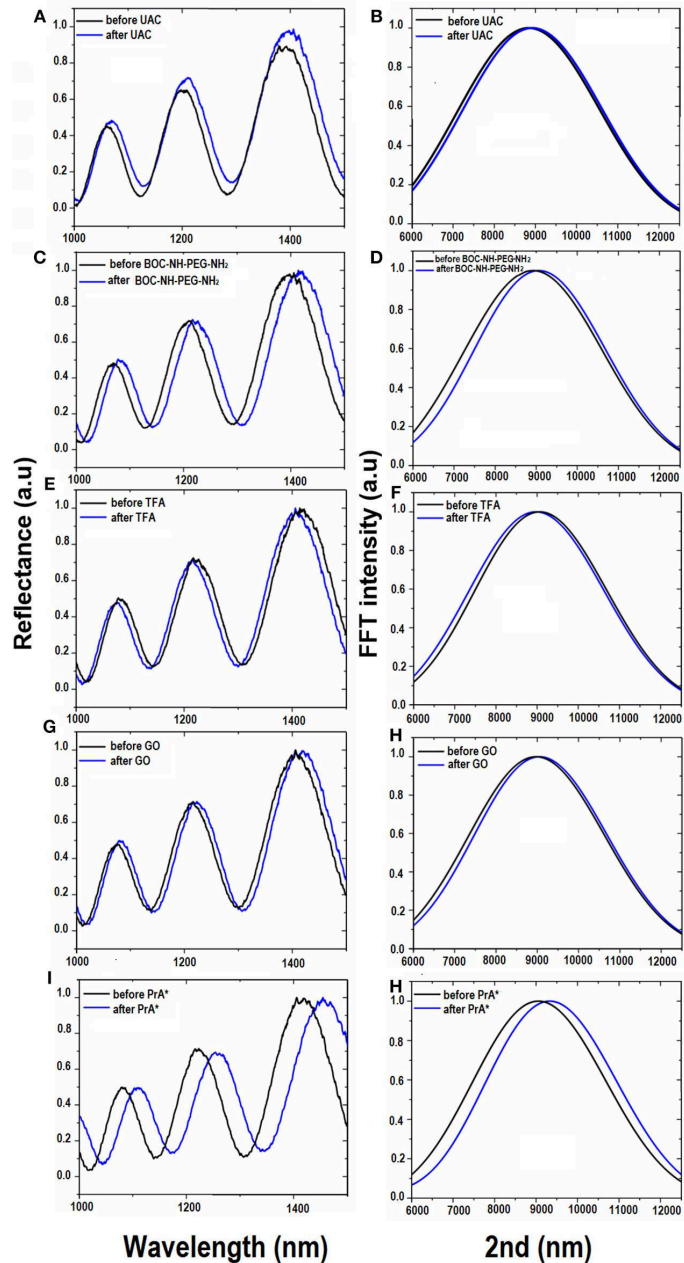


FIGURE 3 | Reflectivity spectra (A) and corresponding Fourier transforms (B) of PSI before (black line), and after (blue line) UDA treatment. Reflectivity spectra (C) and corresponding Fourier transforms (D) of UDA-PSi before and after PEGylation with BOC-NH-PEG-NH₂ (blue line). Reflectivity spectra (E) and corresponding Fourier transforms (F) of PEGylated PSI before (black line) and after selective deprotection of -NH-BOC by TFA treatment (blue line). Reflectivity spectra (G) and corresponding Fourier transforms (H) of deprotected PEG-PSi before (black line) and after GO immobilization (blue line). Reflectivity spectra (I) and corresponding Fourier transforms (J) after PrA* functionalization.

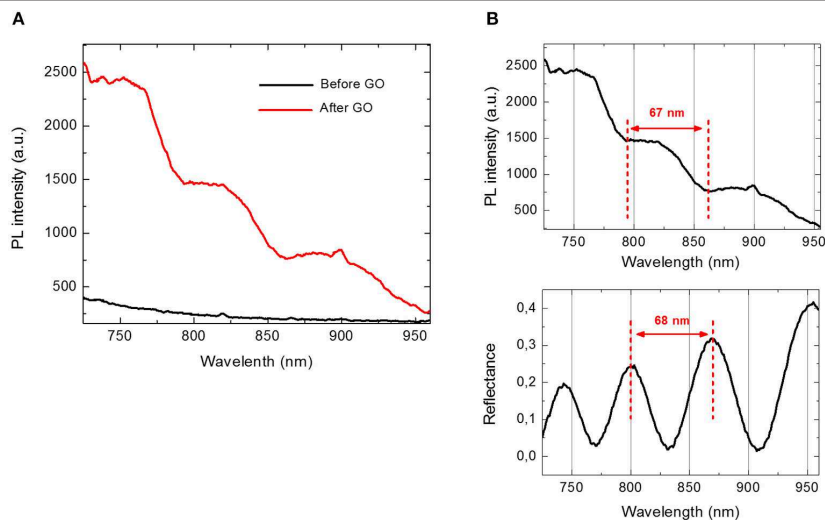


FIGURE 4 | (A) Photoluminescence spectra of PSi before (black line) and after GO covalent immobilization (red line) at an excitation wavelength of 442 nm. **(B)** Comparison between photoluminescence spectrum (upper graph) and reflectivity spectrum (lower graph) of GO-PSi device.

Spectroscopic Reflectometry

The reflectivity spectra of PSi sample were measured at normal incidence by means of a Y optical reflection probe (Avantes), connected to a white light source and to an optical spectrum analyser (Ando, AQ6315B). The spectra were collected over the range 600–1,600 nm with a resolution of 1 nm. Reflectivity spectra shown in the work are the average of three measurements.

Steady-State Photoluminescence (PL)

Steady-state photoluminescence (PL) spectra were excited by a continuous wave He-Cd laser at 442 nm (KIMMON Laser System). PL was collected at normal incidence to the surface of samples through a fiber, dispersed in a spectrometer (Princeton Instruments, SpectraPro 300i), and detected using a Peltier cooled charge coupled device (CCD) camera (PIXIS 100F). A long pass filter with a nominal cut-on wavelength of 458 nm was used to remove the laser line at monochromator inlet.

Laser Scanning Confocal Microscopy

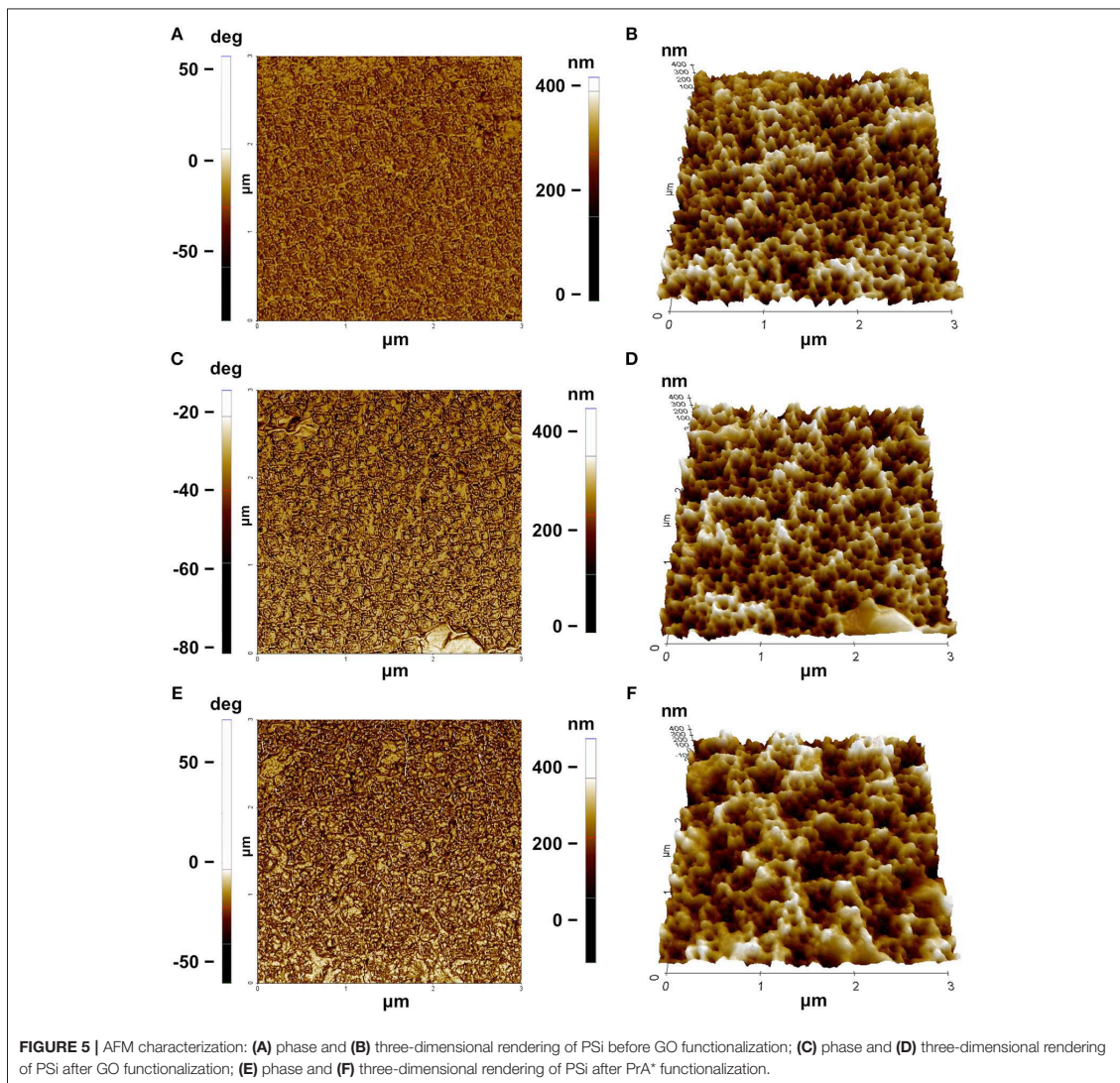
Fluorescent samples were imaged using an inverted fully automated confocal Nikon AR-1 microscope. The NIS elements software was used for image acquisition/elaboration.

RESULTS AND DISCUSSION

The structure of GO is characterized by a large amount of hydroxyl, epoxy, and carboxyl groups distributed on the whole surface, which makes this material much more hydrophilic than graphene (Dreyer et al., 2010). GO can be thus processed in aqueous solution in order to directly link biomolecules to its surface for the realization of a biosensor, whose sensing

mechanism could be based on changes of GO photoluminescence (Morales-Narváez and Merkoçi, 2012).

The fabrication of a multiparametric hybrid transducer, based on GO covalently immobilized on macroporous PSi surface, required the optimization of GO infiltration, and, before this step, a proper characterization of its behavior in aqueous solutions. GO solubility could be not assured in presence of a biological molecule, so that in **Supplementary Information (SI)** the interaction of free GO sheets and a FITC labeled PrA*, dispersed in demineralized water, is reported. The formation of the complex GO-PrA* was evaluated by DLS (Figure S1), ζ -potential measurements, UV-Vis (Figure S2), and photoluminescence (Figure S3). These results evidenced slight aggregation after GO-PrA* conjugation by EDC/NHS chemistry and a strong interaction between the two systems, which led to changes in UV-Vis absorbance and PL emission. Before infiltration, GO nanosheets had been sonicated until sheets size showed values lower than 100 nm to DLS (data not showed here). After size reduction, GO was covalently bound to the PSi surface following the functionalization scheme reported in **Figure 1**. Since the main drawback of PSi is its chemical instability in oxidizing environment, such as biological conditions (Ghulinyan et al., 2008), a method to stabilize the surface is mandatory in biosensing applications. A hydrosilylation process has thus been used as a valid strategy to make the PSi a more stable platform. After hydrosilylation, the Si-H surface bonds, typical of as-etched PSi, were converted in Si-C bonds, making the material more robust and resistant to hydrolysis and oxidation (**Figure 1**, Reaction 1). The thermal reaction between UDA and as-etched PSi induced the formation of an organic monolayer covalently attached to the surface through the formation of Si-C bonds



(Boukherroub et al., 2002). The carboxyl acid groups exposed on the surface could be used for further functionalization steps.

The GO grafting to the hydrosilylated-PSi surface required a cross-linker with exposed amino groups. In this study, the PEG molecule was used as bi-functional cross-linker. The covalent grafting of the BOC-NH-PEG-NH₂ was achieved by carbodiimide chemistry and, after amine group deprotection by acid hydrolysis of BOC with TFA (Figure 1, Reaction 2), the GO sheets were bound on amino-terminal PSi by essentially using the same chemistry (Figure 1, Reaction 3) (Harris et al., 1992). A biosensor transducer always includes a specific bioprobe that recognizes a ligand of interest. Placing a biomolecule into

a complex matrix, leaving its properties untouched, requires proper design and stability test of the final hybrid device. In this frame, the interaction between the GO-PSi architecture and a model biological molecule, the Protein A [pure and in its FITC labeled form (PrA*)] was studied. The PrA* was covalently bound to the hybrid device using same EDC/NHS chemistry (Figure 1, Reaction 4). In order to verify the effective covalent bond between GO-nanosheets/amino-modified PSi and PrA/GO-modified PSi promoted by carbodiimide chemistry, two negative control samples (NH₂-PSi_CTRL and GO-PSi_CTRL) were incubated with GO and PrA (pure and in its FITC labeled form), respectively, without EDC/NHS treatment. Since

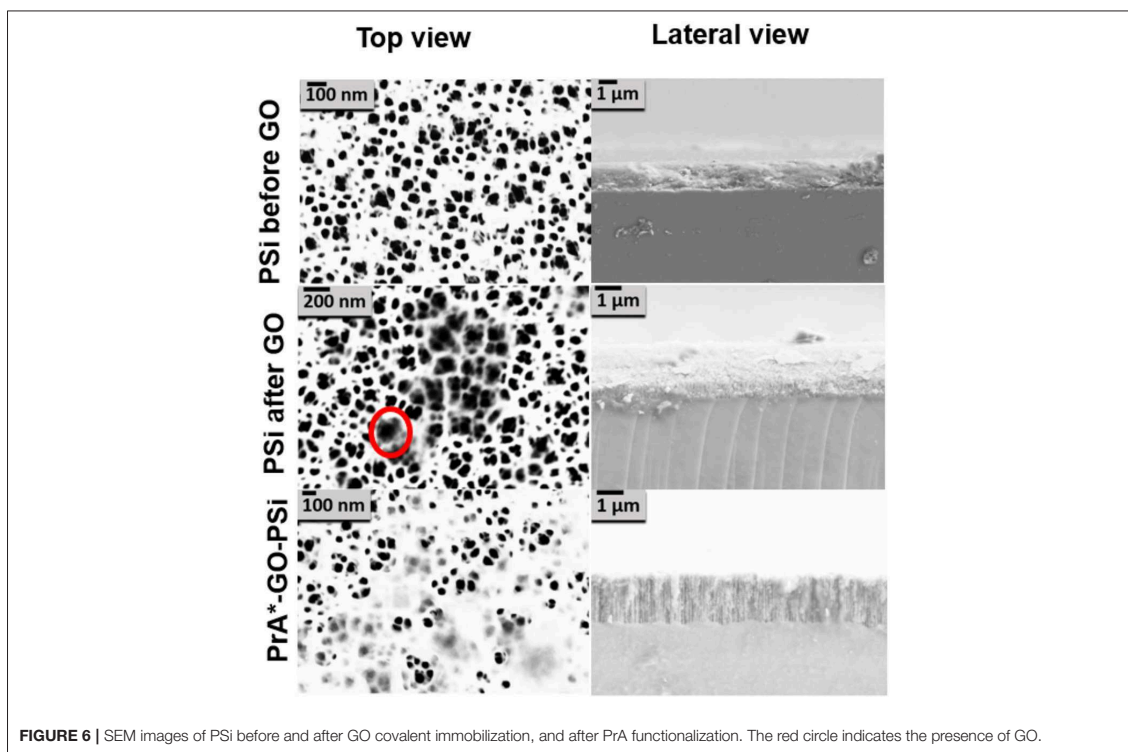


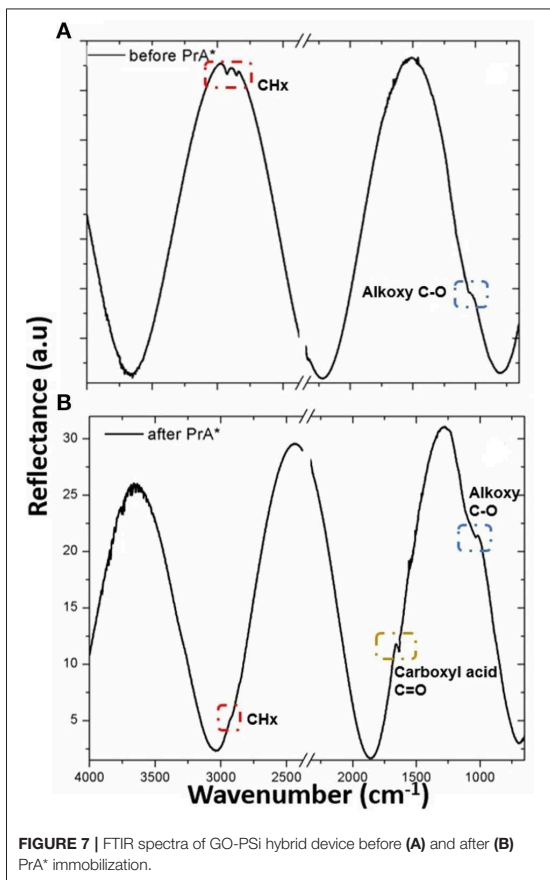
FIGURE 6 | SEM images of PSi before and after GO covalent immobilization, and after PrA functionalization. The red circle indicates the presence of GO.

carbodiimide conjugation should activate carboxyl groups by direct reaction with primary amines via amide bond formation, without EDC/NHS surface treatment, it was not possible to obtain any experimental evidence of covalently bonded GO and PrA on control samples.

Evaluation of surface wettability is a fundamental analysis in the development of such hybrid devices. After each functionalization step, different functional groups were exposed on the GO-PSi chip causing a change in the surface wettability. The as-etched PSi showed a hydrophobic surface quantified by a WCA value of $135 \pm 2^\circ$ (Figure 2A); a weak decrease of wettability value was evaluated after the hydrosilylation process (WCA = $120 \pm 1^\circ$), mainly due to carboxyl-terminal chain (Figure 2B); the introduction of the hydrophilic group BOC-NH-PEG-NH₂ induced a further decrease of WCA value to $85 \pm 3^\circ$ (Figure 2C); the removal of the BOC group and the exposure of the hydrophilic amino group, present in the PEG chain, was responsible of a WCA value of $60 \pm 2^\circ$ (Figure 2D); after the GO sheets binding, the presence of the oxygen functional groups made the PSi substrate more hydrophilic with a WCA of $50 \pm 5^\circ$ (Figure 2E); finally, the PrA* bioconjugation on GO-PSi surface increased the wettability of the surface up to a WCA of $70 \pm 2^\circ$ due to the presence of hydrophobic amino acids in the protein structure (Figure 2F). No change of surface wettability was observed in the case of negative

control samples (NH₂-PSi_CTRL and GO-PSi_CTRL, data not shown).

Since chemical functionalization and bioconjugation are additive processes from the material point of view, the optical thickness (i.e., the product of physical thickness, d , by the average refractive index n of the layer) of the obtained GO-PSi hybrid device, calculated by the FFT of the reflectivity spectrum, was expected to increase. The FFT peak position along the x-axis corresponds to two times the optical thickness (2OT) of the layer (Rea et al., 2014). In Figure 3 are reported the normal incidence reflectivity spectra of PSi before and after hydrosilylation (Figure 3A), and PEGylation process (Figure 3C) together with their corresponding FFTs (Figures 3B,D). Since the physical thickness d of PSi layer was fixed, the FFT peak shifts of about 90 nm, after UDA treatment, and of 145 nm after the PEGylation process were due to the increase of the average refractive index of the composite material. This result clearly indicated the two chemical functionalization steps added material layers to the PSi matrix. Figure 3D shows the reflectivity spectrum with the corresponding FFTs (Figure 3E) after the removal of the BOC protector group. The optimization of the reaction was confirmed as a blue shift of the peak of ~ 100 nm (Figure 3F), since the chemical substance has been removed. The GO functionalization and the PrA* conjugation on GO-PSi surface is reported in Figures 3G–J. A FFT peak shift of 90 nm after



the PSi surface grafting by GO was an evidence of the occurred functionalization. Finally, the PrA* covalently linked to the hybrid surface induced a further red shift of 275 nm. The analysis of reflectivity spectra of negative control samples (NH₂-PSi_CTRL and GO-PSi_CTRL) showed no significant change before and after treatment with GO and PrA solution, respectively, (data not shown).

The infiltration of GO into PSi was also analyzed by PL measurements. As it can be noted in **Figure 4A**, in the case of bare PSi, no signal of PL could be detected; on the contrary, the covalent grafting of GO into GO-PSi structure was revealed by a modulation of the PL signal. This was a clear evidence of the GO infiltration into the PSi matrix. The concentration of GO covalently conjugated to PSi was estimated as about 7.5 μg/mL; this value was obtained by comparing the PL spectrum of GO-PSi device with those of some solutions containing different concentrations of GO (**Figure S4**).

Figure 4B shows a comparison between PL and reflectivity spectra recorded by GO infiltrated in PSi monolayer. The modulation of PL intensity could be explained by considering

the optical theory of Fabry-Perot interferometer. Among all the wavelengths, λ_{em} emitted by GO infiltrated in PSi, only those fulfilling the relationship $L = m (\lambda_{em}/2n_{PSi})$, with L thickness of the PSi layer and m integer, could constructively interfere producing maxima in the PL spectrum of the hybrid structure. The distance between two consecutive photoluminescence maxima was about 67 nm, which well matched the free spectral range of the GO-PSi hybrid structure. In a previous work, we demonstrated that the presence of an interferometer under the GO layer was able to modulate GO photoluminescence (Rea et al., 2014). No change of PL spectra was observed in the case of negative control samples (NH₂-PSi_CTRL and GO-PSi_CTRL).

Morphological features of the surface were highlighted by AFM (**Figures 5A–F**). The AFM images of bare PSi revealed the presence of hillocks and voids (black zones) of about 100 nm distributed on the whole surface; after the functionalization of the PSi chip with GO, partial pore blocking was evident due to the presence of big GO nano-sheets (white zones) on the PSi surface and some coverage of the surface was visible after the PrA* bioconjugation. The roughnesses of the sample surfaces were calculated by analyzing the AFM images obtaining values of roughness statistical media (Rsm) equal to $0.22 \pm 0.01 \mu\text{m}$ for PSi sample before GO, $Rsm = 0.45 \pm 0.03 \mu\text{m}$ after GO, and $Rsm = 0.34 \pm 0.02 \mu\text{m}$ after PrA*. SEM images of conjugated sample are reported in **Figure 6**. In the top view, traces of GO (highlighted by red circle) on the PSi surface could be seen, and, in the lateral views, the few GO sheets into the porous matrix were visible. The final PrA*-GO-PSi hybrid device had quite almost covered surface and partially blocked pores.

A further analysis of GO-PSi hybrid device functionalization with PrA* was obtained by FTIR spectroscopy (**Figure 7**). The presence of GO onto hybrid device was confirmed by the presence of CH_x at 2,929–2,851 cm⁻¹ of carbon networks and the alkoxy C–O at 1,024 cm⁻¹ (Yang et al., 2009). After the incubation with the PrA*, the hybrid device PrA*-GO-PSi showed the stretching bands of CH_x at 2,924 cm⁻¹ peak, the amide I band at 1,651 cm⁻¹ associated with C=O stretching vibration and the alkoxy C–O band at 1,037 cm⁻¹ (Socrates, 2007). These data confirmed the covalent bonding of PrA* onto GO-PSi hybrid device.

Confocal microscopy was used for a deeper characterization of the PrA* infiltration process. In particular, **Figure 8A** is a 3D representation of all focal planes fluorescence recorded by the instrument, confirming the covalent bioconjugation of PrA*. In case of the negative control, the corresponding 3D image was completely dark (**Figure 8B**), and there was not any evidence of aspecific absorption to sample surface. **Figure 8C** shows the sequence of confocal laser scanning microscope images of the PSi monolayer infiltrated by the PrA*: the first image was the one of the top surface while the last was the one recorded at the bottom. **Figure 8D** quantifies the intensity profiles of the average fluorescence signal and it could be clearly seen that the labeled protein was distributed as a Gaussian function having its maximum value close to the center of the layer. This result

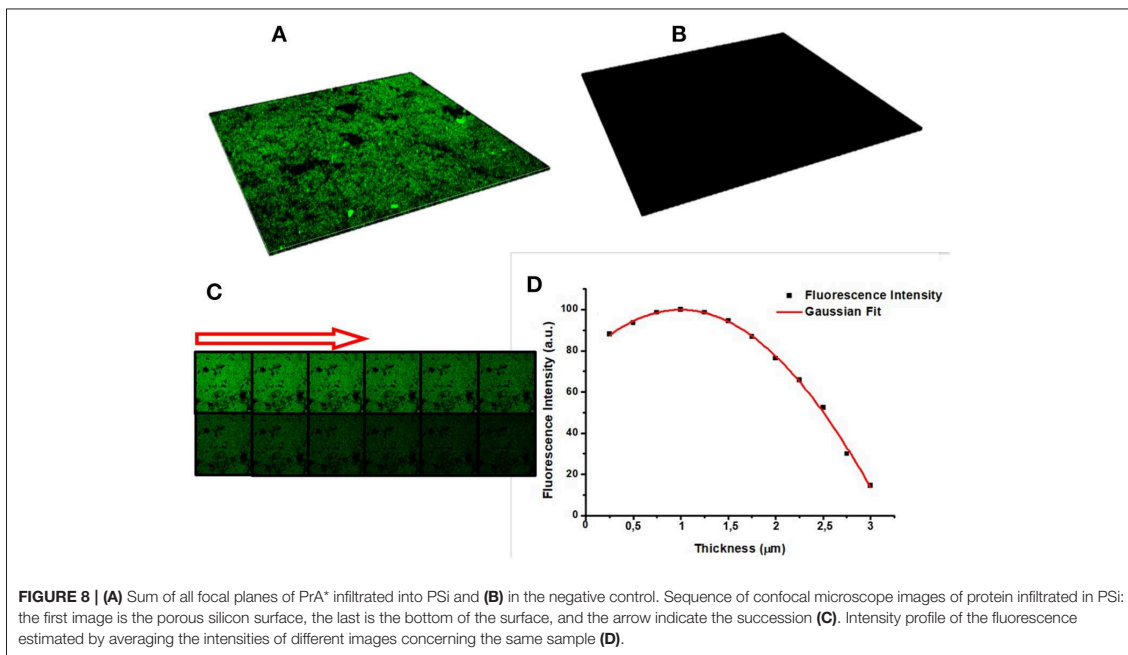


FIGURE 8 | (A) Sum of all focal planes of PrA* infiltrated into PSI and **(B)** in the negative control. Sequence of confocal microscope images of protein infiltrated in PSI: the first image is the porous silicon surface, the last is the bottom of the surface, and the arrow indicate the succession **(C)**. Intensity profile of the fluorescence estimated by averaging the intensities of different images concerning the same sample **(D)**.

further confirm that the protein was penetrated inside the pores (De Stefano and D'Auria, 2007).

CONCLUSIONS

A robust and chemically stable hybrid transducer for biosensing application based on GO, Psi, and PrA*, as a model bioprobes, has been designed and demonstrated. EDC/NHS coupling chemistry has efficiently grafted GO to Psi and PrA* to the GO-Psi matrix. Changes in reflectivity optical spectrum and in photoluminescence have been used to characterize the fabrication process but also the transducing features. AFM, SEM, and confocal imaging revealed the main features of the composite

structure. The results highlighted promising performances for next generation of multi-parametric biosensors.

AUTHOR CONTRIBUTIONS

All authors listed have made a substantial, direct and intellectual contribution to the work, and approved it for publication.

SUPPLEMENTARY MATERIAL

The Supplementary Material for this article can be found online at: <https://www.frontiersin.org/articles/10.3389/fchem.2018.00583/full#supplementary-material>

REFERENCES

- Boukherroub, R., Wojtyk, J. T. C., Wayner, D. D. M., and Lockwood, D. J. (2002). Thermal hydrosilylation of undecylenic acid with porous silicon. *J. Electrochem. Soc.* 149, H59–H63. doi: 10.1149/1.1432679
- Canham, L. (2017). *Properties of Porous Silicon*. Available online at: <http://trove.nla.gov.au/work/20545070?selectedversion=NBD13544299> (accessed August 2, 2017).
- Chien, C. T., Li, S. S., Lai, W. J., Yeh, Y. C., Chen, H. A., Chen, I. S., et al. (2012). Tunable Photoluminescence from graphene oxide. *Angew. Chemie Int. Ed.* 51, 6662–6666. doi: 10.1002/anie.201200474
- De Stefano, L., and D'Auria, S. (2007). Confocal imaging of protein distributions in porous silicon optical structures. *J. Phys. Condens. Matter* 19:395009. doi: 10.1088/0953-8984/19/39/395009
- Dreyer, D. R., Park, S., Bielawski, C. W., and Ruoff, R. S. (2010). The chemistry of graphene oxide. *Chem. Soc. Rev.* 39, 228–240. doi: 10.1039/B917103G
- Eda, G., Lin, Y. Y., Mattevi, C., Yamaguchi, H., Chen, H. A., Chen, I. S., et al. (2010). Blue photoluminescence from chemically derived graphene oxide. *Adv. Mater.* 22, 505–509. doi: 10.1002/adma.200901996
- Ghulinyan, M., Gelloz, B., Ohta, T., Pavesi, L., Lockwood, D. J., and Koshida, N. (2008). Stabilized porous silicon optical superlattices with controlled surface passivation. *Appl. Phys. Lett.* 93:061113. doi: 10.1063/1.2969294
- Gokus, T., Nair, R. R., Bonetti, A., Böhmeler, M., Lombardo, A., Novoselov, K. S., et al. (2009). Making graphene luminescent by oxygen plasma treatment. *ACS Nano* 3, 3963–3968. doi: 10.1021/nn9012753
- Gupta, A., Shaw, B. K., and Saha, S. K. (2014). Bright green photoluminescence in aminoazobenzene-functionalized graphene oxide. *J. Phys. Chem. C* 118, 6972–6979. doi: 10.1021/jp412156x
- Harris, J. M., Sedaghat-Herati, M. R., Sather, P. J., Brooks, D. E., and Fyles, T. M. (1992). "Synthesis of new poly(ethylene glycol) derivatives," in *Poly(Ethylene Glycol) Chemistry*, ed J. M. Harris (Boston, MA: Springer US), 371–381.

- Jung, J. H., Cheon, D. S., Liu, F., Lee, K. B., and Seo, T. S. (2010). A graphene oxide based immuno-biosensor for pathogen detection. *Angew. Chemie Int. Ed.* 49, 5708–5711. doi: 10.1002/anie.201001428
- Liu, Y., Dong, X., Chen, P. et al. (2012). Biological and chemical sensors based on graphene materials. *Chem. Soc. Rev.* 41, 2283–2307. doi: 10.1039/C1CS15270J
- Loh, K. P., Bao, Q., Eda, G., and Chhowalla, M. (2010). Graphene oxide as a chemically tunable platform for optical applications. *Nat. Chem.* 2, 1015–1024. doi: 10.1038/nchem.907
- Morales-Narváez, E., and Merkoçi, A. (2012). Graphene oxide as an optical biosensing platform. *Adv. Mater.* 24, 3298–3308. doi: 10.1002/adma.201200373
- Park, S., and Ruoff, R. S. (2009). Chemical methods for the production of graphenes. *Nat. Nanotechnol.* 4, 217–224. doi: 10.1038/nnano.2009.58
- Rea, I., Casalino, M., Terracciano, M., Sansone, L., Politi, J., and De Stefano, L. (2016). Photoluminescence enhancement of graphene oxide emission by infiltration in an aperiodic porous silicon multilayer. *Opt. Exp.* 24, 24413–24421. doi: 10.1364/OE.24.024413
- Rea, I., Sansone, L., Terracciano, M., De Stefano, L., Dardano, P., Giordano, M., et al. (2014). Photoluminescence of graphene oxide infiltrated into mesoporous silicon. *J. Phys. Chem. C* 118, 27301–27307. doi: 10.1021/jp506539n
- Sailor, M. J. (2012). *Porous Silicon in Practice: Preparation, Characterization and Applications*. San Diego, CA: Wiley-VCH.
- Sam, S., Touahir, L., Salvador Andresa, J., Allongue, P., Chazalviel, J. N., Gouget-Laemmel, A. C., et al. (2010). Semiquantitative study of the EDC/NHS activation of acid terminal groups at modified porous silicon surfaces. *Langmuir* 26, 809–814. doi: 10.1021/la902220a
- Shabir, Q., Webb, K., Nadarassan, D. K., Loni, A., Canham, L. T., Terracciano, M., et al. (2017). Quantification and reduction of the residual chemical reactivity of passivated biodegradable porous silicon for drug delivery applications. *Silicon* 10:349. doi: 10.1007/s12633-016-9454-4
- Socrates, G. (2007). *Infrared and Raman Characteristic Group Frequencies: Tables and Charts*. John Wiley & Sons. Available online at: <https://www.wiley.com/en-us/Infrared+and+Raman+Characteristic+Group+Frequencies%3A+Tables+and+Charts%2C+3rd+Edition-p-9780470093078> (accessed April 14, 2018).
- Terracciano, M., De Stefano, L., Borbone, N., Politi, J., Oliviero, G., Nici, F., et al. (2016). Solid phase synthesis of a thrombin binding aptamer on macroporous silica for label-free optical quantification of thrombin. *RSC Adv.* 6, 86762–86769. doi: 10.1039/C6RA18401D
- Wu, M., Kempaiah, R., Huang, P. J., Maheshwari, V., and Liu, J. (2011). Adsorption and desorption of DNA on graphene oxide studied by fluorescently labeled oligonucleotides. *Langmuir* 27, 2731–2738. doi: 10.1021/la1037926
- Yang, X., Zhang, X., Ma, Y., Huang, Y., Wang, Y., and Chen, Y. (2009). Superparamagnetic graphene oxide-Fe₃O₄ nanoparticles hybrid for controlled targeted drug carriers. *J. Mater. Chem.* 19, 2710–2714. doi: 10.1039/b821416f
- Zhang, J., Zhang, F., Yang, H., Huang, X., Liu, H., Zhang, J., et al. (2010). Graphene oxide as a matrix for enzyme immobilization. *Langmuir* 26, 6083–6085. doi: 10.1021/la904014z
- Zhang, Y., Wu, C., Guo, S., and Zhang, J. (2013). Interactions of graphene and graphene oxide with proteins and peptides. *Nanotechnol. Rev.* 2, 27–45. doi: 10.1515/ntrev-2012-0078

Conflict of Interest Statement: The authors declare that the research was conducted in the absence of any commercial or financial relationships that could be construed as a potential conflict of interest.

Copyright © 2018 Moretta, Terracciano, Dardano, Casalino, De Stefano, Schiattarella and Rea. This is an open-access article distributed under the terms of the Creative Commons Attribution License (CC BY). The use, distribution or reproduction in other forums is permitted, provided the original author(s) and the copyright owner(s) are credited and that the original publication in this journal is cited, in accordance with accepted academic practice. No use, distribution or reproduction is permitted which does not comply with these terms.

2.1.2 Early detection of Brugada Syndrome

The hybrid device discussed in the section 2.1.1 has been used for the development of a biosensor for the diagnosis of Brugada Syndrome, a genetic cardiac disease that can cause a sudden cardiac death in patients with a structural normal heart. The difficulty to detect this pathology makes it necessary to develop a device for early detection. Peptide nucleic acid (PNA) suits well for this purpose. Among the oligonucleotides, PNAs are the most powerful, showing a strong and sequence specific hybridization to complementary single strand DNA. Moreover, PSi is an ideal transducer material for the development of highly sensitive and selective biosensors. Furthermore, the integration of GO inside the PSi matrix gives the possibility to develop a multiparametric device.

Abstract

Brugada Syndrome (BS) is a genetically determined disease, often a cause of ventricular tacharrhythmias and that can lead syncope, cardiac arrest and sudden cardiac death. The syndrome is characterized by a typical electrocardiographic pattern which is often intermittent and difficult to detect. For this reason, there is the necessity to diagnose the disease in the early phase and, in this study, a PNA-GO-PSi multiparametric device is proposed for this purpose. To obtain a stable platform, a chemical procedure to bind covalently GO to PSi surface is developed. The GO-PSi hybrid device is further covalently conjugated to a probe, a peptide nucleic acid (PNA) sequence. The PNA plays an important role in the fabrication of a highly specific and sensitive biosensor for the detection of a specific SCN5A point-mutation responsible of BS.

Introduction

Brugada syndrome is a genetic disorder with autosomal dominant transmission, predisposing to the risk of malignant ventricular tacharrhythmias and associated to sudden death in young patients with a structurally healthy heart [56]. More than 500 genetic mutations have been identified as responsible of BS, most of which associated to the SCN5A gene, responsible of 20% of sudden deaths [57]. Diagnosis is based on the identification of a characteristic electrocardiographic pattern, observed either spontaneously or after the subministration of sodium-channel blocker drugs, in addition to genetic analysis [58]. As this pathology is difficult to diagnose, forward steps have been made in the field of nanotechnologies. Recently, nanostructured materials have

had rapid advancements in a wide range of applications, including electronic, medicine, food, pharmaceutical and so on [59], [60]. Applications of nanostructured materials in biomedical field show several advantages because they can bring new and unique properties, compared to traditional materials. It is reported the use of organic and inorganic materials for biomedical applications and, in particular, in this work, the attention is focused on the use of two inorganic nanostructured materials: graphene oxide and porous silicon.

Graphene oxide is a nanostructured material generally obtained by oxidation of graphite. The precise structure of GO is uncertain but all the models proposed assume the presence of reactive functional groups on its surface [61], [62]. GO is characterized by hydrophobic parts, derivate from graphite structure, but also hydrophilic parts, characterized by oxygen functional groups in the form of hydroxyl, epoxy, carboxyl and carbonyl groups on the basal plane and edge [63]. The oxygen-containing functional groups ensure the water-solubility of the material and they serve as site for chemical functionalization [64], [65]. These properties, in addition to mechanic, optical, electronic and thermal ones, make GO useful for the development of novel biological and chemical platforms. Moreover, GO exhibits a broad PL emission from 500 to 800 nm on exposure to UV near radiation, opening new perspectives in optoelectronic [55]. Unfortunately, the GO PL is very weak because of the oxygen-containing functional groups producing non radiative recombination between their electrons and holes present in sp^2 clusters [66]. Oxidation or reduction mechanisms can be used to get higher the PL of GO [67], [68]. Another valid approach to enhance the PL emission of GO consists in the infiltration of the material into large specific area substrate, such as PSi.

PSi is a nanostructured material obtained by electrochemical dissolution of crystalline silicon in hydrofluoric acid (HF) -based solution. Modulating opportunely the etching parameters (i.e., HF concentration, current density) and the characteristics of silicon substrate (i.e., dopant type, resistivity), there is the possibility to have tunable pore size and morphology [1]. Moreover, due to its optical properties and a sponge-like morphology, PSi has been largely used as a material for drug delivery and biosensing applications [1], [69]. In particular, the combination of GO and PSi, in a single hybrid nanosystem, was widely explored for targeting brain tissue [70].

Moreover, in recent papers, the electrostatic infiltration of GO onto aminomodified PSi or its covalent grafting onto hydrosilylated PSi were reported. In the first case, GO nanosheets were infiltrated by spin coating using homogeneous monolayer and Thue-Morse multi-layered

structure, made of 64 layers, observing, in both cases, an intense and modulated PL signal emitted from GO, adsorbed on the hybrid structure. This effect was not observed in the case of GO deposited on crystalline silicon [53], [54]. The same effect was obtained in the case of the covalent grafting of GO onto macroporous silicon [71]. Rather than the electrostatic interaction, the covalent bond leads a robust and stable hybrid device useful for biosensing applications. For this reason, the goal of this work is to use the covalent strategy to graft the GO to PSi matrix, as described in [71], and use this hybrid device for the detection of BS. Our basic approach involves the covalent immobilization of a peptide nucleic acid (PNA) as probe onto PSi-GO device, followed by the hybridization with DNA target. The advantages of using a PNA as probe rather than a DNA molecule is due to its intrinsic properties. In particular, thanks to its neutral charge, a PNA shows strong and specific hybridization to complementary single stranded DNA: as a consequence, PNA/DNA base mismatches are more destabilizing than a similar mismatch in a DNA/DNA duplex [72]. This feature makes it particularly useful for the diagnosis of genetic mutations. In summary, the device developed is a multiparametric optical biosensor whose operating mechanism is based on the changes of PSi reflectance and GO photoluminescence. Furthermore, the PNA, used in this study, is able to detect SCN5A point-mutation region responsible of BS.

Materials and Methods

Chemicals

Hydrofluoric acid (HF), undecylenic acid (UDA), N-(3-Dimethylaminopropyl)-N'-ethylcarbodiimide hydrochloride (EDC), N-hydroxysuccinimide (NHS), MES hydrate, Dimethyl sulfoxide (DMSO), tert-Butyloxycarbonyl-NH-PEG-Amine (BOC-NH-PEG-NH₂), trifluoroacetic acid (TFA), chloroform, tetrahydrofuran were purchased from Sigma Aldrich (St. Louis, MO, USA). Graphene oxide (GO) nanosheets were purchased from Biotool.com (Houston, TX, USA) as a batch of 2 mg/ml in water with a nominal size sheets between 50 and 200 nm.

Preparation of Graphene oxide

Graphene oxide (GO), 1.5 mg ml⁻¹, was sonicated using an ultrasonic processor for 1h in ice at 50% of available power amplitude. The GO solution was centrifuged for 90 min at 15000 rpm and the pellet was dissolved in DMSO.

Porous silicon layer fabrication and Hydrosilylated process

PSi structure was fabricated by electrochemical etching of n-type crystalline silicon (0.01-0.02 Ω cm resistivity, <100> oriented and 500 μm in thick) in HF (5% in weight)/ethanol solution at room temperature (RT). To remove the oxide layer native, the silicon substrate was immersed in HF solution for 2 min before the etching process. A current density of 20 mA cm^{-2} for 90s was applied to obtain a single layer of PSi with 61% in porosity ($n_{ps} = 1.83$ at $\lambda = 1.2 \mu\text{m}$), thickness L of 2.1 μm and pore dimension between 50 and 250 nm. The as-etched PSi was placed in a Schlenk tube containing deoxygenate neat UDA (99% v/v). The reaction was conducted at 110°C for 18h in argon. The hydrosilylated-PSi was extensively washed in chloroform and tetrahydrofuran [73].

PEGylation of PSi Layer and Covalent grafting of GO

The carboxyl acid groups of UDA were activated by EDC/NHS (0.005 M in 0.1 M MES buffer) for 90 min at RT. Afterwards, a solution containing BOC-NH-PEG-NH₂ (0.004 M, overnight at 4°C) was used to recover completely the PSi chip. To remove the excess of reagent, the sample was rinsed in deionized water. A solution of TFA (95% v/v, 90min, RT) was used to deprotect the amino group of the PEG molecule. The PSi chip was washed with deionized water. The sonicated GO was activated by EDC/NHS (0.029:0.020 M in DMSO, overnight, RT) and added to the PSi chip, to allow the covalent bond. Then, the sample was rinsed in deionized water to remove the unreacted GO.

Covalent grafting of PNA on PSi Layer

The GO-PSi device was exposed to 100 μM of PNA (COOH-KKTCGTGGCTCGGGNHCOCH₃) in presence of EDC/NHS (0.040:0.016 M in MES buffer, overnight, RT) and, then, washed in deionized water.

DNA hybridization

Complementary (5'-AGGAGAGCACCGAGCCCCTGAG-3') and non-complementary (5'-CCTTTTTTTTTT-3') DNA sequence were incubated on the chip for two hours. The sample was gently rinsed in deionized water to remove the unhybridized target.

Spectroscopic Reflectometry

The reflectivity spectra of PSi were measured at normal incidence by means of a Y optical reflection probe (Avantes), connected to a white light source and to an optical spectrum analyser (Ando, AQ6315B). The spectra were collected over a range of 600-1600 nm with a resolution of 1 nm. Reflectivity spectra shown in the work are the average of three measurements. The error bars represent the standard deviations (SD)

associated to the mean values obtained on the triplicated measurements.

Steady-State Photoluminescence

Steady-state photoluminescence spectra were excited by a continuous wave He-Cd laser at 442 nm (KIMMON Laser System). PL was collected at normal incidence to the surface of sample through a fiber, dispersed in spectrometer (Princeton Instruments, SpectraPro 300i), and detected using a Peltier cooled charge coupled device (CCD) camera (PIXIS 100F). A long pass filter with a nominal cut-on wavelength of 458 nm was used to remove the laser line at monochromator inlet. The PL graphs reported are the average of three measurements.

Laser Scanning Confocal Microscopy

Fluorescent samples were imaged using an inverted fully automated confocal Nikon AR-1 microscope. The NIS elements software was used for image acquisition/elaboration.

Results and Discussion

Graphene oxide is a layered material obtained by the oxidation of graphite. Differently from graphene, it contains oxygenated functional groups (i.e., alcohol, epoxide, ketone, aldehyde and carboxyl), giving to the material high hydrophilic properties [61]. Due to the presence of these groups, GO can be functionalized with different substrates (i.e., polymers, gold nanoparticles, DNA, protein and so on) for the development of GO-based devices [74], [75]. In this work, the carboxyl groups of GO were covalently bound to an opportunely-modified macroporous silicon substrate. Moreover, the fabrication of the multiparametric device requires the optimization of GO infiltration. A sonication process was mandatory to obtain nanosheets of GO small in size. Size distribution of GO was investigated by DLS analysis, revealing the presence of two peaks corresponding to 30 ± 10 and 130 ± 70 size populations. It is important to underline that the peaks, obtained by DLS measurements, are relative to the scattering intensity of the material. Macroporous porous silicon, with a size pore >50 nm, was used to allow a better infiltration of GO sheets.

Prior to the infiltration of GO into PSi matrix, a passivation process was required to avoid the aging of the transducer material. In fact, PSi reacts spontaneously to form an oxide layer when it is exposed to air or water [1], [76]. A schematic diagram of PSi surface functionalization is reported in Figure 2.1.

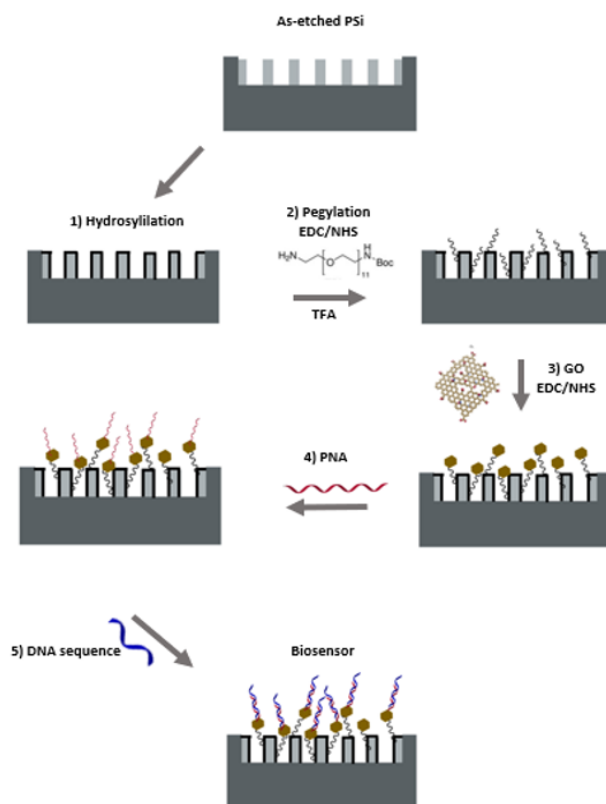


Figure 2.1 - Functionalization scheme of GO-PSi hybrid device. **Reaction 1:** hydrosilylation process of PSi by UDA, 18h at 110°. **Reaction 2:** PEGylation process of PSi by EDC/NHS chemistry and deprotection of NH-BOC by TFA treatment. **Reaction 3:** GO conjugation to PEGylated-PSi by EDC/NHS. **Reaction 4:** immobilization of PNA by covalent chemistry. **Reaction 5:** DNA hybridization.

The passivation of the PSi surface was performed through the hydrosilylation. This process involves the addition of an alkene or alkyne to hydrogen-terminated-PSi, converting Si-H bonds in Si-C bonds, thus conferring to the material increased stability and resistance to atmospheric or chemical attacks. In this case, UDA was the alkene that thermally reacted for the passivation of the surface. After thermal hydrosilylation, a wide variety of organic functional groups can be placed on PSi surface, available for the coupling with several molecules. In particular, the reaction between UDA and as-etched PSi led to the formation of an organic monolayer covalently attached on the

surface through Si-C bonds and having carboxyl acid groups at the end of the carbon chain [77].

The binding of GO to PSi surface was allowed by a homofunctional cross-linker, bearing two amino functionalities (BOC-NH-PEG-NH₂). This linker was bound to PSi substrate via carbodiimide chemistry. After the deprotection of amino group through TFA treatment, GO nanosheets were bound to amino-terminal PSi by using the same chemistry [78]. At this step, the carboxyl groups of GO were available to bind the biomolecular probe. The goal of this work was the development of a device for the early diagnosis of BS.

In recent years, oligonucleotides-based biosensors, having DNA or RNA as sensing elements, have been extensively developed. These have attracted great attention due to their potential application for the diagnosis of several kinds of disease [79]. More recently, the introduction of peptide nucleic acid (PNA) has opened exciting opportunities for DNA biosensors, thanks to their unique physico-chemicals properties. A PNA is an artificially synthesized polymer similar to DNA. It differs from DNA because the deoxyribose-phosphate backbone is replaced by a pseudo-peptide backbone, N-(2-aminoethyl) glycine. Due to the neutral peptide backbone, the PNA/DNA hybridization is stronger than the one between DNA/DNA strands, due to the lack of electrostatic repulsion. Furthermore, the capability to discriminate the single point mutations, makes PNA a powerful tool for the diagnosis of genetic diseases. In this work, a specific PNA molecule, has been used as bioprobe to interact specifically with an appropriate sequence of sodium channel 5A (SCN5A) gene.

Each step of functionalization was opportunely verified by several techniques.

PSi layer acts as a Fabry-Perot interferometer in which the substitution of air inside the pores induces a change of refractive index and, as a consequence, a shift of the reflectivity spectra [80]. The shifts, analysed after each functionalization step, are schematically reported in the bar graph, shown in Figure 2.2. The hydrosilylation caused a red-shift of the reflectivity spectrum of 12 nm, followed by further 25 nm of red-shift, after the PEGylation process. This effect clearly highlights the addition of material layers to PSi matrix. On the contrary, the deprotection of amino groups by TFA treatment was confirmed by 12 nm of blue shift of the spectrum, due to the removal of BOC protector group. It is important to emphasize that also the superficial oxidation of the porous matrix can cause the blue shift of the reflectivity spectra. Therefore, as described above, to avoid the oxidation process, in this work, the PSi surface was opportunely passivated, inducing the formation of Si-C

bonds. These bonds are much less polar than Si-O bonds and, as consequence, more resistant to nucleophilic attack by water or other oxidizing agents [81].

Finally, the GO binding and the subsequently immobilization of PNA to PSi surface were confirmed by a further red shift of the corresponding spectra (9 and 8 nm, respectively). These data are an evidence of an effective functionalization of the device.

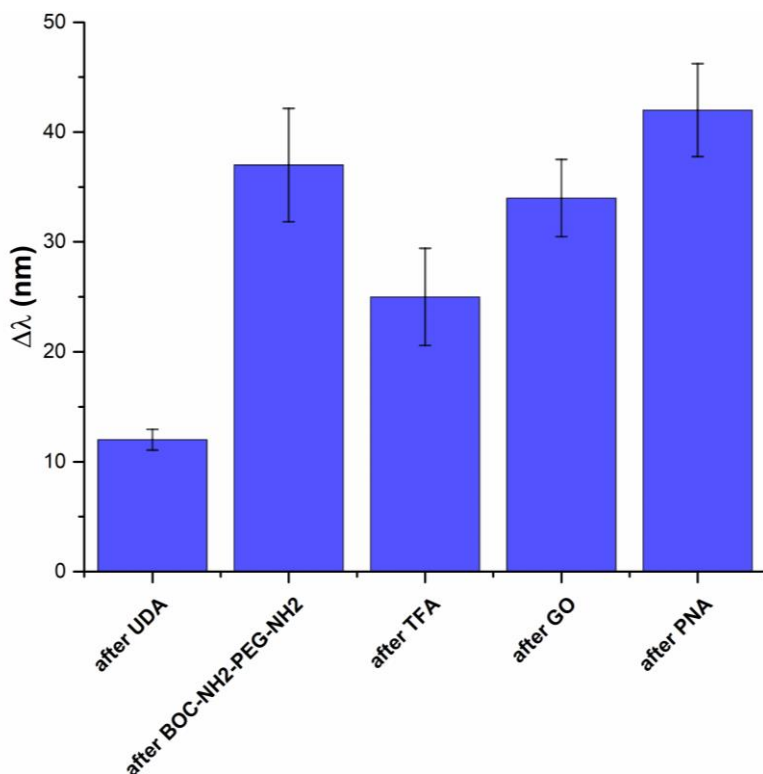


Figure 2.2 – Reflectivity spectra shifts obtained after each functionalization step. The $\Delta\lambda$ is computed with respect to the bare PSi, taken as a 0 reference value.

PL measurements, by using an excitation wavelength of 442 nm, were performed to evaluate the infiltration of GO inside the porous matrix. The data, shown in Figure 2.3 (A), underlined that no PL was measured in the case of bare PSi, while a modulation of the signal was revealed after the covalent grafting of GO. A comparison between PL and reflectivity spectra of GO infiltrated in PSi matrix is shown in Figure 2.3 (B). The modulation of PL signal can be explained by considering the theory of Fabry-Perot interferometer. Among all the wavelengths, λ_{em} , emitted by GO infiltrated in PSi, only those fulfilling the relationship

$L=m(\lambda_{em}/2n_{PSi})$, with L thickness of P*Si* layer and m integer, can constructively interfere forming maxima in PL spectrum of the hybrid structure. The distance between two consecutive PL maxima is 63 nm, corresponding with the free spectral range of GO-P*Si* hybrid structure [54].

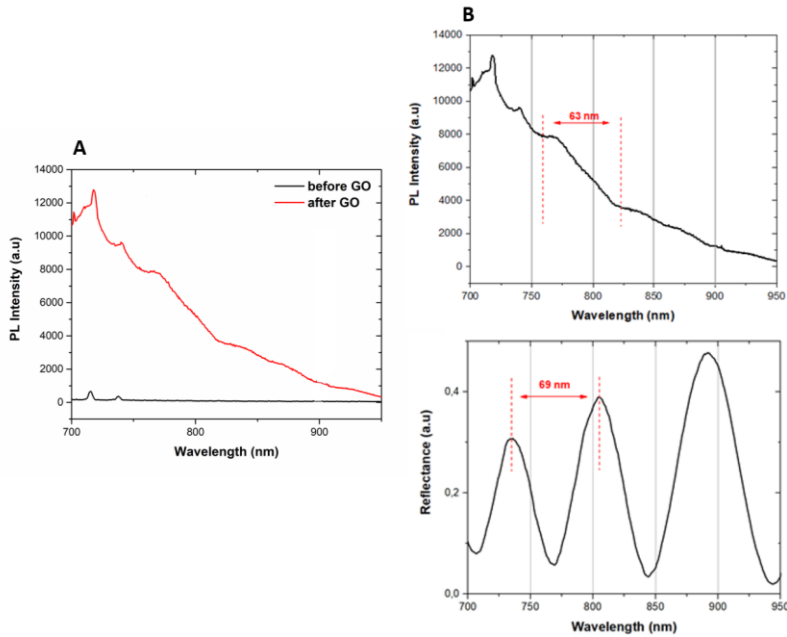


Figure 2.3 - (A) Photoluminescence spectra of P*Si* before (black line) and after (red line) GO infiltration at an excitation wavelength of 442 nm. **(B)** Comparison between photoluminescence spectrum (upper graph) and reflectivity spectrum (lower graph) of GO-P*Si* hybrid device.

The grafting of the bioprobe to the GO nanosheets was demonstrated by the quenching of GO PL, shown in Figure 2.5 (A). As described previously, GO is characterized by the presence of oxygen-functionalities on the basal plane and edges, responsible of defects on the two-dimensional surface, on which optoelectronic properties of the material depend. Some of these sites are involved in the covalent grafting of PNA, reducing the available radiative emission sites and as a consequence the PL emission [55].

The interest in the use of PNA as bioprobe is essentially due to its capability to discriminate the single-point mutations associated to genetic diseases. In our case, the Brugada Syndrome is the disease of

interest. To evaluate the capability of the device detecting the occurred hybridization, the PNA-PSi device was incubated with a complementary sequence of DNA and the response obtained was analysed by reflectance.

It was noted that by varying the pH of the hybridization conditions, different reflectivity spectra were registered. In fact, by conducting the experiment in PBS solution at pH 7.4, a 3 nm shift of the spectrum to lower wavelengths was measured (data not shown). This effect could be ascribed to the corrosion of the material due to the accumulation of surface charges [82], obtained by the sum of deprotonated carboxyl acid groups on graphene oxide [83], and DNA charges.

In contrast, using aqueous solution at pH 5, the reflectivity analysis showed the effective interaction between PNA-GO-PSi hybrid device and *c*-DNA sequence. In particular, small red shifts of 1, 3 and 5 nm were measured using 25, 50 and 75 μM of DNA, respectively. Saturation was reached by using a target concentration of 100 μM (Figure 2.4 A). Moreover, a dose-response curve is reported in Figure 2.4 B. The specificity of the device was also confirmed by exposing the chip to non-complementary DNA sequence, in fact, no shift was recorded in the reflectivity spectrum (Figure 2.4C).

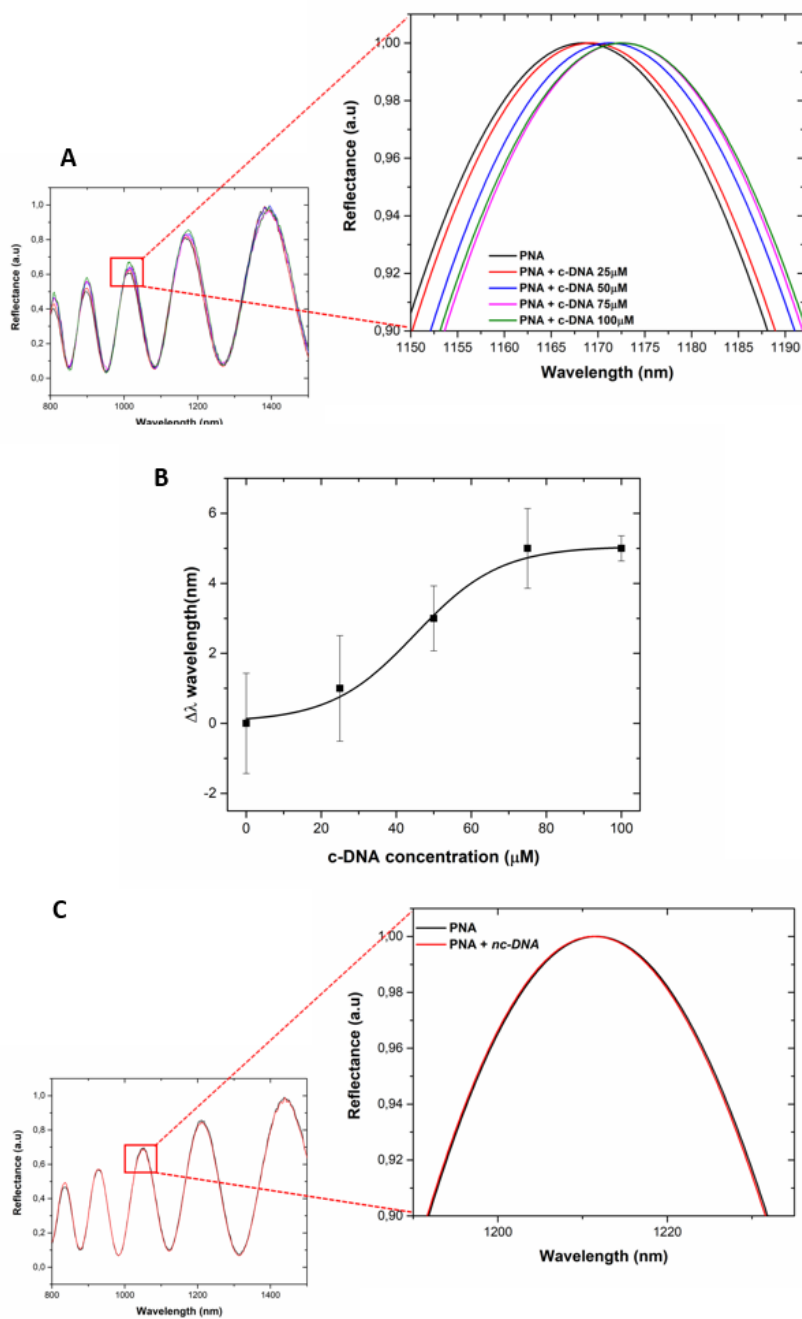


Figure 2.4 - (A) Reflectivity spectra of PNA-GO-PSi device after the *c*-DNA incubation. **(B)** Dose-response curve as a function of the *c*-DNA concentration. **(C)** Reflectivity spectra of PNA-GO-PSi device after the *nc*-DNA incubation.

The PNA/DNA interaction was not detectable by using PL analysis because no variation of signals was measured (Figure 2.5 B).

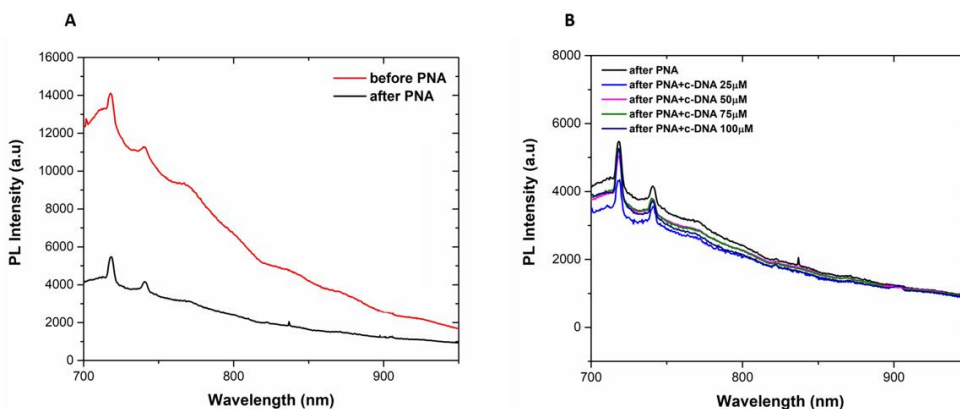


Figure 2.5 - (A) Photoluminescence spectra of PSi before (red line) and after (black line) PNA immobilization, at an excitation wavelength of 442 nm. **(B)** Photoluminescence spectra of PSi-PNA after DNA hybridization.

The samples were also monitored *via* fluorescence microscopy by using *c*-DNA and *nc*-DNA sequences, both labelled. No fluorescent signal was detected when the chip was incubated with the *nc*-DNA, while a fluorescent signal was measured in the sample incubated with the complementary sequence (Figure 2.6 A). Moreover, an increasing fluorescence trend is observed as function of the *c*-DNA* concentration (Figure 2.6 B). Confocal microscopy was used as further technique to confirm the infiltration of DNA* into the pores. Figure 2.6 (C) is a 3D representation of all the fluorescent focal planes recorded by the instrument while, a side view of the collected focal planes is shown in Figure 2.6 (D). In the case of hybridization, performed at pH 5, the fluorescence confirmed the occurred hybridization between the hybrid device and the corresponding target. In contrast, the negative control, in which DNA* was infiltrated into GO-PSi device, showed a slight fluorescence related to aspecific adsorption phenomena whose intensity is negligible (Figure 2.6 E).

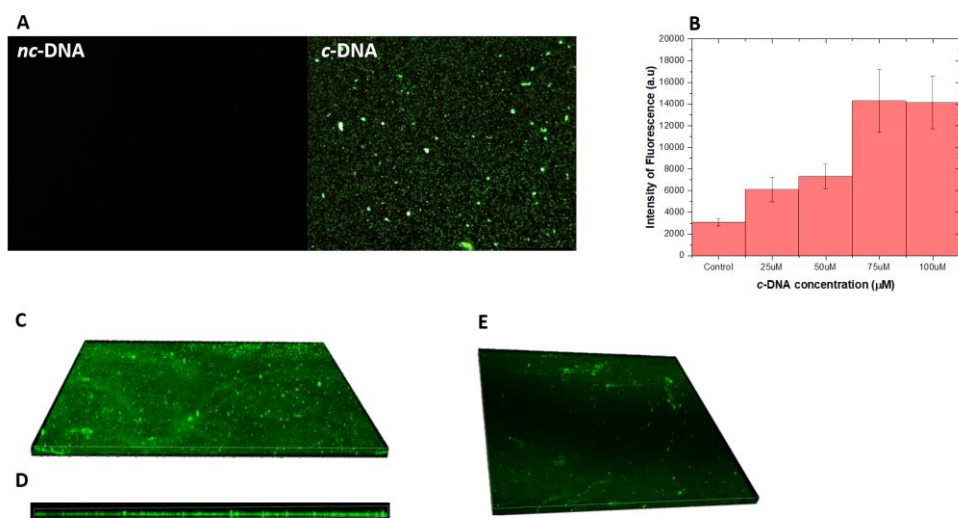


Figure 2.6 - (A) Fluorescence images of PNA-GO-PSi device incubated with *nc*-DNA and *c*-DNA. **(B)** Intensity of fluorescence as a function of *c*-DNA concentration. The intensity of fluorescence was calculated recording different spots of the same sample. Top view **(C)** and side view **(D)** of the DNA* infiltrated in the PNA-GO-PSi device, **(E)** top view of the DNA* infiltrated in GO-PSi device (negative control), analysed by confocal microscopy.

Conclusions

A stable multiparametric device was developed in order to detect the SCN5A point mutation sequence region responsible for Brugada Syndrome. A PNA sequence was chosen as probe, covalently linked to the device, and able to recognise the complementary DNA sequence, thanks to its high specificity. The changes in the reflectivity optical spectra and photoluminescence have been used to analyse the functionalization steps. Reflectivity analysis, fluorescence and confocal microscopy were used to detect the hybridization process. Data obtained confirm the development of a label-free biosensor with high stability, fast response time, high sensibility and specificity for the detection of BS.

2.2 Porous silicon Quantum Dots for bioimaging

Quantum dots (QDs) are semiconductor nanocrystals with dimension between about 1 and 10 nm, that have attracted great interest in the scientific community thanks to their unique optoelectronic characteristics, completely different from those of their bulk counterpart. They show a broad absorption spectra, size-tunable PL emission, high quantum yield (QY) and high stability against photobleaching and chemical degradation [84]. Optoelectronic devices, solar cells are only few examples of applications for this class of materials [85], [86]. Moreover, they have been intensively studied for possible use in biomedical area, such as bioimaging and bioanalysis [87]. In this context, the heavy-metals QDs are not applicable in medicine because of their toxicity. Instead, porous silicon NPs (PSiNPs) represent a valid alternative because of their biocompatibility, biodegradability and tunable porous structure. Hence, the biomedical applications require the choice of a stable material with a steady-state PL. However, PSiNPs tend to oxidize in aqueous medium, leading, as consequence, the PL degradation. To avoid these phenomena, they need a passivation process that will be discussed in the section 2.2.1. Moreover, the PSiNPs as label-free luminescent probe for *in vivo* imaging will be proposed in section 2.2.2.

2.2.1 Characterization of chemically modified PSiNPs

Photoemissive properties and stability of undecylenic acid-modified porous silicon nanoparticles in physiological medium

Cite as: Appl. Phys. Lett. **114**, 113701 (2019); <https://doi.org/10.1063/1.5079469>

Submitted: 31 October 2018 . Accepted: 05 March 2019 . Published Online: 19 March 2019

Chiara Schiattarella , Monica Terracciano, Thomas Defforge , Gaël Gautier, Bartolomeo Della Ventura, Rosalba Moretta, Luca De Stefano , Raffaele Velotta , and Ilaria Rea



View Online



Export Citation



CrossMark

ARTICLES YOU MAY BE INTERESTED IN

Droplet actuation on superhydrophobic substrates via electric field gradients

Applied Physics Letters **114**, 113702 (2019); <https://doi.org/10.1063/1.5080241>

Bandgap narrowing and Mott transition in Si-doped $\text{Al}_{0.7}\text{Ga}_{0.3}\text{N}$

Applied Physics Letters **114**, 113501 (2019); <https://doi.org/10.1063/1.5086052>

Coexistence of dielectric relaxation and magnetic relaxation in compressively strained $\text{BiFeO}_3/\text{Ba}_{0.7}\text{Sr}_{0.3}\text{TiO}_3$ superlattices

Applied Physics Letters **114**, 112902 (2019); <https://doi.org/10.1063/1.5085350>

Lock-in Amplifiers up to 600 MHz

starting at

\$6,210



Zurich Instruments

Watch the Video 

Photoemissive properties and stability of undecylenic acid-modified porous silicon nanoparticles in physiological medium

Cite as: Appl. Phys. Lett. **114**, 113701 (2019); doi: [10.1063/1.5079469](https://doi.org/10.1063/1.5079469)

Submitted: 31 October 2018 · Accepted: 5 March 2019 ·

Published Online: 19 March 2019



Chiara Schiattarella,^{1,2} Monica Terracciano,¹ Thomas Defforge,³ Gaël Gautier,³ Bartolomeo Della Ventura,² Rosalba Moretta,^{1,4} Luca De Stefano,^{1,a)} Raffaele Velotta,^{2,a)} and Ilaria Rea¹

AFFILIATIONS

¹Institute for Microelectronics and Microsystems, National Research Council, Via P. Castellino 111, 80131 Naples, Italy

²Department of Physics "E. Pancini," University of Naples "Federico II," Via Cinthia, 80126 Naples, Italy

³Université de Tours, GREMAN UMR 7347, INSA-CVL, CNRS, 16 Rue Pierre et Marie Curie, 37071 Tours Cedex 2, France

⁴Department of Chemical Sciences, University of Naples "Federico II," Via Cinthia, 80126 Naples, Italy

^{a)}Authors to whom correspondence should be addressed: luca.destefano@na.imm.cnr.it and raffaele.velotta@unina.it

ABSTRACT

Porous silicon nanoparticles (PSiNPs) are non-toxic photoluminescence imaging agents whose potential for biophotonic applications has been widely reported in recent years. However, this material suffers from intrinsic limitations, due to its chemical instability and rapid photoluminescence extinction on exposure to the physiological environment. In this letter, a mild functionalization procedure for PSiNP stabilization, based on undecylenic acid conjugation *via* hydrosilylation, is proven to be effective under simulated biological conditions [phosphate-buffered saline (PBS) 0.1 M, pH = 7.4]. Once stored in isopropanol, bare and hydrosilylated PSiNPs (h-PSiNPs) show similar photoemissive properties: photoluminescence quantum yield (>10%), steady-state spectra, and emission lifetime. Interestingly, the behaviour of these nanoparticles is completely different in the physiological medium: the morphology and the photoluminescence emission of bare PSiNPs completely degrade within 2 h, whereas a full preservation of the same features up to 6 h is demonstrated for h-PSiNPs.

Published under license by AIP Publishing. <https://doi.org/10.1063/1.5079469>

Porous silicon (PSi) can be fabricated *via* electrochemical etching of crystalline silicon in hydrofluoric acid (HF)-based solution.¹ The dissolution process produces a hydrophobic (since hydrogen terminated) nanostructured material, constituting a network of empty spaces (i.e., pores) and nanometric columns of silicon with a distribution of nanocrystalline domains. In nanocrystals, band-to-band recombination of quantum-confined excitons occurs, resulting in an efficient photoluminescence (PL) emission from PSi at room temperature.^{2,3} The intrinsic PL emission of PSi is characterized by a lifetime in the microsecond range, due to the low transition rates of the radiative recombination channels, which is significantly higher than that of standard organic dyes or direct-bandgap semiconductor quantum dots (from tens of nanoseconds on up⁴). This unique feature, together with the PL quantum yield (QY) up to 20%⁵ and other properties such as biocompatibility,⁶ as well as tunable surface chemistry,⁷ makes photoluminescent PSi nanoparticles (PSiNPs) of great appeal in the bioimaging field. Unlike heavy metal-based quantum dots, PSiNPs allow

in vitro and *in vivo* monitoring without toxic effects in biological organisms.⁸ Promising results were obtained in fluorescence imaging using biocompatible silicon nanoparticles as photoluminescent probes⁸ or by exploiting their long-lived PL emission for time-gated *in vivo* imaging.⁹

PSiNPs suffer from poor chemical stability in aqueous media. The Si-H bonds on a freshly prepared PSi surface rapidly change to Si-O-Si bonds in an oxidizing environment. The PSi crystalline nanostructure is strongly modified due to the introduction of surface defects which may crucially affect PL emission.¹⁰ Signal degradation and fast PL quenching make untreated PSiNPs unsuitable for long-term observations, thus limiting their application in bioimaging. Several surface passivation protocols were developed for PL stabilization, including controlled oxidation of PSiNPs in sodium tetraborate¹¹ or coating with polymers.¹² Among all the possible strategies, the covalent addition of functional groups to the PSi surface is an interesting alternative approach to PSi passivation.¹³

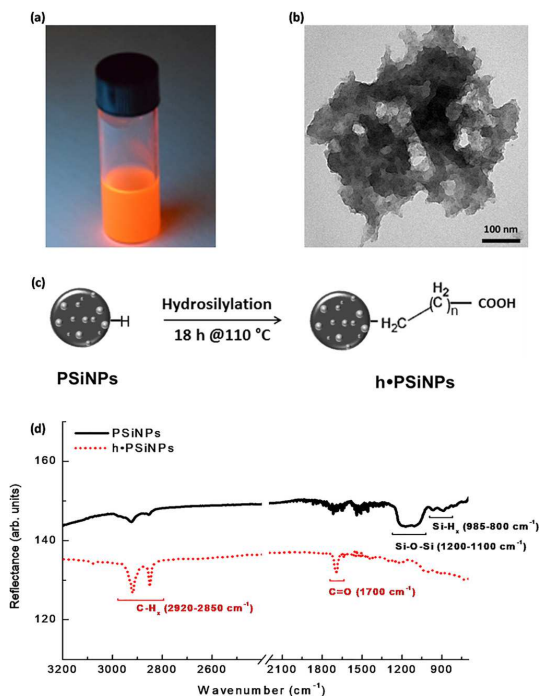


FIG. 1. (a) Colloidal suspension of PSiNPs in IPA, illuminated by a low power UV light. (b) Representative TEM image of a PSiNP. (c) Hydroxylation of PSiNPs. (d) Comparison between FT-IR spectra of bare PSiNPs and hydroxylated PSiNPs (h-PSiNPs); the spectra were vertically shifted for clarity.

In this work, photoluminescent PSiNPs, fabricated by electrochemical etching, are chemically modified *via* hydrosilylation with undecylenic acid (UA). Replacing metastable Si-H bonds with more stable Si-C ones leads to covalent surface passivation that prevents uncontrolled surface oxidation and PL degradation. The functionalization process does not modify the emission properties of nanoparticles in isopropanol, while it stabilizes the PL under physiological conditions.

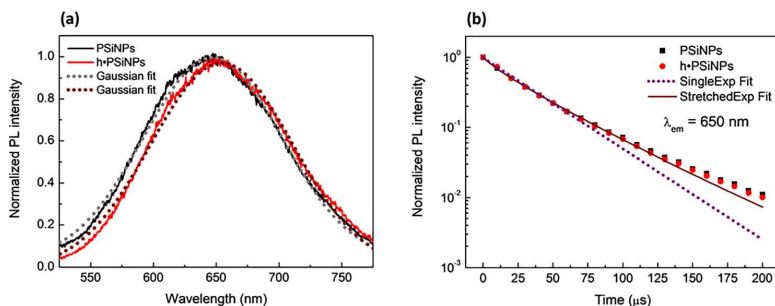


FIG. 2. (a) Normalized steady-state PL spectra of PSiNPs and h-PSiNPs suspended in IPA ($\lambda_{ex} = 365$ nm). The data were fitted by a Gaussian function ($R^2_{PSiNPs} = 0.994$; $R^2_{h-PSiNPs} = 0.992$). (b) Normalized PL decays of PSiNPs and h-PSiNPs suspended in IPA measured at $\lambda_{em} = 650$ nm ($\lambda_{ex} = 365$ nm); the stretched exponential curve well fitted the experimental data ($R^2_{PSiNPs} = 0.998$). The fitted values of τ and β , for both samples, are reported in Table II.

TABLE I. Measured size and ζ potential values of PSiNPs and h-PSiNPs dispersed in deionized water (pH = 7).

Material	Size (nm)	ζ potential (mV)
PSiNPs	420 ± 90	-0.3 ± 0.1
h-PSiNPs	480 ± 70	-15 ± 4

PSiNPs were obtained *via* electrochemical etching of low-doped p-type silicon wafers [1–5 Ω cm, (100) oriented, Siltronic-Wacker] in an aqueous hydrofluoric acid (HF) (30 wt.%) and sulfuric acid (H₂SO₄) (38 wt.%) mixture.¹⁴ The resulting microporous silicon layer was detached from the wafer by additional anodization in diluted HF-based solution, dispersed in isopropanol (IPA) to avoid air exposure, and sonicated for 180 min to obtain micro- and nano-particles (NPs).⁵ The NP suspension was centrifuged 3 times at 6000 rpm for 10 min; the supernatant containing PSiNPs was then collected and characterized. The concentration of PSiNPs in IPA was 2 mg/ml, as determined by gravimetry using a Radwag AS82/220.R2 balance.

Under illumination of a low-power UV lamp (wavelength of 376 nm), the freshly prepared PSiNP suspension exhibited remarkable red-orange PL readily visible to the naked eye [Fig. 1(a)].

The morphology of the as-prepared PSiNPs was investigated by transmission electron microscopy (TEM). To this aim, 10 μ l of NPs dispersed in IPA were placed on a TEM copper grid with a lacy carbon film, dried at room temperature and then observed using a FEI Tecnai G2 Spirit BT TEM at an accelerating voltage of 100 kV. The TEM analysis revealed NPs with an irregular shape and a lateral dimension of about 450 nm, constituting a network of holes and ensembles of nanometric crystallites [Fig. 1(b)].

Surface chemistry modification was achieved *via* hydrosilylation. Briefly, PSiNPs were placed in a Schlenk tube with deoxygenated neat undecylenic acid (99% v/v, all chemicals are from Sigma Aldrich) and allowed to react overnight in an Ar atmosphere at 110 °C. The reaction scheme is reported in Fig. 1(c).¹⁵ Hydrosilylated PSiNPs (h-PSiNPs) were extensively washed in tetrahydrofuran and chloroform in order to remove residual unreacted or physisorbed reagents.

The presence of UA covalently conjugated to the surface of PSiNPs was investigated by Fourier Transform Infrared spectroscopy (FT-IR). The spectra of bare PSiNPs and h-PSiNPs were obtained using a Nicolet Continuum XL microscope (Thermo Scientific) in the wavenumber region of ~ 3200 – 700 cm⁻¹ with a resolution of 4 cm⁻¹.

TABLE II. Estimated PL lifetimes and stretching factors for PSiNPs (1.3 mg/ml) and h-PSiNPs (0.9 mg/ml) in IPA at different emission wavelengths.

λ (nm)	PSiNPs		h-PSiNPs	
	τ (μ s)	β	τ (μ s)	β
600	19.6 ± 0.2	0.825 ± 0.008	20.2 ± 0.4	0.86 ± 0.02
650	31.5 ± 0.3	0.86 ± 0.01	31.8 ± 0.6	0.90 ± 0.02
700	47.6 ± 0.6	0.90 ± 0.01	46.8 ± 0.7	0.91 ± 0.01

The results of FT-IR analysis, reported in Fig. 1(d), demonstrated the effective UA bonding to PSiNPs. The FT-IR spectrum of air-dried bare PSiNPs showed peaks corresponding to Si-O-Si and Si-H_x bonds at 1200–1100 cm⁻¹ and 985–800 cm⁻¹, respectively.^{16,17} After reaction, other peaks due to C-H_x (2920–2850 cm⁻¹) and carboxylic acid C=O (1700 cm⁻¹) vibrations appeared;¹⁶ the decrease of Si-H_x peak intensity was compatible with the functionalization process that consumed silicon-hydrogen bonds inducing the formation of silicon-carbon ones.

The hydrodynamic diameter (size) and the surface charge (ζ potential) of NPs dispersed in deionized water (pH = 7) were estimated by dynamic light scattering (DLS) using a Zetasizer Nano ZS (Malvern Instruments, U.K.) equipped with a He-Ne laser (633 nm), at a fixed scattering angle of 173°, T = 25 °C. The results of DLS

characterization are summarized in Table I: according to TEM analysis, PSiNPs were characterized by a mean size of 420 nm, whereas after the surface modification by UA, the size of h-PSiNPs was estimated to be 480 nm, comparable to that of bare PSiNPs within the experimental error. On the other hand, hydrosilylation strongly modified the surface charge of NPs: the absolute increase in the value of ζ potential, from -0.3 mV to -15 mV, can be ascribed to the presence of negatively charged carboxyl groups added subsequently to the functionalization. This result also indicated an increase in the repulsive electrostatic interaction between NPs and, as a consequence, a higher stability of h-PSiNP suspension.

Steady-state photoluminescence (ssPL) and time-resolved photoluminescence (trPL) analyses of bare and modified PSiNP suspensions in IPA were performed in a cuvette (1.3 mg/ml for PSiNPs and 0.9 mg/ml for h-PSiNPs), exposing the samples to a LED pump (LLS, Ocean Optics, 365 nm). Emitted light was collected at 90° with respect to the pump through an optical fiber, dispersed in a spectrometer (ANDOR SR-163) and detected using an ANDOR iStar iCCD camera. For the stationary characterization, the LED pump was kept in a continuous wave regime and the iCCD was set in an internal trigger mode at a gate pulse width of 1 ms, whereas for trPL measurements, the pump and the iCCD were externally modulated using a Keysight 33220A pulse generator at a repetition rate of 500 Hz, a wide gate pulse width of 5 μ s, and at 10 μ s steps; the intensity was integrated within 10 nm spectral intervals. In both analyses, a long-pass filter (nominal cut-on wavelength, 410 nm) was used to remove undesired photons

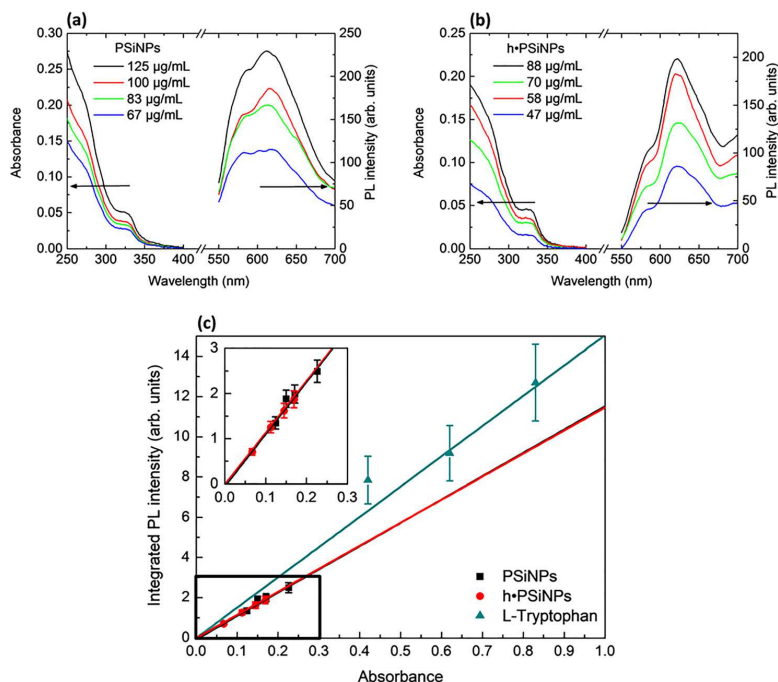


FIG. 3. Absorption and emission spectra (at $\lambda_{exc} = 265$ nm) of (a) PSiNPs and (b) h-PSiNPs at different concentrations in IPA. (c) Corresponding plots of the integrated PL intensity versus the absorbance. The fitted lines were used to calculate the QY of PSiNPs and h-PSiNPs dispersed in IPA. L-Tryptophan was used as the reference.

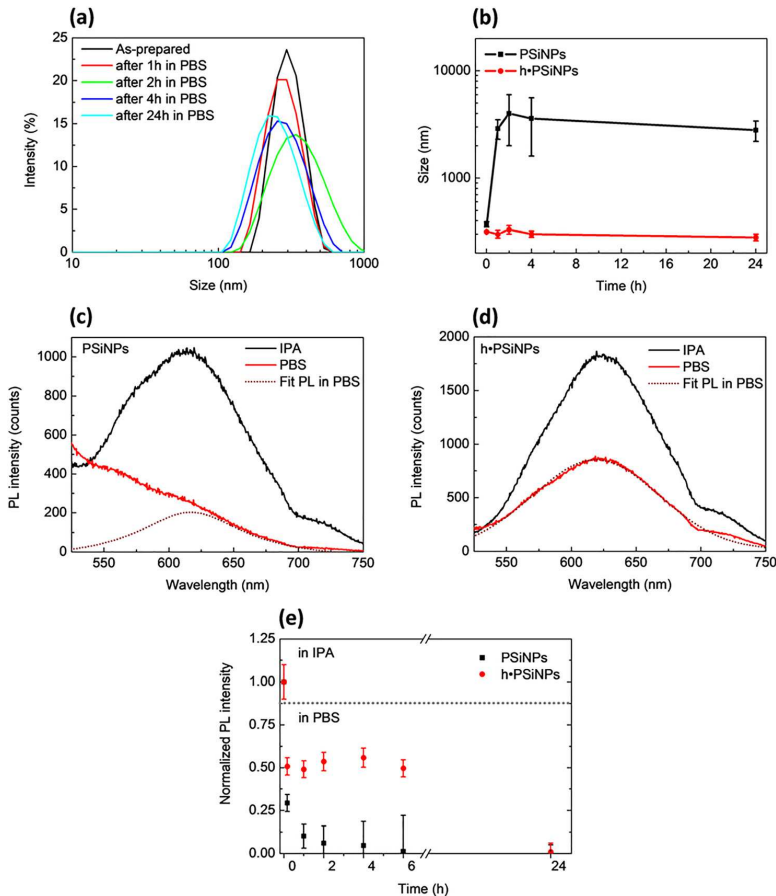


FIG. 4. (a) Size distributions of h-PSiNPs, measured in IPA and after different incubation times in PBS. (b) Hydrodynamic diameter (size) of PSiNPs and h-PSiNPs versus incubation time in PBS. (c) PL spectra (at $\lambda_{ex} = 365$ nm) of PSiNPs and (d) h-PSiNPs in IPA and after 1 h of incubation in PBS. The fit reported in (c) highlights the residual signal ascribed to quantum-confined nanocrystals after dramatic oxidation in PBS. (e) Normalized integrated PL intensity calculated for PSiNPs and h-PSiNPs after different incubation times in PBS. The values of integrated PL intensity in PBS were normalized with respect to the value in IPA (PL intensity = 1).

from the excitation source at the monochromator entrance. All the measurements were carried out at room temperature ($T = 25^\circ\text{C}$).

The ssPL spectra of PSiNPs and h-PSiNPs are presented in Fig. 2(a): a typical Gaussian distribution between 550 and 750 nm was observed for both samples. Gaussian fits revealed that the spectra of PSiNPs and h-PSiNPs are centered at 646 nm and 655 nm, respectively. The red shift of 9 nm was imputed to the presence of UA in the nanometric pores of functionalized nanoparticles, which increased the average refractive index of the structures.¹⁸

The stationary characterization was validated by trPL analysis. Radiative relaxation processes in porous silicon can be distinguished into two main classes: a fast decay with a lifetime of the order of $\sim 10^{-9}$ s and a slow decay, related to quantum-confined excitons in single Si nanocrystals, with characteristic times in the microsecond range.¹⁹ In the case of PSiNP and h-PSiNP samples, the PL decay curves [Fig. 2(b)] were in full agreement with a stretched exponential function [Eq. (1)], used to model the relaxation dynamics of complex systems²⁰

$$I(t) = I_0 e^{-(t/\tau)^\beta}. \quad (1)$$

Equation (1) represents a more accurate descriptive model with respect to the exponential law [as reported in Fig. 2(b)] and depicts the PL emission behavior due to the dispersive diffusion phenomena of photoexcited carriers;²⁰ in particular, the stretching factor β can be related to the characteristics of the environment surrounding the nanoemitters rather than their intrinsic crystalline structure, size, and properties.²¹ In this frame, the slightly different values of β highlighted how the photo-physical properties of the nanocrystals on the PSiNP surface were fully maintained after UA conjugation. Moreover, the decay curves showed a dependence of the PL lifetime on the emission wavelength, as predicted by the quantum confinement model,⁵ i.e., increasing decay times at longer emission wavelengths. The estimated values for τ and β did not substantially change for both PSiNPs and h-PSiNPs (Table II).

The PL quantum yields (QYs) of nanoparticles in IPA were determined by measuring the absorbance (A) and the integrated PL

intensity (I), in the interval of 550–700 nm, at different material concentrations, at a fixed excitation wavelength of $\lambda_{\text{exc}} = 265$ nm. The UV-Vis absorbance curves were obtained by using a Cary 100 spectrophotometer (VARIAN), whereas the emitted light was registered using a JASCO FP-8200 spectrofluorometer.

The PL spectra, in the investigated excitation spectral region, showed a slight modification in the shape probably due to the local interactions between UA anchored on the h-PSiNP surface and IPA medium²² [Figs. 3(a) and 3(b)]. QYs were estimated relative to L-tryptophan (L-Trypt) used as standard dye [QY_{L-Trypt} in water is $(15 \pm 1)\%$, absolute measurements are done with an integrating sphere²³] and calculated using the following equation:²⁴

$$\frac{QY_{\text{NPs}}}{n_{\text{IPA}}^2 \alpha_{\text{NPs}}} \bigg|_{\lambda_{\text{exc}}} = \frac{QY_{\text{L-Trypt}}}{n_{\text{H}_2\text{O}}^2 \alpha_{\text{L-Trypt}}} \bigg|_{\lambda_{\text{exc}}}, \quad (2)$$

where n^2 are the squared refractive indices of the media (H₂O or IPA) and α represents the ratio between integrated PL intensity and absorbance, I/A, at $\lambda = 265$ nm. The coefficients $\alpha_{\text{PSiNPs}} = (1.1 \pm 0.3) \times 10^5$ and $\alpha_{\text{h-PSiNPs}} = (1.2 \pm 0.2) \times 10^5$ were obtained *via* linear regression from the plots of I versus A for PSiNPs and h-PSiNPs, respectively [Fig. 3(c)]. The coefficient $\alpha_{\text{L-Trypt}} = (1.5 \pm 0.2) \times 10^5$ was calculated for L-Trypt in water. Using $n_{\text{IPA}} = 1.422$ and $n_{\text{H}_2\text{O}} = 1.357$ as refractive indices for IPA and water, respectively (at 265 nm), QY values equal to $12\% \pm 5\%$ and $13\% \pm 5\%$ were determined from Eq. (2). Since the QY was very similar for PSiNPs and h-PSiNPs, it was confirmed that the UA passivation procedure fully preserved the surface nature and the crystalline structure of NPs and, consequently, their PL behavior in terms of global emission.

In order to probe the surface functionalization under physiological conditions, PSiNPs and h-PSiNPs stored in IPA were centrifuged and re-suspended in phosphate-buffered saline (PBS) 0.1 M, at pH = 7.4. The size of NPs was monitored by DLS at different incubation times in PBS. After 1 h, significant aggregation was evidenced for bare PSiNPs since the instrumental measured size value was well above the micron range. Under the same conditions, h-PSiNPs preserved their nanometric size for 24 h. Figure 4(a) shows the size distributions of h-PSiNPs at different incubation hours in PBS; the curves, compared to those of h-PSiNPs in IPA, did not evidence any substantial change. The temporal behavior of (h-)PSiNP samples' size in PBS is reported in Fig. 4(b).

In order to disclose the influence of the physiological medium on the emitted signal, the PL spectra of the (h-)PSiNP samples were compared with the corresponding curves in IPA at an excitation wavelength of 365 nm, as highlighted in Figs. 4(c) and 4(d). The shape of the PL spectrum of PSiNPs dramatically changed due to the fast degradation of the quantum-confined nanocrystals into oxide-related radiative sites [Fig. 4(c)]. Figure 4(e) reports the integrated PL intensity of PSiNPs and h-PSiNPs (in the 550–700 nm interval) measured after different incubation times in PBS. The PL emission from bare PSiNPs was strongly affected by exposure to the PBS environment and decreased by 94% in 2 h [black squares in Fig. 4(e)]. This effect could be a severe limitation to the use of PSiNPs as luminescent probes in bioimaging experiments, where the diffusion of the probes within the tissues could last several hours. Much better stability was obtained in the case of h-PSiNPs: PL intensity was attenuated by only 50% of its value in IPA once placed in the PBS medium [Fig. 4(d)], then remained constant at least for the following 6 h, as it can be seen in

Fig. 4(e) (red dots). Anyway, for both PSiNPs and h-PSiNPs, no emitted light was observed after 24 h of incubation. The PL quenching was mainly due to the progressive bulk transformation of the silicon nanocrystals into silicon oxide nanostructures, which were not emissive at the same wavelength. On the other hand, the size of the nanoparticles was preserved by surface charge so that the observed quenching dynamics was disjointed from the overall stability of the colloid.

In conclusion, the experimental results demonstrated that hydro-silylation, leading to covalent UA conjugation, is an effective method to preserve the morphology of PSiNPs and stabilize the emission properties up to 6 h under simulated biological conditions, preventing the uncontrolled degradation of the material. The quite high value of PL QY (>10%) and the long wavelength-dependent PL lifetime (>30 μ s at maximum emission) make h-PSiNPs useful for longer-term optical observations and time-gated imaging.

The authors wish to thank Professor L. T. Canham of Birmingham University, UK, for his helpful suggestions.

REFERENCES

- 1 A. Uhlir, *Bell Syst. Tech. J.* **35**, 333 (1956).
- 2 L. T. Canham, *Appl. Phys. Lett.* **57**, 1046 (1990).
- 3 V. Lehmann and U. Gösele, *Appl. Phys. Lett.* **58**, 856 (1991).
- 4 X. Michalet, F. F. Pinaud, L. A. Bentolila, J. M. Tsay, S. Doose, J. J. Li, G. Sundaresan, A. M. Wu, S. S. Gambhir, and S. Weiss, *Science* **307**, 538 (2005).
- 5 J. Joo, T. Defforge, A. Loni, D. Kim, Z. Y. Li, M. J. Sailor, G. Gautier, and L. T. Canham, *Appl. Phys. Lett.* **108**, 153111 (2016).
- 6 S. P. Low, N. H. Voelcker, L. T. Canham, and K. A. Williams, *Biomaterials* **30**, 2873 (2009).
- 7 H. A. Santos, E. Mäkilä, A. J. Airaksinen, L. M. Bimbo, and J. Hirvonen, *Nanomedicine* **9**, 535 (2014).
- 8 J.-H. Park, L. Gu, G. von Maltzahn, E. Ruoslahti, S. N. Bhatia, and M. J. Sailor, *Nat. Mater.* **8**, 331 (2009).
- 9 L. Gu, D. J. Hall, Z. Qin, E. Anglin, J. Joo, D. J. Mooney, S. B. Howell, and M. J. Sailor, *Nat. Commun.* **4**, 2326 (2013).
- 10 A. Loni, A. J. Simons, P. D. J. Calcott, and L. T. Canham, *J. Appl. Phys.* **77**, 3557 (1995).
- 11 J. Joo, J. F. Cruz, S. Vijayakumar, J. Grondek, and M. J. Sailor, *Adv. Funct. Mater.* **24**, 5688 (2014).
- 12 M. B. Gongalsky, A. Kharin, L. A. Osminkina, V. Timoshenko, J. Jeong, H. Lee, and B. Chung, *Nanoscale Res. Lett.* **7**, 446 (2012).
- 13 R. Boukherroub, D. D. M. Wayner, D. J. Lockwood, and L. T. Canham, *J. Electrochem. Soc.* **148**, H91 (2001).
- 14 A. Loni, L. T. Canham, T. Defforge, and G. Gautier, *ECS J. Solid State Sci. Technol.* **4**, P289 (2015).
- 15 Q. Shabir, K. Webb, D. K. Nadarassan, A. Loni, L. T. Canham, M. Terracciano, L. De Stefano, and I. Rea, *Silicon* **1**, 349–359 (2017).
- 16 G. Socrates, *Infrared and Raman Characteristic Group Frequencies: Tables and Charts* (John Wiley & Sons, 2007).
- 17 M. J. Sailor, *Porous Silicon in Practice: Preparation, Characterization and Applications* (Wiley-VCH, 2012).
- 18 L. De Stefano, I. Rendina, M. De Stefano, A. Bismuto, and P. Maddalena, *Appl. Phys. Lett.* **87**, 233902 (2005).
- 19 D. I. Kovalev, I. D. Yaroshetzki, T. Muschik, V. Petrova-Koch, and F. Koch, *Appl. Phys. Lett.* **64**, 214 (1994).
- 20 L. Pavesi and M. Ceschini, *Phys. Rev. B* **48**, 17625 (1993).
- 21 M. Dvornat, Y. Goshen, J. Jedrzejewski, I. Balberg, and A. Sa'ar, *Phys. Rev. B* **69**, 155311 (2004).
- 22 C. Reichardt, *Chem. Rev.* **94**, 2319 (1994).
- 23 K. Suzuki, A. Kobayashi, S. Kaneko, K. Takehira, T. Yoshihara, H. Ishida, Y. Shiina, S. Oishi, and S. Tobita, *Phys. Chem. Chem. Phys.* **11**, 9850 (2009).
- 24 J. R. Lakowicz, *Principles of Fluorescence Spectroscopy* (Springer, 2006).

2.2.2 PSiNPs for *in vivo* imaging

Abstract

In the last years, luminescent porous silicon nanoparticles have gained great attention as label-free probes for bioimaging and theranostic applications. They represent a promising alternative to conventional semiconductor quantum dots. In this study, an *in vivo* assay exploiting highly luminescent biocompatible porous silicon nanoparticles (PSiNPs) as label-free probes is presented. *Hydra vulgaris* is used as *in vivo* model for internalization studies. To stabilize the emissive nanocrystals in biological conditions and to allow the internalization in *Hydra*, PSiNPs surface has been hydrosilylated with undecylenic acid (UDA) and modified with poly-L-Lysine (PLL). The morphological preservation of *Hydra* has been verified by direct microscope observation, demonstrating the biosafety of the material.

Unfortunately, the bright tissue autofluorescence limits the visibility of PLL- hydrosilylated PSiNPs (PLL@hPSiNPs) in *Hydra vulgaris*. This problem can be bypassed thanks to the long PL lifetime of PLL@hPSiNPs, making them prone to the use of time-gated imaging technique.

Introduction

The optical properties of QDs make them attractive for biomedical applications but their toxicity, associated to the content of heavy metals, may limit their use in medicine and biology. In this context, PSiNPs offer a valid alternative to the conventional QDs. Their biocompatibility, biodegradability, intrinsic PL and the versatility in surface modification make them interesting for applications in biomedical fields [70], [88]–[90].

Here, *Hydra vulgaris* was used as *in vivo* model to explore the effect of PSiNPs. *Hydra* is one of the simplest multicellular organisms at the base of metazoan evolution known. *Hydra* is very sensitive to the presence of environmental pollutants and it has been used as a biological indicator of water pollution [91]. In fact, the exposure of *Hydra* to organic or inorganic contaminants may cause alteration of morphological traits, delayed growth, induction of apoptosis and alteration of gene expression. Herein, we present an imaging study employing biocompatible surface-modified PSiNPs as label-free probes. Moreover, their toxicity, as well their uptake in *Hydra*, were evaluated.

Materials and Methods

PSiNPs fabrication and Hydrosilylation process

PSiNPs were obtained by electrochemical etching of low-doped p-type silicon wafers [1-5 Ωcm , (100) oriented, Siltronic-Wacker] in a mixture of hydrofluoric acid (HF) (30wt%) and sulfuric acid (H_2SO_4) (38wt%). The resulting microporous silicon layer was detached from the wafer by additional anodization in diluted HF-based solution, dispersed in isopropanol (IPA) and sonicated for 180 min to obtain micro- and nanoparticles (NPs). The NPs suspension was centrifuged 3 times at 6000 rpm for 10 min; the supernatant containing PSiNPs was collected and characterized.

Surface modification was obtained *via* hydrosilylation process. Briefly, PSiNPs were placed in Schlenk tube containing deoxygenated neat undecylenic acid (99% v/v) and allow to react at 110°C in Argon atmosphere. Then, the hydrosilylated-PSiNPs (hPSiNPs) were extensively washed in IPA to remove the excess of reagents.

Poly-L-Lysine conjugation to hPSiNPs

PLL was conjugated to hPSiNPs *via* electrostatic interaction. To obtain an effective coverage, hPSiNPs and PLL were allowed to react at a mass ratio 1:1 at RT under mild agitation for 30 min, in aqueous solution pH 5. Then, the sample was washed in Milli-Q-water at the same pH range, to remove the unreacted PLL. Finally, PLL@hPSiNPs were resuspended in the desired medium (water or buffer for *in vivo* experiments) at pH 6 and characterized.

Dynamic Light Scattering

Size distribution and ζ -potential of hPSiNPs and PLL@hPSiNPs were analysed by dynamic light scattering (DLS) using a Zetasizer Nano ZS (Malvern Instruments, U.K) equipped with a He-Ne laser (633 nm, fixed scattering angle of 173°, 25°C).

Steady-state Photoluminescence

The samples were put in a quartz cuvette and exposed to continuous He-Cd laser pump (KIMMON Laser System) by using an excitation wavelength at 325 nm. Emitted light was collected at 90° with respect to the pump through an optical fibre, dispersed in a spectrometer and detected using a Peltier-cooled CCD camera (PIXIS 100F). A long-pass filter with a nominal cut-on wavelength of 350 nm was used to remove the laser line at monochromator inlet.

Bright field and fluorescence microscopy

The toxicity of the NPs in *Hydra* was evaluated incubating the polyps at different concentrations of hPSiNPs and PLL@hPSiNPs (1 mg/mL, 0.5 mg/mL and 0.25 mg/mL). The hPSiNPs (in IPA) and PLL@hPSiNPs (in water) were centrifuged three times at 15000 rpm for 50 min and the

pellets were resuspended in *Hydra* medium buffer (NaHCO₃ and CaCl₂ 1:2 v/v aqueous mixture, pH 6). Then, five animals were incubated in the as-prepared samples and observed in bright field by LEICA DM6 M microscope at room temperature, using 5x magnification. The same number of animals were incubated in freshly prepared medium and used as control.

To study the NPs uptake in *Hydra*, three animals were incubated with PLL@hPSiNPs at 0.25 mg/mL, previously resuspended in *Hydra* buffer (at pH 6). The polyps are observed in fluorescence mode (365 nm excitation; long-pass emission filter) for up 2h by using LEICA DM6 M microscope at 5x magnification.

Results and Discussion

In vivo experiments require the use of low toxicity, biocompatible, biodegradable and high stability products and PSiNPs represent good candidates for this task. They can be used as diagnostics or therapeutic agents and their luminescent nature makes them attractive as label-free probes.

The PSiNPs, used in this study, were obtained by electrochemical etching of crystalline silicon in HF solution containing sulfuric acid as additive. This process allows to obtain PSi powders characterized by nanocrystals of different shapes and dimension lower than 2.5 nm. Moreover, these powders present a high micropore content, a large surface area per unit mass (1150 m²/g), a high pore volume (>1 cm³/g) and a large average pore size (~3.3 nm). Furthermore, the reduction in structural disorders and in non-radiative defects on the silicon skeleton has, as consequence, an enhancement of PL quantum yield and a longer excited state lifetime in comparison with other nanocrystalline silicon [92].

The as-obtained PSiNPs suffer of poor chemical stability in aqueous media, causing the substitution of Si-H bonds in Si-O-Si bonds in an oxidizing environment. As a consequence, this effect strongly modifies the PL emission, limiting their application in bioimaging [93]. To overcome this inconvenient, a passivation process is needed. In this work, PSiNPs were hydrosilylated by using undecylenic acid (UDA), in order to replace Si-H bonds in Si-C bonds, more robust and resistant in biological media. However, consequently to the interaction with UDA, hPSiNPs exposed carboxyl acid groups, having a negative surface charge, thus representing a limit for *in vivo* experiments. Since, the phospholipidic layer of membrane cells exposed negative groups too, the internalization process of the hPSiNPs could be inhibited by electrostatic repulsion.

For this reason, the hPSiNPs surface was further modified by poly-L-Lysine (PLL), a positively charged amino acid polymer, *via* electrostatic interaction. In Figure 2.8, the bare PSiNPs functionalization process is shown.

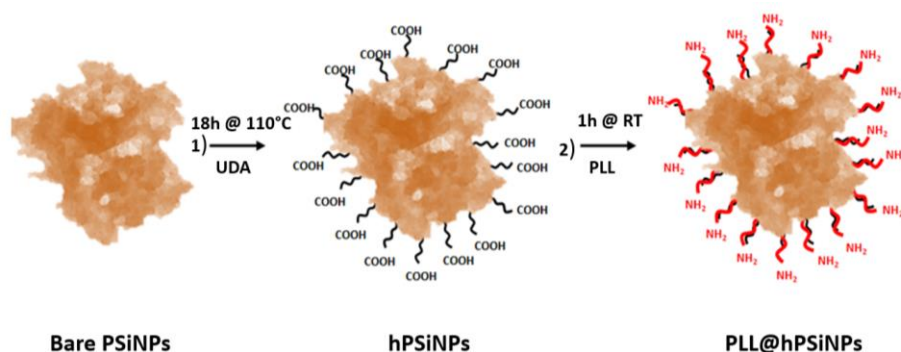


Figure 2.8 – Functionalization scheme of PSiNPs: **Reaction 1:** hydrosilylation process of bare PSiNPs by UDA, 18h at 110°. **Reaction 2:** electrostatic interaction of PLL to hPSiNPs, 1h at RT.

The hPSiNPs were analysed by DLS, before and after the modification process. No variation of the hydrodynamic diameter was observed after PLL conjugation, except for a slight increase of the polydispersity index (from 0.26 ± 0.04 nm to 0.4 ± 0.1 nm), confirming an effective coverage of hPSiNPs, without any formation of agglomerates. Moreover, the exposure of amine groups, induced a significative change of surface charge, from -16 ± 1 mV to 16 ± 4 mV (Figure 2.9 A). A partial oxidation of the material and a consequent PL quenching was measured (Figure 2.9 B). This effect could be ascribed to an incomplete Si-C surface passivation after the hydrosilylation treatment. In fact, comparing the two samples at the same concentration and in the same spectral range, a decrease of 45% of the PL integrated intensity (I) was registered. Consequently, because of the direct proportionality between PL quantum yield (QY) and I , there was a decrease of QY value, from 0.13 to 0.08. Such QY value was still acceptable for the use of PLL@hPSiNPs as luminescent bioprobe.

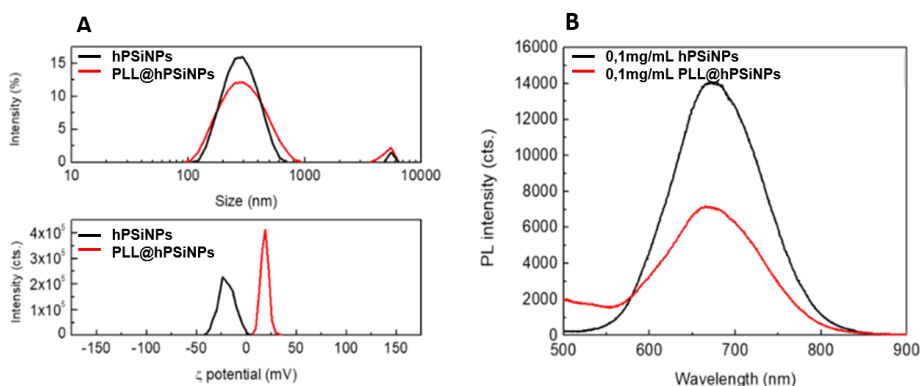


Figure 2.9 - (A) DLS, ζ -potential and **(B)** Steady-state PL spectra at 325 nm excitation of hPSiNPs and PLL@hPSiNPs.

In order to develop safe nanodevices for biomedical applications, the *in vivo* studies are extremely important to evaluate the NPs toxicity. In this context, *Hydra vulgaris* is used as *in vivo* model.

Hydra is a simple multicellular organism consisting of a cylindrical tubular body with a single apical opening (mouth) located into the head, surrounded by 6-8 tentacles, and a foot presenting a basal disc, used by the polyp to anchor itself to a substrate [94]. *Hydra* tissue is characterized by two cell layers, an outer ectoderm and an inner endoderm separated by a noncellular mesoglea layer [95]. Its structural complexity, simpler than vertebrates but more complex than cultured cells, makes *Hydra* comparable to a living tissue whose cells and distant regions are physiologically connected. *Hydra* is very sensitive to the presence of contaminants in the environment, whose toxicity is measured and quantified observing alterations in the animal morphology, in the regeneration or pattern formation and in the population growth rates [91]. Herein, it was examined the morphological alterations in *Hydra*, induced by PSiNPs. These modifications were measured by the Wilby's classification, used to attribute a score from 10 (healthy polyps) to 0 (animal disintegration); score 10-6 is reversible while score 5-0 is considered as endpoint for lethality [96].

In this context, due to the PSiNPs instability in aqueous environments, the *in vivo* experiments were conducted only with hPSiNPs and PLL@hPSiNPs. The results pointed out that *Hydra* morphology did not result altered by a concentration of hPSiNPs, high as 1 mg/ml, up to 72h incubation (score 10), indicating that hPSiNPs were non-toxic (Figure 2.10). In contrast, 1 mg/mL of PLL@hPSiNPs caused the

complete disintegration of the polyps after 2h incubation. Perhaps, this effect could be due to ectodermal cells damages induced by the high amount of PLL [97], [98]. Several factors seem to be responsible for the cytotoxicity of cationic polymers, such as the high molecular weight, the type of cationic functionalities and the charge density. Moreover, the toxicity is also related to the arrangement of cationic charges on the polymeric chains. This factor depends on the three-dimensional structure and on the flexibility of the macromolecules, thus determining the accessibility of the charges to the cell membrane [99], [100]. In the specific case of PLL, a possible mechanism that could suggest the cytotoxic effect is the conformational change (from random coil to α -helix) that the polycation may undergo after the interaction with the cell membrane; this causes the exposure of a large number of lysins to the membrane that could lead to its destabilization [101]. Furthermore, the cytotoxicity effect is time and dose-dependent. In fact, by reducing the PLL@hPSiNPs concentrations (0.5 mg/ml and 0.25 mg/mL), a progressive increase of biocompatibility was observed. In particular, the polyps exposed to PLL@hPSiNPs at 0.25 mg/mL for 2h did not show morphological alterations (score 10).

Thanks to both the short uptake times required for positively charged materials and the high PL, the latter condition is the best compromise for the use of PLL-modified PSiNPs.

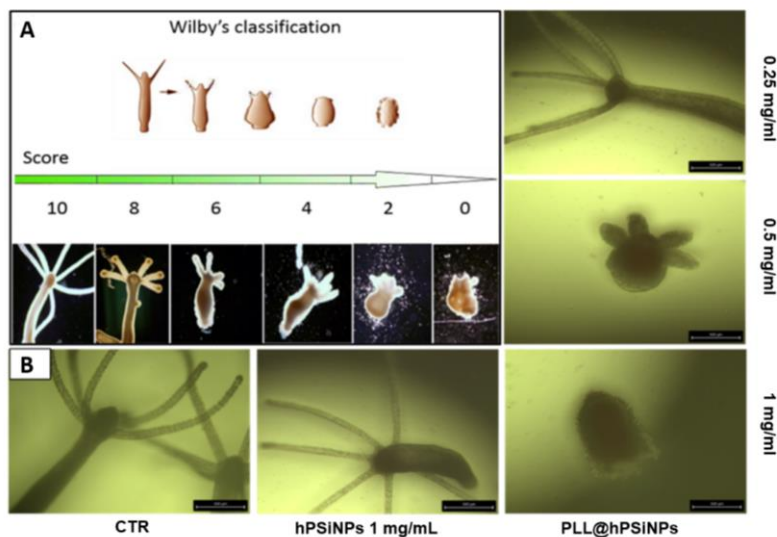


Figure 2.10 - (A) Scheme of toxicity score attribution according to Wilby's criterion. **(B)** Evaluation of toxicity of hPSiNPs and PLL@hPSiNPs. The scale bar is 500 μ m.

These obtained data are only preliminary results. Others studies will be carried out to establish the stability and the exact degree of toxicity of PLL@hPSiNPs over different incubation times as well as the analysis on the growth rate.

At this step, the feasibility of PLL@hPSiNPs as label-free luminescent probes for bioimaging will be tested. The NPs internalization was monitored through real-time observation of the animals, both in bright field and fluorescent mode. The uptake of PLL@hPSiNPs in *Hydra* was already observed after 1h incubation (Figure 2.11). Moreover, it was assumed that the luminescent probe uptake could be driven by an endocytosis mechanism [102].

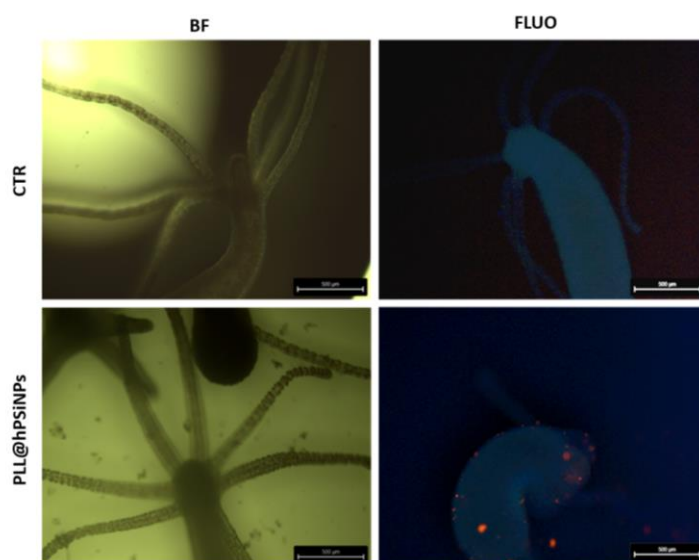


Figure 2.11 - Real-time *in vivo* imaging of *Hydra vulgaris* during incubation at 0.25 mg/mL of PLL@hPSiNPs. Control animals were observed as well. The acquisitions herein reported were taken at ~ 1 h incubation.

After 2h incubation, the animals were strayed from the incubation environment, fixed on a microscope slide and re-observed to evaluate the NPs internalization. Even if the differences between the control and the treated animals are evident, the intense tissue autofluorescence limits the visibility of PLL@hPSiNPs (Figure 2.12). This phenomenon represents a limit because it leads to a broad emission over the whole visible spectra range.

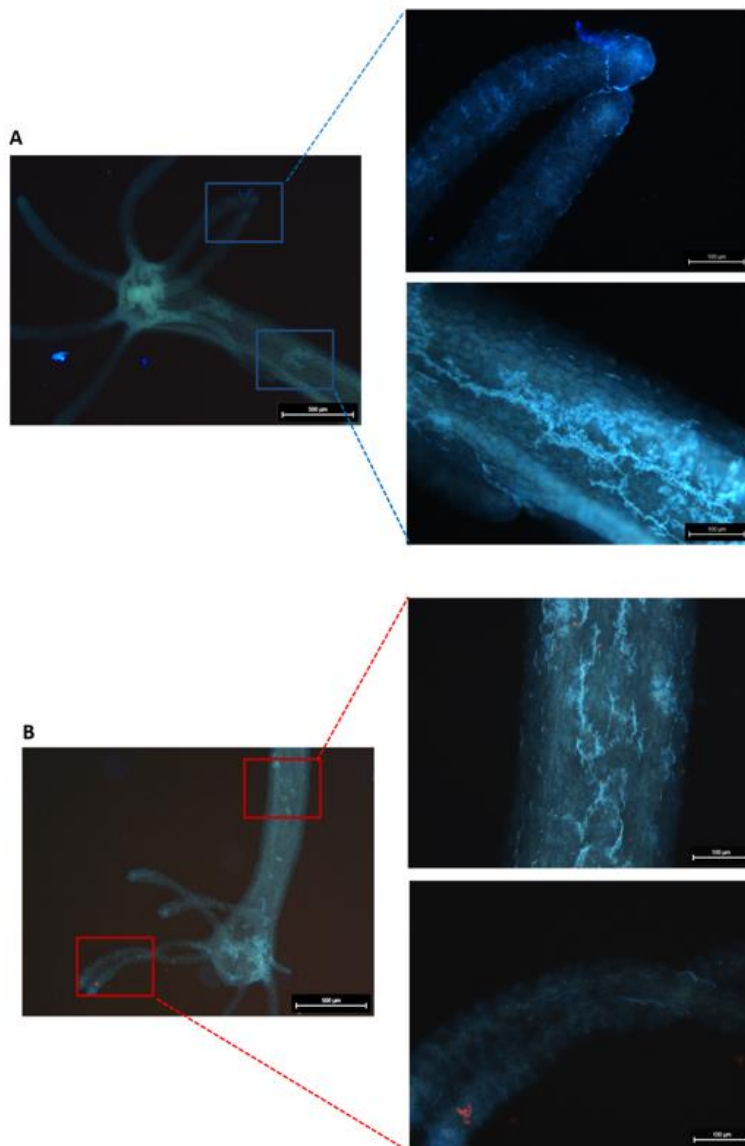


Figure 2.12 – Fluorescence imaging of *Hydra vulgaris* after fixation. The images represent the animal **(A)** before and **(B)** after incubation with PLL@hPSiNPs (0.25 mg/mL, 2h incubation). The highlighted areas correspond to the images at higher magnification (20x) on the lateral panel.

For this reason, several strategies have been developed to overcome this issue, such as the use of fluorophores that emit in the near-infrared

(NIR), where the contribution of tissue autofluorescence is reduced, or the use of longer-lived probes (i.e., quantum dots), imaged by time-gated luminescence [103]–[107]. Time-gated imaging is performed *via* a highly sensitive instrumentation. It allows the imaging of a system with several components whose radiative lifetimes are slightly different. PSiNPs represent a promising nanomaterial for this technique thanks to the very long radiative lifetime (μs range).

Conclusions

In this study, the internalization of PSiNPs has been studied by using *Hydra vulgaris* as *in vivo* model. PSiNPs surface has been opportunely functionalized with a positively charged polymer, PLL, to allow the interaction between the polyp cells membrane and the polymer. The NPs uptake has been evaluated by fluorescence microscopy but, the tissue autofluorescence limits the visibility of PSiNPs. The problem has been solved with time-gated imaging technique, allowing the discrimination of the single components contribution in the system. Obviously, the data reported in this study are only preliminary results. Many other efforts are required in order to optimize the NPs biocompatibility and the targeted uptake, starting from PSiNPs functionalization.

2.3 ZnO-based nanostructured platform for label free optical biosensor

Nanostructured ZnO (nZnO) is considered one of the most interesting transducer materials especially for sensing applications thanks to its properties, such as chemical stability, biocompatibility and intense PL emission at room temperature under laser irradiation. The possibility to chemically modify the surface of ZnO allows the development of a biosensor whose sensing mechanism is based on PL changes. Moreover, various dopant agents can be used to improve the physical properties of the material, such as fluorine atoms, which strongly influences the morphology of the nanostructured material. This is extensively explained in section 2.3 in which the use of nZnO·F as platform for label-free optical sensor is underlined.

Article

Synthesis and Surface Modification of Nanostructured F-Doped ZnO: Toward a Transducer for Label-Free Optical Biosensing

Giovanna Chianese ¹, Monica Terracciano ¹, Rosalba Moretta ^{1,2}, Paolo Cappiello ¹, Giuseppe Vitiello ³, Antonio Aronne ³, Chiara Schiattarella ^{1,4}, Luca De Stefano ^{1,*} and Ilaria Rea ¹

¹ National Research Council, Institute for Microelectronics and Microsystems, Unit of Naples, 80131 Naples, Italy

² Department of Chemical Sciences, Federico II University of Naples, 80138 Naples, Italy

³ Department of Chemical, Materials and Production Engineering, Federico II University of Naples, 80138 Naples, Italy

⁴ Department of Physics, Federico II University of Naples, 80138 Naples, Italy

* Correspondence: luca.destefano@na.imm.cnr.it; Tel.: +39-081-613-2375

Received: 9 July 2019; Accepted: 12 August 2019; Published: 16 August 2019



Abstract: In this work, the surface of nanostructured fluorine-doped ZnO (nZnO-F) is functionalized with protein A (PrA), and used as a model biomolecule. The chemical procedure is characterized by several analytical techniques such as Fourier Transform Infrared Spectroscopy, water contact angle analysis, and fluorescence microscopy. The surface modification of nZnO-F by binding increasing concentrations of PrA is also investigated by two label-free optical techniques, i.e., the spectroscopic reflectometry and the steady-state photoluminescence. The results are compared with those obtained using undoped nZnO substrates in order to highlight the better performances of nZnO-F due to the fluorine doping. The results of this study pave the way for the design and realization of a ZnO-based nanostructured platform for label-free optical sensing.

Keywords: nanostructured zinc oxide; hydrothermal synthesis; bioconjugation; photoluminescence

1. Introduction

A biosensor is an analytical device constituted by a biological recognition element, generally defined as a probe immobilized on a transduction system, which converts a molecular interaction into a useful signal. There are several types of biosensors based on different sensing recognition mechanisms such as amperometric, electrochemical, optical, and thermometric. In an optical biosensor, the interaction between the biomolecular probe, bound on its surface, and the target analyte is transduced in a change of an optical signal (e.g., phase, intensity, color, and fluorescence) [1–3]. In the last few decades, the market of optical biosensors has grown very rapidly due to their high sensitivity, specificity, real-time response, and the possibility of performing remote sensing in flammable environments.

The semiconductors currently used in the microelectronic industry, such as silicon and its related materials (silicon oxide, silicon nitrides, and porous silicon), have been extensively exploited in biosensor fabrication, and hundreds of papers and reviews can be found in recent literature [4–8]. On the other hand, nanostructured metal oxides showed great potential for the detection of biomolecules, owing to several characteristics such as the controllable size/shape, large specific surface area, biocompatibility, catalytic and optical properties, and chemical stability [9]. Among them, nanostructured zinc oxide (nZnO) is considered an interesting transducer material due to its multifunctional characteristics.

The nZnO is an n-type semiconductor with a wide direct band gap of 3.37 eV, and a large excitonic binding energy of 60 meV, thus allowing an efficient excitonic emission even at room temperature [10,11]. Under UV laser irradiation, nZnO is able to emit intense photoluminescence (PL) of which the spectrum is characterized by a peak at 380 nm, due to free exciton recombination and a broad visible band related to the surface and lattice defects [12]. Different methods for fabrication of nZnO-based devices are available, such as Vapor–Liquid–Solid growth (VLS), Metal Organic Chemical Vapor Deposition (MOCVD), and High-Pressure Pulsed Laser Deposition (HP-PLD) [13,14]. Recently, hydrothermal synthesis was proposed as an advantageous alternative approach because it requires mild experimental conditions, simple equipment, low-cost reagents, and it can be indifferently used on several surfaces [15].

One of the key issues in the developing of biosensors is the functionalization strategy used to correctly immobilize the bioprobes on the material surfaces. From this point of view, the nZnO allows covalent binding of the biomolecules on its surface by using a soft chemical strategy, preserving the specific functionalities of the biological compounds and controlling their orientation. The use of the ZnO nanowires obtained by the hydrothermal method as a photoluminescent biosensor was demonstrated [14].

In this work, nanostructured fluorine (F)-doped ZnO (nZnO:F) was directly grown on a crystalline silicon substrate via hydrothermal synthesis, and chemically modified in order to fabricate a technological platform for biosensing purposes [15]. F⁻ ions, usually used as a doping precursor, played a significant role in the morphological, electrical and optical properties of nanostructured ZnO [16]. Extensive studies reported in Reference [15], demonstrated that F atoms mainly occupy oxygen vacancies present in the material, without producing any substantial change of plasma frequency but only the enhancement of scattering rate due to an increase of grain boundary density. A proper functionalization procedure was developed to covalently immobilize the Protein A (PrA), used as a model molecule on the semiconductor surface. The functionalized nZnO:F was characterized by the Fourier Transform Infrared Spectroscopy, water contact angle, and fluorescence microscopy. The surface modification with different concentrations of PrA was also studied by label-free optical techniques, spectroscopic reflectometry, and PL analysis. The results were compared with those obtained by investigating undoped nZnO.

2. Materials and Methods

2.1. Materials

(3-Aminopropyl)triethoxysilane (APTES), toluene, bis(sulfosuccinimidyl)suberate (BS³), and FITC-labeled Protein A were purchased from Sigma Aldrich (Milan, Italy). The chips were fabricated in collaboration with the Department of Chemical Engineering of the University of Naples Federico II.

2.2. Hydrothermal Synthesis

Nanostructured undoped and F-doped ZnO films were prepared by the following steps: A solution containing a 1:1 molar ratio of triethylamine (TEA) and zinc acetate dihydrate (ZAD) was firstly prepared by mixing TEA (0.21 mL) and ZAD (0.33 g) into ethanol (90 mL) under constant stirring. After complete dissolution of ZAD, water (10 mL) was added dropwise, producing a whitish suspension which was transferred within a Teflon recipient (the liquid volume corresponding to 75% of the whole). The same procedure was used to prepare the nanostructured F-doped ZnO (nZnO:F) sample, by adding a specific amount (2.14 mg) of ammonium hydrogen fluoride (NH₄FHF) in the starting solution to obtain a final atomic F concentration of 5 at.%. Two silicon supports with sputtered ZnO thin films were alternatively immersed upside down in the prepared suspensions within the Teflon recipients and heated at 90 °C for 4 h. The obtained samples were rinsed with de-ionized water, dried with nitrogen, and finally calcined at 400 °C for 2 h.

2.3. Functionalization Procedure

Hydroxyl (OH) groups were activated on the surfaces of nanostructured ZnO samples by exposing the devices to oxygen plasma for 40 s. The cold plasma activation is a standard technique used to induce the formation of surface chemical functional groups through the use of plasma gases such as oxygen, hydrogen, nitrogen, and ammonia, which dissociate and react with the surface. Samples were then silanized using a 5% APTES solution in anhydrous toluene for 30 min at room temperature. Excess ungrafted silane was removed by intensive washing in dry toluene followed by curing performed at 100 °C for 10 min. Samples were treated with a 1.7 mM solution of BS³ in PBS pH 7.4 at 4 °C for 5 h. After the washing in PBS, samples were dried by a nitrogen stream and incubated with a 2 mg/mL solution of fluorescein-labeled Protein A (PrA*) in PBS pH 7.4 overnight at 4 °C. Excess PrA* was removed by washing the samples five times in PBS. Any variation of the optical signals (both reflectance and photoluminescence) of devices was not observed after the last washing step, demonstrating that the unbound or non-specific bound PrA was completely removed.

2.4. Scanning Electron Microscopy

Scanning electron microscopy was performed through a FESEM ULTRA-PLUS (Zeiss, Oberkochen, Germany) at 20 kV with the SE2 detector and a 15.9 mm working distance. The samples were gold sputtered (3 nm thickness) with a HR208Cressington sputter coater.

2.5. Fourier Transform Infrared Spectroscopy

Surface chemical composition of samples was investigated by Fourier Transform Infrared (FTIR) spectroscopy. FTIR spectra were acquired before and after PrA immobilization using a Nicolet Continuum XL (Thermo Scientific, Waltham, MA, USA) microscope in the wavenumber region of 4000–1200 cm⁻¹ with a resolution of 4 cm⁻¹.

2.6. Water Contact Angle Measurements

Water contact angle (WCA) measurements were performed to investigate the wettability of samples using a First Ten Angstroms FTA 1000 C Class coupled with drop shape analysis software. The WCA values reported in this work are the average of at least three measurements on the same sample.

2.7. Fluorescence Microscopy

Leica Z16 APO fluorescence microscope equipped with a camera Leica DFC300 was used for the fluorescence analysis of the samples functionalized with PrA*. The imaging was performed using an I3 filter cube constituted by a 450–490 nm band-pass excitation filter, a 510 nm dichromatic mirror and a 515 nm suppression filter.

2.8. Label-Free Optical Spectroscopies

The interaction between nZnO-F and nZnO samples and unlabeled PrA at different concentrations (2 mg/mL (48 μM); 4 mg/mL (95 μM); 6 mg/mL (143 μM)) was investigated by using label-free optical techniques: Spectroscopic reflectometry and steady-state photoluminescence analysis.

Reflectivity spectra were acquired by sending a white light on the samples by means of a Y optical reflection probe (Avantes). The same probe was used to guide the output signal to an optical spectrum analyzer (Ando AQ6315A). The spectra were acquired at normal incidence over the range 600–1200 nm with a resolution of 1 nm. Reflectivity spectra reported in this work are the average of three measurements.

Steady-state photoluminescence (PL) spectra of samples were excited by a continuous wave He-Cd laser at 325 nm (KIMMON Laser System). PL was collected at normal incidence to the surface of samples through a fiber, dispersed in a spectrometer (Princeton Instruments, Trenton, NJ, USA SpectraPro 300i), and detected using a Peltier cooled charge-coupled device (CCD) camera (PIXIS 100F).

A long pass filter with a nominal cut-on wavelength of 350 nm was used to remove the laser line at the monochromator inlet.

3. Results and Discussion

The presence of F atoms as doping agent in ZnO powders strongly affected all the intrinsic properties of ZnO nanocrystals, in particular its morphology, by inducing the formation of a clear granular nanometric phase [16]. This effect was well evident when the fluorinated nZnO-F and the undoped nZnO films were directly grown on solid substrates and studied for comparison. Both nZnO-F and nZnO films were grown on flat crystalline silicon by a hydrothermal synthesis, which required a seed layer of ZnO sputtered on the substrates before the synthesis. Due to the nanometric features of these samples, their morphological characterization was performed by SEM imaging. The results, reported in Figure 1, highlighted an impressive difference of the morphology in the different materials: The nZnO-F appeared as a packed film constituted by flake-like nanograins of about 600 nm; while the nZnO was formed by standard hexagonal nanocolumns of 200 nm in diameter almost perpendicular to the plane. The surface roughness of doped and undoped nZnO was measured by a profilometric technique; the nZnO-F was characterized by a rms (root mean squared) of 20 ± 2 nm, while the nZnO surface result was smoother (rms of only 9 ± 1 nm).

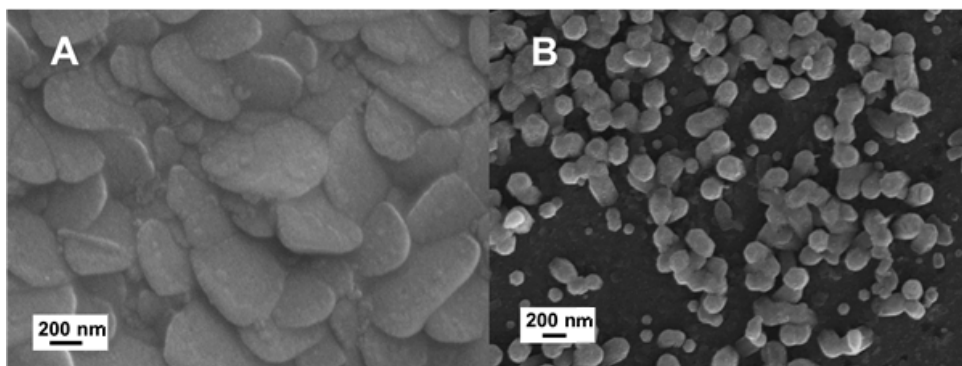
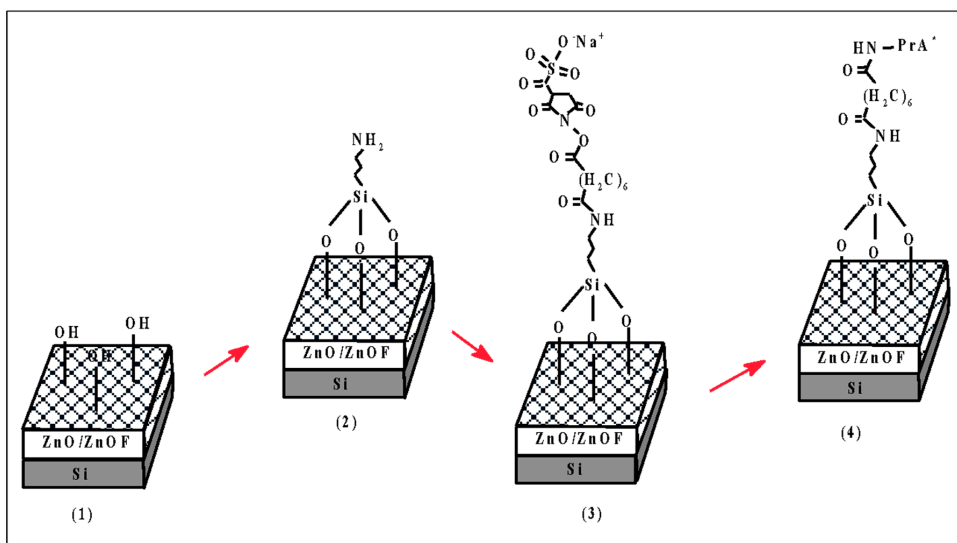


Figure 1. Representative SEM images of nanostructured fluorine (F)-doped ZnO (nZnO-F) (A) and nZnO (B).

The two samples were functionalized with FITC-labeled PrA (PrA*) following the chemical procedure described in Scheme 1. PrA was used as a model molecule since it has great relevance from a sensing point of view and for the biosensors surface chemical modification. PrA is often covalently coupled to the surface of transducer materials by several methods which span from direct adsorption to click chemistry [17–19]. PrA can be found in nature as a virulence factor specific for *Staphylococcus aureus*, bound to glycans on the bacterial cell surface. PrA is also able to link to the von Willebrand factor that is a protein for the hemostasis process. Moreover, more important is the fact that PrA selectively binds the Fc-region of human antibodies, thus resulting essentially in the correct orientation of the antibodies fixed on a support surface.

The chemical modification strategy of nZnO and nZnO-F was based on two steps. In the first one, the covalent binding of a FITC-labelled PrA was monitored by the FT-IR spectroscopy, WCA analysis, and fluorescence imaging in order to assess the silanization of a zinc oxide nanostructured surface. The hydrothermal grown zinc oxide had a hydrophilic surface after the synthesis, which was made in aqueous solution (see Scheme 1 (1)). The presence of OH groups promoted the Zn-O-Si bounds after the silanization with APTES, resulting in an amino-terminated surface (Scheme 1 (2)). The BS³ crosslinker and the exposure to a PrA solution completed the functionalization procedure

(Scheme 1 (3) and (4)). In the second step, increasing concentrations of PrA were grafted on both surfaces in search of which was better functionalized by the same procedure.



Scheme 1. Functionalization scheme of nZnO-F and nZnO surfaces. (1) Oxygen plasma. (2) Silanization by APTES. (3) BS³ crosslinker modification. (4) PrA* immobilization.

Figure 2 shows the FT-IR spectra of the nZnO-F acquired before and after the last functionalization step with PrA*; spectra related to intermediate functionalization steps (i.e., APTES and BS³) were not reported because any substantial variation was not observed. The features at 1540 and 1400 cm⁻¹ were attributed to asymmetric and symmetric stretching modes of the acetate groups (-COO) absorbed during the synthesis process [20]. The peaks at 1650 cm⁻¹ and about 3300 cm⁻¹, only visible in the spectrum of the functionalized sample, were due to the amide I band and to N-H stretching vibration of protein, respectively [21]. Differently, the FTIR spectrum of nZnO, after the PrA* immobilization procedure, did not present any evident change, which corresponded to a very low amount of protein bound on its surface (data not shown here).

The surface wettability of nZnO-F and nZnO samples were investigated by measuring the WCA values before and after each functionalization step. The results are reported in Figure 3. Due to the hydrothermal synthesis process, samples were mostly hydrophobic; the WCA values of (117 ± 7)° and (110 ± 10)° were measured for nZnO and nZnO-F, respectively. After the plasma oxygen process, the hydroxyl groups activated on the sample surfaces induced a strong decreasing of the WCA values down to (45 ± 5)° for the nZnO-F and to (61 ± 9)° for the nZnO. As expected, after the amino-silanization process, increased values of WCA up to (106 ± 12)° and (98 ± 2)° were measured for the nZnO-F and the nZnO, respectively, due to the replacement of -OH groups by the hydro-carbons and -NH₂ functional groups of the APTES molecules. The high increase of the WCA values was attributed to an efficient capping of hydroxyl groups by the aminosilane, probably oriented in a way that mainly exposed the hydrophobic hydro-carbon groups [22].

The BS³ crosslinker introduced the hydrophilic N-hydroxysulfosuccinimide groups (NHS) on the surfaces, resulting in a WCA value decrease down to (68 ± 9)°, in the case of the nZnO-F, and to (54 ± 8)° for the nZnO. After the incubation with the PrA*, the WCA values of both samples remained unchanged within the errors: This result was compatible with the presence of both the hydrophilic and hydrophobic domains, and characteristic of the protein structure [21].

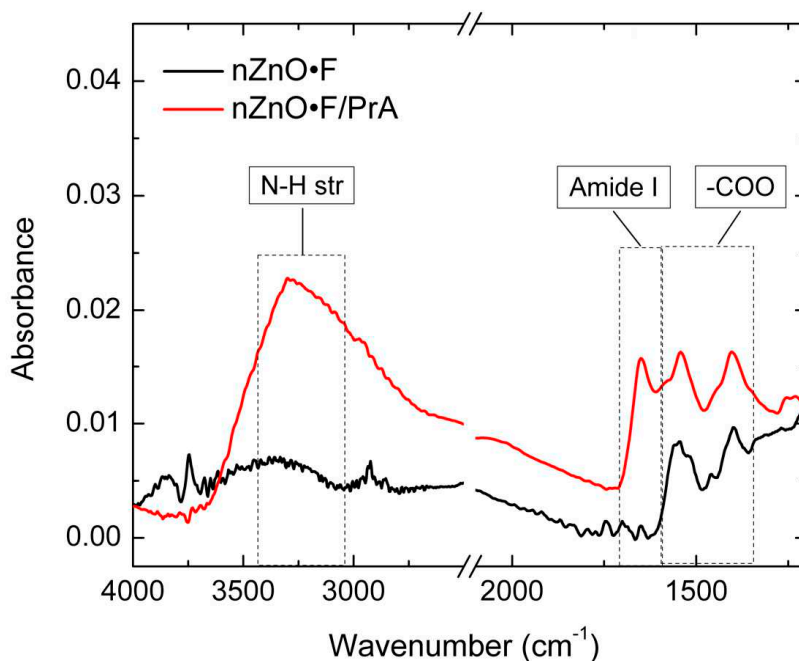


Figure 2. FTIR spectra of nZnO·F sample before (black line) and after (red line) functionalization with PrA.

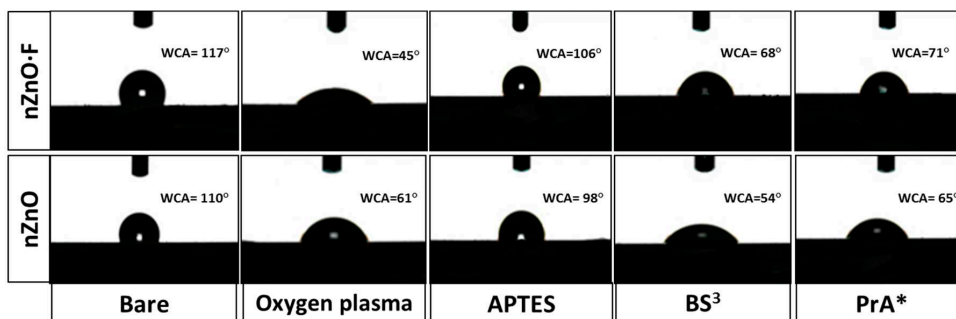


Figure 3. Wettability investigation of nZnO·F (upper line) and nZnO (lower line) samples. WCA measurements were performed after each functionalization step.

The fluorescence microscopy imaging was used to support the presence of the PrA* on the sample surfaces after the last functionalization step. The images, reported in Figure 4, showed a fluorescence homogeneously clustered on the whole surface of PrA*-modified nZnO·F (mean fluorescence intensity = 20 ± 1 counts), while only few luminescent spots, corresponding to a mean fluorescence intensity of 13 ± 1 counts, occurred on the surface of nZnO after PrA*. Analyzing the percentage difference between the values of the mean fluorescence intensities in both samples, we estimated that about 35% as much protein was immobilized on the doped one.

The control samples, i.e., the nZnO·F and nZnO without the PrA*, appeared completely dark (mean fluorescence intensity = 5 ± 1). The fluorescence microscopy imaging was thus in perfect agreement with the results obtained by FTIR spectroscopy.

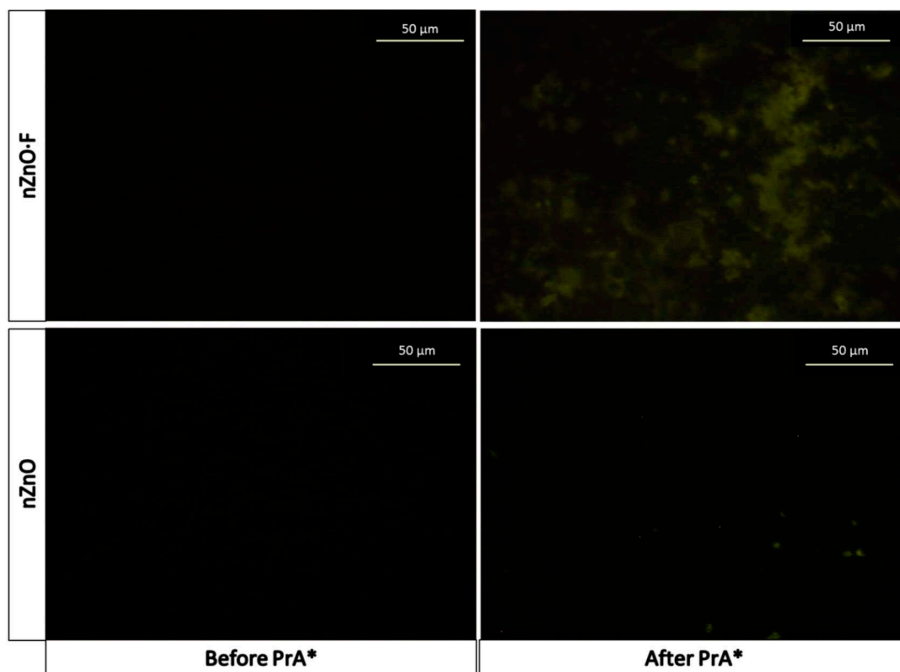


Figure 4. Fluorescence microscopy imaging of nZnO-F (upper line) and nZnO (lower line) before and after functionalization with PrA*.

After the characterization of the surface functionalization by the standard methods of confirming the immobilization of the labeled protein, new samples of nZnO-F and nZnO were grown on silicon and functionalized with unlabeled PrA at different concentrations; in this case, the surface modification was monitored using two label-free techniques, i.e., the spectroscopic reflectometry and the photoluminescence analysis, exploiting the intrinsic optical properties of the semiconductor film.

The layers of nanostructured ZnO acted as Fabry-Perot interferometers from the optical point of view. Their reflectance spectra consisted of fringe patterns due to the interference occurring at air/nZnO-F (or nZnO) and nZnO-F (or nZnO)/bulk silicon interfaces. The optical thickness, OT, of a layer could be quantified as nL where n is the average refractive index of the material and L is the physical thickness. The OT could be calculated counting the fringe maxima satisfying the relationship $m\lambda = 2nL$, with m integer and λ wavelength of the incident light. A faster method was based on the fast Fourier transform (FFT) of the reflectance spectrum; FFT of the spectrum was characterized by a peak whose position along x -axis was two times the optical thickness of the layer.

The covalent immobilization of PrA on the sample surfaces induced the red-shift of their reflectance spectra due to an increase of the optical thicknesses. Since the physical thickness L was fixed, the optical thickness increased due to the change of the average refractive index caused by the infiltration of PrA inside the voids of the layers. Figure 5A,C report the reflectance spectra of nZnO-F and nZnO layers after the interaction with different concentrations of PrA (i.e., 2 mg/mL; 4 mg/mL; 6 mg/mL); the increment of the OT was well evident from Figure 5B,D, which show the FFT of the spectra. By calculating the differences between the OT of the samples before and after the protein functionalization, maximum ΔOT of 110 nm and 70 nm were determined in the case of nZnO-F and nZnO, respectively. The result suggested that about 37% as much protein was immobilized on the surface of nZnO-F sample with respect to nZnO one; this value, calculated as the percentage difference between the two maxima ΔOT , was in agreement with that calculated by fluorescence imaging. Fitting ΔOT data with a dose-response

curve, the PrA concentration useful for surface saturation was estimated to be 4 mg/mL for both samples (Figure 5E).

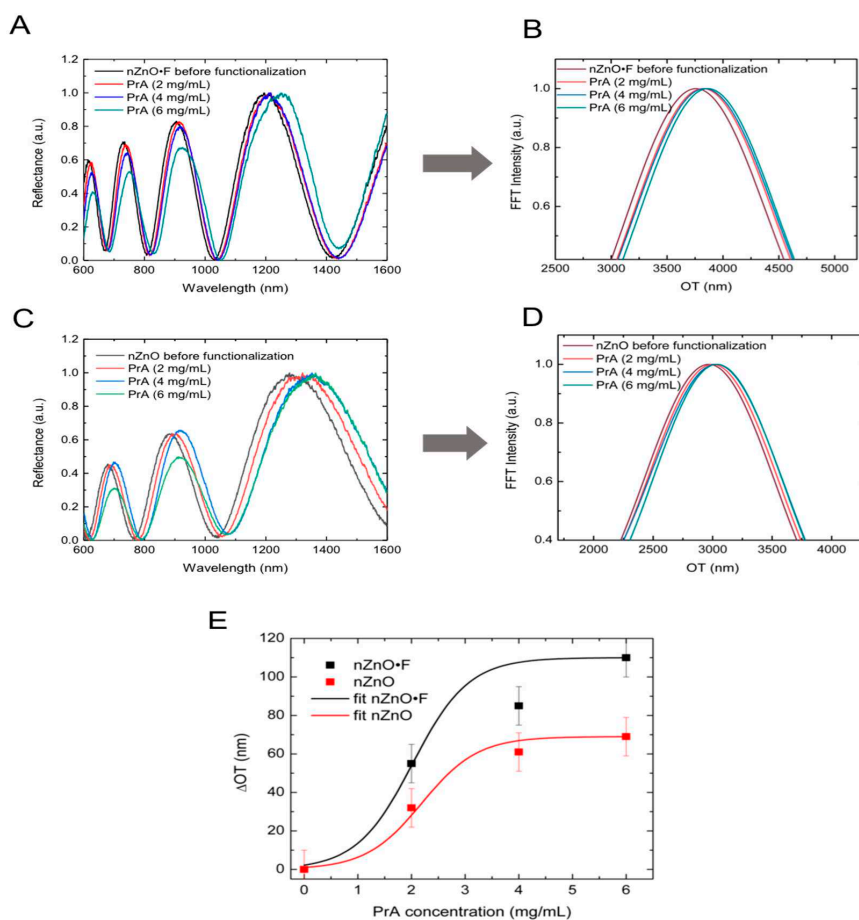


Figure 5. Reflectivity spectra of nZnO-F (A) and nZnO (C) before and after modification with different concentrations of PrA; corresponding Fourier transforms (B,D). ΔOT as function of PrA concentrations, calculated for nZnO-F and nZnO; experimental data were fitted by using a dose-response curve (E).

The PL emission of the nanostructured ZnO is sensitive to the chemical modification of the material surface and it can be used for monitoring the biomolecular interactions in the experiments of label-free optical sensing [14]. For this reason, the interaction between the nZnO-F and nZnO samples and the PrA was also investigated measuring their PL spectra. Figure 6A,B report the PL spectra of the nZnO-F and nZnO, respectively, after the surface functionalization with 2 mg/mL, 4 mg/mL and 6 mg/mL of PrA; the spectra of functionalized samples were compared with the spectra acquired before the functionalization. For both the materials, any variation of the peak at 380 nm ascribed to near band edge excitonic transitions, was not observed. On the contrary, the intensity of the broad visible band, included between 500 and 800 nm and mainly related to the surface defects, decreased at the increasing of protein concentration. By calculating the integrated PL (IPL) intensities and plotting them as a function of the PrA concentration (Figure 6B,D), a variation of 20% was obtained for the

fluorine doped sample and only 5% for the undoped sample. The integrated PL intensity variations were calculated as:

$$\Delta I_{PL} = \left(\frac{I_{PL}(0) - I_{PL}(6)}{I_{PL}(0)} \right) * 100 \quad (1)$$

The results of the optical investigations, i.e., the spectroscopic reflectometry and the photoluminescence spectroscopy, clearly demonstrated that nZnO-F could be functionalized with a higher efficiency with respect to the undoped nZnO. This effect was mainly ascribed to the peculiar flake-like morphology of the fluorine-doped material, made of nanograins much larger than the nZnO nanocolumns and with a more exposed area that could sustain a stronger surface interaction with the PrA biomolecules.

The silanization procedure for the functionalization of nanostructured zinc oxide, undoped and fluorine doped, with protein A was already successfully used in the case of porous silicon [23]. Since silanization was well established in the substitution of Si-OH bonds by Si-C ones, which were much more stable from the thermodynamic point of view, we firstly verified that silanization was able to substitute Zn-OH bonds by Zn-Si-C ones by grafting FITC-labelled protein A to both surfaces. Then, we exploited the amount of protein A that could be covalently linked to the semiconductors surface. Even if the porous silicon had a greater surface area, that could reach hundreds of m²/gr, the nanostructured fluorine doped zinc oxide could be surface modified with a very similar concentration of protein A, from about 50 uM up to 140 uM.

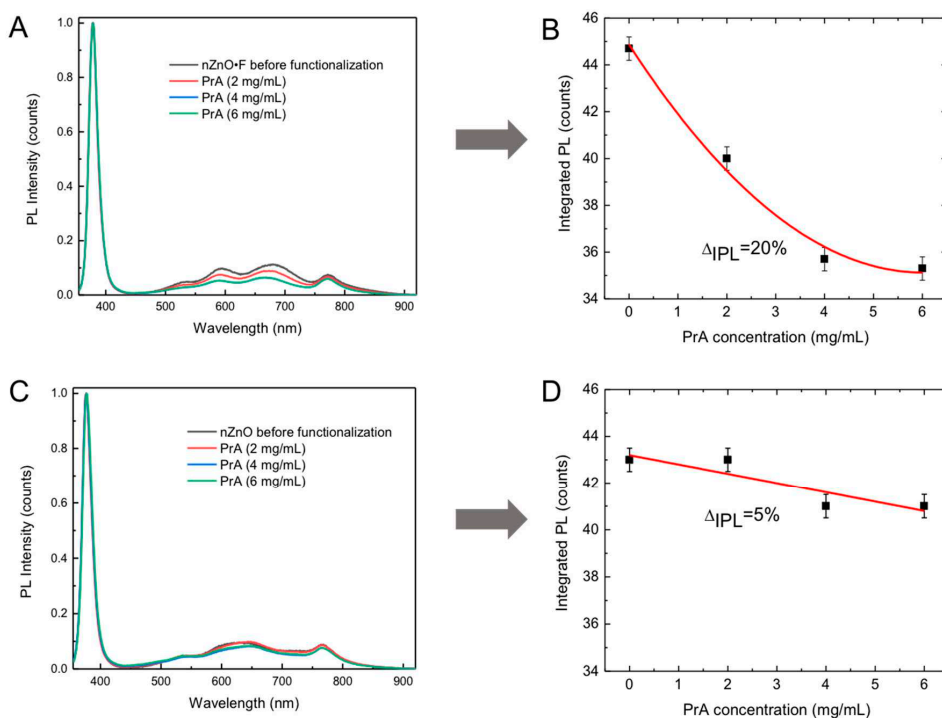


Figure 6. PL spectra of nZnO-F (A) and nZnO (C) measured after incubation with different concentrations of PrA; corresponding values of integrated PL as function of PrA concentration (B,D).

4. Conclusions

In this study, nZnO-F was synthesized on a silicon substrate by a hydrothermal process performed in presence of ammonium hydrogen fluoride. Compared to the undoped nZnO, nZnO-F was

characterized by a rougher morphology constituted by nanograins of about 600 nm with a flake-like shape. A mild chemical procedure based on the aminosilane modification followed by a cross-linker (bis-sulfosuccinimidyl suberate) immobilization was used to covalently bind a model biomolecule, fluorescein-labeled protein A, on the nZnO-F surface. All the FTIR, WCA and fluorescence microscopy characterizations revealed a successful functionalization of the surface. The interaction between nZnO-F and increasing concentrations of unlabeled PrA was also characterized by two label-free optical techniques, i.e., the spectroscopic reflectometry and the photoluminescence analysis. The results of the optical characterizations demonstrated that the fluorine doped nZnO-F matrix could be better functionalized with respect to the undoped one, nZnO; the effect was attributed to the wrinkled flake-like morphology, which allowed the immobilization of a higher percentage of the biomolecule under investigation compared to the highly packed hexagonal nanocolumns of the undoped sample. The data reported in this study also highlighted that nZnO-F could be effectively modified in order to fabricate a useful platform for label-free optical sensing.

Author Contributions: All authors equally contributed to this work.

Funding: This work was partially supported by the project POR FESR Campania 2014/2020 B63D18000250007.

Acknowledgments: The authors thank Maurizio Casalino of Institute for Microelectronics and Microsystems, National Research Council, for FFT analysis.

Conflicts of Interest: The authors declare no conflict of interest.

References

1. Holzinger, M.; le Goff, A.; Cosnier, S. Nanomaterials for biosensing applications: A review. *Front. Chem.* **2014**, *2*, 1–10. [[CrossRef](#)] [[PubMed](#)]
2. Bhat, S.S.; Qurashi, A.; Khanday, F.A. ZnO nanostructures based biosensors for cancer and infectious disease applications: Perspectives, prospects and promises. *TrAC Trends Anal. Chem.* **2017**, *86*, 1–13. [[CrossRef](#)]
3. Gooding, J.J. Biosensor technology for detecting biological warfare agents: Recent progress and future trends. *Anal. Chim. Acta* **2006**, *559*, 137–151. [[CrossRef](#)]
4. Tripathy, N.; Kim, D.-H. Metal oxide modified ZnO nanomaterials for biosensor applications. *Nano Converg.* **2018**, *5*, 27. [[CrossRef](#)] [[PubMed](#)]
5. De Stefano, L.; Oliviero, G.; Amato, J.; Borbone, N.; Piccialli, G.; Mayol, L.; Rendina, I.; Terracciano, M.; Rea, I. Aminosilane functionalizations of mesoporous oxidized silicon for oligonucleotide synthesis and detection. *J. R. Soc. Interface* **2013**, *10*, 160. [[CrossRef](#)] [[PubMed](#)]
6. De Stefano, L.; Rossi, M.; Staiano, M.; Mamone, G.; Parracino, A.; Rotiroli, L.; Rendina, I.; Rossi, M.; D'Auria, S. Glutamine-binding protein from escherichia coli specifically binds a wheat gliadin peptide allowing the design of a new porous silicon-based optical biosensor. *J. Proteome Res.* **2006**, *5*, 1241–1245. [[CrossRef](#)] [[PubMed](#)]
7. De Stefano, L.; Moretti, L.; Rendina, I.; Rossi, A.M. Time-resolved sensing of chemical species in porous silicon optical microcavity. *Sens. Actuators B Chem.* **2004**, *100*, 168–172. [[CrossRef](#)]
8. Arshavsky-Graham, S.; Massad-Ivanir, N.; Segal, E.; Weiss, S. Porous silicon-based photonic biosensors: Current status and emerging applications. *Anal. Chem.* **2018**, *91*, 441–467. [[CrossRef](#)]
9. Kong, Y.C.; Yu, D.P.; Zhang, B.; Fang, W.; Feng, S.Q. Ultraviolet-emitting ZnO nanowires synthesized by a physical vapor deposition approach. *Appl. Phys. Lett.* **2001**, *78*, 407–409. [[CrossRef](#)]
10. Park, W.I.; Jun, Y.H.; Jung, S.W.; Yi, G.C. Excitonic emissions observed in ZnO single crystal nanorods. *Appl. Phys. Lett.* **2003**, *82*, 964–966. [[CrossRef](#)]
11. Kumar, S.A.; Chen, S.M. Nanostructured zinc oxide particles in chemically modified electrodes for biosensor applications. *Anal. Lett.* **2008**, *41*, 141–158. [[CrossRef](#)]
12. Okada, T.; Agung, B.H.; Nakata, Y. ZnO nano-rods synthesized by nano-particle-assisted pulsed-laser deposition. *Appl. Phys. A Mater. Sci. Process.* **2004**, *79*, 1417–1419. [[CrossRef](#)]
13. Park, W.I.; Yi, G.C.; Kim, M.; Pennycook, S.J. ZnO nanoneedles grown vertically on Si substrates by non-catalytic vapor-phase epitaxy. *Adv. Mater.* **2002**, *14*, 1841–1843. [[CrossRef](#)]

14. Politi, J.; Rea, I.; Dardano, P.; de Stefano, L.; Gioffrè, M. Versatile synthesis of ZnO nanowires for quantitative optical sensing of molecular biorecognition. *Sens. Actuators B Chem.* **2015**, *220*, 705–711. [[CrossRef](#)]
15. Papari, G.P.; Silvestri, B.; Vitiello, G.; De Stefano, L.; Rea, I.; Luciani, G.; Aronne, A.; Andreone, A. Morphological, structural, and charge transfer properties of F-doped ZnO: A spectroscopic investigation. *J. Phys. Chem. C* **2017**, *121*, 16012–16020. [[CrossRef](#)]
16. Zhang, J.; Liu, T.; Zhang, Y.; Zeng, W.; Pan, F.; Peng, X. Hydrothermal synthesis and growth mechanisms of different ZnO nanostructures and their gas-sensing properties. *J. Mater. Sci. Mater. Electron.* **2015**, *26*, 1347–1353. [[CrossRef](#)]
17. Luo, B.; Wu, S.; Zou, W.; Zhang, Z.; Zhao, M.; Shi, S.; Yan, Z. Label-free immunoassay for porcine circovirus type 2 based on excessively tilted fiber grating modified with staphylococcal protein A. *Biosens. Bioelectron.* **2016**, *86*, 1054–1060. [[CrossRef](#)] [[PubMed](#)]
18. Vranken, T.; Redeker, E.S.; Miszta, A.; Billen, B.; Hermens, W.; de Laat, B.; Cleij, T.J. In situ monitoring and optimization of CuAAC-mediated protein functionalization of biosurfaces. *Sens. Actuators B Chem.* **2017**, *238*, 992–1000. [[CrossRef](#)]
19. Urmann, K.; Reich, P.; Walter, J.G.; Beckmann, D.; Segal, E.; Scheper, T. Rapid and label-free detection of protein A by aptamer-tethered porous silicon nanostructures. *J. Biotechnol.* **2017**, *257*, 171–177. [[CrossRef](#)]
20. Socrates, G. *Infrared and Raman Characteristic Group Frequencies: Tables and Charts*, 3rd ed.; Wiley and Sons: Chichester, UK, 2001; Volume 124.
21. Brown, N.L.; Bottomley, S.P.; Scawen, M.D.; Gore, M.G. A study of the interactions between an IgG-binding domain based on the B domain of staphylococcal protein A and rabbit IgG. *Appl. Biochem. Biotechnol. Part B Mol. Biotechnol.* **1998**, *10*, 9–16. [[CrossRef](#)]
22. Kyaw, H.H.; Al-Harhi, S.H.; Sellai, A.; Dutta, J. Self-organization of gold nanoparticles on silanated surfaces. *Beilstein J. Nanotechnol.* **2015**, *6*, 2345–2353. [[CrossRef](#)] [[PubMed](#)]
23. Moretta, R.; Terracciano, M.; Rea, I.; Casalino, M.; Dardano, P.; De Stefano, L. Functionalization of macroporous silicon for optical detection of bacteria. In Proceedings of the 19th Italian National Conference on Photonic Technologies Fotonica IET 2017, Padua, Italy, 11–18 June 2017; pp. 1–3.



© 2019 by the authors. Licensee MDPI, Basel, Switzerland. This article is an open access article distributed under the terms and conditions of the Creative Commons Attribution (CC BY) license (<http://creativecommons.org/licenses/by/4.0/>).

3. Gold nanoparticles for biomolecular and industrial applications

Gold nanoparticles (AuNPs) are the most investigated nanostructured materials due to their intrinsic properties which make them particularly attractive for applications in different fields of science. The development of innovative synthetic protocol for preparing functionalized AuNPs represents an active research area, with the purpose to improve the control over their size and shape. Sensing, photothermal therapy, drug delivery applications are only few possible uses of this fascinating nanostructured material.

The design, the synthesis and the cytotoxic effects of hybrid AuNPs, complexed with copper ions, for biological applications will be discussed in section 3.1, while the engineering and the antibacterial activity of two different nanocomplexes, made of AuNPs and an antimicrobial peptide, the temporin, will be discussed in the section 3.2.

3.1 Design and synthesis of hybrid gold nanoparticles for biomedical applications

Recently, researchers have focused on the synthesis of hybrid metal-organic nanoparticles and their possible use in biomedical applications. Following this trend, in the present work, two NPs systems, composed of gold and copper, mixed into the same structure, were developed. The two systems only differ by the chelation or not of the Cu(II) ions during the synthesis procedure. *In vitro* tests were used to evaluate the cytotoxicity effects of the hybrid-AuNPs using undifferentiated and neural differentiated embryonic stem cells.



Design and Synthesis of Hybrid PEGylated Metal Monopicolinate Cyclam Ligands for Biomedical Applications

Fatima Aouidat,[†] Zakaria Halime,[‡] Rosalba Moretta,[§] Ilaria Rea,[§] Stefania Filosa,^{||} Stella Donato,^{||} Rosarita Tatè,[⊥] Luca de Stefano,^{*,§,ⓑ} Raphaël Tripier,^{‡,ⓑ} and Jolanda Spadavecchia^{*,†,ⓑ}

[†]CNRS, UMR 7244, CSPBAT, Laboratoire de Chimie, Structures et Propriétés de Biomateriaux et d'Agents Therapeutiques Université Paris 13, 1 rue Chablis 93000, Sorbonne Paris Cité, 93000 Bobigny, France

[‡]Université de Brest, UMR-CNRS 6521/IBSAM, UFR Sciences et Techniques, 6 Avenue Victor le Gorgeu, C.S. 93837, 29238 Brest, France

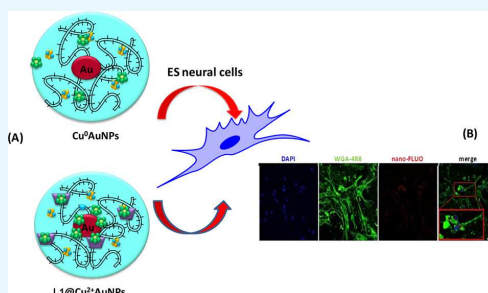
[§]Institute for Microelectronics and Microsystems, Unit of Naples, CNR, Via P. Castellino 111, 80131 Naples, Italy

^{||}Institute of Biosciences and Bioresources (IBBR), National Research Council (CNR), Naples, Italy-IRCCS, Neuromed, Via Università, 133, 80055 Pozzilli, Isernia, Italy

[⊥]Institute of Genetics and Biophysics "Adriano Buzzati-Traverso", CNR, Via P. Castellino 111, 80131 Naples, Italy

Supporting Information

ABSTRACT: In this study, we report, for the first time, the synthesis of two original nanosystems, based on gold Au(III) and copper Cu(II): simple gold–copper nanoparticles (Cu^0AuNPs) and enriched monopicolinate cyclam (L1)–Cu(II)–Au(III)-complex ($\text{L1@Cu}^{2+}\text{AuNPs}$). The two nanomaterials differ substantially by the chelation or not of the Cu(II) ions during the NPs synthesis process. The two hybrid nanoparticles (Cu^0AuNPs ; $\text{L1@Cu}^{2+}\text{AuNPs}$) were deeply studied from the chemical and physical point of view, using many different analytical techniques such as Raman and UV–vis spectroscopy, electron transmission microscopy, and dynamic light scattering. Both nanosystems show morphological and good chemical stability at pH 4 values and in physiological conditions during 98 h. Undifferentiated and neural differentiated murine embryonic stem cells were used as a model system for in vitro experiments to reveal the effects of NPs on these cells. The comparative study between Cu^0AuNPs and $\text{L1@Cu}^{2+}\text{AuNPs}$ highlights that copper chelated in its +2 oxidation state in the NPs is more functional for biological application.



Undifferentiated and neural differentiated murine embryonic stem cells were used as a model system for in vitro experiments to reveal the effects of NPs on these cells. The comparative study between Cu^0AuNPs and $\text{L1@Cu}^{2+}\text{AuNPs}$ highlights that copper chelated in its +2 oxidation state in the NPs is more functional for biological application.

1. INTRODUCTION

Hybrid metal–organic nanoparticles (NPs) have been recently used as diagnostic and therapeutic tools to better understand, detect, and treat several human diseases.^{1,2} Metal-based NPs have been proposed as performing contrast agents that can increase signal intensity in magnetic resonance imaging (MRI) and positron emission tomography imaging, or as nanovectors for specifically delivering of drugs inside cells.

The insertion of copper (Cu), especially as Cu^{2+} atoms, in NPs structures is still challenging because it has an important impact in many scientific fields from catalysis and plasmonics up to nanomedicine applications.^{3–6} Because cationic metals take part in biological systems (charge balancing, stabilizing structures, reactions catalyzing, and so on), copper ions should be chelated to avoid the in vivo metal releasing that could induce several undesirable effects.

Biocompatible copper(II) chelators are commonly those that yield thermodynamically stable and kinetically inert complexes so that transchelation of Cu due to competition with other biological ligands, metals, or reductive media is

avoided. Among known copper(II) ligands, azacycloalkanes present the highest complexation properties.⁷ By *N*-functionalization of their properties, especially in terms of kinetic of formation (maximizing the complexation rate) and dissociation (decreasing of the decomplexation rate), could also be improved. A special category of rigid tetraazamacrocycles, indicated as cross-bridged derivatives, has been the source of great interest because of the outstanding behavior in complexing different metals, including copper(II).^{8–10} Due to an ethylene linker connecting two opposite nitrogen atoms of the macrocycle, these ligands produced some of the most inert metal complexes ever reported.

We recently have published a size-adapted azamacrocycle, the cb-te1pa chelator^{11–13} (see its structure in Figure 1), which combines all the criteria for Cu(II) chelation, i.e., the presence of cyclam, the ethylene cross bridge and an efficient chelating

Received: December 2, 2018

Accepted: December 28, 2018

Published: February 1, 2019

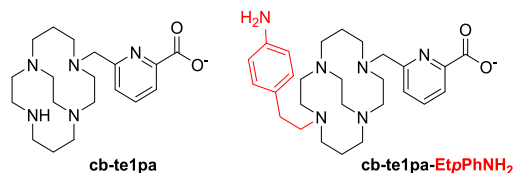


Figure 1. Ligand *cb-te1pa* and its bifunctionalized analogue *cb-te1pa-EtpPhNH₂*.

functionalization, in particular the methyl picolinic acid, a cross-bridged cyclam bearing a methylpicolinate pendant. This compound was able to chelate copper(II) after fast complexation, yielding a highly thermodynamical stable and an exceptionally inert product, even if Cu was in the (+1) oxidation state. Due to the presence of a secondary amine, an additional functional group, which could be dedicated to the conjugation of *cb-te1pa* with a solid support, was then easily added as an aniline moiety. To preserve a sufficient distance between the coordination center and the anchoring point, an ethylene linker was chosen to take away the aromatic part. The bifunctionalized analogue *cb-te1pa-EtpPhNH₂* (L1) was then the final Cu ligand (Figure 1).

In the present study, we synthesized two new nanoparticle systems including gold and copper wrapped in their structure. In the first case, Cu(II) was introduced as “free” cation and in the second case, in its $[\text{Cu}(\text{cb-te1pa})]^+-\text{EtpPhNH}_2$ chelated form (L1Cu^+). According to the NPs formation procedure, the first material included Cu^0 , whereas the second one the Cu^{2+} chelated ions. Characterizations were performed to investigate the structure of both NPs. Potential cytotoxic effects was evaluated in vitro on undifferentiated and neural differentiated embryonic stem cells (ESCs). ESCs can be used as a model system in basic research, drug discovery, biomedical applications, and nanotechnology because they combine the potential of unlimited self-renewal with the ability to differentiate into a wide range of tissue-specific cells.

2. RESULTS AND DISCUSSION

2.1. Formation Mechanisms of Au–Cu-Based Nanoparticles. Peculiar molecular interactions between organic compounds and metal chlorides was extensively studied for many biochemical and physical applications.^{19–22} The aim of this study was to use a copper–gold chloride blend as the building blocks of hybrid nanoparticles under specific conditions of reaction. For this purpose, in the first step, we mixed $\text{HAuCl}_4 \cdot 3\text{H}_2\text{O}$ and $\text{CuCl}_2 \cdot 6\text{H}_2\text{O}$ in water solution at

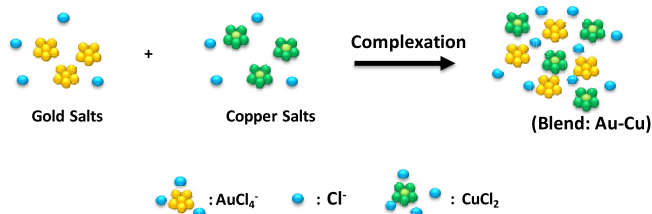
room temperature under specific pH conditions (Scheme 1). The formation of Au–Cu blend (Figure S1 in the Supporting Information) could be deduced by looking at the fingerprints of each single solution ($\text{HAuCl}_4 \cdot 3\text{H}_2\text{O}$, $\text{CuCl}_2 \cdot 6\text{H}_2\text{O}$) present in the UV–vis spectrum of their mix (Au–Cu). In particular, the UV–vis spectrum of $\text{HAuCl}_4 \cdot 3\text{H}_2\text{O}$ (black line in Figure S1) showed typical signatures with two prominent peaks at 256 and 290 nm. The UV–vis spectrum of $\text{CuCl}_2 \cdot 6\text{H}_2\text{O}$ solution showed a peak at 256 nm, a small peak at 280 nm and a broadened peak at 800 nm (red line in Figure S1). When $\text{CuCl}_2 \cdot 6\text{H}_2\text{O}$ was added to $\text{HAuCl}_4 \cdot 3\text{H}_2\text{O}$ solution, the UV–vis spectrum (blue line in Figure S1) slightly changed. Main difference in the spectra was due to the increase and the shift of the peak from 280 to 320 nm due to electronic transitions. Moreover, the dramatic decrease of the peak at 800 nm confirmed that the hybrid system (Au–Cu) was obtained.²⁰

Raman spectroscopy (Figure S1B) also displayed the peak at 254 cm^{-1} due to Cu–Au–Cl and Cu–OH stretching, which were assigned to vibrations mainly within the coordination sphere of Cu^{2+} , confirming the successful reaction.²⁰

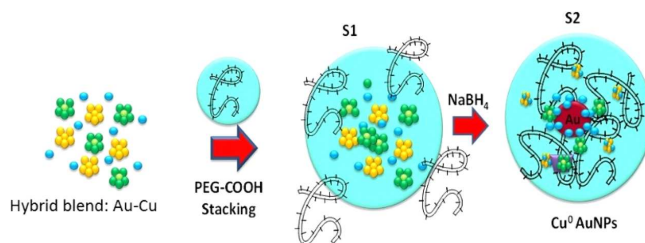
Figure S2a,b in the Supporting Information shows the localized surface plasmon (LSP) resonance spectra before and after incubation of HAuCl_4 mixed to CuCl_2 under specific conditions (pH: 4.0–7.0–9.0; time: 96 h). At pH 4, we observed an increase in the peak intensity at 256 nm probably due to CuCl_2 fingerprint associated to AuCl_2 ions upon complexation. The increase of the peak at 800 nm confirmed the reaction under acidic conditions. A different behavior was observed in the case of pH 7 and pH 9 (Figure S2 panel b), in which the LSP bands could not be observed any more after incubation at pH 7 and 9 for 96 h. This spectroscopic behavior during pH release gave evidence of the change of reagent conformation when it was encapsulated into gold nanoparticles.

2.2. Formation Mechanism of Cu^0 –AuNPs and L1@Cu^{2+} –AuNPs. Recently, Spadavecchia et al. have designed and produced different novel hybrid nanomaterials based on gold, polymers, proteins, and drug complexes by original chemical synthetic methodology.^{17,23,24} These authors have investigated the formation mechanism and the competition effect between various capping agents on the growth process of hybrid nanoparticles.²⁵ Some chemical–physical characterizations and the analysis of biological activity have fully elucidate that conformation change of biomolecules (i.e., polymer, drug, protein) during the formation of hybrid gold nanostructures by chelation had a good impact on its therapeutic activity. In case of Cu, other authors showed that copper influenced the optical plasmonic features of the gold nanorods when incorporated in

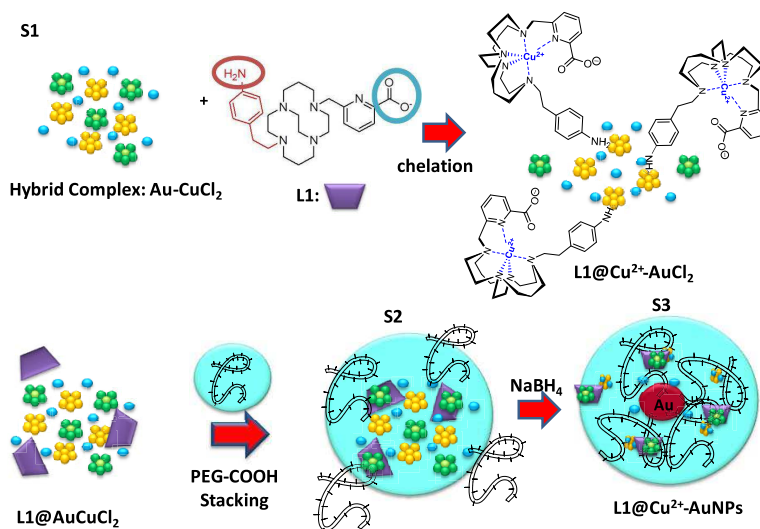
Scheme 1. Schematic Representation of the Hybrid Blend (Au–Cu)



^aPlease note that drawings are not in scale and are not intended to be representative of the full samples composition.

Scheme 2. Schematic Representation of the Synthesis of Cu^0 -AuNPs via a Two-Step Process^a

^aPlease note that drawings are not in scale and are not intended to be representative of the full samples composition.

Scheme 3. Schematic Representation of the Synthesis of L1@Cu²⁺-AuNPs via a Three-Step Process^a

^aPlease note that drawings are not in scale and are not intended to be representative of the full samples composition.

the growth solution during the seed-mediated synthesis.⁴ The aim of this research was to prove the formation of stable hybrid complexes based on PEGylated Au-Cu and PEGylated L1@Au-Cu, respectively. Some synthesis procedures of Cu²⁺AuNPs by chemical and physical adsorption using chelator linkers can be found in recent literature.^{19,26} The main difference with previously reported synthetic procedures was that L1 ligand totally bound Cu²⁺ and participated in the stabilization of PEGylated Cu²⁺-AuNPs via electrostatic interaction between their amino groups with chloride copper-auric ions. Moreover, the chelation of Cu²⁺ avoided its reduction during the NPs synthesis process. Indeed, the macrocyclic chelation added extremely high stability to the copper(I) complex and allowed the stability of the chelate all along the formation of the final material.

The formation of hybrid gold-copper NPs from Cu-Au mixture is summarized in Schemes 2 and 3. Step (1) was the complexation of solutions CuCl₂-AuCl₄⁻ and generation of copper-gold clusters (see Scheme 2). Step (2) is the initial reduction of Au(III) ions by dicarboxylic acid-terminated poly(ethylene glycol) (PEG) that adsorbed onto Cu-Au clusters (Scheme 2); the last step (3) is the reduction of metal

ions in that vicinity and the growth of hybrid gold particles (Cu⁰-AuNPs) together with the colloidal stabilization due to the molecules of PEG polymers.

In this frame, L1 ligands take part in the reaction, thanks to their amino group onto copper-gold clusters in which copper was kept in oxidation state Cu²⁺ and chelated with them (Scheme 3). The positive charge of the amino group onto L1 ligand in water solutions showed strong electrostatic interaction with negatively charged Cu²⁺-AuCl ions and formed a complex L1@Cu²⁺-AuCl that played a final role in the growth of NPs. A large excess of L1 ligand in the mixture was required to chelate completely all Cu²⁺. The addition of diacid PEG improved the kinetics of reduction by complexation of Cu-Au ions,^{27,25} just tuning the growth process of hybrid nanoparticles. During the S2 phase (Scheme 3), L1@Cu²⁺-AuCl complexes migrated through PEG molecules. Thus, an appreciable amount of complexes diffused and were captured inside the PEG layer via a mechanism similar to the other ligand complexes loaded onto nanostructures.^{16,23,28} Based on previously research studies,²⁹ we suppose that when PEG was added to the L1@Cu²⁺-AuCl, the PEG initially was bound to hybrid complex in a mushroom conformation

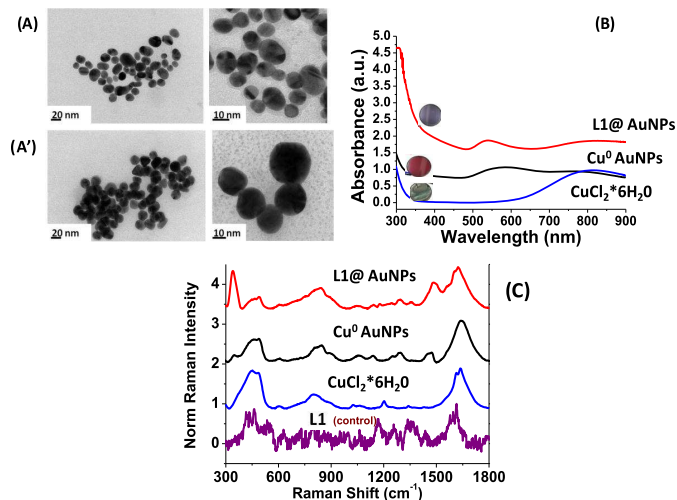


Figure 2. (A, A') TEM images of Cu^0 -AuNPs (panel A) and L1@Cu^{2+} -AuNPs (panel A'). (B) Normalized UV-vis absorption and scale bars: 50 and 20 nm for Cu -AuNPs and $0.2 \mu\text{m}$ and 100 nm for L1@Cu^{2+} -AuNPs and $\text{CuCl}_2 \cdot 6\text{H}_2\text{O}$ as control. (C) Raman spectra of Cu -AuNPs and L1@Cu^{2+} -AuNPs products compared to free L1 and $\text{CuCl}_2 \cdot 6\text{H}_2\text{O}$ as control. Raman spectra. Experimental conditions: $\lambda_{\text{exc}} = 785 \text{ nm}$; laser power 20 mW ; accumulation time 180 s .

followed by a conformational change to brush mode.^{15,17} The final reduction by NaBH_4 completed the grow process to form L1@Cu^{2+} -AuNPs. All products of our synthetic procedure were characterized by UV-vis absorption spectroscopy, transmission electron microscopy (TEM), and Raman spectroscopy.

2.3. Comparative Physicochemical Characterization of Cu^0 -AuNPs and L1@Cu^{2+} -AuNPs. TEM images of Cu^0 -AuNPs showed a well dispersion of the nanoparticles with an average size of $20 \pm 1 \text{ nm}$ (Figure 2A overpanel). Different nanostructures were obtained with L1@Cu^{2+} -AuNPs: they exhibited a nanocapsule-like shape embedded in a shell of PEG, in which metal nanoparticles showed a diameter of around $28 \pm 2 \text{ nm}$ (Figure 2A underpanel). The synthesis of Au/Cu alloy nanoparticles using biocompatible liquid polymer²² and the fabrication of snowflakes nanoparticles by catalytic CO oxidation¹¹ have been already reported. Anyway, a study about the grafting of L1 ligands onto Cu^0 -AuNPs has not been reported. When L1 ligands were added to the Cu^{2+} -AuCl solution, the picolinate amino group was initially electrostatically bound to Au-Cu clusters, followed by a conformational change of the ligand L1 that chelated Cu^{2+} ions completely and successively embedded in the dicarboxylic PEG in a mushroom conformation.¹⁵

Figure 2B black line reports the absorption spectra of hybrid Cu^0 -AuNPs, all characterized by a surface plasmon band in the range of 560 nm , together with a small peak at 775 nm . The slow shift of the band position depended on the ratio of the gold salt and the capping materials during the reaction processes.^{30,31} This peak could be generally ascribed to collective oscillation, known as the surface plasmon oscillation of the metal electrons in the conduction band, due to interaction of electrons with light of a certain wavelength. PEG could be used as a stabilizing polymer for AuNPs because the dispersed solutions could be obtained due to the formation of coordination bands between Au and Cu ions with the

carboxylic group. The chelation effect even better dispersed Au and Cu ions, which were reduced to form single Cu^0 -AuNPs of relatively uniform size. Figure 2B red line displays a UV-vis absorption spectrum of L1@Cu^{2+} -Au NPs. Compared with Cu^0 -AuNPs spectrum, a blue shift of the plasmon peak from 560 to 535 nm and a red shift of the peak at 775 – 810 nm could be observed. The latter was associated to π - π^* electronic transitions due to interactions between the L1 ring and CuAuCl_2 ions and gave a clear evidence of the complex formation with a change of color of the colloidal solution from pink red (Cu^0 -AuNPs) to bright violet (L1@Cu^{2+} -Au NPs).

The NP sizes were confirmed by dynamic light scattering (DLS) measurements (Table 1). ζ -Potential measurements

Table 1. ζ -Potential and Hydrodynamic Diameter of Cu^0 -AuNPs and L1@Cu^{2+} -AuNPs

synthetic product	ζ -potential (mV)	hydrodynamic diameter (nm)	PdI
Cu^0 -AuNPs	-25 ± 3	20 ± 2	0.3
L1@Cu^{2+} -AuNPs	-20 ± 2	28 ± 2	0.3

showed that Cu^0 -AuNPs and L1@Cu^{2+} -AuNPs were stable colloids at physiological pH (ζ -potential = -25 ± 3 and $-20 \pm 2 \text{ mV}$ with a PdI equal to 0.3) (Table 1). This stability was enhanced by the presence of the PEG layer around nanoparticles.²⁵

Raman spectra of Cu^0 -AuNPs exhibited many bands in the region 500 – 2000 cm^{-1} (Figure 3C black line). The wide band observed around 1600 cm^{-1} on the Raman spectra was assigned to the water. The strong band at 1712 cm^{-1} was assigned to C=O carbonyl stretching of PEG diacid. The intense doublet at 720 – 760 cm^{-1} was due to the C-H plane deformation and a strong peak at 1439 cm^{-1} was assigned to $\nu\text{C-C}$ stretching. These bands were due to the variation of the steric conformation of the PEG diacid and became more

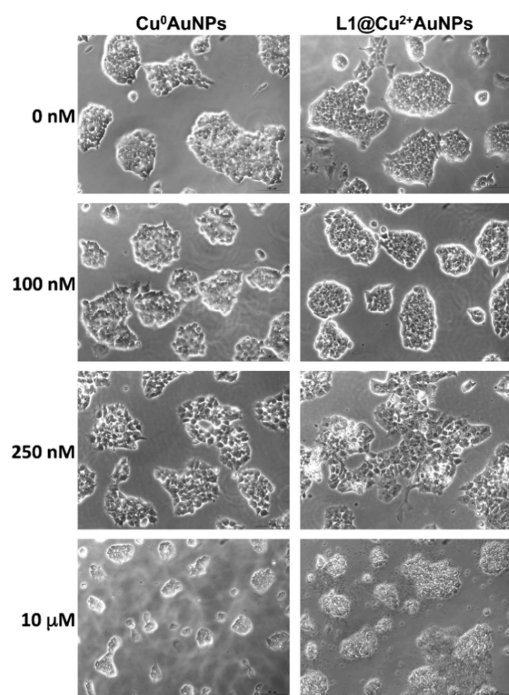


Figure 3. Cytotoxicity of ES cells incubated with different concentrations of Cu^0 -AuNPs or L1@Cu^{2+} -AuNPs nanoparticles (0–10 μM) for 24 h. Bar = 50 μm .

prominent upon complexation with Cu-AuCl_2 , as previously described.^{16,20} As matter of fact, when C=O and hydroxyl groups of PEG diacide interacted with a metal, the sterical conformation became more tilted with respect to the planar one. Focusing on the spectral range 200–500 cm^{-1} (Figure 2C), we can observe several spectral changes, which confirmed a chemical modification of Cu after complexation with gold ions and PEG diacide molecules. One of the Raman fingerprint of the Cu-PEG-AuNPs was the presence of a band around 263 cm^{-1} , and a double peak at 235–285 cm^{-1} was observed. These bands could be assigned to the gold chloride stretches, $\nu(\text{Au-Cl})$, and $\delta(\text{O-Au-O})$ and $\delta(\text{Cu-Au-O})$ are a clear evidence of the formation of a complex between AuCl_2^- and Cu and PEG diacide in the solution. The peak at 430 cm^{-1} was due to the vibrations $\delta(\text{OH}\cdots\text{O})$, $\nu(\text{OH}\cdots\text{O})$ of the PEG, as previously described.^{15,16} The bands in the region 3000 cm^{-1} could be assigned to the aromatic C–H stretching (Figure 2C). A broad band composed of some peaks appeared in the spectral range 2850–2930 due to the symmetric $\text{CH}_2\text{-CH}_3$ stretch vibration of PEG diacide molecules, confirming the main role of the polymer in the synthesis of the nanoparticle. The sterical arrangement of L1 ligand during the synthesis process of PEGylated copper–gold nanoparticles was confirmed by Raman spectroscopic analysis (Figure 2C).

Raman spectra of free L1@Cu^{2+} -AuNPs in water showed SERS effect in the range 300–1800 cm^{-1} . The spectral modifications were evidence of the sterical conformational change of the L1 after grafting on the copper–gold nanoparticles. One of the Raman fingerprints of the L1@

Cu^{2+} -AuNPs was the presence of a band around 340 cm^{-1} due to the copper(II) peroxide complex, where L1 chelates Cu^{2+} . The common peak at 450 cm^{-1} was due to the vibrations $\delta(\text{OH}\cdots\text{O})$, $\nu(\text{OH}\cdots\text{O})$ of the PEG as previously described.^{15,16} On the basis of the spectrochemical and previously theoretical findings, we assumed that Au^{3+} ions promoted the deprotonation of the L1 amino group. These bands were due to variation of the sterical conformation of the L1 and became more prominent upon electrostatic interaction with gold cluster and then chelation with Cu^{2+} .

2.4. Cytotoxicity of Cu^0 -AuNPs and L1@Cu^{2+} -AuNPs. Murine ES cells and neural-derived ES cells were exposed to Cu^0 -AuNPs and L1@Cu^{2+} -AuNPs nanoparticles at different concentrations (0–1000 nM) for 24 h (Figure 3), and cytotoxicity was analyzed by live–dead staining, and LC50 was calculated. At maximum used concentration (10 μM), both kinds of nanoparticles determined the death of almost all the cells. They resulted not cytotoxic for concentrations up to 100 nM, suggesting a fair good biocompatibility at this concentration. However, the NPs were found to display significant cytotoxicity still at the concentration of 250 nM. The nanoparticles showed concentration-dependent cytotoxicity in both cells: the neural-derived ES cells were more sensitive toward the toxicity of both particles than the undifferentiated ES cells. The results highlight the difference of cytotoxicity between nanoparticles used and differential sensitivity of cells to Cu^0 -AuNPs or L1@Cu^{2+} -AuNPs. However, the toxic response varied depending on the type of cell exposed due to differential sensitivity.

The results obtained on ES cells were used to identify the range of NPs concentrations to test the cytotoxicity on neural-derived ES cells. These cells were exposed to the same concentration of Cu^0 -AuNPs and L1@Cu^{2+} -AuNPs, i.e., 0–100–250–1000 nM, for 24 h. The 50% of lethal dose for both NPs, reported in Table 2, was determined using trypan blue dye exclusion.

Table 2. LD50 of Neural-Derived ES Cells after 24 h of Treatment with Cu^0 -AuNPs or L1@Cu^{2+} -AuNPs Nanoparticles

	LD50% (nM)	LD50% ($\mu\text{g/mL}$)
Cu^0 -AuNPs	600	0.16
L1@Cu^{2+} -AuNPs	950	0.25

On neural-derived ES cells, the Cu^0 -AuNPs were more toxic, with LD50 value of 600 nM, than the L1@Cu^{2+} -AuNPs nanoparticles, with LD50 value of 950 nM. Light microscopy analysis characterized the effect of different concentrations of NPs on neural-derived ES cells morphology. Even at 100 nM, both NPs preserved the cell viability and morphology, with quite equal toxicity profile observed for both NPs; at 250 nM, neural-derived ES cells treated with L1@Cu^{2+} -Au NPs exhibited more neurite reduction than those treated with Cu^0 -AuNPs. At 1000 nM of both NPs, the cells appeared to refract the light, suggesting a typical apoptotic phenotype (Figure 4).

2.5. Determination of Cellular Uptake of NPs by Confocal Microscopy. The neural-derived ES cells were plated on a gelatin-coated microscope slide and left to adhere overnight before adding Cu^0 -AuNPs and L1@Cu^{2+} -AuNPs labeled with the fluorophore at 200 nM, a concentration well below the LD50 for both kinds of NPs. As shown in Figure 5,

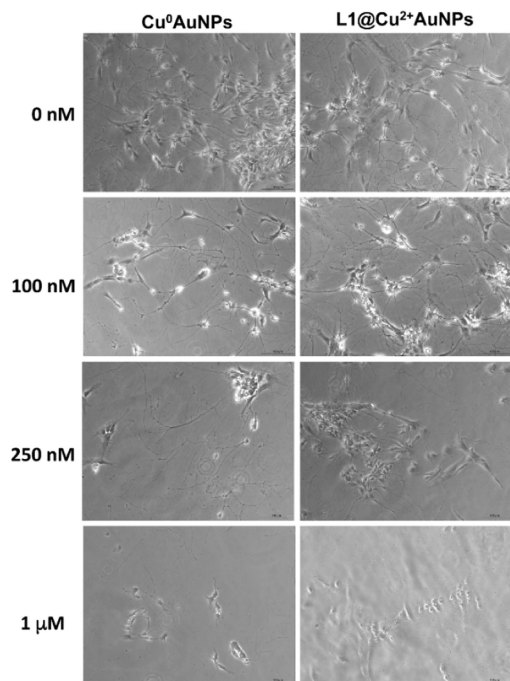


Figure 4. Cytotoxicity of neural-derived ES cells incubated with different concentrations of $\text{Cu}^0\text{-AuNPs}$ or $\text{L1@Cu}^{2+}\text{-AuNPs}$ nanoparticles (0–100–250–1000 nM) for 24 h. Bar = 50 μm .

both NPs synthesized were internalized into neural-derived ES cells but with some qualitative differences. Confocal images showed $\text{Cu}^0\text{-AuNPs}$ internalized more than $\text{L1@Cu}^{2+}\text{-AuNPs}$. Moreover, even if slightly larger, the $\text{Cu}^0\text{-AuNPs}$ were internalized also inside the nucleus. This capability may be caused by a more efficient interaction with mammalian cell membranes.

Confocal images confirmed that NPs were mainly located within the cell and not adhered to the cell surface: the

fluorescent signal of $\text{Cu}^0\text{-AuNPs}$ was predominantly observed in the cytoplasm and also in the nuclei; on the contrary, the fluorescent signal of $\text{L1@Cu}^{2+}\text{-AuNPs}$ was prevalently present in the cytoplasm (Figure 5).

From data collected in biological experiments, a type-selective difference in NP toxicity was observed. A possible reason for the difference in uptake and distribution inside the neural-derived ES cells could be the different surface chemistry of two NPs synthesized, which could improve the endocytosis mechanisms up to the nucleus in case of $\text{Cu}^0\text{-AuNPs}$. Experimental results indicated that the differences between $\text{Cu}^0\text{-AuNPs}$ and $\text{L1@Cu}^{2+}\text{-AuNPs}$ nanoparticles as well as the target cell type were critical determinants of intracellular responses and degree of cytotoxicity. At this stage, it was not possible to completely highlight the mechanism underlying the differential toxicity. The evidence emerging from the experimental results was that apoptosis is the predominant death pathway for moderate concentrations of NPs in the solution, whereas necrosis was the predominant pathway for high concentrations of NPs, according to the data reported in literature.^{32,33} Large amount of Cu-based nanoparticles, once internalized in neurons, caused severe alterations of cell morphology up to membrane disruption, according to the images reported in Figure 4 from concentrations of 100 nM onward. Light concentration of copper NPs inside neuron cells caused apoptosis as a consequence of oxidative stress induced by reactive oxygen species associated to metallic nanoparticles.

2.6. Optical Imaging of Cells. Internalization of cells of the synthesized colloids (Cu^0AuNPs and $\text{L1@Cu}^{2+}\text{AuNPs}$) was carried out with a confocal microscope (Horiba Scientific) under bright- and dark-field illumination. The images reported in Figures S3 and S4 are from the treated ES neuronal cells in different areas, the same sample region was seen in bright-field (a) and dark-field conditions (b). The dark-field image showed a high density of bright, small scattering centers dispersed all over the glass slide. The density of these bright spots clearly showed an effect of concentration addition when the colloids were incubated. It appears that the colloids had a tendency to accumulate inside the cells in the experimental conditions previously described.¹⁷

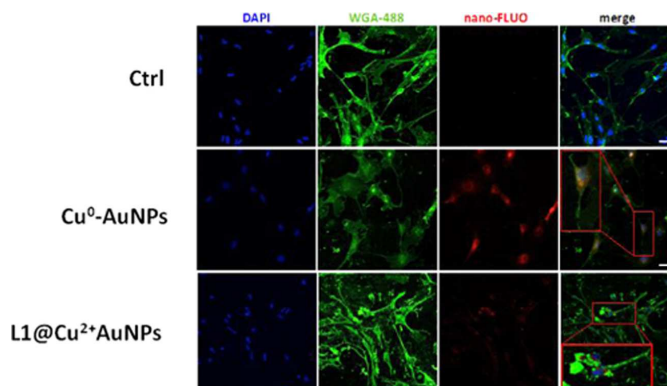
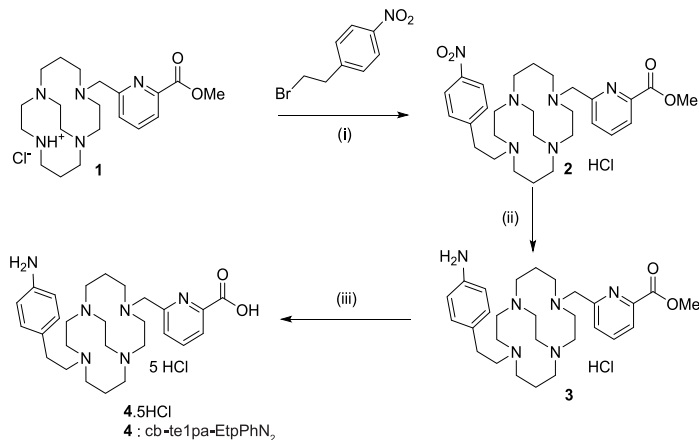


Figure 5. Confocal fluorescence images of neural-derived ES cells incubated with $\text{Cu}^0\text{-AuNPs}$ or $\text{L1@Cu}^{2+}\text{-AuNPs}$ (200 $\mu\text{g/mL}$) for 24 h. Bar = 50 μm .

Scheme 4. Synthesis of L1 (cb-te1pa-EtpPhNH₂): L1^a

^a(i) K₂CO₃, CH₃CN, 12 h, reflux, 85%; (ii) tin chloride MeOH/HCl aq 12 M, room temperature, 12 h, 83%; and (iii) hydrochloric acid 6 M, reflux, 12 h, quant.

3. MATERIALS AND METHODS

All chemicals were of reagent grade or higher and used as received unless otherwise specified. Tetrachloroauric acid (HAuCl₄·H₂O), CuCl₂·6H₂O, sodium borohydride (NaBH₄), poly(ethylene glycol)-600 (PEG 600), and phosphate buffered saline (PBS, 0.1 M, pH 7.0, pH 4.0, pH 9.0) were purchased from Organics and from Aldrich Chemical Co.

3.1. L1 Synthesis. L1 synthesis was based on previous work that is summarized in Scheme 4. Briefly, starting from compound 1, the methyl ester of te1pa, the addition of 4-nitrophenylethyl bromide led to compound 2 with 85% yield. The specific reduction of the nitrophenyl was managed with tin chloride with 83% yield and produced compound 3. A final hydrolysis removed the ester function and generated the bifunctional cb-te1pa-EtpPhNH₂ (compound 4). In the following sections, the final product cb-te1pa-EtpPhNH₂ will be simply called L1.

NMR was performed on Bruker 300 advance spectrometers. ²D NMR ¹H–¹H homonuclear, ¹H–¹³C heteronuclear correlations, and homonuclear decoupling experiments were used for assignment of the ¹H and ¹³C signals. The δ scales are relative to tetramethylsilane (¹H, ¹³C). The signals are indicated as follows: chemical shift, intensity, multiplicity (s, singlet; br s, broad singlet; d, doublet; t, triplet; m, multiplet; q, quartet), coupling constants *J* in hertz (Hz). The high resolution mass spectrometry (HR-MS) analyses were performed at the Institute of Analytic and Organic Chemistry, ICOA in Orleans. In details, compound L1 was synthesized by a three-step procedure, which is reported in the following section. Results of HR-MS are reported for each step in the Supporting Information.

3.1.1. Step (i): trans-Di-N-functionalization of Cross-Bridged Monomethylpicolinate Cyclam (Compound 1) Yielding Compound 2. 4-Nitrophenylethyl bromide (0.968 g, 4.20 mmol) and potassium carbonate (0.872 g, 6.31 mmol) were added to a solution of 1 (0.865, 2.10 mmol) in 200 mL of distilled acetonitrile. The mixture was refluxed overnight. After the evaporation of the solvent, the crude product was purified

by column chromatography in silica gel (CHCl₃/MeOH 8:2) to yield compound 2 as a yellow oil (1.000 g, 85%).

3.1.2. Step (ii): Reduction of Compound 2 Yielding Compound 3. Tin chloride (1.810 g, 9.55 mmol) and compound 2 (0.500 g, 0.95 mmol) were added to a 40 mL solution 1:9 of MeOH/HCl aq 12 M. The mixture was stirred at room temperature overnight and then excess HCl was neutralized using potassium carbonate. The desired compound 3 was obtained by extraction with chloroform at pH 14 as yellow oil (420 mg, 83%).

3.1.3. Step (iii): Hydrolysis of Compound 3 Yielding Compound 4 (L1). Hydrochloric acid (10 mL, 6 M) was slowly added to compound 3 (0.200 g, 0.38 mmol) and the mixture was refluxed overnight. After cooling to room temperature, the solvent was evaporated to yield compound 4 (L1) as an off-white solid in quantitative yield.

3.2. Synthesis of Cu⁰–AuNPs. Twenty milliliters of 0.0001 M aqueous HAuCl₄ was mixed with 5 mL of CuCl₂·6H₂O solution (6.10 × 10^{−5} M in water) at room temperature for 1 h under magnetic stirring to form a Au–Cu blend. Then, 250 μL of poly(ethylene glycol) 600 diacid (PEG) was mixed to the blend solution under stirring for 2 h. After this time, 3.6 mL of NaBH₄ (0.01 M) was added dropwise, followed by rapid stirring and kept without agitation for 2 h. The color of the dispersion indeed instantly changed from green-yellow to pink-red when sodium borohydride was added to a solution of copper–gold precursor in the presence of the PEG diacid polymer, with a complete reduction of metal ions confirming the formation of hybrid nanoparticles in the solution. The as-prepared Cu⁰–AuNPs solution was purified by centrifugation and dialysis to remove excess of not-conjugated dicarboxylic PEG.¹⁴

3.3. Synthesis of L1@Cu²⁺–AuNPs. The synthesis of L1@Cu²⁺–AuNPs colloids is described here. Twenty milliliters of HAuCl₄ aqueous solution (2.5 × 10^{−4} M in water) was added to CuCl₂ solution (5 mL, 6.10 × 10^{−5} M in water) under stirring for 1 h. After this time, 5 mL of L1 (2.3 × 10^{−4} M in water) was mixed to this hybrid blend solution during 1 h, and the mixture was stirred at room temperature. At the end

of this reaction, 250 μL of dicarboxylic PEG was mixed to the solution and stirred for 1 h. Finally, 3.6 mL of aqueous 0.01 M NaBH_4 was added at once until stabilization and reduction to hybrid nanoparticles. The “as-prepared” $\text{L1@Cu}^{2+}\text{-AuNPs}$ solution was centrifuged at 5000 rpm for 20 min for three times and then the supernatant was discarded. This was repeated twice to remove excess of not-conjugated reagents. $\text{L1@Cu}^{2+}\text{-AuNPs}$ were stored at 8 $^\circ\text{C}$ and characterized by UV–vis spectroscopy, transmission electron microscopy, and Raman spectroscopy.

3.4. Physicochemical Characterization. All the measurements were performed in triplicate to validate the reproducibility of the synthetic and analytical procedures.^{15,16}

3.4.1. UV–Vis Measurements. Absorption spectra were recorded using a PerkinElmer Lambda UV/Vis 950 spectrophotometer in plastic cuvettes with an optical path of 10 mm. The wavelength range was 200–900 nm.

3.4.2. Transmission Electron Microscopy (TEM). Size and morphology of NPs were characterized by transmission electron microscopy (TEM) (JEM-1011 TEM, Jeol, Inc., Peabody, MA) using a Morada CCD camera at an accelerating voltage of 100 kV.

3.4.3. Raman Spectroscopy. The Raman experiments have been performed on an Xplora spectrometer (Horiba Scientific-France).^{15,16}

3.4.5. Optical Imaging. The optical images of the cells were carried out as previously reported.¹⁷

3.4.6. Dynamic Light Scattering (DLS). The size measurements were performed using a Zetasizer Nano ZS (Malvern Instruments, Malvern, U.K.) equipped with a He–Ne laser (633 nm, fixed scattering angle of 173 $^\circ$) at room temperature.

3.4.7. ζ -Potential Measurements. The ζ -potential of AuNPs dispersed in water was measured using the electrophoretic mode of a Zetasizer Nano ZS (Malvern Instruments Ltd, U.K.).

3.5. ES Cells Culture Conditions. Embryonic stem cells (ESCs) can be used as a model system in basic research, drug discovery, biomedical applications, and nanotechnology because they combine the potential of unlimited self-renewal with the ability to differentiate into a wide range of tissue-specific cells. The present study was designed to determine if the nanoparticles $\text{Cu}^0\text{-AuNPs}$ and $\text{L1@Cu}^{2+}\text{-AuNPs}$ could have toxic effects on undifferentiated and neural differentiated ES cells. Wild-type mouse AK7 ES cells were maintained in an undifferentiated state by culture on a monolayer of mitomycin-C-inactivated fibroblast in the presence of leukemia-inhibiting factor as previously described.¹⁸ At 24 h before treatment, the cells were seeded on gelatin-coated plates at a density of 4×10^4 cells/cm 2 to allow attachment.

3.5.1. In Vitro Neurons Differentiation. Neural progenies can be generated from ESC with high standards of accuracy and reliability. To induce neural differentiation, essentially according to Fico et al.,¹⁸ AK7 ES cells at 48 h before inducing differentiation were seeded on gelatin-coated plates. At day 0, the ES cells were dissociated in a single-cell suspension and 1500 cells/cm 2 were plated on gelatin-coated plates. The cells were maintained in differentiation medium until day 7 when neural precursors cells were detached using 0.05% trypsin/ethylenediaminetetraacetic acid solution and frozen in 90% FBS + 10% dimethyl sulfoxide. Frozen cells were thawed and immediately plated at 66 000 cells/cm 2 in Matrigel-coated plates. The medium was changed every day until day 13.

3.6. Cell Death Assay. The lethal dose 50 (LD50) is the amount of a chemical, calculated as the concentration of chemicals that produces death in 50% of a cellular population.

To determine the lethal dose 50 (LD50) of the nanoparticles $\text{Cu}^0\text{-AuNPs}$ and $\text{L1@Cu}^{2+}\text{-AuNPs}$ on undifferentiated ES and neural-derived ES cells, these cells were seeded, respectively, on gelatin-coated or Matrigel-coated plates. The cells were untreated or treated with different concentrations (0–1000 nM) of $\text{Cu}^0\text{-AuNPs}$ or $\text{L1@Cu}^{2+}\text{-AuNPs}$ nanoparticles for 24 h, then collected, counted, and analyzed for their ability to incorporate the cell-permeable dye trypan blue. Concomitantly, other cells, untreated or treated in the same way, were visualized by phase-contrast microscopy using the DMI6000B inverted fully automated microscope with DFC 420 RGB camera (Leica Microsystems, Wetzlar, Germany). Leica LAS V5.4 software was used for image acquisition/elaboration (contrast/ γ adjusting).

3.7. Immunofluorescence Analysis. For nanoparticles internalization experiments, neural-differentiated ESCs were seeded in six-well plates and cultured for 24 h. $\text{Cu}^0\text{-AuNPs}$ or $\text{L1@Cu}^{2+}\text{-AuNPs}$ conjugated with Alexa-Fluor-594, suspended in culture medium at 200 nM, were incubated with cells for 24 h. After the incubation, the cells were rinsed twice in PBS to remove the noninternalized nanoparticles, fixed in 4% paraformaldehyde for 30 min, and washed in PBS 1 \times . After washing, the cells were incubated with WGA-488 (Invitrogen) as membrane marker following manufacturer's instructions. Nuclei were counterstained with Hoechst 33342 (Invitrogen). Fluorescent labeling was visualized using the inverted fully automated confocal Nikon AR-1 microscope. The NIS elements software was used for image acquisition/elaboration.

4. CONCLUSIONS

Designing hybrid functional nanoparticles for biomedical applications is still a current challenge in terms of performance, stability, and safety in biological media. In particular, if gold nanoparticles are known for their high in vivo inertness and their use in several applications, including their photophysical properties, the use of copper(II) into the hybrid nanoparticles is still not a trivial task. Once copper is inside the metallic aggregates, it is usual to obtain unstable and/or cytotoxic effects coming from the hybrid nanostructure.

The success of this study was then to provide the design, the synthesis, and the characterization of new potential nanocomplexes based on the incorporation of chelated copper(II) in gold nanoparticles. Highly thermodynamically stable and kinetically and electrochemically inert copper(II) chelates have been used based on a proven cyclam cross-bridged ligand, the cb-te1pa chelator. Its insertion was facilitated by the presence of aniline moiety, a carboxylic function, and its overall charge and proved all along the nanomaterials characterization. In conclusion, from the results obtained, there is evidence of a type-selective difference in NP toxicity in favor of $\text{L1@Cu}^{2+}\text{-AuNPs}$. Possible reason to explain nanoparticle-specific uptake and distribution inside the neural-derived ES cells may be attributed to the peculiar features of $\text{Cu}^0\text{-AuNPs}$ or $\text{L1@Cu}^{2+}\text{-AuNPs}$ nanoparticles. Our results indicated that the differences between $\text{Cu}^0\text{-AuNPs}$ or $\text{L1@Cu}^{2+}\text{-AuNPs}$ nanoparticles as well as the target cell type are critical determinants of intracellular responses and degree of cytotoxicity. These results allow us to hypothesize that the apoptosis is the predominant death pathway for moderate concentrations of

NPs in the solution, whereas necrosis is the predominant pathway for high concentrations of NPs.

Toxicity comparison with respect to previously reported results in literature is not straightforward because ES neuron cells are not very commonly diffused in many laboratories; nevertheless, the synthesized Cu-based NPs showed LD levels of the same order of those mentioned in critical review study, recently published.³⁴

■ ASSOCIATED CONTENT

Supporting Information

The Supporting Information is available free of charge on the ACS Publications website at DOI: 10.1021/acsomega.8b03266.

UV-vis absorption of HAuCl₄·6H₂O (black line), CuCl₂·6H₂O (red line); and Au-Cu blend (blue line) (Figure S1); UV-vis spectra of each solutions: HAuCl₄, CuCl₂, and HAuCl₄-CuCl₂ (Figure S2); bright field (a) and dark field (b) images (100×, 0.9 NA objective) of neural derived-ES cells incubated with Cu⁰-AuNPs or Li@Cu²⁺-AuNPs (250 nM) (Figure S3); bright field (a) and dark field (b) images (100×, 0.9 NA objective) of neural derived-ES cells incubated with Cu⁰-AuNPs or Li@Cu²⁺-AuNPs (750 nM) (Figure S4) (PDF)

■ AUTHOR INFORMATION

Corresponding Authors

*E-mail: luca.destefano@na.imm.cnr.it (L.d.S.).

*E-mail: jolanda.spadavecchia@univ-paris13.fr (J.S.).

ORCID

Luca de Stefano: 0000-0002-9442-4175

Raphaël Triquier: 0000-0001-9364-788X

Jolanda Spadavecchia: 0000-0001-6697-1174

Author Contributions

The manuscript was written through contributions of all authors. All authors have given approval to the final version of the manuscript.

Notes

The authors declare no competing financial interest.

■ ACKNOWLEDGMENTS

With the support of SATT IDF Innov, J.S. has filed a patent application on the nanoparticles presented in this manuscript (Cu⁰-AuNPs). Nanomaterial and method of production of a nanomaterial for medical applications, such as MRI or SERS—Inventor: J.S., European Patent Application number EP17305087.3, filed January 27, 2017, and PCT application PCT/EP2018/051988 filed January, 26, 2018. This work has been partly performed on the CNano Mat platform of the University Paris 13. This work was partially funded by Italian Ministry of Health “Ricerca Corrente”, PONPE_00060_7 and PONPE_00060_3 to S.F. The authors acknowledge the Integrated Microscopy Facility at Institute of Genetics and Biophysics “Adriano Buzzati Traverso”, CNR in Naples for optical and confocal microscopy.

■ REFERENCES

- (1) Miller, M. R.; Raftis, J. B.; Langrish, J. P.; McLean, S. G.; Samutrtai, P.; Connell, S. P.; Wilson, S.; Vesey, A. T.; Fokkens, P. H. B.; Boere, A. J. F.; Krystek, P.; Campbell, C. J.; Hadoke, P. W. F.; Donaldson, K.; Cassee, F. R.; Newby, D. E.; Duffin, R.; Mills, N. L. *ACS Nano* **2017**, *11*, 4542–4552.
- (2) Boonruamkaew, P.; Chonpathompikunlert, P.; Vong, L. B.; Sakaue, S.; Tomidokoro, Y.; Ishii, K.; Tamaoka, A.; Nagasaki, Y. *Sci. Rep.* **2017**, *7*, No. 3785.
- (3) Chatterjee, A. K.; Chakraborty, R.; Basu, T. *Nanotechnology* **2014**, *25*, No. 135101.
- (4) Henkel, A.; Jakob, A.; Brunklaus, G.; Sönnichsen, C. *J. Phys. Chem. C* **2009**, *113*, 2200–2204.
- (5) Shokeen, M.; Anderson, C. *J. Acc. Chem. Res.* **2009**, *42*, 832–841.
- (6) Rout, L.; Kumar, A.; Dhaka, R. S.; Reddy, G. N.; Giri, S.; Dash, P. *Appl. Catal., A* **2017**, *538*, 107–122.
- (7) Cai, Z.; Anderson, C. *J. Labelled Compd. Radiopharm.* **2014**, *57*, 224–230.
- (8) Lu, H. D.; Wang, L. Z.; Wilson, B. K.; McManus, S. A.; Jumai'an, J.; Padakanti, P. K.; Alavi, A.; Mach, R. H.; Prud'homme, R. K. *ACS Appl. Mater. Interfaces* **2018**, *10*, 3191–3199.
- (9) Mewis, R. E.; Archibald, S. *J. Coord. Chem. Rev.* **2010**, *254*, 1686–1712.
- (10) Odendaal, A. Y.; Fiamengo, A. L.; Ferdani, R.; Wadas, T. J.; Hill, D. C.; Peng, Y.; Heroux, K. J.; Golen, J. A.; Rheingold, A. L.; Anderson, C. J.; Weisman, G. R.; Wong, E. H. *Inorg. Chem.* **2011**, *50*, 3078–3086.
- (11) Wong, E. H.; Weisman, G. R.; Hill, D. C.; Reed, D. P.; Rogers, M. E.; Condon, J. S.; Fagan, M. A.; Calabrese, J. C.; Lam, K.-C.; Guzei, I. A.; Rheingold, A. L. *J. Am. Chem. Soc.* **2000**, *122*, 10561–10572.
- (12) Weisman, G. R.; Rogers, M. E.; Wong, E. H.; Jasinski, J. P.; Paight, E. S. *J. Am. Chem. Soc.* **1990**, *112*, 8604–8605.
- (13) Lima, L. M.; Halime, Z.; Marion, R.; Camus, N.; Delgado, R.; Platas-Iglesias, C.; Triquier, R. *Inorg. Chem.* **2014**, *53*, 5269–5279.
- (14) You, J.; Zhang, G.; Li, C. *ACS Nano* **2010**, *4*, 1033–1041.
- (15) Spadavecchia, J.; Movia, D.; Moore, C.; Maguire, C. M.; Moustouai, H.; Casale, S.; Volkov, Y.; Prina-Mello, A. *Int. J. Nanomed.* **2016**, *11*, 791–822.
- (16) Moustouai, H.; Movia, D.; Dupont, N.; Bouchemal, N.; Casale, S.; Djaker, N.; Savarin, P.; Prina-Mello, A.; de la Chapelle, M. L.; Spadavecchia, J. *ACS Appl. Mater. Interfaces* **2016**, *8*, 19946–19957.
- (17) Monteil, M.; Moustouai, H.; Picardi, G.; Aouidat, F.; Djaker, N.; de La Chapelle, M. L.; Lecouvey, M.; Spadavecchia, J. *J. Colloid Interface Sci.* **2018**, *513*, 205–213.
- (18) Fico, A.; Pagliarunga, F.; Cigliano, L.; Abrescia, P.; Verde, P.; Martini, G.; Iaccarino, I.; Filosa, S. *Cell Death Differ.* **2004**, *11*, 823–831.
- (19) Ly, N. H.; Nguyen, T. D.; Zoh, K. D.; Joo, S. W. *Sensors* **2017**, *17*, No. 2628.
- (20) Emmenegger, F. P.; Rohrbasser, C.; Schläpfer, C. W. *Inorg. Nucl. Chem. Lett.* **1976**, *12*, 127–131.
- (21) Pal, U.; Sanchez Ramirez, J. F.; Liu, H. B.; Medina, A.; Ascencio, J. A. *Appl. Phys. A* **2004**, *79*, 79–84.
- (22) Nguyen, M. T.; Zhang, H.; Deng, L.; Tokunaga, T.; Yonezawa, T. *Langmuir* **2017**, *33*, 12389–12397.
- (23) Marguerit, G.; Moustouai, H.; Haddada, M. B.; Djaker, N.; de la Chapelle, M. L.; Spadavecchia, J. *Part. Part. Syst. Character.* **2018**, *35*, No. 1700299.
- (24) Politi, J.; De Stefano, L.; Longobardi, S.; Giardina, P.; Rea, I.; Methivier, C.; Pradier, C. M.; Casale, S.; Spadavecchia, J. *Colloids Surf., B* **2015**, *136*, 214–221.
- (25) Spadavecchia, J.; Apchain, E.; Alberic, M.; Fontan, E.; Reiche, I. *Angew. Chem., Int. Ed.* **2014**, *53*, 8363–8366.
- (26) Lu, H. D.; Wang, L. Z.; Wilson, B. K.; McManus, S. A.; Jumai'an, J.; Padakanti, P. K.; Alavi, A.; Mach, R. H.; Prud'homme, R. K. *ACS Appl. Mater. Interfaces* **2018**, *10*, 3191–3199.
- (27) Gammage, M. D.; Stauffer, S.; Henkelman, G.; Becker, M. F.; Keto, J. W.; Kovar, D. *Surf. Sci.* **2016**, *653*, 66–70.
- (28) Gautier, J.; Allard-Vannier, E.; Munnier, E.; Souce, M.; Chourpa, I. *J. Controlled Release* **2013**, *169*, 48–61.

- (29) Lee, K. Y. J.; Wang, Y.; Nie, S. *RSC Adv.* **2015**, *5*, 65651–65659.
- (30) Sajanalal, P. R.; Sreeprasad, T. S.; Samal, A. K.; Pradeep, T. *Nano Rev.* **2011**, *2*, No. 5883.
- (31) Toma, H. E.; Zamarion, V. M.; Toma, S. H.; Araki, K. *J. Braz. Chem. Soc.* **2010**, *21*, 1158–1176.
- (32) Prabhu, B. M.; Ali, S. F.; Murdock, R. C.; Hussain, S. M.; Srivatsan, M. *Nanotoxicology* **2010**, *4*, 150–160.
- (33) Liu, Z.; Shichang, L.; Guogang, R.; Taoc, Z.; Zhuo, Y. *J. Appl. Toxicol.* **2011**, *31*, 439–445.
- (34) Bondarenko, O.; Juganson, K.; Ivask, A.; Kasemets, K.; Mortimer, M.; Kahru, A. *Arch. Toxicol.* **2013**, *87*, 1181–1200.

3.2 The antibacterial activity of gold nanoparticles-antimicrobial peptide complex

Abstract

The massive use of antibiotics has led to the development of multidrug-resistant microorganisms, which represent a serious threat for the public health.

The limited number of available antibiotics, the similarity in their activity spectrum and the mode of action emphasize the need to identify novel and non-conventional antimicrobial therapies. In this context, antimicrobial peptides (AMPs), a class of natural and synthetic peptides with a wide spectrum of targets, are good candidates as novel drugs. The antimicrobial activity of AMPs can be stabilized and enhanced by their conjugation to gold nanoparticles (AuNPs). In this study, PEGylated-AuNPs and citrate-AuNPs were functionalized by temporin TL48, an AMP active against several bacteria but also yeast strains. The stability of the solutions was evaluated by spectroscopic techniques, DLS and ζ -potential analyses while the immobilization yield was monitored via RP-HPLC. Preliminary studies were conducted on *Staphylococcus aureus* to test the antimicrobial activity of the developed hybrid complexes.

Introduction

The massive use of antibiotics generated the development of multi-resistant antibiotic pathogens, whose treatment is very difficult and sometimes impossible. Drug-resistant bacteria are often organized as biofilm, a consortium of different bacteria colonies or single type of cells, adhering to biotic or abiotic surfaces. Biofilms provide protection to the microorganisms from several non-physiological conditions (i.e., altered pH, lack of nutrients) and block the drugs access, thus increasing tolerance to antibiotics and chemical disinfectants [108]–[110]. In this scenario, the antibiotic resistance is spreading rapidly, representing a serious public health risk. For this reason, the discovery of new compounds against drug-resistant microorganisms is strongly required. Recent studies demonstrated the potential antimicrobial effect of metal or semiconductor nanoparticles (NPs). NPs perform their antimicrobial activity through three different pathways: oxidative stress induction [111], metal ion release [112], and/or non-oxidative mechanisms [113]. The antibacterial effect of NPs can be summarized in four major steps: 1) disruption of the bacterial cell membrane; 2) generation of ROS; 3) penetration of the bacterial cell membrane; and 4) induction of intracellular antibacterial effects, including interactions with DNA and

proteins [114]. Moreover, NPs can be used as drug carriers. In particular, it has been shown that the combination of NPs with antimicrobial compounds enhances the antipathogenic activity, reducing the dosage of the drugs in question.

Recently, antimicrobial peptides (AMPs) have emerged as a valid alternative to conventional antibiotic drugs. They are characterized by a short sequence of amino-acids, an overall net positive charge and, most of them, have amphipathic domains. Some of them exhibit a broad-spectrum activity against a wide range of microorganisms including Gram-positive, Gram-negative, viruses, bacteria, fungi and parasites. The AMPs action mechanism is matter of controversy but the most accepted hypothesis is based on the selective destruction of the plasma membrane by the amphipathic region of AMPs [115].

One of the largest family of AMPs are the temporins, natural peptides produced by the dermal glands of *Rana temporaria*. They are small peptides, composed of 10-16 amino-acid residues, with 1 or 2 basic residues in the whole sequence, an amide group at the C-terminal and showing a net positive charge at physiological pH [116]. They are active against Gram-positive bacteria but the isoform L shows a broader spectrum of action, being also active against Gram-negative bacteria and yeast strains [116]. In this work, the temporin TL48 was bound to AuNPs in order to verify the stability and the antimicrobial activity of the hybrid complex AuNPs-TL48. When used in complex matrix, such as biological fluids, the half-life of peptides could be very short. The peptides can lose their structure and become inert. One way to prevent this effect and stabilize the peptides is binding them to a surface, in this case a nano-surface.

Two different kinds of AMPs-AuNPs complexes have been engineered in this study. In the first approach, TL48 was covalently bound to polymeric-AuNPs by using carbodiimide chemistry while, the latter method exploits the interaction of a modified peptide, Cys-TL48 with citrate AuNPs.

Materials and Methods

Chemicals

Tetrachloroauric acid (HAuCl_4), sodium borohydride (NaBH_4), polyethylene glycol 600 Diacid (DPEG, $M_w=600\text{Da}$), trisodium citrate dihydrate ($\text{C}_6\text{H}_9\text{Na}_3\text{O}_9$), N-hydroxysuccinimide (NHS), 1-(3-dimethylaminopropyl)-N'-ethylcarbodiimide hydrochloride (EDC) were purchased from Sigma Aldrich (St. Louis, MO, USA).

Synthesis of PEGylated AuNPs and covalent conjugation peptide
PEG-AuNPs were obtained by using a one-pot method, in which PEG-diacid was used as the stabilizer molecules in spite of the citrate molecules. Briefly, poly(ethylene glycol) diacid (600 μ L) was mixed to chloroauric acid (0.25 mM, 25 mL; $\text{HAuCl}_4 \cdot 3\text{H}_2\text{O}$) under stirring for 10 min. After that, 20 mL of NaBH_4 was added at once. A solution of EDC/NHS (5:2, 5 mM, in MES buffer pH 5.5) and 125 μ M of TL48 were added to PEG-AuNPs. The solution was kept in static overnight. After bioconjugation, the TL48-PEG-AuNPs were centrifuged twice in order to remove the unbound peptide and the pellet was resuspended in Milli-Q-water.

Synthesis of citrate AuNPs and peptide conjugation

Citrate AuNPs (c-AuNPs) were prepared by reduction of HAuCl_4 by citrate. Briefly, $\text{HAuCl}_4 \cdot 3\text{H}_2\text{O}$ (0.25 mM, 50 mL) was heated on a hot plate while stirring. When the solution starts to boil, $\text{C}_6\text{H}_9\text{Na}_3\text{O}_9$ (0.060 M, 875 μ L) was added under stirring. After the colour solution changed from dark blue to red, the solution was left to boil for another 10 min. Finally, the solution was brought to RT under stirring for 20 minutes. The Cys-TL48-c-AuNPs interaction was conducted by addition of 125 μ M of peptide to AuNPs. The solution was kept in static overnight. Then, the sample was centrifuged to remove the unbound peptide and the pellet resuspended in Milli-Q-water.

Characterization of bare and TL48 modified AuNPs

The hydrodynamic diameter (size) and the surface charge (ζ -potential) of NPs dispersed in water, were measured by dynamic light scattering (DLS) using a Zetasizer Nano ZS instrument (Malvern Instruments, Malvern, U.K.) equipped with a He-Ne laser [633 nm, fixed scattering angle of 173° , room temperature (25°)]. Absorption spectra of bare and modified AuNPs were recorded using a Cary 100 (VARIAN), in the range between 400-700 nm.

Functionalization Yield Analysis of AuNPs

Functionalization yield analyses of PEG-AuNPs-TL48 and c-AuNPs-CysTL48 were performed by using reverse-phase high-performance liquid chromatography (RP-HPLC). After the functionalization process, the supernatants, containing the unbound peptide, were recovered after centrifugation. Then, the peaks area due to the unbound peptides, i.e. the ones not attached to AuNPs surface, were calculated. All measurements have been made in triplicate.

Results and Discussion

Gold nanoparticles functionalization and characterization

In this study, two different functionalization strategies have been developed with the purpose to bind a small synthetic AMP to AuNPs.

In our previous paper, we reported a one-pot synthesis method of PEGylated-AuNPs, forming a highly stable colloidal solution that, thanks to the exposure of carboxyl acid groups provided by PEG-diacid, can be conjugated to different biomolecules [117]. AuNPs, obtained through the reported protocol, were covalently grafted, by using carbodiimide chemistry as schematized in Figure 3.1 A, to the TL48 temporin, an antimicrobial peptide, whose sequence is highlighted in Figure 3.1 B.

The formation and the stability of the complex AuNPs-TL48 were monitored by using several techniques.

In Figure 3.1 C, the ultraviolet-visible (Uv-vis) spectroscopy of PEG-AuNPs before and after interaction with TL-48 is reported. This measurement revealed a 15 nm red shift of the local surface plasmon resonance (LSPR) of the absorbance spectrum, due to the peptide-AuNPs interaction. Moreover, a change of the colour solution from red to violet confirms qualitatively the occurred functionalization. The change in the hydrodynamic diameter of AuNPs and the surface charge are further characterizations useful to evaluate the formation of the hybrid NPs. An increase of the AuNPs size, from 6 ± 3 nm to 35 ± 19 nm, suggests the complex formation, in addition to the change in charge surface, from -25 ± 9 mV to 22 ± 9 mV, due to the exposure of positive amino acids groups (Figure 3.1 D).

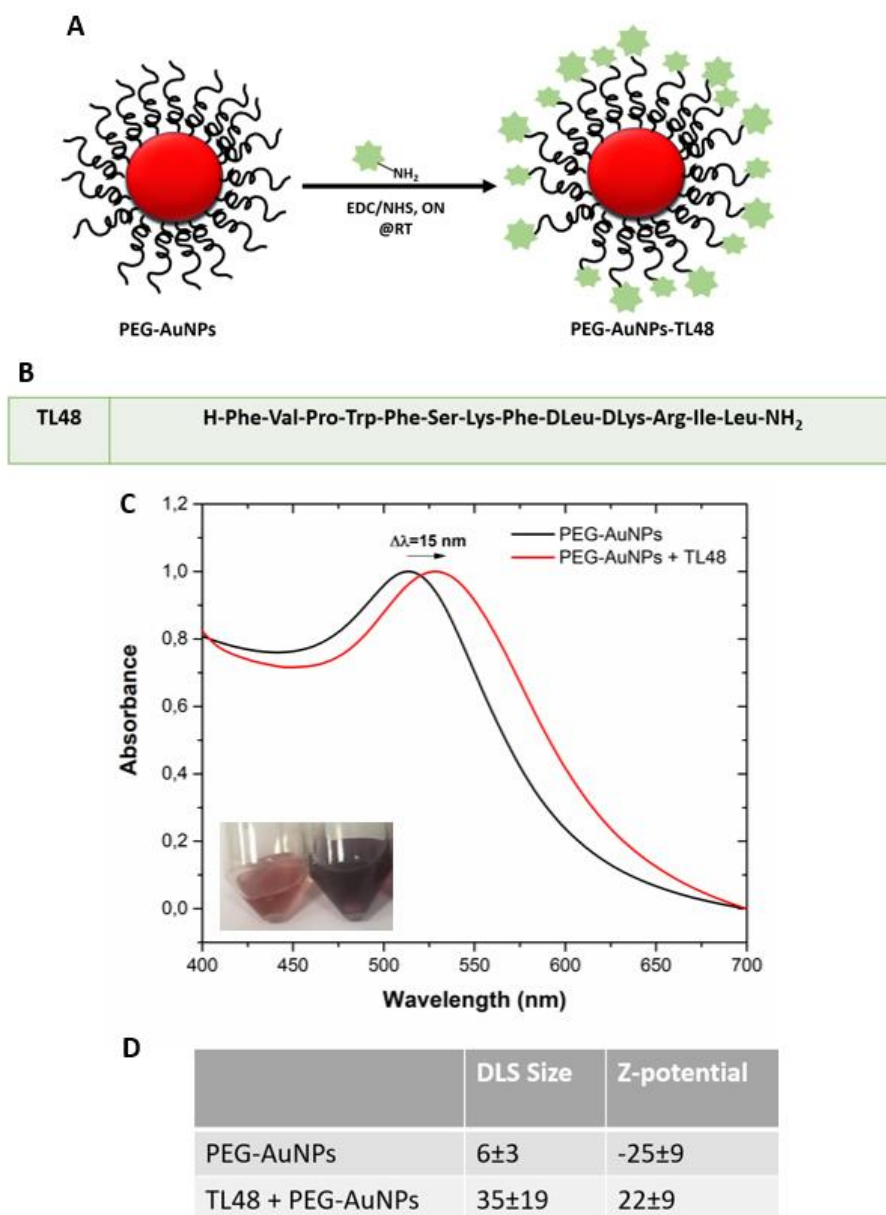


Figure 3.1 - (A) Scheme of conjugation of TL48 peptide to PEG-AuNPs. **(B)** TL48 sequence. **(C)** Uv-vis spectra of PEG-AuNPs before and after peptide conjugation. The colour changing of PEG-AuNPs after peptide conjugation is reported in the inset. **(D)** Hydrodynamic diameters and surface charges before and after bioconjugation.

The citrate AuNPs, synthesized by Turkevich protocol, were used in order to graft a modified temporin, Cys-TL48, according to the scheme in Figure 3.2 A. The peptide sequence, shown in Figure 3.2 B, was obtained by the addition of a Cys to the N-terminal domain of the peptide chain. In fact, it is well known that Cys-containing peptides can be bound to metal NPs making a covalent linkage to the gold surfaces, exploiting the sulfhydryl group in its side chain [118].

The interaction between Cys-TL48 and c-AuNPs was monitored by recording the absorbance spectrum which red shifted by 8 nm and, also in this case, the complex formation was followed by the colour change of the solution, from red to purple (Figure 3.2 C). Therefore, DLS analysis underlined an increase in size of the hydrodynamic diameter of c-AuNPs, from 14 ± 4 to 22 ± 11 nm and the change of the charge of zeta-potential, from -29 ± 6 mV to 36 ± 6 mV, as shown in Figure 3.2 D. The data obtained confirm the occurred coupling in both the used procedures.

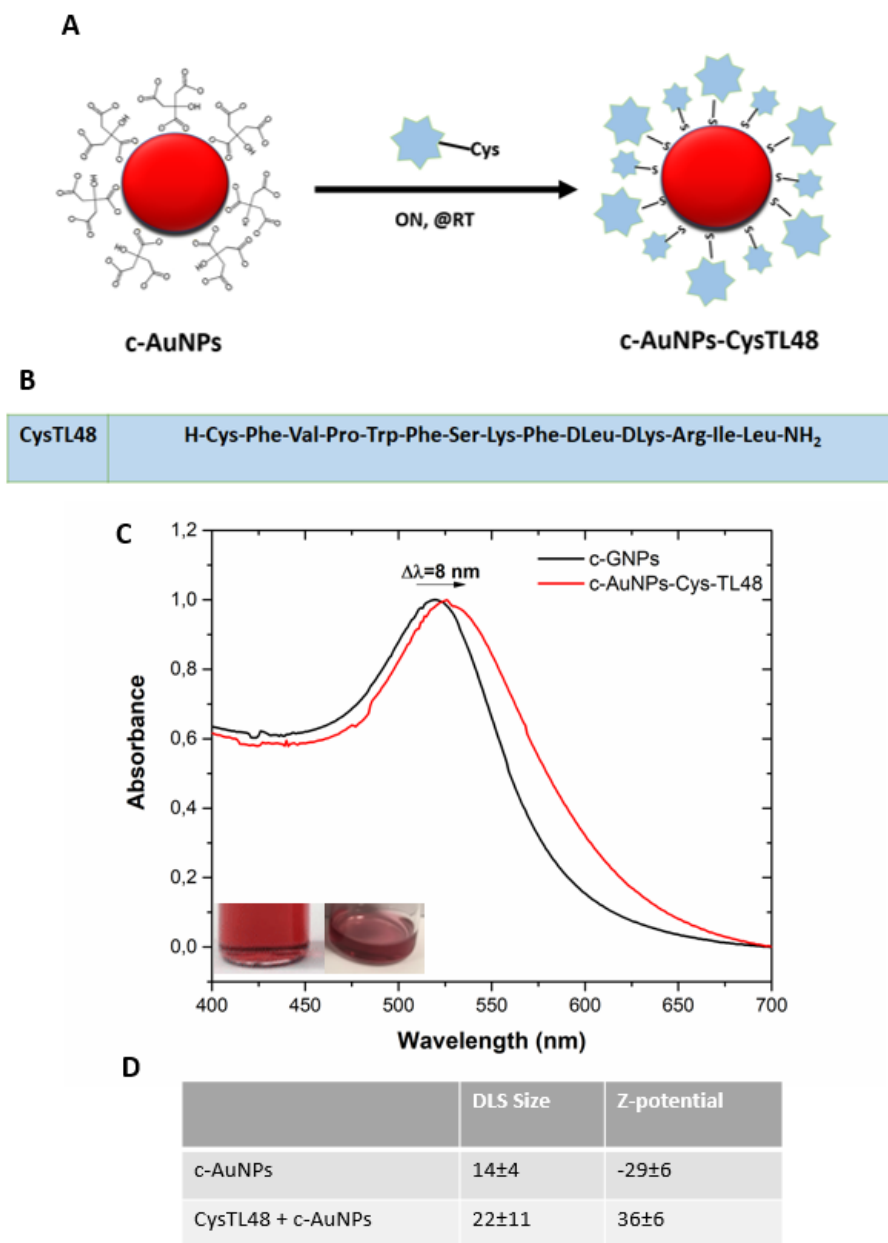


Figure 3.2 - (A) Scheme of conjugation of CysTL48 peptide to c-AuNPs. **(B)** CysTL48 sequence. **(C)** Uv-vis spectra of c-AuNPs before and after peptide conjugation. The colour changing of c-AuNPs after peptide conjugation is reported in the inset. **(D)** Hydrodynamic diameters and surface charges before and after bioconjugation.

It is well known that the biological activity of a peptide could undergo to a modification after its interaction to solid supports. For this reason, there is the necessity to compare the activity of free and tethered peptide. An indirect quantification method was used to determine the conjugation yield of peptide immobilized on AuNPs. Briefly, PEG-AuNPs-TL48 and c-AuNPs-CysTL48 were centrifuged to remove the peptide excess and the supernatant was quantified by RP-HPLC. Through the peak area analysis, the amount of unbound peptide to the NPs surface was quantified. Good results of conjugation yields were obtained for both the used functionalization procedures, especially in the case of the AuNPs-Cys-TL48 complex.

It is important to underline that the immobilization yield could depend on the amount of peptide conjugated to AuNPs. Aiming to obtain stable and active nanoparticles, several temporin concentrations were tested. Table 1 shows that the optimal coupling condition can be obtained with 125 μM of peptide, both for PEG-AuNPs and c-AuNPs. Indeed, reducing the peptide concentrations, a decrease in the immobilization yield was observed in both cases. For this reason, only for the best coupling condition (125 μM), the effective amount of bound peptide was estimated. As reported in Table 1, while PEG-AuNPs showed a 92,3% of bound peptide, this percentage reached 97% in the case of AuNPs Cys-TL48. Therefore, on average, 116 μM and 121 μM of peptide were estimated to be linked to PEG-AuNPs and c-AuNPs, respectively.

A

Sample	Concentration (μM)	% of unbound peptide ^c	% bound peptide
PEG-AuNPs-TL48	125	8	92
	62	24	76
	31	50	50

B

Sample	Concentration (μM)	% of unbound peptide	% bound peptide
c-AuNPs-CysTL48	125	3	97
	62	24	76
	31	14	86

Table 1 - Immobilization yield of **A)** PEG-AuNPs functionalized with TL48 and **B)** c-AuNPs functionalized with Cys-TL48. Different concentrations of peptides were added to AuNPs.

Once the nanocomplexes stability was verified, their antimicrobial activity was evaluated *in vitro* against the Gram-positive *Staphylococcus aureus* ATCC. Preliminary experiments were performed by culturing 100000 colony-forming units (CFU/mL) of the bacteria. For this experiment, the nanocomplexes with the higher immobilization yield (125 μ M of peptide) were used. While the bare AuNPs do not have lethal activity, the TL48 peptide, at a concentration of 1 μ M, causes 50% reduction in the number of viable bacterial cells, within 60 min, as shown in Figure 3.3. Comparable results (50% killing activity) were obtained after the interaction of TL48 to PEG-AuNPs, using the same experimental conditions. Interestingly, the immobilization of CysTL48 to c-AuNPs, not only preserves the antimicrobial activity of the peptide, but also enhances the killing activity (70% killing). The different results, obtained with the two nanocomplexes, could be related to the conformational changes that the peptide undergoes when tethered to gold surface. In fact, it is well known that the antimicrobial power of AMPs strongly depends on their α -helix structure. However, the interaction of the peptide with the nanoparticles could cause some variations in the peptide secondary structure with effects on its antimicrobial activity. Therefore, it will be necessary to evaluate the peptide structural changes, when immobilized on gold surfaces.

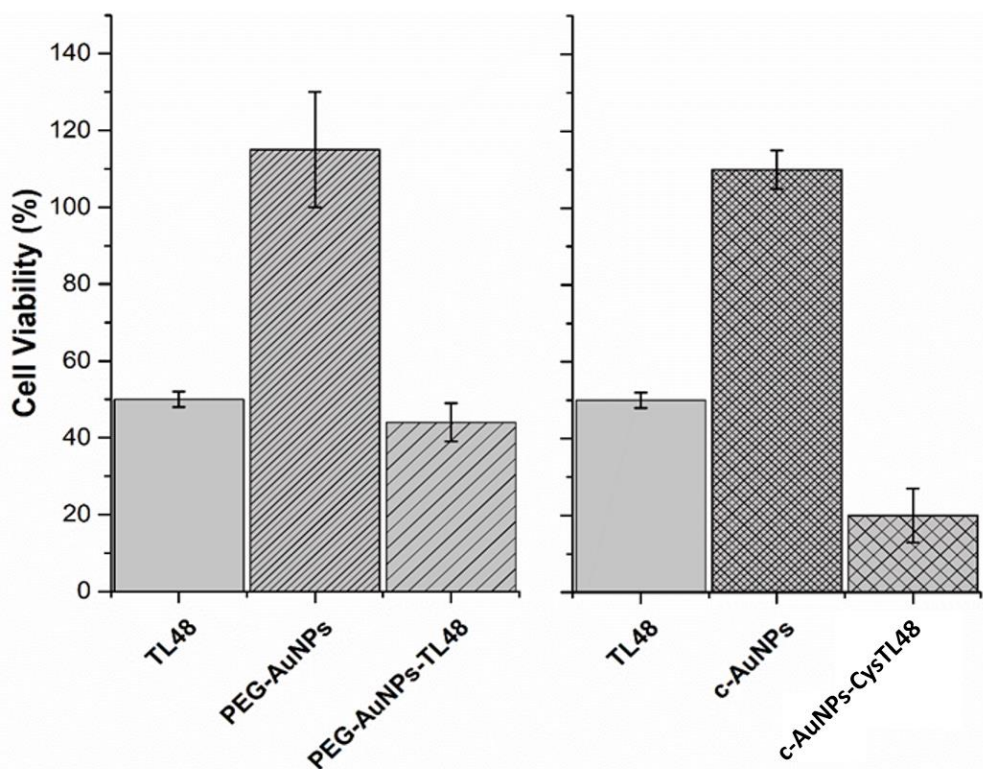


Figure 3.3 - Cell viability of *Staphylococcus aureus* after exposure to the antimicrobial peptide TL48, bare AuNPs, PEG-AuNPs-TL48 and c-AuNPs-CysTL48. The cells (100000 CFU) were incubated using a fixed concentration of the peptide and nanocomplexes (1 μ M). The error bars represent the standard deviation (SD) from the mean for a triplicate experiment (n=3).

Although the data obtained with c-AuNPs-Cys-TL48 are promising, many other efforts are required to enhance the antimicrobial activity of both the nanocomplexes.

Conclusions

Two different hybrid nanocomplexes, PEG-AuNPs-TL48 and c-AuNPs-CysTL48, were engineered. Their stability and immobilization yield were monitored *via* different techniques. Effective functionalization procedures were obtained for both the nanocomplexes, even if, the best coupling condition was achieved in the case of c-AuNPs-CysTL48.

Preliminary studies were conducted on *Staphylococcus aureus* to establish if the antimicrobial activity of the developed complexes could be enhanced when compared to that of the unbound peptide. While

c-AuNPs-CysTL48 showed an increased killing activity compared to the free peptide, the interaction of TL48 to PEG-AuNPs did not improve the antimicrobial activity. Future studies aim to improve the functionalization chemistry of both the developed nanosystems to increase the local peptide concentration surrounding each nanoparticle and to understand how the immobilization of the peptide onto solid surfaces affects its conformation.

4. Conclusions

The PhD thesis entitled “DESIGN, FABRICATION AND CHARACTERIZATION OF NANOSTRUCTURED HYBRID BIO/NON-BIO INTERFACES FOR BIOMOLECULAR INTERACTIONS STUDY AND INDUSTRIAL APPLICATIONS”, performed at the National Research Council – Institute of Microelectronics and Microsystems, in collaboration with the Department of Chemical Sciences, University of Naples under the co-tutoring of Dr. Luca De Stefano and Prof. Paola Giardina, was focused on the development of novel hybrid devices, made of support surfaces functionalized with biological elements. In particular, through the appropriate design of the interfaces, the specificity and the properties of the single elements of the device were significantly enhanced and exploited for novel applications. Nanostructured materials such as porous silicon, gold nanoparticles, were used as surface for anchoring biological elements.

Porous silicon is a nanostructured material typically obtained by electrochemical etching of a single-crystal Si wafer in hydrofluoric acid (HF) solution. In recent study, the PSi-based nanomaterials (i.e., nanoparticles, thin films, nanowires) have given rise interest for a wide range of applications, including biosensing, bioimaging and theranostic nanomedicine, due to their unique physiochemical properties.

In the last years, there was a need to develop biosensors able to detect pathologies, such as cancer or genetic diseases, in the early stage. This condition requires the development of a sensing tool able to detect biomarkers (i.e., enzymes, DNA, metabolites) associated to a specific disease in a very short time. In this context, PSi, was used as biosensing platform, taking advantage of its ease surface modification, of its simple fabrication and its high internal surface area. In particular, the design and the development of a multiparametric PSi device, having great stability, high specificity and sensitivity was demonstrated in the first part of this PhD thesis work. The PSi surface, used as transducer material, was hydrosilylated by using undecylenic acid. Through this process, Si-H bonds convert into Si-C bonds forming a covalently attached organic monolayer on the surface. Nanosheets of graphene oxide were covalently grafted to the device. The final product is an optical biosensor whose operating mechanism is based on the variation of PSi reflectance and on the GO photoluminescence.

Spectroscopic reflectometry, PL analysis, water contact angle, AFM and SEM have been used to monitor each step of the functionalization process. The as-designed device was exploited for the detection of

Brugada Syndrome, a genetic disease, often causing sudden cardiac death. For this purpose, a PNA, used as probe for the specific discrimination of the single-point mutation, associated to the genetic disease, was covalently immobilized on the PSi-based device.

The effective hybridization between PNA-GO-PSi device with *c*-DNA was confirmed by spectroscopic reflectometry. In particular, using increasing concentrations of DNA target, shifts of the spectrum to higher wavelengths were measured, confirming the occurred hybridization. These data were further verified *via* the confocal microscopy, in which, the fluorescence of a labelled *c*-DNA, confirms the infiltration and, as a consequence, the recognition of the hybrid device by the molecular target. The encouraging results obtained suggest the potentiality to develop a wide range of PNA-PSi based biosensors for the detection of genetic diseases.

Porous silicon is a material used not only for biosensing purpose but also as biomedical probes for drug delivery and imaging applications.

This is widely discussed in the second part of the present work.

Luminescent PSi nanoparticles (PSiNPs) represent a valid alternative to conventional QDs thanks to their biodegradability, biocompatibility, tunable porous structure, intrinsic PL and the feasibility of surface functionalization for targeting ligands. These characteristics make them attractive for applications in biomedical fields. PSiNPs were opportunely modified in order to obtain a product that could be exploitable as label-free luminescent probe for *in vivo* imaging. For this purpose, they were opportunely passivated by hydrosilylation process to avoid the oxidation of the material and, finally, they were chemically modified with a positive charge amino acid polymer, poly-L-Lysine. This chemical modification turned out to be essential for *in vivo* experiments, conducted using *Hydra vulgaris* as target organisms. Moreover, the toxicity and the uptake of modified-PSiNPs was monitored through direct observation of the polyps in real-time, both in bright field and fluorescence mode. The reported data show that, the high concentrations of PLL-modified PSiNPs were toxic for the animals while lower concentrations did not induce morphologic alterations of *Hydra*. However, the tissue autofluorescence represented a limit to the PSiNPs visibility. Fortunately, this problem was successfully bypassed with time-gated imaging technique, taking advantage of long emission lifetime of photoluminescent PSiNPs. In conclusion, the efficient NPs functionalization and their internalization in *Hydra* were demonstrated. Other studies will be carried out to improve the functionalization process

and to optimize the PSiNPs biocompatibility and their internalization in *Hydra*.

In the third part of the thesis, other nanostructured materials were explored, with different morphological properties relative to PSi material. In particular, the attention was focused on ZnO, a nanostructured material that could have novel applications in biomedical sciences. In particular, nZnO and its doped form nZnO·F were investigated to develop a platform for label-free optical sensing. nZnO is a semiconductor characterized by a large band-gap and a large excitonic binding energy, providing an excitonic emission at room temperature. nZnO shows an intense photoluminescence under UV laser irradiation, characterized by a peak at 380 nm and a broad visible band, related to the free excitonic recombination and to surface and lattice defects, respectively. To improve the physical properties of this nanostructured materials, fluorine (F)-nZnO was obtained, doping nZnO with fluorine atoms.

The nZnO and nZnO·F surfaces, obtained *via* hydrothermal synthesis, were functionalized by using a mild chemical approach, based on the aminosilane modification, followed by a cross-linker immobilization, in order to covalently graft protein A, a model biomolecule. The interaction between nZnO and nZnO·F and PrA was characterized by spectroscopic reflectometry, PL analysis, water contact angle and fluorescence microscopy. The results showed that nZnO·F matrix was better functionalized with respect to nZnO, probably due to the wrinkled flake-like morphology, allowing the immobilization of a higher percentage of the biomolecule. In conclusion, nZnO·F can be effectively used as platform label-free for optical sensing.

To sum up, two different kinds of optical biosensors were proposed in this thesis work: the first one is made of two different nanostructured materials, graphene oxide and porous silicon, while, for the second one, nZnO·F was used as transducer material. The successful functionalization of both systems was obtained *via* a covalent surface chemistry and analysed through suitable techniques. While a complex process was used to covalently graft GO into the PSi matrix, a milder chemistry was required to functionalize the nZnO surface. Despite the functionalization of GO-PSi optical biosensor required much more efforts, it can be used in dual-mode and it showed a greater response compared to nZnO·F.

This thesis presents an overview of the design and characterization of nanostructured nanosystems. Among these, gold nanoparticles have

gained prominence due to their unique optical and physical properties, such as the large surface area to volume ratio, easy functionalization, stability over high temperature. These characteristics make them an interesting material for a broad range of applications in a variety of research fields (i.e., sensing, bioimaging, drug delivery, photothermal therapy, etc). In particular, the possible use of AuNPs as a promising contrast agent in biomedical applications and their antimicrobial activity were explored.

The synthesis techniques of AuNPs represent an active research area in constant evolution in order to improve the control over their size and shape. In particular, in the last years, researchers are focusing their attention on the development of hybrid-gold nanosystems because they have the potential to generate enhanced properties due to the coupling of the single elements. In particular, in the fourth part of the thesis is widely discussed the synthesis of hybrid complexes, made of AuNPs and Cu (II) in which the two developed nanosystems differ from the chelation of Cu(II): single gold-copper NPs (Cu^0AuNPs), in which no chelating agents are used, and enriched monopicolinate cyclam (L1)-Cu(II)-Au(III)-complex ($\text{L1@Cu}^{2+}\text{AuNPs}$), in which the Cu(II) is chelated. The stability of the complexes was evaluated through Raman and Uv-vis spectroscopy, TEM, DLS and ζ -potential. Moreover, the cytotoxicity and the uptake of these complexes were studied using undifferentiated and neural differentiated embryonic stem cells. Both the nanosystems showed a good biocompatibility for concentrations up to 100 nM. Moreover, for both cell lines, NPs showed a concentration-dependent cytotoxicity. In particular, neural-derived ES cells resulted more sensitive towards the toxicity of both the hybrid nanoparticles than the undifferentiated ES cells. The cellular uptake of NPs, observed *via* confocal microscopy, reported that, while $\text{L1@Cu}^{2+}\text{-AuNPs}$ were internalized into the cytoplasm, the $\text{Cu}^0\text{-AuNPs}$ were observed both in the cytoplasm and in the nucleus. This effect could be attributable to a more efficient interaction of $\text{Cu}^0\text{-AuNPs}$ to mammalian cell membranes. In conclusion, $\text{L1@Cu}^{2+}\text{-AuNPs}$ can be used for possible biological applications.

Gold nanoparticles are also known to be active against drug-resistant bacteria through several modes of action. Moreover, they are also excellent candidate for transporting drugs, antibiotics or other antibacterial therapeutic agents. AMPs are considered a valid alternative to conventional antibiotics but their poor enzymatic stability, low permeability across the biological barrier represent some limitations in therapeutic approach. The immobilization of these peptides on

metallic surfaces represents a possible strategy to overcome this problem obtaining a nanocomplex able to enhance the antimicrobial activity of both components of the system.

The last part of thesis was focused on the functionalization of AuNPs to AMPs. Starting from two different kinds of AuNPs (PEG-AuNPs and citrate AuNPs), different strategies were used to covalently graft the temporin to the gold surface. The stability of the complexes was analysed by Uv-vis spectroscopy, DLS and ζ -potential, highlighting good functionalization procedure for both nanocomplexes. The amount of bound peptide, evaluated by RP-HPLC, was high for both the complexes: it was estimated to be 92% in the case of PEG-AuNPs-TL48 and 97% for c-AuNPs-CysTL48. Preliminary studies, conducted on *Staphylococcus aureus*, showed an enhancement of the antimicrobial activity of c-AuNPs-CysTL48 nanocomplexes compared with free peptide. Other studies will be conducted to analyse the conformational change of the peptide when is grafted to NPs. This will be the first step for understanding how increase the antimicrobial activity of the developed nanocomplexes.

5. References

- [1] M. J. Sailor, *Porous silicon in practice: preparation, characterization and applications*. Wiley-VCH, 2012.
- [2] C. Pacholski, "Photonic Crystal Sensors Based on Porous Silicon," *Sensors*, vol. 13, no. 4, pp. 4694–4713, Apr. 2013.
- [3] J. Turkevich, P. C. Stevenson, and J. Hillier, "A study of the nucleation and growth processes in the synthesis of colloidal gold," *Discussions of the Faraday Society*, vol. 11. pp. 55–75, 1951.
- [4] Z. Huo, C. Tsung, W. Huang, X. Zhang, and P. Yang, "Sub-Two Nanometer Single Crystal Au Nanowires," *Nano Lett.*, vol. 8, no. 7, pp. 2041–2044, Jul. 2008.
- [5] J. Manson, D. Kumar, B. J. Meenan, and D. Dixon, "Polyethylene glycol functionalized gold nanoparticles: The influence of capping density on stability in various media," *Gold Bull.*, vol. 44, no. 2, pp. 99–105, 2011.
- [6] J. Spadavecchia, E. Apchain, M. Albéric, E. Fontan, and I. Reiche, "One-Step Synthesis of Collagen Hybrid Gold Nanoparticles and Formation on Egyptian-like Gold-Plated Archaeological Ivory," *Angew. Chemie Int. Ed.*, vol. 53, no. 32, pp. 8363–8366, Aug. 2014.
- [7] S. Her, D. A. Jaffray, and C. Allen, "Gold nanoparticles for applications in cancer radiotherapy: Mechanisms and recent advancements," *Advanced Drug Delivery Reviews*, vol. 109. Elsevier B.V., pp. 84–101, 15-Jan-2017.
- [8] Z. Gan, J. Ju, T. Zhang, and D. Wu, "Preparation of rhodamine B fluorescent poly(methacrylic acid) coated gelatin nanoparticles," *J. Nanomater.*, vol. 2011, 2011.
- [9] M. Mirhosseini and F. B. Firouzabadi, "Antibacterial activity of zinc oxide nanoparticle suspensions on food-borne pathogens," *Int. J. Dairy Technol.*, vol. 66, no. 2, pp. 291–295, May 2013.
- [10] J. W. Rasmussen, E. Martinez, P. Louka, and D. G. Wingett, "Zinc oxide nanoparticles for selective destruction of tumor cells and potential for drug delivery applications," *Expert Opinion on Drug Delivery*, vol. 7, no. 9. pp. 1063–1077, Sep-2010.
- [11] E. Fortunato *et al.*, "Zinc oxide, a multifunctional material: From material to device applications," *Appl. Phys. A Mater. Sci. Process.*, vol. 96, no. 1, pp. 197–205, Jul. 2009.
- [12] G. M. Whitesides, "The 'right' size in nanobiotechnology," *Nature Biotechnology*, vol. 21, no. 10. pp. 1161–1165, 01-Oct-2003.
- [13] "Nanostructured Materials - Processing, properties and

- applications, 2nd Edition". Edited by Carl C. Koch, 2007
- [14] A. Uhler, "Electrolytic Shaping of Germanium and Silicon," *Bell Syst. Tech. J.*, vol. 35, no. 2, pp. 333–347, 1956.
 - [15] X. G. Zhang, "Morphology and formation mechanisms of porous silicon," *J. Electrochem. Soc.*, vol. 151, no. 1, 2004.
 - [16] L. T. Canham, "Silicon quantum wire array fabrication by electrochemical and chemical dissolution of wafers," *Appl. Phys. Lett.*, vol. 57, no. 10, pp. 1046–1048, 1990.
 - [17] R. L. Smith and S. D. Collins, "Porous silicon formation mechanisms," *J. Appl. Phys.*, vol. 71, no. 8, 1992.
 - [18] V. Lehmann and U. Gösele, "Porous silicon formation: A quantum wire effect," *Appl. Phys. Lett.*, vol. 58, no. 8, pp. 856–858, 1991.
 - [19] A. E. Pap *et al.*, "Thermal oxidation of porous silicon: Study on structure," *Appl. Phys. Lett.*, vol. 86, no. 4, 2005.
 - [20] M. Terracciano, I. Rea, J. Politi, and L. De Stefano, "Optical characterization of aminosilane-modified silicon dioxide surface for biosensing," *J. Eur. Opt. Soc.*, vol. 8, Dec. 2013.
 - [21] J. M. Buriak, "Organometallic chemistry on silicon and germanium surfaces," *Chem. Rev.*, vol. 102, no. 5, pp. 1271–1308, May 2002.
 - [22] J. M. Buriak and M. J. Allen, "Lewis Acid Mediated Functionalization of Porous Silicon with Substituted Alkenes and Alkynes," *J. Am. Chem. Soc.*, vol. 120, no. 6, pp. 1339–1340, Feb. 1998.
 - [23] R. Boukherroub, J. T. C. Wojtyk, D. D. M. Wayner, and D. J. Lockwood, "Thermal Hydrosilylation of Undecylenic Acid with Porous Silicon," *J. Electrochem. Soc.*, vol. 149, no. 2, p. H59, Feb. 2002.
 - [24] L. M. Bonanno and E. Segal, "Nanostructured porous silicon-polymer-based hybrids: From biosensing to drug delivery," *Nanomedicine*, vol. 6, no. 10, pp. 1755–1770, Dec-2011.
 - [25] E. Secret *et al.*, "Antibody-Functionalized Porous Silicon Nanoparticles for Vectorization of Hydrophobic Drugs," *Adv. Healthc. Mater.*, vol. 2, no. 5, pp. 718–727, May 2013.
 - [26] K. Urmann, S. Arshavsky-Graham, J. G. Walter, T. Scheper, and E. Segal, "Whole-cell detection of live: *Lactobacillus acidophilus* on aptamer-decorated porous silicon biosensors," *Analyst*, vol. 141, no. 18, pp. 5432–5440, Sep. 2016.
 - [27] K. Urmann, P. Reich, J. G. Walter, D. Beckmann, E. Segal, and T. Scheper, "Rapid and label-free detection of protein a by aptamer-tethered porous silicon nanostructures," *J. Biotechnol.*, vol. 257, pp. 171–177, Sep. 2017.

- [28] L. Authier, C. Grossiord, P. Brossier, and B. Limoges, "Gold nanoparticle-based quantitative electrochemical detection of amplified human cytomegalovirus DNA using disposable microband electrodes," *Anal. Chem.*, vol. 73, no. 18, pp. 4450–4456, Sep. 2001.
- [29] S. K. Ghosh and T. Pal, "Interparticle coupling effect on the surface plasmon resonance of gold nanoparticles: From theory to applications," *Chemical Reviews*, vol. 107, no. 11, pp. 4797–4862, Nov-2007.
- [30] M. A. El-Sayed, "Some interesting properties of metals confined in time and nanometer space of different shapes," *Acc. Chem. Res.*, vol. 34, no. 4, pp. 257–264, 2001.
- [31] M.-C. D. and D. Astruc*, "Gold Nanoparticles: Assembly, Supramolecular Chemistry, Quantum-Size-Related Properties, and Applications toward Biology, Catalysis, and Nanotechnology," 2003.
- [32] M. Brust, M. Walker, D. Bethell, D. J. Schiffrin, and R. Whyman, "Synthesis of thiol-derivatised gold nanoparticles in a two-phase liquid-liquid system," *J. Chem. Soc. Chem. Commun.*, no. 7, pp. 801–802, 1994.
- [33] P. Vijaya Kumar, S. Mary Jelastin Kala, and K. S. Prakash, "Green synthesis of gold nanoparticles using Croton Caudatus Geisel leaf extract and their biological studies," *Mater. Lett.*, vol. 236, pp. 19–22, Feb. 2019.
- [34] E. H. Ismail, A. M. A. Saqer, E. Assirey, A. Naqvi, and R. M. Okasha, "Successful green synthesis of gold nanoparticles using a corchorus olitorius extract and their antiproliferative effect in cancer cells," *Int. J. Mol. Sci.*, vol. 19, no. 9, Sep. 2018.
- [35] B. Syed, N. N. Prasad, and S. Satisha, "Endogenous mediated synthesis of gold nanoparticles bearing bactericidal activity," *J. Microsc. Ultrastruct.*, vol. 4, no. 3, p. 162, 2016.
- [36] S. Menon, R. S., and V. K. S., "A review on biogenic synthesis of gold nanoparticles, characterization, and its applications," *Resour. Technol.*, vol. 3, no. 4, pp. 516–527, Dec. 2017.
- [37] A. G. Kanaras, F. S. Kamounah, K. Schaumburg, C. J. Kiely, and M. Brust, "Thioalkylated tetraethylene glycol: A new ligand for water soluble monolayer protected gold clusters," *Chem. Commun.*, vol. 20, pp. 2294–2295, 2002.
- [38] V. Venkatpurwar, A. Shiras, and V. Pokharkar, "Porphyrin capped gold nanoparticles as a novel carrier for delivery of anticancer drug: In vitro cytotoxicity study," *Int. J. Pharm.*, vol. 409, no. 1–2, pp. 314–320, May 2011.

- [39] K. V. Chakravarthy *et al.*, "Gold nanorod delivery of an ssRNA immune activator inhibits pandemic H1N1 influenza viral replication," *Proc. Natl. Acad. Sci. U. S. A.*, vol. 107, no. 22, pp. 10172–10177, Jun. 2010.
- [40] P. Mishra *et al.*, "Facile bio-synthesis of gold nanoparticles by using extract of Hibiscus sabdariffa and evaluation of its cytotoxicity against U87 glioblastoma cells under hyperglycemic condition," *Biochem. Eng. J.*, vol. 105, pp. 264–272, Jan. 2016.
- [41] U. Rajchakit and V. Sarojini, "Recent Developments in Antimicrobial-Peptide-Conjugated Gold Nanoparticles," *Bioconjug. Chem.*, vol. 28, no. 11, pp. 2673–2686, Nov. 2017.
- [42] X. Wang *et al.*, "Gold nanorod-based localized surface plasmon resonance biosensor for sensitive detection of hepatitis B virus in buffer, blood serum and plasma," *Biosens. Bioelectron.*, vol. 26, no. 2, pp. 404–410, Oct. 2010.
- [43] Y. C. Chuang *et al.*, "An optical biosensing platform for proteinase activity using gold nanoparticles," *Biomaterials*, vol. 31, no. 23, pp. 6087–6095, Aug. 2010.
- [44] P. Yang *et al.*, "Controlled Growth of ZnO Nanowires and Their Optical Properties," *Adv. Funct. Mater.*, vol. 12, no. 5, p. 323, May 2002.
- [45] S. A. Kumar and S. M. Chen, "Nanostructured zinc oxide particles in chemically modified electrodes for biosensor applications," *Analytical Letters*, vol. 41, no. 2, pp. 141–158, Jan-2008.
- [46] W. I. Park, Y. H. Jun, S. W. Jung, and G. C. Yi, "Excitonic emissions observed in ZnO single crystal nanorods," *Appl. Phys. Lett.*, vol. 82, no. 6, pp. 964–966, Feb. 2003.
- [47] Ü. Özgür *et al.*, "A comprehensive review of ZnO materials and devices," *Journal of Applied Physics*, vol. 98, no. 4. American Institute of Physics, pp. 1–103, 15-Aug-2005.
- [48] G. P. Papari *et al.*, "Morphological, Structural, and Charge Transfer Properties of F-Doped ZnO: A Spectroscopic Investigation," *J. Phys. Chem. C*, vol. 121, no. 29, pp. 16012–16020, Jul. 2017.
- [49] T. Okada, B. H. Agung, and Y. Nakata, "ZnO nano-rods synthesized by nano-particle-assisted pulsed-laser deposition," in *Applied Physics A: Materials Science and Processing*, 2004, vol. 79, no. 4–6, pp. 1417–1419.
- [50] G. Mattson, E. Conklin, S. Desai, G. Nielander, M. D. Savage, and S. Morgensen, "A practical approach to crosslinking," *Mol. Biol. Rep.*, vol. 17, no. 3, pp. 167–183, Apr. 1993.
- [51] J. C. Love, L. A. Estroff, J. K. Kriebel, R. G. Nuzzo, and G. M.

- Whitesides, "Self-Assembled Monolayers of Thiolates on Metals as a Form of Nanotechnology," *Chem. Rev.*, vol. 105, no. 4, pp. 1103–1170, Apr. 2005.
- [52] J. Chen, R. E. Ruther, Y. Tan, L. M. Bishop, and R. J. Hamers, "Molecular Adsorption on ZnO(10 $\bar{1}$ 0) Single-Crystal Surfaces: Morphology and Charge Transfer," *Langmuir*, vol. 28, no. 28, pp. 10437–10445, Jul. 2012.
- [53] I. Rea, M. Casalino, M. Terracciano, L. Sansone, J. Politi, and L. De Stefano, "Photoluminescence enhancement of graphene oxide emission by infiltration in an aperiodic porous silicon multilayer.," *Opt. Express*, vol. 24, no. 21, pp. 24413–24421, Oct. 2016.
- [54] I. Rea *et al.*, "Photoluminescence of Graphene Oxide Infiltrated into Mesoporous Silicon," *J. Phys. Chem. C*, vol. 118, no. 47, pp. 27301–27307, Nov. 2014.
- [55] C.-T. Chien *et al.*, "Tunable Photoluminescence from Graphene Oxide," *Angew. Chemie Int. Ed.*, vol. 51, no. 27, pp. 6662–6666, Jul. 2012.
- [56] P. Brugada and J. Brugada, "Right bundle branch block, persistent ST segment elevation and sudden cardiac death: A distinct clinical and electrocardiographic syndrome. A multicenter report," *J. Am. Coll. Cardiol.*, vol. 20, no. 6, pp. 1391–1396, Nov. 1992.
- [57] Q. Chen *et al.*, "Genetic basis and molecular mechanism for idiopathic ventricular fibrillation," *Nature*, vol. 392, no. 6673, pp. 293–296, Mar. 1998.
- [58] S. G. Priori *et al.*, "2015 ESC Guidelines for the management of patients with ventricular arrhythmias and the prevention of sudden cardiac death the Task Force for the Management of Patients with Ventricular Arrhythmias and the Prevention of Sudden Cardiac Death of the European Society of Cardiology (ESC) Endorsed by: Association for European Paediatric and Congenital Cardiology (AEPC)," *European Heart Journal*, vol. 36, no. 41. Oxford University Press, p. 2793–2867I, 2015.
- [59] W. R. Sanhai, J. H. Sakamoto, R. Canady, and M. Ferrari, "Seven challenges for nanomedicine," *Nature Nanotechnology*, vol. 3, no. 5. Nature Publishing Group, pp. 242–244, 2008.
- [60] V. Wagner, A. Dullaart, A. K. Bock, and A. Zweck, "The emerging nanomedicine landscape," *Nature Biotechnology*, vol. 24, no. 10. pp. 1211–1217, Oct-2006.
- [61] D. R. Dreyer, S. Park, C. W. Bielawski, and R. S. Ruoff, "The chemistry of graphene oxide.," *Chem. Soc. Rev.*, vol. 39, no. 1,

- pp. 228–40, Jan. 2010.
- [62] †,‡ Tamás Szabó *et al.*, “Evolution of Surface Functional Groups in a Series of Progressively Oxidized Graphite Oxides,” 2006.
- [63] L. J. Cote, J. Kim, Z. Zhang, C. Sun, and J. Huang, “Tunable assembly of graphene oxide surfactant sheets: Wrinkles, overlaps and impacts on thin film properties,” *Soft Matter*, vol. 6, no. 24, pp. 6096–6101, Dec. 2010.
- [64] J. Zhang *et al.*, “Graphene Oxide as a Matrix for Enzyme Immobilization,” *Langmuir*, vol. 26, no. 9, pp. 6083–6085, 2010.
- [65] M. Wu, R. Kempaiah, P.-J. Jimmy Huang, V. Maheshwari, and J. Liu, “Adsorption and Desorption of DNA on Graphene Oxide Studied by Fluorescently Labeled Oligonucleotides,” 2011.
- [66] A. Gupta, B. K. Shaw, and S. K. Saha, “Bright Green Photoluminescence in Aminoazobenzene-Functionalized Graphene Oxide,” *J. Phys. Chem. C*, vol. 118, no. 13, pp. 6972–6979, Apr. 2014.
- [67] T. Gokus *et al.*, “Making Graphene Luminescent by Oxygen Plasma Treatment,” *ACS Nano*, vol. 3, no. 12, pp. 3963–3968, Dec. 2009.
- [68] G. Eda *et al.*, “Blue Photoluminescence from Chemically Derived Graphene Oxide,” *Adv. Mater.*, vol. 22, no. 4, pp. 505–509, Jan. 2010.
- [69] L. Canham, *Handbook of Porous Silicon*. Springer International Publishing, 2014.
- [70] J. Joo *et al.*, “Porous silicon-graphene oxide core-shell nanoparticles for targeted delivery of siRNA to the injured brain,” *Nanoscale Horizons*, vol. 1, no. 5, pp. 407–414, Sep. 2016.
- [71] R. Moretta *et al.*, “Toward multi-parametric porous silicon transducers based on covalent grafting of Graphene oxide for biosensing applications,” *Front. Chem.*, vol. 6, no. NOV, Nov. 2018.
- [72] R. P. Singh, B. K. Oh, and J. W. Choi, “Application of peptide nucleic acid towards development of nanobiosensor arrays,” *Bioelectrochemistry*, vol. 79, no. 2, pp. 153–161, Oct-2010.
- [73] Q. Shabir *et al.*, “Quantification and Reduction of the Residual Chemical Reactivity of Passivated Biodegradable Porous Silicon for Drug Delivery Applications,” *Silicon*, pp. 1–11, Apr. 2017.
- [74] L. B. Kong, *Carbon nanomaterials based on graphene nanosheets*. .
- [75] X. Yang, X. Zhang, Y. Ma, Y. Huang, Y. Wang, and Y. Chen, “Superparamagnetic graphene oxide–Fe₃O₄ nanoparticles hybrid for controlled targeted drug carriers,” *J. Mater. Chem.*, vol.

- 19, no. 18, p. 2710, Apr. 2009.
- [76] M. Ghulinyan, B. Gelloz, T. Ohta, L. Pavesi, D. J. Lockwood, and N. Koshida, "Stabilized porous silicon optical superlattices with controlled surface passivation," *Appl. Phys. Lett.*, vol. 93, no. 6, p. 061113, Aug. 2008.
- [77] R. Boukherroub, J. Wojtyk, and D. Wayner, "Thermal hydrosilylation of undecylenic acid with porous silicon," *J.*, 2002.
- [78] J. M. Harris, M. R. Sedaghat-Herati, P. J. Sather, D. E. Brooks, and T. M. Fyles, "Synthesis of New Poly(Ethylene Glycol) Derivatives," in *Poly(Ethylene Glycol) Chemistry*, Boston, MA: Springer US, 1992, pp. 371–381.
- [79] F. Lucarelli, G. Marrazza, A. P. F. Turner, and M. Mascini, "Carbon and gold electrodes as electrochemical transducers for DNA hybridisation sensors," *Biosensors and Bioelectronics*, vol. 19, no. 6. Elsevier Ltd, pp. 515–530, 15-Jan-2004.
- [80] C. Pacholski, M. Sartor, M. J. Sailor, F. Cunin, and G. M. Miskelly, "Biosensing Using Porous Silicon Double-Layer Interferometers: Reflective Interferometric Fourier Transform Spectroscopy," *J. Am. Chem. Soc.*, vol. 127, no. 33, pp. 11636–11645, Aug. 2005.
- [81] M. P. Schwartz, F. Cunin, R. W. Cheung, and M. J. Sailor, "Chemical modification of silicon surfaces for biological applications," in *Physica Status Solidi (A) Applications and Materials Science*, 2005, vol. 202, no. 8, pp. 1380–1384.
- [82] C. Steinem, A. Janshoff, V. S. Y. Lin, N. H. Völcker, and M. Reza Ghadiri, "DNA hybridization-enhanced porous silicon corrosion: Mechanistic investigations and prospect for optical interferometric biosensing," *Tetrahedron*, vol. 60, no. 49, pp. 11259–11267, Nov. 2004.
- [83] B. Konkena and S. Vasudevan, "Understanding aqueous dispersibility of graphene oxide and reduced graphene oxide through pK_a measurements," *J. Phys. Chem. Lett.*, vol. 3, no. 7, pp. 867–872, Apr. 2012.
- [84] U. Resch-Genger, M. Grabolle, S. Cavaliere-Jaricot, R. Nitschke, and T. Nann, "Quantum dots versus organic dyes as fluorescent labels," *Nature Methods*, vol. 5, no. 9. pp. 763–775, 2008.
- [85] P. Bhattacharya and Z. Mi, "Quantum-dot optoelectronic devices," *Proc. IEEE*, vol. 95, no. 9, pp. 1723–1740, Sep. 2007.
- [86] J. Wu, S. Chen, A. Seeds, and H. Liu, "Quantum dot optoelectronic devices: Lasers, photodetectors and solar cells," *Journal of Physics D: Applied Physics*, vol. 48, no. 36. Institute of Physics Publishing, 16-Sep-2015.

- [87] P. Zrazhevskiy, M. Senaw, and X. Gao, "Designing multifunctional quantum dots for bioimaging, detection, and drug delivery," 2009.
- [88] E. Tasciotti *et al.*, "Mesoporous silicon particles as a multistage delivery system for imaging and therapeutic applications," *Nat. Nanotechnol.*, vol. 3, no. 3, pp. 151–157, 2008.
- [89] L. M. Bimbo *et al.*, "Biocompatibility of thermally hydrocarbonized porous silicon nanoparticles and their biodistribution in rats," *ACS Nano*, vol. 4, no. 6, pp. 3023–3032, Jun. 2010.
- [90] J. L. Heinrich, C. L. Curtis, G. M. Credo, K. L. Kavanagh, and M. J. Sailor, "Luminescent colloidal silicon suspensions from porous silicon," *Science (80-.)*, vol. 255, no. 5040, pp. 66–68, 1992.
- [91] B. Quinn, F. Gagné, and C. Blaise, "Hydra, a model system for environmental studies," *Int. J. Dev. Biol.*, vol. 56, no. 6-7–8, pp. 613–625, 2012.
- [92] A. Loni, L. T. Canham, T. Defforge, and G. Gautier, "Supercritically-Dried Porous Silicon Powders with Surface Areas Exceeding 1000 m²/g," *ECS J. Solid State Sci. Technol.*, vol. 4, no. 8, pp. P289–P292, 2015.
- [93] A. Loni, A. J. Simons, P. D. J. Calcott, and L. T. Canham, "Blue photoluminescence from rapid thermally oxidized porous silicon following storage in ambient air," *J. Appl. Phys.*, vol. 77, no. 7, pp. 3557–3559, 1995.
- [94] R. E. Steele, "Developmental signaling in Hydra: What does it take to build a 'simple' animal?," *Developmental Biology*, vol. 248, no. 2. Elsevier, pp. 199–219, 2002.
- [95] P. T. Sandridge, "Ecology and Classification of North American Freshwater Invertebrates . James H. Thorp , Alan P. Covich ," *J. North Am. Benthol. Soc.*, vol. 10, no. 4, pp. 466–467, Dec. 1991.
- [96] W. Karntanut and D. Pascoe, "A comparison of methods for measuring acute toxicity to *Hydra vulgaris*," *Chemosphere*, vol. 41, no. 10, pp. 1543–1548, 2000.
- [97] E. Mayhew, J. P. Harlos, and R. L. Juliano, "The Effect of Polycations on Cell Membrane Stability and Transport Processes," 1973.
- [98] P. Symonds, J. C. Murray, A. C. Hunter, G. Debska, A. Szewczyk, and S. M. Moghimi, "Low and high molecular weight poly(L-lysine)s/poly(L-lysine)-DNA complexes initiate mitochondrial-mediated apoptosis differently," *FEBS Lett.*, vol. 579, no. 27, pp. 6191–6198, Nov. 2005.
- [99] D. Sgouras and R. Duncan, "Methods for the evaluation of biocompatibility of soluble synthetic polymers which have

- potential for biomedical use: 1 - Use of the tetrazolium-based colorimetric assay (MTT) as a preliminary screen for evaluation of in vitro cytotoxicity," *J. Mater. Sci. Mater. Med.*, vol. 1, no. 2, pp. 61–68, Jul. 1990.
- [100] S. Choksakulnimitr, S. Masuda, H. Tokuda, Y. Takakura, and M. Hashida, "In vitro cytotoxicity of macromolecules in different cell culture systems," *J. Control. Release*, vol. 34, no. 3, pp. 233–241, Jun. 1995.
- [101] W. Hartmann and H. J. Galla, "Binding of polylysine to charged bilayer membranes. Molecular organization of a lipid · peptide complex," *BBA - Biomembr.*, vol. 509, no. 3, pp. 474–490, Jun. 1978.
- [102] C. Tortiglione, A. Quarta, M. A. Malvindi, A. Tino, and T. Pellegrino, "Fluorescent Nanocrystals Reveal Regulated Portals of Entry into and Between the Cells of Hydra," *PLoS One*, vol. 4, no. 11, p. e7698, Nov. 2009.
- [103] H. Kobayashi, M. Ogawa, R. Alford, P. L. Choyke, and Y. Urano, "New strategies for fluorescent probe design in medical diagnostic imaging," *Chem. Rev.*, vol. 110, no. 5, pp. 2620–2640, May 2010.
- [104] D. M. Shcherbakova and V. V. Verkhusha, "Near-infrared fluorescent proteins for multicolor in vivo imaging," *Nat. Methods*, vol. 10, no. 8, pp. 751–754, Aug. 2013.
- [105] M. K. So, C. Xu, A. M. Loening, S. S. Gambhir, and J. Rao, "Self-illuminating quantum dot conjugates for in vivo imaging," *Nat. Biotechnol.*, vol. 24, no. 3, pp. 339–343, Mar. 2006.
- [106] L. Zhang *et al.*, "Practical implementation, characterization and applications of a multi-colour time-gated luminescence microscope," *Sci. Rep.*, vol. 4, Oct. 2014.
- [107] X. Liu, Z. Ye, W. Wei, Y. Du, J. Yuan, and D. Ma, "Artificial luminescent protein as a bioprobe for time-gated luminescence bioimaging," *Chem. Commun.*, vol. 47, no. 28, pp. 8139–8141, Jul. 2011.
- [108] J. W. Costerton, Z. Lewandowski, D. E. Caldwell, D. R. Korber, and H. M. Lappin-Scott, "Microbial Biofilms - Annual Review of Microbiology, 49(1):711," *Annu. Rev. Microbiol.*, vol. 49, pp. 711–45, Jan. 1995.
- [109] J. W. Costerton, P. S. Stewart, and E. P. Greenberg, "Bacterial biofilms: A common cause of persistent infections," *Science*, vol. 284, no. 5418, pp. 1318–1322, 21-May-1999.
- [110] C. A. Fux, J. W. Costerton, P. S. Stewart, and P. Stoodley, "Survival strategies of infectious biofilms," *Trends in*

- Microbiology*, vol. 13, no. 1. pp. 34–40, Jan-2005.
- [111] S. Gurunathan, J. W. Han, A. Abdal Dayem, V. Eppakayala, and J. H. Kim, “Oxidative stress-mediated antibacterial activity of graphene oxide and reduced graphene oxide in *Pseudomonas aeruginosa*,” *Int. J. Nanomedicine*, vol. 7, pp. 5901–5914, 2012.
- [112] A. Nagy, A. Harrison, S. Sabbani, R. S. Munson, P. K. Dutta, and W. J. Waldman, “Silver nanoparticles embedded in zeolite membranes: release of silver ions and mechanism of antibacterial action.,” *Int. J. Nanomedicine*, vol. 6, pp. 1833–1852, 2011.
- [113] Y. H. Leung *et al.*, “Mechanisms of antibacterial activity of mgo: Non-ros mediated toxicity of mgo nanoparticles towards *escherichia coli*,” *Small*, vol. 10, no. 6, pp. 1171–1183, Mar. 2014.
- [114] L. Wang, C. Hu, and L. Shao, “The antimicrobial activity of nanoparticles: Present situation and prospects for the future,” *International Journal of Nanomedicine*, vol. 12. Dove Medical Press Ltd., pp. 1227–1249, 14-Feb-2017.
- [115] K. A. Brogden, “Antimicrobial peptides: Pore formers or metabolic inhibitors in bacteria?,” *Nature Reviews Microbiology*, vol. 3, no. 3. pp. 238–250, Mar-2005.
- [116] M. L. Mangoni *et al.*, “Structure-function relationships of temporins, small antimicrobial peptides from amphibian skin,” *Eur. J. Biochem.*, vol. 267, no. 5, pp. 1447–1454, 2000.
- [117] G. Palmieri *et al.*, “Small Synthetic Peptides Bioconjugated to Hybrid Gold Nanoparticles Destroy Potentially Deadly Bacteria at Submicromolar Concentrations,” 2018.
- [118] D. Thompson, “Gold: Progress in chemistry, biochemistry and technology,” *Gold Bull.*, vol. 31, no. 4, pp. 134–136, Dec. 1998.

APPENDIX I. Publications, communications, experiences in foreign laboratories, courses and workshops

Scientific publications

J1. **R. Moretta**, M. Terracciano, P. Dardano, M. Casalino, I. Rea and L. De Stefano, "Covalent grafting of graphene oxide on functionalized macroporous silicon", *De Gruyter, Open Mater. Sci.* 2018, 4:15-22.

J2. **R. Moretta**, M. Terracciano, P. Dardano, M. Casalino, L. De Stefano, C. Schiattarella, I. Rea, "Toward multi-parametric porous silicon transducers based on covalent grafting of graphene oxide for biosensing applications", *Front. Chem.* 2018, 6, 583

J3. F. Aouidat, Z. Halime, **R. Moretta**, I. Rea, S. Filosa, S. Donato, R. Tate, L. De Stefano, R. Tripier, J. Spadavecchia, "Design and Synthesis of Hybrid PEGylated Metal Complexes Monopicolinate Cyclam Ligands: From Tunable Chemical Design to Hybrid Nanovectors for Neurological-Medical Applications", *ACS Omega*, 2019, 4, 2500-2509

J4. B. Agrillo, M. Balestieri, M. Gogliettino, G. Palmieri, **R. Moretta**, Y. T.R. Proroga, I. Rea, A. Cornacchia, F. Capuano, G. Smaldone and L. De Stefano, "Functionalized polymeric materials with bio-derived antimicrobial peptide for Active packaging", *Int. J. Mol. Sci.* 2019, 20, 601

J5. C. Schiattarella, M. Terracciano, T. Defforge, G. Gautier, B. Della Ventura, **R. Moretta**, L. De Stefano, R. Velotta and I. Rea, "Photoemissive properties and stability of undecylenic acid-modified porous silicon nanoparticles in physiological medium", *Appl. Phys. Lett.* 2019, 114, 113701

J6. M. Terracciano, I. Rea, N. Borbone, **R. Moretta**, G. Oliviero, G. Piccialli and L. De Stefano, "Porous silicon-based aptasensors: the next generation of label-free devices for health monitoring", *Molecules* 2019, 24, 2216

J7. G. Chianese, M. Terracciano, **R. Moretta**, P. Cappiello, G. Vitiello, A. Aronne, C. Schiattarella, L. De Stefano and I. Rea, "Synthesis and surface modification of nanostructured F-Doped ZnO: Toward a

transducer for label-free optical biosensing”, *Appl. Sci* 2019, 9 (16), 3380

J8. M. Gogliettino, M. Balestrieri, R. L. Ambrosio, A. Anastasio, G. Smaldone, Y. T. R. Proroga, **R. Moretta**, I. Rea, L. De Stefano, B. Agrillo and G. Palmieri, “Extending the Shelf-Life of Meat and Dairy Products via PET-Modified Packaging Activated with the Antimicrobial Peptide MTP1”, *Front. Microbiol.* 2020, <https://doi.org/10.3389/fmicb.2019.02963>

Proceedings

P1. **R. Moretta**, M. Terracciano, I. Rea, M. Casalino, P. Dardano and L. De Stefano, “Functionalization of macroporous silicon for optical detection of bacteria”, Published in: 19th Italian National Conference on Photonic Technologies (Fotonica 2017), *IEEE Xplore Digital Library*

P2. **R. Moretta**, M. Terracciano, I. Rea, T. Defforge, S. Vijayakumar, G. Gautier and L. De Stefano, “Towards luminescent porous silicon nanoparticles for in vivo imaging”, Published in: 19th Italian National Conference on Photonic Technologies (Fotonica 2017), *IEEE Xplore Digital Library*

P3. A De Lucia, I. Rea, **R. Moretta**, M. Terracciano, J. Spadavecchia, G. Fiorentino, C. Forestiere and L. De Stefano, “Optical modelling of hybrid nanoparticles for theranostic applications”, Published in: 19th Italian National Conference on Photonic Technologies (Fotonica 2017), *IEEE Digital Library*

P4. C. Schiattarella, G. Vitiello, M. Terracciano, **R. Moretta**, I. Rea, B. Silvestri, A. Aronne and L. De Stefano, “Highly photo-emissive F-doped ZnO for optical biosensing”, Published in: 20th Italian National Conference on Photonic Technologies (Fotonica 2018), *IEEE Xplore Digital Library*

P5. C. Schiattarella, M. Terracciano, T. Defforge, G. Gautier, B. Della Ventura, R. Moretta, **R. Moretta**, L. De Stefano, R. Velotta and I. Rea, “Nanostructured silicon-based nanoparticles as label-free photoluminescent probes for *in vivo* imaging”, Published in: 20th Italian

Communications at Conferences and Workshops

- B. Miranda, I. Rea, M. Terracciano, **R. Moretta**, J. Spadavecchia, C. Forestiere, L. De Stefano, “Inverse identification of the optical properties of Hybrid spherical nanoparticles”, Plasmonica 2017, July 2017, Lecce (Italy)
- I. Rea, M. Terracciano, P. Dardano, **R. Moretta**, L. De Stefano, “Silica – gold nanodevices for biomedical applications”, Plasmonica 2017, July 2017, Lecce (Italy)
- C. Schiattarella, M. Terracciano, T. Defforge, G. Gautier, C. Tortiglione, **R. Moretta**, B. Della Ventura, L. De Stefano, R. Velotta, I. Rea, “Emission properties of functionalized porous silicon nanoparticles for *in vivo* imaging”, 7th EOS Topical Meeting on Optical Microsystems, September 2017, Capri (Italy)
- L. De Stefano, **R. Moretta**, P. Dardano, M. Casalino, I. Rea, M. Terracciano, “Covalent grafting of graphene oxide on functionalized macroporous silicon”, “PSST 2018”, March 2018, La Grande Motte (France)
- M. Terracciano, M. Napolitano, L. De Stefano, A. Chiara De Luca, **R. Moretta**, I. Rea, “Gold decorated bioderived porous silica hybrid nanovectors for theranostic applications”, “PSST 2018”, March 2018, La Grande Motte (France)
- C. Schiattarella, M. Terracciano, T. Defforge, G. Gautier, C. Tortiglione, **R. Moretta**, B. Della Ventura, L. De Stefano, R. Velotta, I. Rea, “In vivo imaging by chemically modified photoluminescent porous silicon nanoparticles”, “PSST 2018”, March 2018, La Grande Motte (France)
- C. Schiattarella, M. Terracciano, T. Defforge, G. Gautier, B. Della Ventura, **R. Moretta**, L. De Stefano, R. Velotta, I. Rea, “Functionalized silicon nanostructures for selective label-free bioimaging”, Europt(r)ode XIV, March 2018, Napoli (Italy)

- **R. Moretta**, M. Terracciano, P. Dardano, M. Casalino, I. Rea, L. De Stefano, “Hybrid graphene oxide-porous silicon multiparametric sensor for biomolecules recognition”, Silicon Nanoparticles Workshop, October 2018, Bertinoro (Italy)
- I. Rea, C. Schiattarella, M. Terracciano, T. Defforge, G. Gautier, B. Della Ventura, **R. Moretta**, R. Velotta, L. De Stefano, “Biocompatible luminescent silicon nanocrystals for bioimaging”, Workshop on Silicon Nanoparticles, October 2018, Bertinoro (Italy)
- L. De Stefano, I. Rea, **R. Moretta**, G. Vitiello, B. Silvestri, A. Aronne, “Optical detection of Listeria by functionalized F-doped ZnO”, “EBS 2019”, February, Florence (Italy)
- **R. Moretta**, I. Rea, M. Terracciano, L. De Stefano, G. Piccialli, R. Schettino, N. Borbone, G. Oliviero, “Hybrid graphene oxide-porous silicon biosensor for early diagnosis of Sudden Death Syndrome”, “EBS 2019”, February 2019, Florence (Italy)
- C. Schiattarella, **R. Moretta**, R. Schettino, N. Borbone, G. Piccialli, G. Oliviero, M. Terracciano, P. Dardano, M. Casalino, I. Rea, L. De Stefano, “Graphene Oxide-Porous Silicon Device for Multiparametric Detection of Biomolecular Interactions”, XX AISEM 2019, February 2019, Naples (Italy)
- C. Schiattarella, I. Rea, P. Dardano, **R. Moretta**, M. Terracciano, L. De Stefano, “Porous Silicon-based Hybrid Devices for Multiparametric Photonic Biosensors”, 41st PIERS 2019, June 2019, Rome (Italy)
- I. Rea, M. Terracciano, **R. Moretta**, C. Schiattarella, P. Dardano, L. De Stefano, “Highly Photo-emissive Semiconductor Nanoparticles for Optical Imaging and Sensing”, 41st PIERS 2019, June 2019, Rome (Italy)
- **R. Moretta**, C. Schiattarella, M. Terracciano, I. Rea, P. Dardano, L. De Stefano, “Bioderived porous silica hybrid nanovector for theranostic applications”, invited lecture at “Therapeutic nanoproducts: from biology to innovative technology”, June 2019, Rome (Italy)

- B. Miranda, S. De Martino, **R. Moretta**, P. Dardano, I. Rea, C. Forestiere, L. De Stefano, “From rigid to flexible plasmonic sensors for biomedical applications”, Optical Microsystems OμS19, September 2019, Capri (Italy)
- C. Schiattarella, M. Terracciano, T. Defforge, G. Gautier, C. Tortiglione, **R. Moretta**, B. Della Ventura, L. De Stefano, R. Velotta, I. Rea, “Time-gated imaging of luminescent microporous silicon nanoparticles in living Hydra polyps”, 8th EOS Topical Meeting on Optical Microsystems, September 2019, Capri (NA), Italy
- C. Schiattarella, **R. Moretta**, T. Defforge, G. Gautier, C. Tortiglione, B. Della Ventura, M. Terracciano, L. De Stefano, R. Velotta, I. Rea, “Poly-L-Lysine conjugated porous silicon nanoparticles as label-free luminescent probe for in vivo time-gated imaging of Hydra vulgaris”, accepted at PSST 2020, October 2020, Lido di Camaiore (LU), Italy
- **R. Moretta**, C. Schiattarella, M. Terracciano, N. Borbone, G. Oliviero, I. Rea, L. De Stefano, “Graphene Oxide-Porous Silicon based Biosensor for tempestive diagnosis of Brugada Syndrome, accepted at PSST 2020, October 2020, Lido di Camaiore (LU), Italy
- **R. Moretta**, L. Serpico, S. Pedatella, I. Rea, L. De Stefano, “Porous silicon derivatization by a carboxyl-glucose for protein adsorption”, accepted at PSST 2020, October 2020, Lido di Camaiore (LU), Italy

Courses, conferences and workshops

- Fotonica 2017, May 2017, Padova (Italy)
- “Prima scuola nazionale Sensori Chimici”, May 2017, Naples (Italy)
- “International Summer School on Natural Products 2nd Edition”, July 2017, Naples (Italy)
- “Terza scuola nazionale sui biosensori ottici e biofotonica”, December 2017, Naples (Italy)

- Workshop: “Proteins as drug targets, proteins as drugs, and protein degradation as therapeutic strategy”, May 2018, Salerno (Italy)
- “PSST 2018”, March 2018, La Grande Motte (France)
- “Europt(r)ode XIV”, March 2018, Napoli (Italy)
- “EBS 2019”, February 2019, Florence (Italy)
- Workshop: “Workshop on NanoBioMedicine in Naples: The Next Future of Theranostics”, March 2019, Naples (Italy)
- Workshop: “Novel strategies in Anticancer therapy and diagnostics”, May 2019, Naples (Italy)
- “Therapeutic nanoproducts: from biology to innovative technology”, June 2019, Rome (Italy)
- “Advanced Study Course on Optical Chemical Sensors”, July 2019, Bertinoro (FO), Italy
- “Therapeutic nanoproducts: from biology to innovative technology”, June 2019, Rome (Italy)
- “8th EOS Topical Meeting on Optical Microsystems”, September 2019, Capri (NA), Italy

Visiting in Foreign Laboratory

1st year

15th September 2017 to 18th December 2017 at “Laboratoire de Chimie, Structures, Propriétés de Biomatériaux et d’Agents Thérapeutiques” (CSPBAT), under the supervisor of Dr. Jolanda Spadavecchia

Organized Conferences

- Terza scuola nazionale sui biosensori ottici e biofotonica, December 2017, Naples (Italy)

- Workshop on NanoBioMedicine in Naples: The Next Future of Theranostics, March 2019, Naples (Italy)



Research Article

Rosalba Moretta, Monica Terracciano*, Principia Dardano, Maurizio Casalino, Ilaria Rea, and Luca De Stefano

Covalent grafting of graphene oxide on functionalized macroporous silicon

<https://doi.org/10.1515/oms-2018-0002>

Received Aug 04, 2017; revised Oct 05, 2017; accepted Oct 07, 2017

Abstract: Graphene oxide (GO) is a single-atom-thick and two-dimensional carbon material that has attracted great attention because of its remarkable electronic, mechanical, chemical and thermal properties. GO could be an ideal substrate for the development of label-free optical biosensors, however, its weak photoluminescence (PL) strongly limits the use for this purpose. In this study, we developed a covalent chemical strategy in order to obtain a hybrid GO-macroporous silicon (PSi) structure for biomedical applications. The realized structure was characterized by atomic force microscopy (AFM), scanning electron microscopy (SEM) water contact angle (WCA) measurements, Fourier transform infrared spectroscopy (FTIR) and label-free optical methods based on spectroscopic reflectometry and PL analysis. Investigations showed that the hybrid structure is suitable as a transducer material for biosensing applications due to its peculiar optical properties resulting from the combination of GO and PSi.

Keywords: porous silicon, graphene oxide, surface functionalization, interferometry, photoluminescence

1 Introduction

Graphene oxide (GO) is one-atom-thick planar sheet of sp^2 -bonded carbon atoms, arranged in a hexagonal pattern like a two-dimensional honeycomb lattice [1, 2]. GO

exhibits innovative mechanical, thermal, electrical and optical properties which make this two-dimensional (2D) material attracting and under continuous research [3–5]. It also displays favourable characteristics owing to the heterogeneous chemical and electronic structure; the possibility of being processed in solution and chemically tuned; the hydrophilic nature due to the oxygen containing functional groups (*i.e.*, carboxyl, epoxy and hydroxyl groups) which provide great water dispersibility and biocompatibility. These properties of GO have provided a lot of opportunities for the development of novel biosensing systems [5–11]. Moreover, the discovery of the steady-state photoluminescence (PL) properties of GO, PL emission from 500 to 800 nm reported on exposure to near UV radiation, has opened new perspectives in optoelectronics [12]. Unfortunately, the PL of GO is very weak due oxygen functional groups producing non-radiative recombination as a result of transfer of their electrons to the holes present in sp^2 clusters [13]. A common way to enhance GO light generation is based on reduction or oxidation treatments [14, 15]. A recent approach to increase PL emission from GO is the infiltration of this material into large specific surface area substrates such as porous silicon (PSi) [16]. PSi, obtained by electrochemical partial dissolution of doped crystalline silicon, due to its high specific surface area, optical and electrical properties, tailorable morphology and surface chemistry is one of the most intriguing optical transducer for developing of a wide range of chemical and biological sensors [17, 18]. In our recent papers, we reported the formation of GO-PSi hybrid systems based on electrostatic interaction between GO nanosheets and amino-modified mesoporous silicon. The GO nanosheets were infiltrated by spin-coating into different silanized PSi structures: a homogeneous monolayer and an aperiodic multilayer Thue-Morse formed by 64 layers [19, 20]. Both hybrid structures showed an intense PL signal on a broad range of optical frequencies and enhancement of the PL emitted from GO by several factors with respect to GO deposited on crystalline silicon, without losing sensing abilities. In biosensor development, a covalent bound of functional components onto transducer surfaces is advanta-

*Corresponding Author: **Monica Terracciano:** Institute for Microelectronics and Microsystems, Unit of Naples, Via P. Castellino 111, 80131, Napoli, Italy; Email: monica.terracciano@na.imm.cnr.it

Rosalba Moretta: Institute for Microelectronics and Microsystems, Unit of Naples, Via P. Castellino 111, 80131, Napoli, Italy; Department of Chemical Sciences “Federico II” University of Naples, Via Cynthia, 80126 Naples Italy

Principia Dardano, Maurizio Casalino, Ilaria Rea, Luca De Stefano: Institute for Microelectronics and Microsystems, Unit of Naples, Via P. Castellino 111, 80131, Napoli, Italy

geous, in order to avoid their untimely detachment and device impairment. In this work, GO was covalently immobilized on a PEG-modified macroporous silicon layer via EDC/NHS chemistry. The formation of the hybrid GO-PSi was investigated by atomic force microscopy (AFM), scanning electron microscopy (SEM), water contact angle (WCA) measurements, Fourier transform infrared spectroscopy (FTIR), spectroscopic reflectometry and steady-state photoluminescence (PL). The results highlighted the presence of GO covalently bound to the surface of PSi, suggesting the possibility to use this natural photoluminescent hybrid material as platform for label-free biosensing.

2 Materials and Methods

2.1 Chemicals

Hydrofluoric acid (HF), undecylenic acid (UDA), N-(3-Dimethylaminopropyl)-N'-ethylcarbodiimide hydrochloride (EDC), N-hydroxysuccinimide (NHS), MES hydrate, tert-Butyloxycarbonyl-NH-PEG-Amine (BOC-NH-PEG-NH₂), trifluoroacetic acid (TFA), chloroform, tetrahydrofuran were purchased from Sigma Aldrich (St. Louis, MO, USA). Graphene oxide (GO) nanosheets were purchased from Biotool.com (Houston, TX, USA) as a batch of 2 mg/mL in water with a nominal sheets size included between 50 and 200 nm.

2.2 Porous silicon (PSi) fabrication and hydrosilylation process

Macroporous silicon structure was fabricated by electrochemical etching of n-type crystalline silicon (0.01-0.02 Ω cm resistivity, $\langle 100 \rangle$ oriented and 500 μm thick) in hydrofluoric acid (HF, 5% in weight)/ethanol solution at room temperature (RT). A single layer of PSi with 61% in porosity ($n_{\text{PSi}} = 1.83$ at $\lambda = 1.2 \mu\text{m}$) and thickness L , of 2.1 μm and pore dimensions included between 50 and 250 nm, was obtained applying a current density of 20 mA cm^{-2} for 90 s [21]. Before the etching procedure, the silicon substrate was immersed in HF solution for 2 min to remove the native oxide layer. As-etched PSi device was placed in a Schlenk tube containing deoxygenated neat UDA (99% v/v) and allowed to react at 110°C for 18 h under a stream of argon. Afterwards, the PSi structure was extensively washed in tetrahydrofuran and chloroform so as to remove excess unreacted reagent [22].

2.3 PSi PEGylation and covalent grafting of graphene oxide

The PEGylation of PSi was carried out by immersing the structure in BOC-NH-PEG-NH₂ solution (0.4 M, overnight, at 4°C.) by using EDC/NHS (0.005 M, in MES 0.1 M, 90 min, at RT) [23, 24]. In order to remove excess reagents, the sample was rinsed in MES buffer and deionized water. A solution of TFA (95% v/v, 90 min, at RT) was used to remove the BOC protective group from the second amine portion of PEG molecule, covalently bond to PSi-surface. The excess of TFA was removed by rinsing the sample in deionized water. The GO solution was sonicated for 3 hours and left to decant for 2 days; the supernatant was separated from precipitate and used for the experiment [20]. Finally, GO (1 mg/mL) was covalently conjugated to PEGylated PSi by using EDC/NHS solution (0.005M, in MES 0.1 M, overnight at RT).

2.4 Atomic Force Microscopy

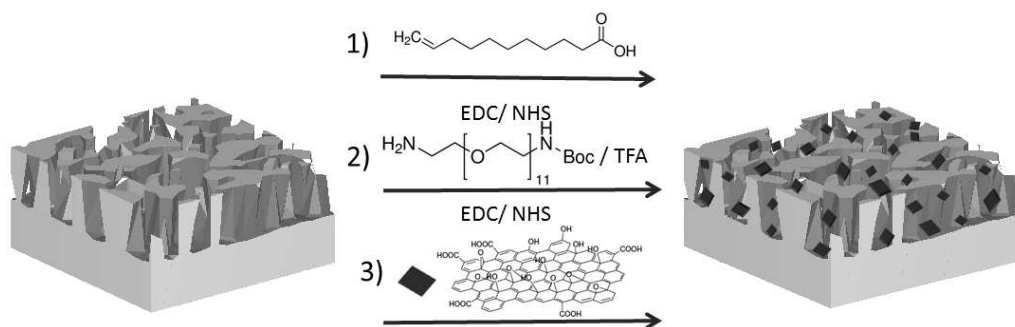
A XE-100 AFM (Park Systems) was used for the imaging of PSi substrate before and after functionalization with GO. Surface imaging was obtained in noncontact mode using silicon/aluminum coated cantilevers (PPP-NCHR 10M; Park Systems) 125 μm long with resonance frequency of 200 to 400 kHz and nominal force constant of 42 N/m. The scan frequency was typically 1 Hz per line.

2.5 Scanning Electron Microscopy

SEM images have been performed at 5kV accelerating voltage and 30 μm wide aperture by a Field Emission Scanning Electron Microscope (Carl Zeiss NTS GmbH 1500 Raith FE-SEM). A InLens detector has been used. A section of the samples has been tilted at 90° in order to perform SEM analysis in lateral view.

2.6 Water contact angle measurements

Sessile drop technique has been used for water contact angle (WCA) measurements on a First Ten Angstroms FTA 1000 C Class coupled with drop shape analysis software. The WCA values reported in this work are the average of at least three measurements on the same sample.



Scheme 1: Schematic representation of the PSi covalent functionalization with GO. Reaction 1, the hydrosilylation process of PSi with undecylenic acid, 18 h @110°C. Reaction 2, the PEGylation of PSi via EDC/NHS (ON @RT) and selective deprotection of -NH-BOC by TFA (90 min @RT). Reaction 3, the GO conjugation of PEGylated PSi via EDC/NHS (ON @RT).

2.7 Fourier Transform Infrared Spectroscopy

The Fourier transform infrared spectra of all samples were obtained using a Nicolet Continuum XL (Thermo Scientific) microscope in the wavenumber region of 4000–650 cm^{-1} with a resolution of 4 cm^{-1} .

2.8 Spectroscopic reflectometry

The reflectivity spectra of PSi sample were measured at normal incidence by means of a Y optical reflection probe (Avantes), connected to a white light source and to an optical spectrum analyzer (Ando, AQ6315B). The spectra were collected over the range 800–1500 nm with a resolution of 5 nm. Reflectivity spectra shown in the work are the average of three measurements.

2.9 Steady-state photoluminescence

Steady-state photoluminescence (PL) spectra were excited by a continuous wave He-Cd laser at 442 nm (KIMMON Laser System). PL was collected at normal incidence to the surface of samples through a fiber, dispersed in a spectrometer (Princeton Instruments, SpectraPro 300i), and detected using a Peltier cooled charge coupled device (CCD) camera (PIXIS 100F). A long pass filter with a nominal cut-on wavelength of 458 nm was used to remove the laser line at monochromator inlet.

3 Results and Discussion

3.1 Realization of GO-PSi structure and morphological surface characterizations

The GO structure is characterized by epoxy and hydroxyl functional groups covalently bonded on either side of a basal plane with carboxyl groups at the edge sites, resulting highly hydrophilic contrary to graphene [25, 26]. Moreover, the carboxyl groups make GO much more attractive than graphene, because they provide handles for the connection of GO sheets to different substrates (e.g., polymer, nanoparticles, DNA, silicon substrates, etc) for the development of functional GO-based materials [27–29]. In order to covalently immobilize GO nanosheets on macroporous silicon, the structure was firstly hydrosilylated by undecylenic acid (Scheme 1, step 1) [22, 30]. PSi suffers from aging phenomena, with a consequent oxidation of the internal surface of the pores and a lowering in the effective refractive index of the structure, which is crucial for a photonic device [31, 32]. A develop of a valid strategy to both stabilize and functionalize PSi support is a key issue for the biosensor realization. The hydrosilylation process is a valid strategy to passivate/functionalize the PSi surface from oxidation and corrosion in aqueous solutions, as described in SI. † The thermal reaction of undecylenic acid with a hydrogen-terminated PSi induced the formation of an organic monolayer covalently attached to the surface through Si-C bonds. The carboxyl group of UDA remained intact and it could be used for a further surface functionalization [33]. In order to improve the hydrophilicity and to promote the GO grafting, the hydrosilylated-PSi (UDA-PSi) was PEGylated by BOC-NH-PEG-NH₂ via EDC/NHS and -NH-BOC deprotected by TFA (Scheme 1, step 2) [24]. Fi-

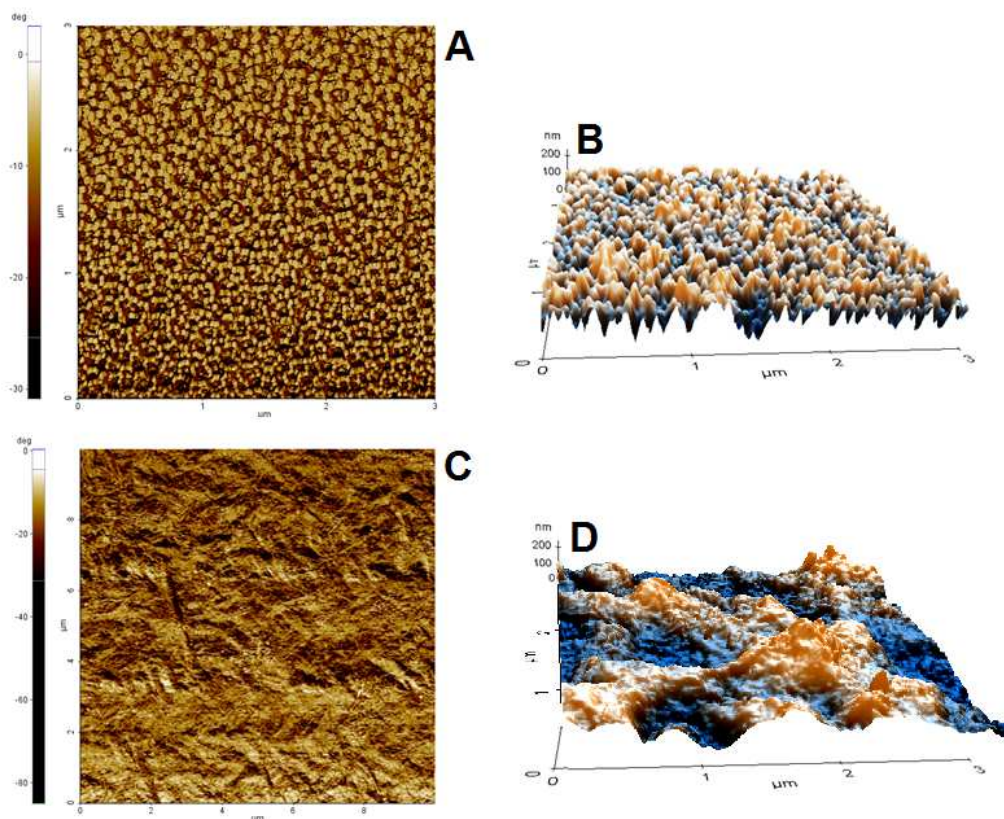


Figure 1: AFM characterization of functionalized PSi before (A: phase; B: three-dimensional rendered) and after (C: phase; D: three-dimensional rendered) GO immobilization.

nally, the GO was covalently immobilized on PEGylated-PSi (NH₂-PEG-NH-PSi) via EDC/NHS. A direct evidence of GO-grafting PSi is the evaluation of PSi morphology by AFM characterization. The AFM images of bare PSi, and GO-modified PSi surfaces are reported in Figure 1. AFM image of PSi reveals a sponge-like structure characterized by hillocks and voids distributed on the whole surface (Figure 1, A; B). After GO grafting (Figure 1, C; D), most voids disappear due to partial pore cloaking by GO nanosheets [34]. The top view SEM images in Figure 2 show the perfect coverage of the PSi substrate (bare PSi in top side) by GO flakes. Moreover, as shows in the lateral view of the tilted section of the GO-PSi compound, GO penetrates into the PSi channels

3.2 Assessment of PSi surface wettability and FTIR analysis

The control of surface wettability plays a key role in the development of hybrid interfaces [35, 36]. The variation of surface wettability after each step of functionalization was evaluated by WCA measurements, as shown in Figure 3. The surface of as-etched PSi was hydrophobic, resulting in the a WCA value of 130 (1)° (Figure 3, A). Undecylenic acid, characterized by a carboxyl terminal-alkyl chain, induced a weak decrease of WCA to 105 (1)° (Figure 3, B). The PEGylation step of UDA-PSi with BOC-NH-PEG-NH₂ induced a further decrease of WCA to 88 (1)° due to the hydrophilicity of PEG chain (Figure 3, C). The removal of the BOC protector group by TFA treatment and the exposure of the amine-group made the PSi surface more hydrophilic with a WCA of 49(1)° (Figure 3, D). Finally, the conjugation of GO to PEG-modified PSi was confirmed by a further decrease

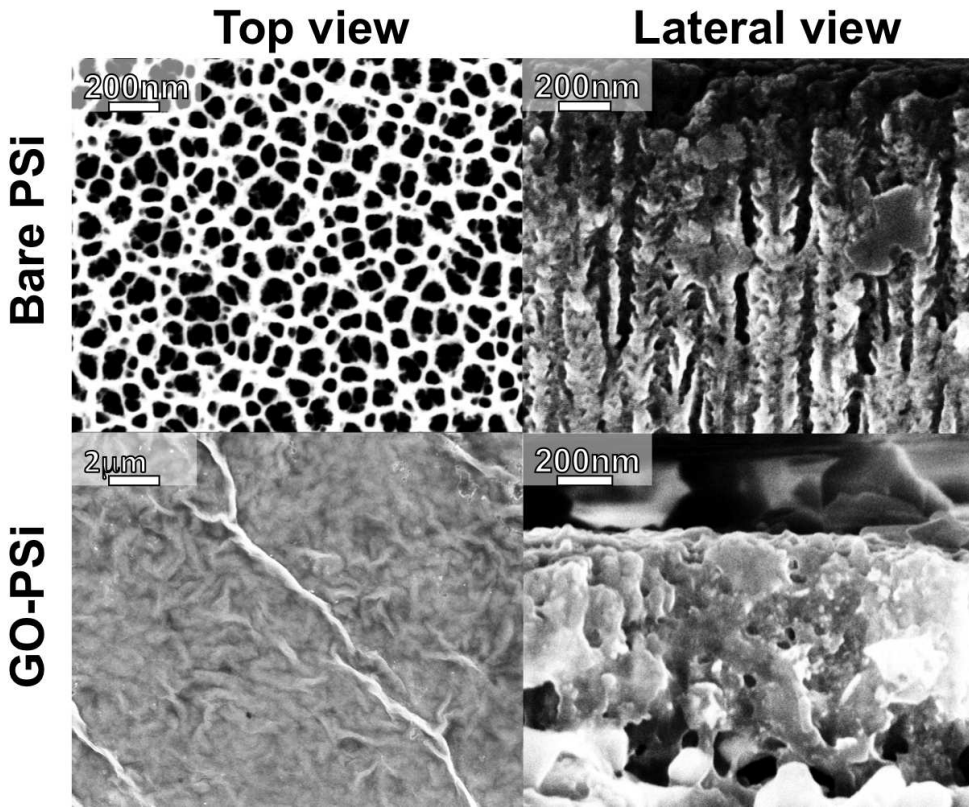


Figure 2: SEM images of bare PSI (upper images) and GO-PSi compound (lower images). Confronting both top and lateral views, the coverage and the penetration of GO into PSI substrate is confirmed by the structural characterization.

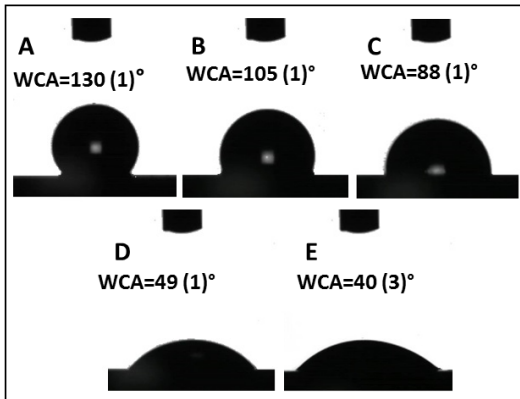


Figure 3: Water contact angle measurements performed on PSI before (A), after hydrosilylation (B), after PEGylation (C), after -NH-BOC deprotection (D) and after GO immobilization (E).

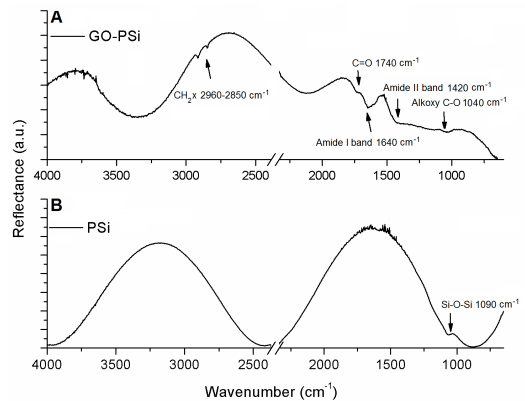


Figure 4: FTIR spectra of PSI structure before (A) and after (B) covalent grafting of GO sheets.

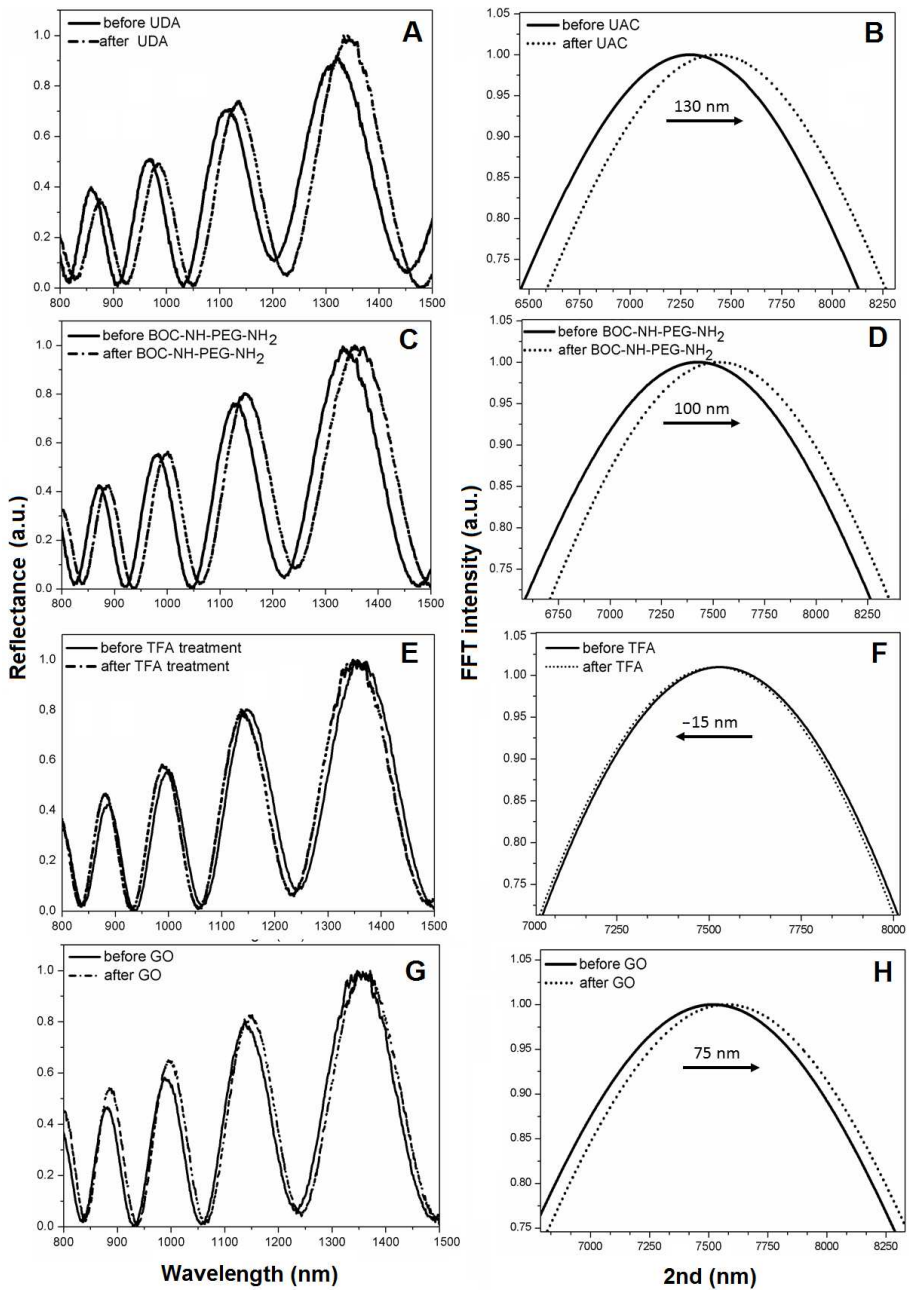


Figure 5: Reflectivity spectra (A) and corresponding Fourier transforms (B) of PSI before (solid line), and after (dashed line) UDA treatment. Reflectivity spectra (C) and corresponding Fourier transforms (D) of UDA-PSi before and after PEGylation with BOC-NH-PEG-NH₂ (dashed line). Reflectivity spectra (E) and corresponding Fourier transforms (F) of PEGylated PSI before (solid line) and after selective deprotection of -NH-BOC by TFA treatment (dashed line). Reflectivity spectra (G) and corresponding Fourier transforms (H) of deprotected PEG-PSi before (solid line) and after GO immobilization (dashed line).

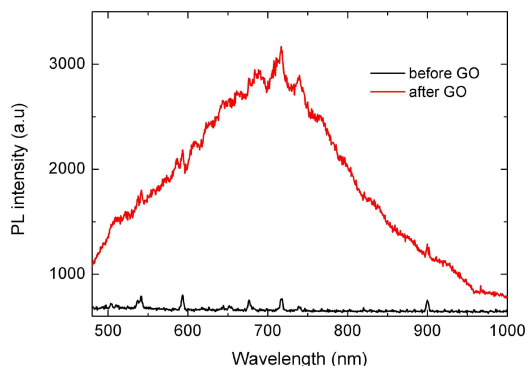


Figure 6: Photoluminescence spectra of macroporous silicon before (black line) and after GO immobilization (red line).

of WCA value to $40 (1)^\circ$ due to the oxygen containing functional groups of GO (Figure 3, E). The covalent grafting of GO on PSi substrate was investigated by FTIR spectroscopy (Figure 4). FTIR spectrum of bare PSi (Figure 4, A) showed a peak of Si–O–Si stretching mode at 1090 cm^{-1} due to spontaneous ageing of PSi during the handling [22]. After the grafting of GO the PSi structure displayed characteristic bands of GO corresponding to the CH_x at $2960\text{--}2850 \text{ cm}^{-1}$ of carbon networks, the C=O carbonyl stretching of –COOH at 1740 cm^{-1} and the alkoxy C–O at 1040 cm^{-1} [37]. Moreover, the GO-PSi spectrum showed peaks at 1640 cm^{-1} and 1420 cm^{-1} of amide band I and II of peptide bond, respectively, confirming the covalent immobilization of GO on PSi (Figure 4, B) [38].

3.3 Characterization of PSi reflectivity and PL spectra

The optical thickness (*i.e.*, OT) of the obtained GO-PSi device was calculated from the reflectivity spectrum by FFT, which displayed a peak whose position along the x-axis corresponded to two times the optical thickness (2OT) of the layer [19]. Normal incidence reflectivity spectra of PSi before and after hydrosilylation with UDA and after the PEGylation are shown in Figure 5 (A; C) together with the corresponding FFTs (Figure 5, B; D). Since the physical thickness d of the PSi layer was fixed, the FFT peak shift of about 130 nm after UDA treatment and 100 nm after the PEGylation, due to an increase of the average refractive index (n) [21]. Figure 5 shows reflectivity spectra (E; G) with corresponding FFTs (F; H) of PEGylated PSi before and after the deprotection of –NH-BOC and after the immobilization of GO. A calculated FFT peak shift of -15 nm after TFA treat-

ment, confirms the removal of BOC protector group from –NH₂. A FFT peak shift of 75 nm after the treatment of PSi with GO, confirms the successful of the GO covalent immobilization on PSi. The presence of GO on the surface of macroporous silicon was also confirmed by PL measurements. Light emission from PSi functionalized with GO nanosheets was investigated at an excitation wavelength of 442 nm. PL spectra of PSi before (black line) and after (red line) GO modification are reported in Figure 6. Any PL signal cannot be detected in the case of bare PSi. Otherwise, after GO immobilization, a strong emission in the range included between 500 and 900 nm with a maximum at about 720 nm was experimentally measured. This PL signal was attributed to the GO nanosheets covalently bond to PSi surface.

4 Conclusions

In summary, in this work we demonstrated the realization of a hybrid GO-PSi device and investigated its properties for application in biosensing. In order to develop a biosensor based on GO-PSi, the PSi structure was passivated by a UDA compound, functionalized by PEG molecules which improved the surface hydrophilicity and provided coupling points to immobilize GO via EDC/NHS chemistry. The device functionalization was confirmed qualitatively and quantitatively by several complementary techniques, such as AFM and SEM microscopy, WCA measurements, FTIR analysis and label-free optical methods based on spectroscopic reflectometry followed by FFT and PL analysis. The GO-PSi hybrid device, obtained by a covalent chemistry approach, can be used as transducer material for a wide range of applications, from biomedical diagnostics and environmental monitoring to food quality control.

References

- [1] Zhu, Y., Murali, S., Cai, W., Li, X., Suk, J. W., Potts, J. R., et al., Graphene and graphene oxide: synthesis, properties, and applications. *Advanced Materials* 22, 2010, 3906–3924.
- [2] Dreyer, D. R., Park, S., Bielawski, C. W., and Ruoff, R. S., The chemistry of graphene oxide. *Chemical Society Reviews* 39, 2010, 228–240.
- [3] Park, S. and Ruoff, R. S., Chemical methods for the production of graphenes. *Nature Nanotechnology* 4, 2009, 217–224.
- [4] Compton, O. C. and Nguyen, S. T., Graphene oxide, highly reduced graphene oxide, and graphene: versatile building blocks for carbon-based materials. *Small* 6, 2010, 711–723.
- [5] Loh, K. P., Bao, Q., Eda, G., and Chhowalla, M., Graphene oxide as a chemically tunable platform for optical applications. *Nature*

- Chemistry 2, 2010, 1015–1024.
- [6] Hunt, A., Dikin, D. A., Kurmaev, E. Z., Boyko, T. D., Bazylewski, P., Chang, G. S., et al., Epoxide speciation and functional group distribution in graphene oxide paper-like materials. *Advanced Functional Materials* 22, 2012, 3950–3957.
- [7] Gao, W., Alemany, L. B., Ci, L., and Ajayan, P. M., New insights into the structure and reduction of graphite oxide. *Nature Chemistry* 1, 2009, 403–408.
- [8] Liu, Y., Dong, X., and Chen, P., Biological and chemical sensors based on graphene materials. *Chemical Society Reviews* 41, 2012, 2283–2307.
- [9] Zhang, Y., Wu, C., Guo, S., and Zhang, J., Interactions of graphene and graphene oxide with proteins and peptides. *Nanotechnology Reviews* 2, 2013, 27–45.
- [10] Wang, Y., Li, Z., Wang, J., Li, J. and Lin, Y., Graphene and graphene oxide: biofunctionalization and applications in biotechnology. *Trends in Biotechnology* 29, 2011, 205–212.
- [11] Chung, C., Kim, Y. K., Shin, D., Ryoo, S. R., Hong, B. H., and Min, D. H., Biomedical applications of graphene and graphene oxide. *Accounts of Chemical Research* 46, 2013, 2211–2224.
- [12] Chien, C. T., Li, S. S., Lai, W. J., Yeh, Y. C., Chen, H. A., Chen, I. S., et al., Tunable photoluminescence from graphene oxide. *Angewandte Chemie International Edition* 51, 2012, 6662–6666.
- [13] Gupta, A., Shaw, B. K., and Saha, S. K., Bright green photoluminescence in aminoazobenzene-functionalized graphene oxide. *The Journal of Physical Chemistry C* 118, 2014, 6972–6979.
- [14] Eda, G., Lin, Y. Y., Mattevi, C., Yamaguchi, H., Chen, H. A., Chen, I. S., Blue photoluminescence from chemically derived graphene oxide. *Advanced Materials* 22, 2010, 505–509.
- [15] Gokus, T., Nair, R. R., Bonetti, A., Lombardo, A., Novoselov, K. S., Geim, A. K., et al., Making Graphene Luminescent by Oxygen Plasma Treatment. *ACS Nano* 3, 2009, 3963–3968.
- [16] Hummers, W. S. and Offeman, R. E., Preparation of graphitic oxide. *Journal of the American Chemical Society* 80, 1958, 1339–1339.
- [17] Canham, L., Properties of porous silicon. *Institution of Electrical Engineers*, 1997.
- [18] Sailor, M. J., Porous silicon in practice: preparation, characterization and applications. *Wiley-VCH*, 2012.
- [19] Rea, I., Sansone, L., Terracciano, M., De Stefano, L., Dardano, P., Giordano, et al., Photoluminescence of graphene oxide infiltrated into mesoporous silicon. *The Journal of Physical Chemistry C* 118, 2014, 27301–27307.
- [20] Rea, I., Casalino, M., Terracciano, M., Sansone, L., Politi, J. and De Stefano, L., Photoluminescence enhancement of graphene oxide emission by infiltration in an aperiodic porous silicon multilayer. *Optics Express* 24, 2016, 24413–24421.
- [21] Terracciano, M., De Stefano, L., Borbone, N., Politi, J., Oliviero, G., Nici, F., et al., Solid phase synthesis of a thrombin binding aptamer on macroporous silica for label free optical quantification of thrombin. *RSC Advances* 6, 2016, 86762–86769.
- [22] Shabir, Q., Webb, K., Nadarassan, D. K., Loni, A., Canham, L. T., Terracciano, M., et al., Quantification and reduction of the residual chemical reactivity of passivated biodegradable porous silicon for drug delivery applications. *Silicon*, 2017, 1–11.
- [23] Sam, S., Touahri, L., Salvador Andresa, J., Allongue, P., Chazalviel, J. N., Gourget-Laemmel, A. C., et al., Semiquantitative study of the EDC/NHS activation of acid aerimal groups at modified porous silicon surfaces. *Langmuir* 26, 2010, 809–814.
- [24] Harris, J. M., *Poly(Ethylene Glycol) Chemistry*. Springer US, 1992.
- [25] Dikin, D. A., Stankovich, S., Zimney, E. J., Piner, R. D., Dommett, G. H. B., Evmenenko, G., et al., Preparation and characterization of graphene oxide paper. *Nature* 448, 2007, 457–460.
- [26] Loh, K. P., Bao, Q., Ang, P. K., and Yang, J., The chemistry of graphene. *Journal of Materials Chemistry* 20, 2010, 2277.
- [27] Kong, L. B., *Carbon nanomaterials based on graphene nanosheets*, CRC Press, 2017.
- [28] Yang, X., Zhang, X., Ma, Y., Huang, Y., Wang, Y., and Chen, Y., Superparamagnetic graphene oxide–Fe₃O₄ nanoparticles hybrid for controlled targeted drug carriers. *Journal of Materials Chemistry* 19, 2009, 2710.
- [29] Lee, S. H., Dreyer, D. R., An, J., Velamakanni, A., Piner, R. D., Park, S., et al., Polymer brushes via controlled, surface-initiated atom transfer radical polymerization (atrp) from graphene oxide. *Macromolecular Rapid Communications* 31, 2010, 281–288.
- [30] Jalkanen, T., Mäkilä, E., Sakka, T., Salonen, J., and Ogata, Y. H., Thermally promoted addition of undecylenic acid on thermally hydrocarbonized porous silicon optical reflectors. *Nanoscale Research Letters* 7, 2012, 311.
- [31] Ghulinyan, M., Gelloz, B., Ohta, T., Pavesi, L., Lockwood, D. J., and Koshida, N., Stabilized porous silicon optical superlattices with controlled surface passivation. *Applied Physics Letters* 93, 2008, 61113.
- [32] De Stefano, L., Oliviero, G., Amato, J., Borbone, N., Piccialli, G., Mayol, L., et al., Aminosilane functionalizations of mesoporous oxidized silicon for oligonucleotide synthesis and detection. *Journal of the Royal Society Interface*, 2013, 10.
- [33] Boukherroub, R., Wojtyk, J. T. C., Wayner, D. D. M., and Lockwood, D. J., Thermal hydrosilylation of undecylenic acid with porous silicon. *Journal of The Electrochemical Society* 59, 2002, 149.
- [34] Terracciano, M., Rea, I., De Stefano, L., Rendina, I., Oliviero, G., Nici, F., et al., Synthesis of mixed-sequence oligonucleotides on mesoporous silicon: chemical strategies and material stability. *Nanoscale Research Letters* 9, 2014, 317.
- [35] Terracciano, M., Galstyan, V., Rea, I., Casalino, M., De Stefano, L., and Sberveglieri, G., Chemical modification of TiO₂ nanotube arrays for label-free optical biosensing applications. *Applied Surface Science* 419, 2017, 235–240.
- [36] Mittal, K. L., *Contact Angle, Wettability and Adhesion*, VSP, 2006.
- [37] Cao, L., Li, Z., Su, K. and Cheng, B., Hydrophilic Graphene preparation from gallic acid modified graphene oxide in magnesium self-propagating high temperature synthesis process. *Scientific reports* 6, 2016.
- [38] Socrates, G., *Infrared and Raman characteristic group frequencies/tables and charts*. Third ed., Wiley, Chichester, 2001.



Article

Functionalized Polymeric Materials with Bio-Derived Antimicrobial Peptides for “Active” Packaging

Bruna Agrillo ¹, Marco Balestrieri ², Marta Gogliettino ², Gianna Palmieri ^{2,*} ,
Rosalba Moretta ³, Yolande T.R. Proroga ⁴, Ilaria Rea ³, Alessandra Cornacchia ⁵ ,
Federico Capuano ⁴ , Giorgio Smaldone ⁶ and Luca De Stefano ³

¹ Materias S.r.l., Corso N. Protopisani, 80146 Napoli, Italy; bruna.agrillo@ibbr.cnr.it

² Institute of Biosciences and BioResources, National Research Council (CNR-IBBR), 80131 Napoli, Italy; marco.balestrieri@ibbr.cnr.it (M.B.); marta.gogliettino@ibbr.cnr.it (M.G.)

³ Institute for Microelectronics and Microsystems, National Research Council (CNR-IMM), 80131 Napoli, Italy; rosalba.moretta@na.imm.cnr.it (R.M.); ilaria.rea@na.imm.cnr.it (I.R.); luca.destefano@na.imm.cnr.it (L.D.S.)

⁴ Department of Food Microbiology, Istituto Zooprofilattico Sperimentale del Mezzogiorno, 80055 Portici, Italy; proroga.yolande@izsmportici.it (Y.T.R.P.); federico.capuano@cert.izsmportici.it (F.C.)

⁵ National Reference Laboratory for *Listeria monocytogenes*, Istituto Zooprofilattico Sperimentale dell’Abruzzo e del Molise, 64100 Teramo, Italy; a.cornacchia@izs.it

⁶ Department of Agricultural Science, University of Naples “Federico II”, 80055 Portici, Italy; giorgio.smaldone@unina.it

* Correspondence: gianna.palmieri@ibbr.cnr.it; Tel.: +39-081-613-2711

Received: 20 December 2018; Accepted: 28 January 2019; Published: 30 January 2019



Abstract: Food packaging is not only a simple protective barrier, but a real “active” component, which is expected to preserve food quality, safety and shelf-life. Therefore, the materials used for packaging production should show peculiar features and properties. Specifically, antimicrobial packaging has recently gained great attention with respect to both social and economic impacts. In this paper, the results obtained by using a polymer material functionalized by a small synthetic peptide as “active” packaging are reported. The surface of Polyethylene Terephthalate (PET), one of the most commonly used plastic materials in food packaging, was plasma-activated and covalently bio-conjugated to a bacteriocin-derivative peptide named 1018K6, previously characterized in terms of antimicrobial and antibiofilm activities. The immobilization of the peptide occurred at a high yield and no release was observed under different environmental conditions. Moreover, preliminary data clearly demonstrated that the “active” packaging was able to significantly reduce the total bacterial count together with yeast and mold spoilage in food-dairy products. Finally, the functionalized-PET polymer showed stronger efficiency in inhibiting biofilm growth, using a *Listeria monocytogenes* strain isolated from food products. The use of these “active” materials would greatly decrease the risk of pathogen development and increase the shelf-life in the food industry, showing a real potential against a panel of microorganisms upon exposure to fresh and stored products, high chemical stability and re-use possibility.

Keywords: active packaging; antimicrobial peptides; food shelf-life; foodborne pathogens; plastic materials

1. Introduction

Today, food preservation, quality maintenance and safety are considered the major growing concerns in the food industry. Food products can undergo different processes of contamination, which lead to loss of colour, texture and nutritive values, allowing the growth of pathogenic microorganisms and deterioration of the quality of the products, making them non-edible. Food contamination can occur

with its exposure to the environment during slaughtering, food processing, packaging, transportation or distribution. In addition, one of the main problems in the food industry is represented by the presence of biofilms, which are considered a serious public health risk. A biofilm is a functional consortium of microorganisms formed principally by exopolysaccharides that can exist on all types of surfaces in food plants ranging from plastic, glass, metal, wood, to food products. For these reasons, biofilms enhance the persistence of several foodborne pathogens on product contact surfaces due to their special structure, and so they are more resistant to antimicrobial agents. Current conventional methods for maintaining food quality and safety over time during drying, freezing, heating or salting have not found to satisfy consumers as recontamination may often occur, rendering the food unpalatable.

Another relevant issue concerning the food industry is the need to feed an ever-increasing global population, which makes it obligatory to reduce the millions of tons of avoidable perishable waste along the food supply chain. In this context, a considerable share of these losses is caused by non-optimal chain processes and management. Shelf-life is defined as the time span under defined storage conditions within which foods remain acceptable for human consumption in terms of safety, nutritional attributes and sensory properties [1]. Unappealing foods and the uncertain safety of food items have been reported as the main causes for discarding food products among consumers and retailers. Indeed, about 15% of perishable foods are actually wasted at retail stores due to damage and spoilage [2]. Consequently, prolonging the shelf-life of food products, ensuring their quality, safety, and integrity, is a crucial aspect to minimize food waste.

All these concerns demand a need for more effective food quality systems for food protection, preservation, and transport to consumers in a wholesome form. Therefore, today, the food industry is more interested in exploring innovative and alternative solutions to presently used methods. In this context, antimicrobial packaging represents a novel strategy to suppress the activities of targeted microorganisms that can contaminate the food products and then strongly affect their shelf-life. One strategy to achieve this goal is to use active materials projected "*ad hoc*" to kill harmful microorganisms or to inhibit their growth on their surface or in the surrounding environments. In this respect, antimicrobial polymers present several advantages because of their high tunability in terms of physico-chemical properties, efficacy, resistance, and prolonged lifetime. However, in spite of the large developments in the preparation and structure-property relationship of this class of antimicrobial polymers, very few of them are practically suitable to solve food-related problems [3]. In this context, plastics are the most commonly used materials for packaging applications because of low-cost, ease of processing and the availability of abundant resources for their production. Indeed, during the last few years, several studies have been focused on the incorporation of antimicrobial peptides (AMPs) into polymeric materials through covalent or physical binding [4,5]. AMPs are essential components of innate immunity [6], contributing to the first line of defence against infections [7,8] and are actually the most promising antimicrobial compounds, mainly because of their broad spectrum of action, high selectivity toward bacterial cells and low risk to promote resistance. The AMP family comprises peptides, which are usually short and amphipathic molecules with a high number of basic residues and a strong tendency to assume prevalently α -helix conformations, which are important to explicate their antimicrobial functions including also antibiofilm activity [9–12]. Amphiphilic AMPs with net positive charge have the capacity to tune their secondary structure upon interacting with the lipid tails inside the membrane, enhancing the membrane rupture activity of these peptides [13]. One of the most studied AMPs, is the innate defence regulator peptide-1018 (IDR-1018), a 12-mer cationic compound (VRLIVAVRIWRR-NH₂), derived from the bovine host-defense peptide (HDP) batenecin, found in the bovine neutrophil granules and belonging to the cathelicidin family [10–12,14,15]. Recently, a new 1018-derivative antimicrobial peptide, named 1018K6, in which the alanine is replaced with a lysine residue (VRLIVKVRIWRR-NH₂), was designed and characterized [16,17]. This single point mutation was revealed to have a strong impact on the conformational status of 1018K6, inducing an increased propensity to assume an α -helix structure in the membrane-mimetic models such as micellar solutions of SDS [16,17]. Furthermore, 1018K6 was revealed to be able to retain its structural integrity better than the cognate IDR-1018 under a wide range of pH and temperature conditions for prolonged

incubation times. In addition, 1018K6 exhibited a significant bactericidal/antibiofilm activity specifically against *L. monocytogenes* isolates from food-products and food-processing environments [16,17].

Actually, wet and dry procedures can be used to link peptides to polymer surfaces [18,19], although it is not trivial to functionalize them with AMPs as they can completely lose their antimicrobial activity, once bound on the surface. Cold plasma is considered an emerging novel technology industrially used for activation of polymer surfaces, which exhibit reactive -COOH^* and -OH^* groups that rapidly interact with the free -NH_2 and -COOH in the peptide sequence. The resulting functionalized surfaces are very stable and can be used in solution under a wide range of pHs and salt conditions [20].

The aim of this study was to develop a new class of packaging materials, functionalized with the bactericidal peptide 1018K6 by cold plasma technology, able to inhibit the biofilm formation of *L. monocytogenes* and to significantly reduce the Aerobic Plate Count (APC) and yeast and mold spoilage of food dairy products.

2. Results and Discussion

2.1. Activation of PET Polymer by 1018K6

Currently, the packaging sector accounts for over 40% of the total worldwide plastic consumption [21,22]. The essential properties for packaging materials are determined by the physical and chemical characteristics of the products, as well as by the external conditions under which the product is stored/transported [21]. As plastics have a wide range of properties which can be tailored according to the specific requirements, they are the most attractive materials for packaging applications.

In this work, polyethylene terephthalate (PET), one of the most common packaging materials accounting for more than 90% of the total volume of plastics used, was functionalized with the already characterized AMP, 1018K6. As the PET surfaces appeared to be hydrophobic, i.e., water contact angle greater than 90° , it was impossible to perform the functionalization by incubating them with the antibacterial peptide 1018K6 in aqueous solutions. Therefore, a possible approach was to pre-activate the PET surfaces by using the radio frequency cold plasma technique and oxygen as gas, which induces the formation of reactive -COOH^* and -OH^* groups [23], allowing the covalent binding with the peptide, as sketched in Figure 1.

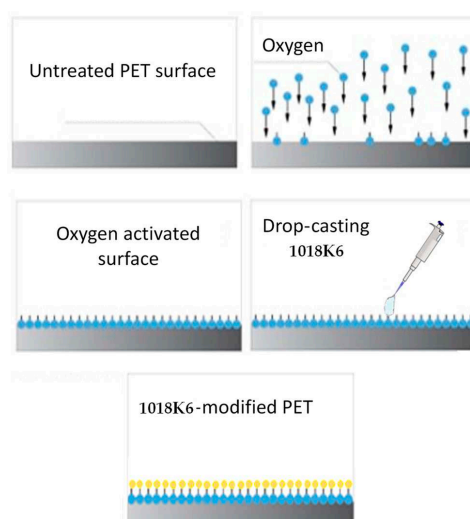


Figure 1. Process diagram for the modification of the PET surface by activation with radiofrequency cold plasma using oxygen as gas and coupling of the synthetic peptide 1018K6 with antibacterial properties.

In this experimental procedure, PET disks were taken directly from the container, used for the preservation of fresh dairy products, specifically buffalo mozzarella cheese, and provided by the customer. To assess quantitatively the PET surface wettability induced by oxygen plasma activation and peptide functionalization, WCA (water contact angle) measurements were carried out on PET samples acquiring the images after 30 sec, before and after treatments (Figure 2).

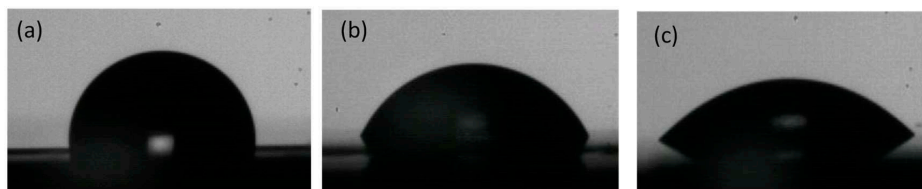


Figure 2. WCA measured on pristine PET (a), oxygen plasma activated-PET (b) and 1018K6-functionalized PET (c). The measurements were performed on five samples in duplicate.

Firstly, the WCA value of the pristine PET disks was equal to $98 \pm 3^\circ$ (Figure 2a). Upon oxygen plasma treatment, the WCA profiles of PET membranes shifted to lower values, indicating that a higher degree of surface hydrophilicity was achieved. Specifically, the change in the surface wettability was quantified, carrying out the measurements at different exposure times (T) and RF powers and varying the concentration and the partial pressure (P) of the oxygen (O_2). The obtained results demonstrated that, already at 50 W and 10 sec of exposure time, the PET surface became less hydrophobic and more hydrophilic ($WCA = 56 \pm 5^\circ$), as shown in Figure 2b. However, no variations were observed in WCA values by changing the oxygen pressure and concentration parameters. On the contrary, it should be noted that when high values of RF power (RF = 300 W) and long exposure times (T = 100–300 sec) were applied, a macroscopic change in the roughness of the PET surface was detectable, indicative of the beginning of a material degradation process. This behaviour suggested that the cold radio frequency plasma treatment was not suitable for PET materials under the aforementioned operating conditions. Generally, the surface of the pristine PET was hydrophobic due to the presence of aliphatic carbonaceous chains. Hence, the plasma treatment induced the formation of extremely reactive radical groups that interrupted the carbon chains and reduced the inborn hydrophobicity of the material, making it more hydrophilic and able to interact strongly with water molecules [24]. Immediately after plasma exposure, the pre-treated PET samples were incubated for a minimum of 8 h in an aqueous solution of 1018K6 peptide, using samples not subjected to radio frequency cold plasma treatment as controls. The PET exposure to the peptide solution favoured the coupling between the peptide chemical groups (typically $-COOH$ and $-NH_2$) and the generated reactive groups ($-COOH^*$, $-OH^*$) on PET, which were not passivated by the atmospheric water. The coupling of the peptide on the polymeric surface resulted in a further modification of the wettability as revealed by the WCA value ($WCA = 36 \pm 2^\circ$), due to the hydrophilic nature of the chemical groups of the amino acid residues along the peptide sequence (Figure 2c). On the other hand, PET control samples not pre-treated by radio frequency cold plasma and incubated for 24 h in aqueous solution containing 1018K6, clearly showed a negligible non-specific adsorption of the peptide on the PET surface.

In order to confirm the 1018K6-PET linkage, the Fourier Transform InfraRed spectroscopy (FTIR) was carried out under inert (N_2) atmosphere. The FTIR spectra of the control samples before radio frequency cold plasma treatment displayed different main peaks corresponding to the C-C, C-H, C-O groups of the polymer and to the $-OH$ groups of the water adsorbed on the polymer surface after the incubations (Figure 3a).

After the plasma treatment, a relevant increase of the $-OH$ group peaks in the FTIR spectra was observed (Figure 3b), consistent with the improvement of the surface wettability quantified by WCA measurements [25,26]. Next, the functionalization of the activated PET samples with 1018K6 was responsible for the appearance, in the FTIR spectra, of the characteristic absorption signals of a peptide,

including the Amide I and Amide II bands (Figure 3c). These bands arise from the peptide bonds that link the amino acids ($\text{O}=\text{C}-\text{NH}$) in the 1018K6 sequence. Specifically, the absorption associated with the Amide I band, which was observed in the $1650\text{--}1560\text{ cm}^{-1}$ interval, produced the stretching vibrations of the $\text{C}=\text{O}$ bond of the amide, whilst the absorption associated with the Amide II band showed in the $1580\text{--}1490\text{ cm}^{-1}$ interval, led primarily to bending vibrations of the $\text{N}-\text{H}$ bond (Figure 3c). Therefore, the FTIR analyses validated the successful bio-conjugation of 1018K6 peptide on the plasma-activated PET surface, in complete agreement with WCA characterization.

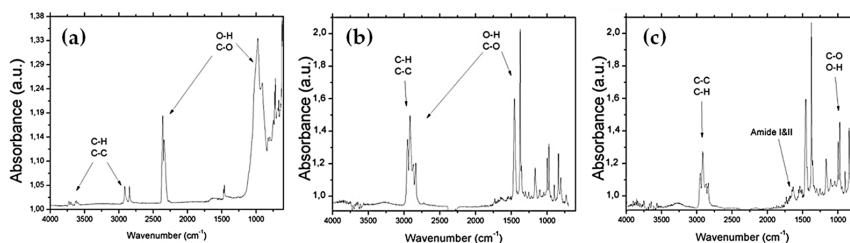


Figure 3. FTIR spectrum of the PET sample before radiofrequency cold plasma treatment (a); after plasma treatment (b); after 1018K6 bio-conjugation (c).

2.2. Immobilization Yield and Leakage of 1018K6 from PET Polymer

One of the most important factors in fabricating antimicrobial packaging is to immobilize on a polymeric surface the functional compounds without losing their activity. Therefore, to keep them active, it is necessary to immobilize the peptides in a way that preserves their folded structural integrity. Firstly, to obtain stable and active packaging, it is crucial to regulate the peptide surface concentration which depends on the binding strategy used, as it can strongly affect the efficiency of peptide immobilization. Therefore, the immobilization yield of different 1018K6 concentrations on the PET surface after the coupling reaction was indirectly estimated by Reverse-Phase High-Performance Liquid Chromatography (RP-HPLC). In this experiment, once the conjugation reaction was completed, the supernatant solutions were recovered after 24 h incubation and analysed by RP-HPLC, evaluating the peak area of the peptide not bound to the polymeric surface. Consequently, by knowing the initial peptide concentration, the quantity of the peptide attached to the PET surface was indirectly determined by comparing the peak area. The data obtained from these analyses showed that the coupling reaction yield varied from 50% using a starting peptide concentration of $25\text{ }\mu\text{M}$, to 25% per $100\text{ }\mu\text{M}$. The representative chromatograms obtained for 1018K6 $50\text{ }\mu\text{M}$ initial concentration, and used to calculate the immobilization yield, are reported in Figure 4. The coupling yields were validated by a six-point calibration curve, which was constructed utilizing known 1018K6 concentrations, and the number of peptide molecules capable of binding to the polymeric surface was determined via interpolation (Figure 4 insert). Based on the yield data, the surface coverage on the polymer was found to be approximately $6.4\text{ nmol}/\text{cm}^2$ per $25\text{ }\mu\text{M}$ peptide concentration, $9.3\text{ nmol}/\text{cm}^2$ per $50\text{ }\mu\text{M}$ and $8.3\text{ nmol}/\text{cm}^2$ per $100\text{ }\mu\text{M}$, thus demonstrating that the surface coverage was clearly concentration-dependent (Figure 5).

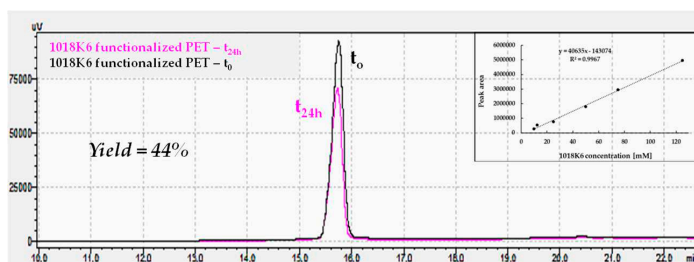


Figure 4. Immobilization yield (%) of 1018K6 on PET surface determined by reverse-phase HPLC chromatography on a C18 column after the coupling reaction (24 h). Pre-activated PET surfaces by plasma were incubated for 24 h with 1018K6 (50 μ M) in PBS pH 7.0. The solutions recovered after incubation were further analysed. The peptide solution placed in contact with the pre-activated surface at time 0 ($t = 0$) was used as control. The chromatograms are representative of three independent experiments. **Insert:** Calibration curve of the C18 column obtained using different 1018K6 concentrations.

The Holliday model was used to assess the peptide concentration effects on the coverage density and to estimate the concentration value producing the best immobilization yield [27]. As shown in the dose-response experiments (Figure 5), the most suitable coupling condition to improve the immobilization yield was obtained with a peptide concentration of 71 μ M, but 50 μ M was selected to perform the further experiments as this value represents a better compromise between the functionalization yield and the peptide costs.

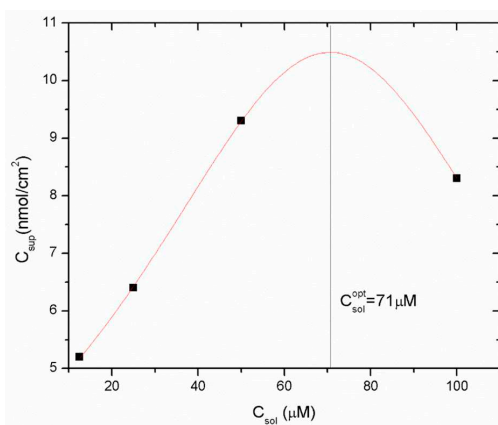


Figure 5. Immobilization yield expressed as nmol of bound 1018K6 per cm^2 of PET surface as function of peptide concentration. The dose-response curve has been built by using the Holliday model. Data are expressed as means \pm standard deviations. Standard deviation values lower than 5% are not shown.

The production process of antimicrobial active packaging, which is able to guarantee the quality, the safety and prolong the shelf-life of food products, requires an efficient immobilization procedure that permits a stable conjugation of AMP on the polymers, avoiding the release of the immobilized active compound after contact with foods or liquids. Fresh dairy products, such as mozzarella cheese, an Italian traditional cheese packaged in saline brine, are ready-to-eat foods having a very short shelf-life of about 3 or 4 days, because they are easily contaminated by undesirable microorganisms.

In this context, the release of 1018K6 from the functionalized PET into mozzarella cheese brine during 24 h of incubation at 4 $^{\circ}$ C was analysed by RP-HPLC, using the free 1018K6 as control. As shown in Figure 6a, no peptide-release process occurred from the functionalized polymeric support. The same

results were obtained after 24 h incubation in pure water at 4 °C (Figure 6b) and at 25 °C suggesting that the peptide was stably coupled on the polymer. In addition, no leakage of 1018K6 was detectable even after prolonged incubations (until to 72 h) under all the conditions explored. The high stability of the peptide-PET bond is important because in this way the peptide-PET system does not require the related EFSA (European Food Safety Authority) standards.

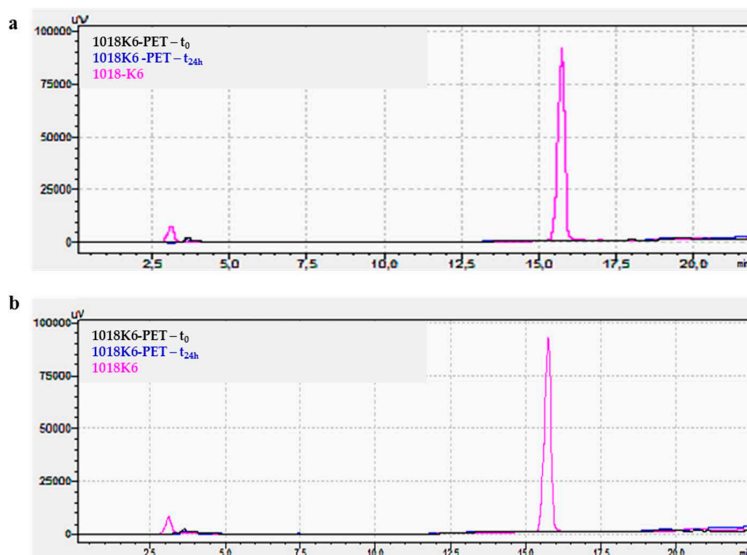


Figure 6. Release analysis of 1018K6 from functionalized PET performed by reverse-phase HPLC chromatography on a C18 column after 24 h incubation at 4 °C in mozzarella brine (a) or pure water (b). After incubation, the solutions were recovered and injected on C18. The solution in contact with 1018K6-PET at time 0 ($t = 0$) and 1018K6 peptide (50 μM) were used as controls.

However, as far as the cytotoxicity of the free 1018K6, preliminary tests clearly indicated that the peptide is not toxic against different fibroblast cell lines at the concentrations used in the bactericidal assays [16], thus suggesting that there is no potential risk for human health associated with the use of 1018K6 in the food industry.

2.3. Effect of 1018K6 Functionalized PETs on Mozzarella Cheese

Microbial contamination, causing approximately one-fourth of the world's food supply loss, has become an enormous economic and ethical problem worldwide [28]. Specifically, fresh dairy products stored in packaging, such as mozzarella cheese, are characterized by reduced shelf-life, which diminishes their commercial value because they are an excellent growth medium for a wide range of troublesome spoilage microorganisms including aerobic mesophiles, yeasts and molds [29].

Hence, it is very important and advantageous for the food industry to extend the shelf-life of mozzarella cheese, which is a good source of protein, vitamins and minerals, and to spread the distribution of this traditional product beyond the market borders.

In this context, the efficacy of 1018K6 functionalized PETs in preventing the growth of spoilage microorganisms in mozzarella was analysed at a preliminary shorter storage time. In a first set of experiments, with the aim to set up the optimal experimental conditions minimizing peptide consumption, PET disks of 3 cm diameter (surface of 7 cm²) were functionalized with 1018K6 and incubated with 3 ml of the conditioning brine in the presence of small slices of mozzarella (about 10 g of weight) in Petri dishes. Sliced mozzarella in the presence of brine with non-modified PETs disks was used as controls. As shown in Table 1, the Aerobic Plate Count (APC), and the yeast and mold

counts of the samples exposed to 1018K6-PETs significantly decreased during the storage period (24 h) compared to the control samples. In a second set of experiments, a scale up of the previous procedure was applied in order to evaluate the effectiveness of 1018K6-PETs in slowing down the growth of the spoilage microorganisms under the storage conditions. Specifically, the effects of 1018K6-PET disks (10 cm diameter, 78 cm²) were studied directly in the package as distributed on the market, which contained two balls of fresh mozzarella (about 25 g each) and 30 mL brine. Control samples were prepared in an identical way, using non-modified PET disks. Results demonstrated that, in one day of storage, mozzarella packaged in the presence of 1018K6-PETs had the lowest bacterial counts with respect to that incubated in conditioning brine with non-modified PETs, in which microbes were able to proliferate (Table 1). In addition, a significant reduction in yeasts and molds count was also observed in the samples with the modified PETs during the storage. Therefore, the projected 1018K6 active packaging could have potential applications in the food market, aiming to ensure and increase the quality and safety of the food products by preventing the growth of spoilage and/or pathogenic microorganisms and promoting a shelf-life extension.

Table 1. Effects of 1018K6-PETs treatment on mozzarella cheese.

Disk Diameter	Microorganisms	PET Disk in Brine + Mozzarella Cheese	1018K6-PET Disk in Brine + Mozzarella Cheese	Inhibition of Growth (% Value)
3 cm	APC	311 ± 29 CFU/mL	11 ± 2 CFU/mL	97%
	Yeasts and Molds	700 ± 75 CFU/mL	280 ± 25 CFU/mL	60%
10 cm	APC	173 ± 21 CFU/mL	44 ± 7 CFU/mL	75%
	Yeasts and Molds	406 ± 37 CFU/mL	137 ± 23 CFU/mL	67%

Further studies will be necessary in order to assess the ability of 1018K6-PETs to affect the APC and the total yeast and mold at prolonged storage times.

2.4. Inhibition of *Listeria* Biofilm Formation

Cross-contamination of pathogenic and spoilage microorganisms from food contact surfaces remains a significant challenge in the safety, quality and security of food supply chain. Indeed, some pathogenic and food spoilage bacteria can form biofilms, which represent one of the main sources of food contamination and foodborne disease outbreaks. To address this challenge, there is an unmet need to develop novel antimicrobial materials able to inhibit and treat biofilms in the food processing industry. Specifically, the use of natural preservatives to inhibit growth of serious pathogens such as *L. monocytogenes* is of great interest as it is considered an important worldwide public health problem [30]. *L. monocytogenes* is one of the most dangerous human food pathogens that causes listeriosis. Foods considered as high-risk sources of listeriosis include meat and dairy products, which are ready-to-eat, require refrigeration and are stored for extended time periods. *Listeria* can persist within food processing environments, due to its ability to grow at wide-ranging temperatures and pH and to form biofilms [31,32].

In this context, the ability of 1018K6-PETs to prevent biofilm formation was assessed against an *L. monocytogenes* strain isolated from dairy products, by the crystal violet staining method [17]. As shown in Figure 7, the biofilm formation on 1018K6-PETs was significantly reduced (75%), compared to the control sample (non-functionalized PETs), indicating a strong anti-adhesion capability of the 1018K6-tethered surfaces against *L. monocytogenes*.

Therefore, packaging films containing 1018K6 peptide can pose a potential solution to reduce spoilage.

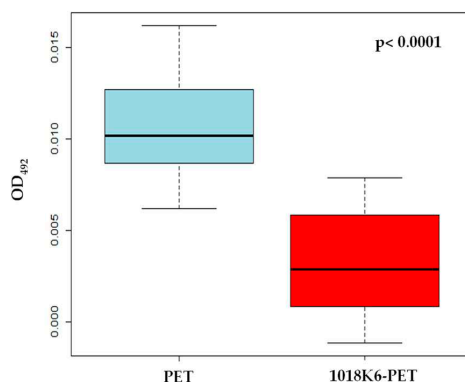


Figure 7. Boxplot of the inhibition activity of the biofilm production of *Listeria monocytogenes* by PET and 1018K6-PET. Average OD measurements of crystal violet-stained biofilms are shown with error bars representing the standard deviation.

3. Materials and Methods

3.1. Plasma Treatment

Plasma treatment was performed using a Reactive Ion Etching (RIE) model PLASMA Plus 80 machine (Oxford Instruments, Abingdon, Oxfordshire, UK). The following process parameters were changed: exposure time [T] (10-20-30-50-100-300 sec); molecular oxygen concentration [O₂] (10-50-100 sccm); partial gas pressure [P] (0.1–0.5 atm); power of radio frequency generator [RF] (50-100-300 W).

3.2. Water Contact Angle Measurements

The sessile drop technique was used for water contact angle (WCA) measurements on a First Ten Angstroms FTA 1000 C Class coupled with drop shape analysis software under static conditions. A 10- μ L drop was deposited on the sample surface, and the image was recorded after 30 sec. Results of WCA are expressed as mean \pm standard deviation (s.d.) of at least three measurements on the same sample in three independent experiments (i.e., at least nine measurements for each result).

3.3. Fourier Transform Infrared Spectroscopy

The Fourier transform infrared spectra of all samples were obtained using a Nicolet Continuum XL (Thermo Scientific, Waltham, MA, USA) microscope in the wavenumber region of 4000–650 cm^{-1} with a resolution of 4 cm^{-1} . The FITR measurements were performed using a micro-ATR (Attenuated Total Reflection) module under inert (N₂) atmosphere.

3.4. Peptide Bio-conjugation

Polymer samples treated by cold plasma were incubated in aqueous solution of 1018K6 (50 μ M) in PBS (10 mM), pH 7.0, for 24 h at 25 °C. After incubation, the solutions containing the peptide not bound to the polymer were removed and the functionalized PETs were extensively washed in water and DMSO in order to completely eliminate traces of unbound peptide before performing surface characterization by WCA, FTIR and the release experiments. The PET containers used in all the analyses were kindly provided by the dairy “Mini Caseificio Costanzo s.r.l.” located in Lusciano (Caserta, Italy).

3.5. Functionalization Yield Analysis of Polymers

Functionalization yield analysis of 1018K6-modified PETs was performed by using a reverse-phase high-performance liquid chromatography (RP-HPLC) system (Waldbronn, Germany). Once functionalization was completed, the supernatant solutions were recovered after 24 h and analyzed to calculate the amount of the peptide not attached to the polymeric surfaces. For the analyses, 200 μ L of the samples were injected over a μ Bondapak C18 reverse-phase column (3.9 mm \times 300 mm, Waters Corp., Milford, MA, USA) connected to a HPLC system (Shimadzu, Milan, Italy) using a linear gradient of 0.1% TFA in acetonitrile from 5 to 95%. A reference solution was prepared with the initial peptide concentration used for the functionalization under the same reaction conditions and run in parallel. Therefore, by knowing the added peptide (reference solution), the amount of peptide not bound to the polymers (expressed as a percentage) was determined by comparing the peak area. A calibration curve of the C18 column using different 1018K6 concentrations was built. All measurements were performed in triplicate in three different preparations.

3.6. Release Test

The release of 1018K6 from the functionalized polymers was examined by the reverse-phase high-performance liquid chromatography (RP-HPLC) system using a μ Bondapak C18 column (3.9 \times 300 mm, Waters) and a linear gradient of 5–95% acetonitrile in 0.1% TFA, at a flow rate of 1 mL/min. A volume of 1 mL of pure water or mozzarella cheese brine was poured onto the functionalized polymers, incubated for 24 h at 4 $^{\circ}$ C and then loaded onto the RP column. The solutions in contact with the functionalized polymers at time $t = 0$ were used as control samples and were run in parallel. The same experiments were conducted in the presence of the non-functionalized polymers. All measurements were performed in triplicate on three different preparations.

3.7. Shelf-life Testing on Mozzarella Cheese

The 1018K6-functionalized PETs were cut into disks of 3 cm diameter (surface of 7 cm²) and immersed in 3 mL mozzarella cheese brine in 5-cm Petri dishes that contained small slices of mozzarella (about 10 g of weight), which were directly placed on the activated PET disks. Non-functionalized PETs were used as a control. The samples were incubated for 24 h at 25 $^{\circ}$ C. Therefore, the mozzarella cheese brine was plated on PCA plates to quantify the APC (Aerobic Plate Count), which was performed according to ISO 4833-1 procedure. Specifically, 1 mL of cheese brine was diluted in 9 mL diluent (0.1% peptone and 0.8% sodium chloride, biomerieux- France), and scalar dilutions of sample up to 10⁻⁵ were set up. Then, 1 mL of brine and 1 mL of each subsequent dilution were seeded by inclusion in PCA plates (Plate Count Agar-Biolife-Italy) which were incubated at 30 \pm 1 $^{\circ}$ C for 72 h. Plates with no more than 300 colonies were considered for the colony count. The presence of yeasts and molds was tested, according to ISO 21527-1, analyzing 1 mL of cheese brine, diluted in 9 mL diluent (0.1% peptone and 0.8% sodium chloride, biomerieux- France) and performing scalar dilutions up to 10⁻⁵. Then, 0.1 mL of each dilution was seeded on Dichloran Rose Bengal Chloramphenicol Agar plates (DRBC - Italian Biolife), which were incubated at 25 \pm 1 $^{\circ}$ C for 5 days for the colony count. Plates with no more than 150 colonies were considered. The same analyses were performed using 1018K6-PET disks of 10 cm diameter (78 cm²), immersed in the package containing two balls of fresh mozzarella (about 25 g each) and 30 mL brine. The samples were incubated for 24 h at 25 $^{\circ}$ C. The analyses were performed in triplicate on three different preparations, and the data were expressed as means \pm s.d.

3.8. Anti-adhesion Activity Assay

L. monocytogenes cultures, isolated from dairy products, were prepared to inoculate BHI broth (Brain Heart Infusion, Sigma-Aldrich, St. Louis, Missouri, USA) at 37 $^{\circ}$ C up to a logarithmic phase of growth. After the incubation, 10 ml of bacterial suspension at a concentration of 5 \times 10⁶ in growth broths was centrifuged, and the cell pellet was washed in PBS pH 7.3 (Thermo Fisher Scientific Inc.,

Waltham, MA, USA) and diluted in BHI broth to reach the useful concentration to obtain biofilm formation. The assays were conducted using PET disks as the food contact surface. PETs were placed into 12-well tissue culture plates (Falcon, Thermo Fisher Scientific Inc., Waltham, MA, USA), with a flat bottom and lid. After washing in sterile ultrapure water, the PETs were incubated in ethanol ($\geq 99.8\%$) for 10 min under gentle shaking and were then washed in sterile ultrapure water, dried and packaged. In each experiment set, 600 μL of the standardized inoculum in the presence of 1018K6- PETs or non-functionalized PETs was added to 12-well tissue culture plates. BHI broth was used as negative control, and the plates were incubated at 37 °C for 72 h under the static condition. Cell counting of *L. monocytogenes*, in agreement with the ISO 11290-2:98 (ISO 11290-2: 1998/ Amd 1, 2004) method, was performed to assess the concentration and purity of the standardized inoculum. After incubation, PETs were washed three times with PBS pH 7.3 and placed in a new plate to dry. At the end of the fixing phase, 1 mL of 0.2% Crystal Violet (Panreac Quimica SAU, Barcelona, Spain) in 95% ethanol was added to each well to stain the PETs. After gentle shaking for 15 min, the PETs were washed three times with sterile water and were then transferred into a new plate to dry at 37 °C. The quantitative analysis of biofilm production was performed by adding 1 mL of 33% acetic acid to destain the PETs, and 200 μL of each solution was transferred to a microtiter plate to measure the level (OD492) of the crystal violet. Anti-adhesion assay was performed in triplicate on three independent sets of experiments. OD492 values were compared through non-parametric analysis of variance (Kruskal-Wallis test), followed by multiple comparisons using Dunn test pairs (with Bonferroni correction) ($p < 0.05$). Statistical analyses were performed using Microsoft®Excel 2000/XLSTAT©-Pro.

4. Conclusions

Adding new functionalities to food packaging is a key issue in the production of the next generation of active materials. In this context, polymers represent good candidates as their production, use and disposal/recovery are well established at very low costs. Among the main useful packaging materials, PET is one of the most widely employed worldwide in the food industry.

The results of this study demonstrated that PET material can be efficiently and quickly pre-activated by the cold oxygen plasma technique, which represents an industrial scalable technology, in order to promote the functionalization with 1018K6, a peptide showing potent antibacterial and anti-adhesion properties, and to obtain antimicrobial packaging. 1018K6-PETs were tested under real conditions, using samples of mozzarella cheese, and it was found that APC, yeast and mold counts of the samples stored in the presence of modified polymers were strongly reduced during the first 24 h, thus demonstrating the 1018K6 was still active and preserved its antimicrobial abilities upon polymer surface immobilization. Moreover, 1018K6-PET was very effective against the formation of *Listeria* biofilms, a non-trivial result since not all antimicrobial agents are able to combat bacterial biofilms.

This work represents a preliminary study, which provides a starting point to develop a new PET-based system, functionalized with a biologically-derived AMP, which can have potential as antimicrobial packaging, providing an innovative and breakthrough technology in food applications, due to its comparable cost, small peptide dimension, effective antimicrobial activity, polymer characteristics and environmental friendliness. However, further investigations will be required to establish whether the projected antimicrobial-polymers may find industrial uses and whether they will be effective to improve the safety and extend the shelf-life of food products.

5. Patents

International Patent, Application No: PCT/EP2018/069304 Publication Date: 16/07/2018. Antimicrobial peptides. BALESTRIERI Marco, PALMIERI Gianna, CAPUANO Federico, DE STEFANO Luca et al.

Author Contributions: Conceptualization, M.B., G.P., M.G. and L.D.S.; methodology, B.A., A.C., Y.T.R.P., R.M.; validation, Y.T.R.P., R.M. and A.C.; investigation, B.A., A.C., Y.T.R.P. and R.M.; resources, G.P. and F.C.; data

curation, L.D.S. and M.G.; writing—original draft preparation, M.B., G.P., M.G., I.R. and L.D.S.; writing—review and editing, M.B., G.P., M.G., I.R. and L.D.S.; supervision, G.P., M.G. and L.D.S.; cytotoxicity tests, G.S.

Funding: This research was funded by the “Packaging innovativi a base di pEptidi antimicrobici per la Sicurezza Alimentare” (PERSIA) project, grant number POR FESR CAMPANIA 2014/2020 n. B63D18000530007 and the “Sviluppo di metodologie innovative per ridurre il rischio di malattie trasmesse da alimenti in prodotti della filiera ittica” Ricerca Corrente 2016 project, grant number IZS ME 01/16 RC.

Acknowledgments: The authors gratefully acknowledge the dairy “Mini Caseificio Costanzo s.r.l.” located in Lusciano (Caserta, Italy) that provided the PET containers necessary for the reported analyses.

Conflicts of Interest: The authors declare no conflict of interest.

References

- Corradini, M.G. Shelf life of food products: From open labeling to real-time measurements. *Annu. Rev. Food Sci. Technol.* **2018**, *9*, 251–269. [[CrossRef](#)] [[PubMed](#)]
- Ferguson, M.; Katzenberg, M.E. Information sharing to improve retail product freshness of perishables. *Prod. Oper. Manag.* **2006**, *15*, 57–73.
- Munoz-Bonilla, A.; Fernandez-Garcia, M. Polymeric materials with antimicrobial activity. *Prog. Polym. Sci.* **2012**, *37*, 281–339. [[CrossRef](#)]
- Sobczak, M.; Dębek, C.; Olędzka, E.; Kozłowski, R. Polymeric systems of antimicrobial peptides—Strategies and potential applications. *Molecules* **2013**, *18*, 14122–14137. [[CrossRef](#)] [[PubMed](#)]
- Irkin, R.; Esmer, O.K. Novel food packaging systems with natural antimicrobial agents. *J. Food Sci. Technol.* **2015**, *52*, 6095–6111. [[CrossRef](#)]
- De Smet, K.; Contreras, R. Human antimicrobial peptides: Defensins, cathelicidins and histatins. *Biotechnol. Lett.* **2005**, *27*, 1337–1347. [[CrossRef](#)]
- Bals, R. Epithelial antimicrobial peptides in host defense against infection. *Respir. Res.* **2000**, *1*, 141–150. [[CrossRef](#)]
- Henzler Wildman, K.A.; Lee, D.K.; Ramamoorthy, A. Mechanism of lipid bilayer disruption by the human antimicrobial peptide, LL-37. *Biochemistry* **2003**, *42*, 6545–6558. [[CrossRef](#)]
- Amer, L.S.; Bishop, B.M.; van Hoek, M.L. Antimicrobial and antibiofilm activity of cathelicidins and short, synthetic peptides against *Francisella*. *Biochem. Biophys. Res. Commun.* **2010**, *396*, 246–251. [[CrossRef](#)]
- De la Fuente-Núñez, C.; Korolik, V.; Bains, M.; Nguyen, U.; Breidenstein, E.B.; Horsman, S.; Lewenza, S.; Burrows, L.; Hancock, R.E. Inhibition of bacterial biofilm formation and swarming motility by a small synthetic cationic peptide. *Antimicrob. Agents Chemother.* **2012**, *56*, 2696–2704. [[CrossRef](#)]
- De la Fuente-Núñez, C.; Reffuveille, F.; Haney, E.F.; Straus, S.K.; Hancock, R.E. Broad-spectrum anti-biofilm peptide that targets a cellular stress response. *PLoS Pathog.* **2014**, *10*, e1004152. [[CrossRef](#)] [[PubMed](#)]
- Overhage, J.; Campisano, A.; Bains, M.; Torfs, E.C.; Rehm, B.H.; Hancock, R.E. Human host defense peptide LL-37 prevents bacterial biofilm formation. *Infect. Immun.* **2008**, *76*, 4176–4182. [[CrossRef](#)] [[PubMed](#)]
- Wang, G.; Li, X.; Wang, Z. APD3: The antimicrobial peptide database as a tool for research and education. *Nucleic Acids Res.* **2016**, *44*, D1087–D1093. [[CrossRef](#)] [[PubMed](#)]
- Pompilio, A.; Scocchi, M.; Pomponio, S.; Guida, F.; Di Primio, A.; Fiscarelli, E.; Gennaro, R.; Di Bonaventura, G. Antibacterial and anti-biofilm effects of cathelicidin peptides against pathogens isolated from cystic fibrosis patients. *Peptides* **2011**, *32*, 1807–1814. [[CrossRef](#)] [[PubMed](#)]
- Reffuveille, F.; de la Fuente-Núñez, C.; Mansour, S.; Hancock, R.E.W. A broad spectrum anti-biofilm peptide enhances antibiotic action against bacterial biofilms. *Antimicrob. Agents Chemother.* **2014**, *58*, 5363–5371. [[CrossRef](#)] [[PubMed](#)]
- Palmieri, G.; Balestrieri, M.; Capuano, F.; Proroga, Y.T.R.; Pomilio, F.; Centorame, P.; Riccio, A.; Marrone, R.; Anastasio, A. Bactericidal and antibiofilm activity of bactenecin-derivative peptides against the food-pathogen *Listeria monocytogenes*: New perspectives for food processing industry. *Int. J. Food. Microbiol.* **2018**, *279*, 33–42. [[CrossRef](#)]
- Palmieri, G.; Balestrieri, M.; Proroga, Y.T.R.; Falcigno, L.; Facchiano, A.; Riccio, A.; Capuano, F.; Marrone, R.; Neglia, G.; Anastasio, A. New antimicrobial peptides against foodborne pathogens: From in silico design to experimental evidence. *Food Chem.* **2016**, *211*, 546–554. [[CrossRef](#)]

18. Holmberg, K.V.; Abdolhosseini, M.; Li, Y.; Chen, X.; Gorr, S.-U.; Aparicio, C. Bio-inspired stable antimicrobial peptide coatings for dental applications. *Acta Biomater.* **2013**, *9*, 8224–8231. [[CrossRef](#)]
19. Hamley, I.W. PEG–Peptide Conjugates. *Biomacromolecules* **2014**, *15*, 1543–1559. [[CrossRef](#)]
20. Jordá-Vilaplana, A.; Fombuena, V.; García-García, D.; Samper, M.D.; Sánchez-Nácher, L. Surface modification of polylactic acid (PLA) by air atmospheric plasma treatment. *Eur. Polym. J.* **2014**, *58*, 23–33. [[CrossRef](#)]
21. Silvestre, C.; Duraccio, D.; Cimmino, S. Food packaging based on polymer nanomaterials. *Prog. Polym. Sci.* **2011**, *36*, 1766–1782. [[CrossRef](#)]
22. Alavi, S.; Thomas, S.; Sandeep, K.P.; Kalarikkal, N.; Varghese, J.; Yaragalla, S. *Polymers for Packaging Applications*, 1st ed.; CRC Press: Boca Raton, FL, USA, 2014; 486p.
23. Pankaj, S.K.; Bueno-Ferrer, C.; Misra, N.N.; Milosavljevic, V.; O'Donnell, C.P.; Bourke, P.; Keener, K.M.; Cullen, P.J. Applications of cold plasma technology in food packaging. *Trends Food Sci. Technol.* **2014**, *35*, 5–17. [[CrossRef](#)]
24. De Stefano, L.; Rotiroli, L.; De Tommasi, E.; Rea, I.; Rendina, I.; Canciello, M.; Maglio, G.; Palumbo, R. Hybrid polymer-porous silicon photonic crystals for optical sensing. *J. App. Phys.* **2009**, *106*, 023109. [[CrossRef](#)]
25. Socrates, G. *Infrared and Raman Characteristic Group Frequencies*, 3rd ed.; John Wiley & Sons Ltd.: New York, NY, USA, 1994.
26. De Stefano, L.; Oliviero, G.; Amato, J.; Borbone, N.; Piccialli, G.; Mayol, L.; Rendina, I.; Terracciano, M.; Rea, I. Aminosilane functionalizations of mesoporous oxidized silicon for oligonucleotide synthesis and detection. *J. R. Soc. Interface* **2013**, *10*, 20130160. [[CrossRef](#)] [[PubMed](#)]
27. Holliday, R. Plant population and crop yield. *Nature* **1960**, *186*, 22–24. [[CrossRef](#)]
28. Huis in't Veld, J.H.J. Microbial and biochemical spoilage of foods: An overview. *Int. J. Food Microbiol.* **1998**, *33*, 1–18. [[CrossRef](#)]
29. Losito, F.; Arienzo, A.; Bottini, G.; Priolisi, F.R.; Mari, A.; Antonini, G. Microbiological safety and quality of Mozzarella cheese assessed by the microbiological survey method. *J. Dairy Sci.* **2014**, *97*, 46–55. [[CrossRef](#)] [[PubMed](#)]
30. Bondi, M.; Lauková, A.; de Niederhausern, S.; Messi, P.; Papadopoulou, C. Natural Preservatives to Improve Food Quality and Safety. *J. Food Qual.* **2017**, *2017*. [[CrossRef](#)]
31. Beresford, M.R.; Andrew, P.W.; Shama, G. *Listeria monocytogenes* adheres to many materials found in food-processing environments. *J. Appl. Microbiol.* **2001**, *90*, 1000–1005. [[CrossRef](#)]
32. Wong, A.C.L. Biofilms in Food Processing Environments. *J. Dairy Sci.* **1998**, *81*, 2765–2770. [[CrossRef](#)]



© 2019 by the authors. Licensee MDPI, Basel, Switzerland. This article is an open access article distributed under the terms and conditions of the Creative Commons Attribution (CC BY) license (<http://creativecommons.org/licenses/by/4.0/>).

Review

Porous Silicon-Based Aptasensors: The Next Generation of Label-Free Devices for Health Monitoring

Monica Terracciano ^{1,*}, Ilaria Rea ¹, Nicola Borbone ², Rosalba Moretta ^{1,3},
Giorgia Oliviero ⁴, Gennaro Piccialli ² and Luca De Stefano ^{1,*}

¹ Institute for Microelectronics and Microsystems, Via P. Castellino 111, 80131 Naples, Italy; ilaria.rea@na.imm.cnr.it (I.R.); rosalba.moretta@na.imm.cnr.it (R.M.)

² Department of Pharmacy, University of Naples Federico II, Via Domenico Montesano 49, 80131 Naples, Italy; nicola.borbone@unina.it (N.B.); piccialli@unina.it (G.P.)

³ Department of Chemical Sciences, University of Naples Federico II, Via Cynthia, 80126 Naples, Italy

⁴ Department of Molecular Medicine and Medical Biotechnologies, University of Naples Federico II, Via S. Pansini 5, 80131 Naples, Italy; golivier@unina.it

* Correspondence: monica.terracciano@na.imm.cnr.it (M.T.); luca.destefano@na.imm.cnr.it (L.D.S.); Tel.: +39-081-6132490 (M.T.); +39-081-6132375 (L.D.S.)

Academic Editor: Derek J. McPhee

Received: 29 April 2019; Accepted: 12 June 2019; Published: 13 June 2019



Abstract: Aptamers are artificial nucleic acid ligands identified and obtained from combinatorial libraries of synthetic nucleic acids through the *in vitro* process SELEX (systematic evolution of ligands by exponential enrichment). Aptamers are able to bind an ample range of non-nucleic acid targets with great specificity and affinity. Devices based on aptamers as bio-recognition elements open up a new generation of biosensors called aptasensors. This review focuses on some recent achievements in the design of advanced label-free optical aptasensors using porous silicon (PSi) as a transducer surface for the detection of pathogenic microorganisms and diagnostic molecules with high sensitivity, reliability and low limit of detection (LoD).

Keywords: aptasensor; porous silicon; surface modification; aptamer; optical label free-sensing

1. Introduction

Biosensors are analytical hybrid devices comprising a bio-receptor (also called bioprobe) immobilized on a transducer surface which is able to selectively recognize a molecular target [1,2]. The most commonly employed bioprobes in biosensors development are enzymes, proteins, and antibodies (Abs), which suffer from various drawbacks, thus limiting their specific applications [3,4]. The enzyme isolation procedure and consequent incorporation in *in vitro* operating environments could result in a loss of their activity [5]. The Abs are produced by the immune system in response to exposure to antigens, i.e., spores, bacterial toxins, and other foreign substrates. Since Abs are difficult to graft with a proper orientation, i.e., keeping their natural tridimensional structure, sometimes they are less effective in antigen recognition [6]. Nowadays, new biomolecular recognition elements which are able to overcome the Ab and enzyme constraints associated with standard bioprobes are in growing demand in molecular sensing. In this context, aptamers are considered as to have the greatest potential among the recognition tools which have developed in recent years. Aptamers are a class of single-stranded RNA or DNA oligonucleotides which are able to fold into specific three-dimensional (3D) structures, generated using the Systematic Evolution of Ligands by EXponential Enrichment (SELEX) technique [7]. This process, relying on DNA or RNA libraries, is able to automatically synthesize a large variety of nucleic acid sequences with great selectivity for non-nucleic acid molecules.

Aptamers are able to interact with their targets through structural recognition similar to that of the antibody-antigen reaction with a dissociation constant in the range of pico- to nano-molar. For these reasons, aptamers are usually referred as chemical Abs [8]. Moreover, an appealing characteristic of aptamers, as opposed to Abs, is their efficacy against small molecules where antibodies fail [9]. Different from Abs, the chemical nature of nucleic acids makes them easy to synthesize and engineer, and thereby, to obtain aptamers with extended bioavailability, regulating ability, and multi-functional properties [10,11]. Aptamers are thermally stable; even after denaturation temperature, they are able to refold into their 3D formations once at room temperature, in contrast to protein-based Abs, which totally lose their activity at high temperatures. The targets of aptamers range from small molecules to proteins, virus-infected cells, stem cells, and cancer cells. The chemical properties and biological activity of aptamers have made them attractive for use in biomedical applications ranging from bioassays to targeted therapy [12]. Moreover, aptamer technology has shown great potential for bioengineering of nanostructured devices. Aptamers used as bioprobes for the development of biosensors have heralded a new generation of biosensors called aptasensors [13]. A variety of aptasensors have been developed based on fluorescence, electrochemiluminescence, surface plasmon resonance (SPR) and surface-enhanced Raman scattering (SERS) [14–16]. Label-free optical aptasensors can be designed using porous silicon (PSi)-based devices. PSi is a nanostructured material which is widely used as a transducer surface in biosensing. Its sponge-like morphology, characterized by a specific surface area of about $500 \text{ m}^2 \text{ cm}^{-3}$, ensures active and rapid interaction with the species to be detected [17]. Additional advantages of PSi are compatibility with semiconductor processing and largely tunable pore size (nanometers to microns), which makes possible the infiltration of appropriate-sized target molecules while excluding larger-sized, non-specific ones [18]. The result of PSi optical transducer response to binding of inorganic/organic matter on pore walls is a change of its average refractive index [19]. A PSi layer acts optically as a Fabry-Perot interferometer: the substitution of air in the pores enhances the average refractive index, resulting in a change in the reflectivity spectrum [20]. The analysis of the optical spectra by fast Fourier transform (FFT) could be used as a simple method to assess variations in the refractive index [21]. This review presents recent progress in the development of label-free PSi optical aptasensors for biomedical applications. Different PSi functionalization strategies for the development of such devices for the detection of molecules of diagnostic interest (i.e., insulin, bacteria, human thrombin) are described. In particular, the improvement of device performance in terms of sensitivity, response time and limit of detection (LoD) will be discussed.

2. Porous Silicon Optical Devices for Label-Free Biosensing

Over the past two decades, great interest has shown by many researchers in the improvement of label-free biosensors. Most standard biosensors need a label attached to the target, and their detection and quantification is assumed to correspond to the number of bound targets [22]. Labels are easily detectable entities, such as fluorophores, magnetic beads, active enzymes. However, the labeling procedure requires sample handling that can drastically change its biomolecule binding properties, as well as the target-label coupling reaction yield. In label-free biosensors, no label is required for the sensing. This technology is based on the direct measurement of a signal (optical, electrical or mechanical) which is generated by the interaction between the bioprobe and the analyte on the transducer surface [23–25]. Sensitive, fast, robust, low cost, label-free biosensors are highly desirable for a broad range of applications including medical disease monitoring, controlled release of drugs, and food security [26–28]. PSi has received remarkable interest as a transducer surface for the construction of low-cost, sensitive and biocompatible optical label-free biosensors [2]. This is mainly due to its intriguing physicochemical properties which makes possible the design of compact biosensors with high performance [29]. Moreover, PSi transducers can be optimized (pore size, pore depth, and porosity) to suit specific applications by controlling the etching parameters [30,31]. Label-free PSi optical biosensors, using interferometric reflectance spectroscopy (IRS), have demonstrated outstanding performance in terms of the rapid and reliable detection of several analytes [32]. IRS technique is

based on a very simple set up: an incident white light is reflected on the two interfaces (air-PSi and PSi-bulk Si) of the porous material, producing a Fabry-Perot interference fringe pattern, depending on the optical thickness (physical thickness L times the refractive index (n) of the porous material) [33,34]. The fringe pattern is described by Equation (1);

$$m\lambda = 2nL \quad (1)$$

where λ is the maximum wavelength of two consecutive fringes with an order of magnitude m , L is the thickness of the porous layer and $2nL$ is the effective optical thickness (EOT). The EOT can be determined by applying FFT to the observed interference fringe pattern; this parameter is usually used to measure the sensor response. When an analyte is captured by the bioprobe-modified PSi, a redshift of the fringe pattern is observed. This phenomenon is due to the substitution of air within the pores with the analyte—which has a higher refractive index—resulting in an increase in the EOT value [35]. Thus, the interferometric reflectance spectroscopy enables the simple detection of analytes by monitoring changes of EOT over time.

Porous Silicon Fabrication and Surface Modification Strategies

The peculiar morphological, physical, and chemical properties of PSi make it one of the most explored nanostructured materials, as evidenced by the great number of papers about its features, and the prevalence of devices based on this material [36–40]. One reason for its success is the easy fabrication process based on a computer-controlled electrochemical etching procedure and a simple power supply. The PSi structure is obtained by electrochemical dissolution of doped crystalline silicon wafers in a hydrofluoric acid (HF) -based solution. Modulating parameters such as current density, type and concentration of crystalline silicon dopant, and the composition of electrolyte solution makes it possible to obtain porous structures with specific morphological and optical properties [31,39]. The silicon hydride (Si-H) terminated pore walls of as-etched PSi are prone to oxidation and dissolution under ambient conditions, such as atmospheric oxygen, water, and aqueous solutions [41]. The oxidation of PSi causes a significant change in the refractive index of the material ($n = 3.5$ for silicon, $n = 1.4$ for silicon dioxide), interfering with transduction signal of PSi optical biosensors. Moreover, dissolution in aqueous buffers leads to even greater changes in the refractive index ($n = 3.5$ for silicon, $n = 1.33$ for water), with a loss of signal due to PSi structural collapse [42]. The PSi surface should be properly stabilized for biosensing applications. A common method to prevent PSi from degradation is to intentionally grow an oxide layer on the surface via thermal oxidation, which reduces or completely removes the Si-H from the entire skeleton, substituting it for SiO₂, which isotropically grows also in the pores [43]. To provide greater stability and protection against dissolution, the oxidized surface could be chemically modified with alkyl silanes. The two most popular silane coupling agents are 3-aminopropyl-triethoxysilane (APTES) and 3-aminopropyl-dimethyl-ethoxysilane (APDMES), both of which are able to form a dense monolayer on the PSi surface through Si–O–Si covalent bonds that limit the access of water to the underlying surface [44]. The hydrosilylation is an alternative surface-chemistry process involving the grafting of alkenes (or alkynes) to the hydride-terminated PSi surface, resulting in the formation of a monolayer of alkyl chains which is covalently attached to the surface through Si–C, showing much greater resistance to attack by nucleophiles such as water or hydroxide [41,45,46]. This reacting mechanism can be promoted by heat, light, Lewis acid catalysts in an inert atmosphere and completely deoxygenated/dried reagents, thus avoiding the formation of silicon oxides during the monolayer formation [47]. The grafting of alkyl silanes and alkanes/alkynes on PSi makes the surface chemically stable in aqueous solution, thereby avoiding surface oxidation or chemical degradation. Moreover, these passivation methods are valid strategies to functionalize the surface with reactive groups (–NH₂, –COOH, –SH, and –CHO) for the subsequent conjugation of biomolecules (i.e., enzymes, proteins, Abs, peptides, DNA, aptamer). Additional methods used for PSi surface stabilization can be found in ref. [48]. From a sensing point of

view, passivation/functionalization methods avoid the zero-point drift without altering the intrinsic sensitivity of the devices.

PSi biosensors are usually prepared by immobilizing the bioprobe on the transducer surface, once it has been synthesized by an ex situ procedure. However, there is also an innovative procedure for the preparation of biosensors based on the direct growth of the bioprobe (i.e., by in situ synthesis) on PSi used as support in so-called solid phase synthesis [49,50].

3. Label-Free Porous Silicon Aptasensor for Human Diseases Diagnosis

Aptamers are an emerging class of single-stranded oligonucleotides which is generated using SELEX technology [8,51]. By folding them into well-defined secondary or tertiary structures, aptamers are able to specifically bind their target molecules with high affinity, and so are classified as powerful ligands for diagnostic and therapeutic applications [52]. They present significant advantages over conventional bioprobes (e.g., Abs), such as relatively low-molecular-weight and high stability, great affinity due to the remarkable low dissociation constants (K_d) aptamer/target ranging from picomolar to nanomolar levels, and great selectivity thanks to their ability to recognize even minor structural differences between targets and their analogs. To date, aptamer-based biosensors have been successfully used for the detection of a large number of analytes of interest due to the highly selective interactions between the aptamer and the target, and the high amplification thanks to the optical, electrical or magnetic properties of the various sensing platforms. These novel integrations highlight the potential of aptamers as emerging tools for the fabrication of new sensing devices for the selective and sensitive detection of a wide range of targets, promising great advances in healthcare applications.

3.1. Aptamer-Decorated Porous Silicon Biosensor for Rapid Detection of Bacteria

Rapid detection and identification of bacterial contaminations in blood are a major challenge in today's medical practice [53]. A bacterial contamination can occur in every environment, causing a specific disease in a variety of ways; even today, microbial diseases are a major cause of death in many countries [54]. The detection and identification of bacterial contaminations is still based on traditional microbiological techniques, which typically require several days to obtain results, making 'real-time' assessments unfeasible. Over the past decade, great efforts have been directed toward the development of new bioassays and biosensors for the rapid detection of pathogenic bacteria [55]. Various biosensors for fast bacteria detection have been reported; among them, the most popular are optical biosensors. These biosensors offer several advantages, including selectivity, speed, sensitivity, and reproducibility of measurements. Recently, Prof. E. Segal and co-workers at Technion, Haifa, Israel [56], described the design of an optical aptamer-based PSi biosensor for the direct capture of *Lactobacillus acidophilus*, employing the Hemag1P aptamer as a capture probe. The Hemag1P aptamer is 78-nucleotide-long sequence selected by the SELEX technique against the *L. acidophilus* membrane, i.e., a strain of bacteria which is important for the functional food and pharmaceutical industry. This aptamer is able to target the S-proteins which are abundantly present on the bacteria membrane. The first step in the Hemag1P-PSi aptasensor preparation was the anodization process of a Si wafer (300 mA cm^{-2} , 30 s) and its thermal oxidation, thus obtaining oxidized PSi (PSiO₂). The PSiO₂ is decorated with the aptamer through the three-step biofunctionalization route, as illustrated in Figure 1. The PSiO₂ is first silanized with 3-mercaptopropyl-trimethoxysilane (MPTMS) and then reacted with acrydite-modified Hemag1P aptamer via a thioether bond. The final functionalization step is the blocking of residual thiol groups of the aptamer with maleimide, in order to reduce non-specific reactions with the buffers. The success of aptamer immobilization on the PSi surface was confirmed using attenuated total reflectance Fourier transform infrared (ATR-FTIR) spectroscopy and Ellman colorimetric assay for thiol-groups. The biosensing mechanism of the Hemag1P-aptasensor was based on monitoring changes in the intensity of fast Fourier transformation (FFT) peaks, obtained from the raw PSi reflectivity spectra during exposure to bacteria suspensions. The Hemag1P-modified PSiO₂ biosensor was exposed to *L. acidophilus* suspensions while the reflectivity spectra changes of the device

were monitored in real time (Figure 2). Firstly, the initial intensity baseline was established by exposing the aptasensor to the aptamer selection buffer solution (SB). Then, the biosensor was incubated with the bacteria solution (10^7 cells per mL in SB) for 20 min, allowing bacteria/aptasensor interactions to occur. Consequent washing of the biosensor with SB was performed to remove unbound bacteria, after which the intensity increased and stabilized at a net intensity decrease value of 5.5%. Several replications of this biosensing experiment have demonstrated similar behavior to that represented in Figure 2, and a highly reproducible net intensity decrease value of 5.5% (0.07%), confirming the ability of the biosensor to detect 10^6 cells per mL of *L. acidophilus*.

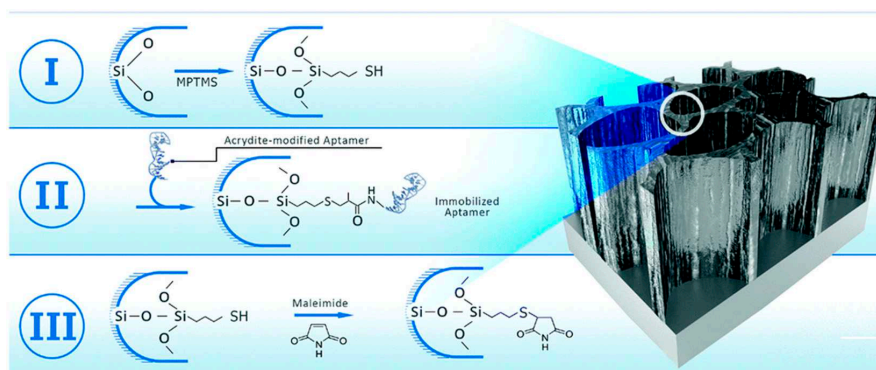


Figure 1. Three-step biofunctionalization process for aptamers immobilization onto PSiO₂ device. (I) Silanization with MPTMS via a thioether bond, (II) reaction with acrydite-modified Hemag1P aptamer via a thioether bond and (III) blocking of residual thiol groups with maleimide. Reproduced with permission from [56].

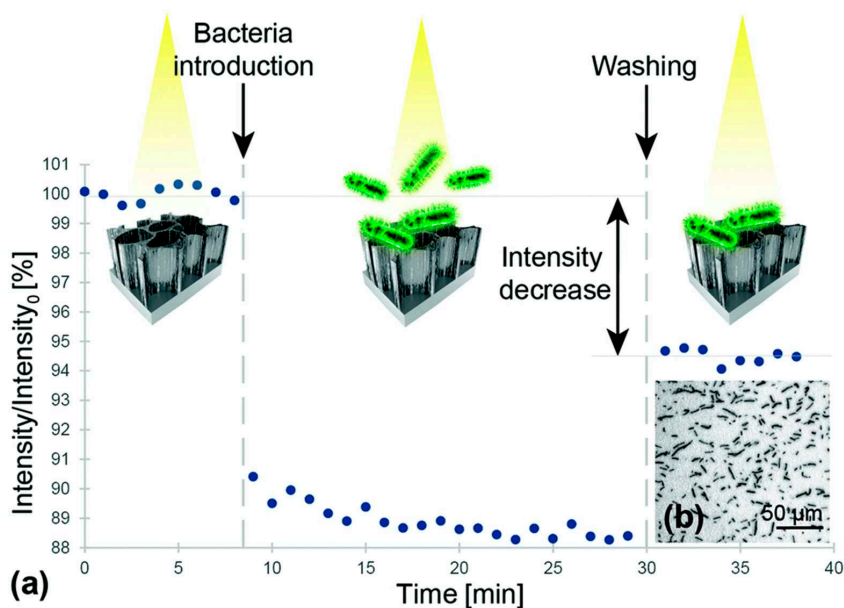


Figure 2. (a) Relative intensity change of the Hemag1P-modified PSiO₂ device upon exposure to *L. acidophilus* bacterial suspensions (10^7 cells per mL). (b) Microscope image taken after the biosensing experiment depicts *L. acidophilus* cells captured onto the aptamer-modified PSiO₂ device. Reproduced with permission from [56].

Staphylococcus aureus is a major cause of bacteremia and infections in humans, as well as food-borne diseases [57]. *S. aureus* treatment is especially challenging due to the bacteria's ability to rapidly adapt and develop resistance to antibiotics; thus, a fast and reliable means of detection of such bacteria is crucial for the effective control of infection. Protein A (PA, 45 kDa), secreted by and displayed on the cell membrane of *S. aureus*, is considered a significant biomarker for this bacteria. K. Urman et al. [58] developed a label-free optical PSi aptasensor for the specific detection of PA. Protein A-targeting aptamers (PAA) are conjugated to APTES-modified PSiO₂ thin films by standard carbodiimide-coupling chemistry [59,60]. PSiO₂ surface modification and aptamer-conjugation were confirmed by ATR-FTIR analyses. The PAA-PSiO₂ biosensor was exposed to PA solutions at different concentrations, and the biosensor response, evaluated as effective optical thickness (EOT) changes, showed a relative EOT increment with increasing PA concentration. The results demonstrated a specific detection and quantification of PA in a range of 2–50 μM , with a binding affinity towards PA of 13.98 μM and LoD of 3.17 μM . Due to the affinity between PA and the antibody, IgG was introduced in a sandwich-assay format to enhance the sensitivity of the biosensor by three fold. In Figure 3, the exposure of a PAA-biosensor to either PA or IgG (as control) gave insignificant signals, i.e., below the critical value ($3 \times \sigma = 0.205$) calculated for the LoD. The values obtained by the sandwich assay were six times higher (1.2 ± 0.3 as $\Delta\text{EOT}/\text{EOT}_0 \times 10^3$), resulting in a PA LoD value of 1 μM . This work demonstrated a proof-of-concept scheme for increasing three-fold the sensitivity of PAA-functionalized PSi biosensors by taking advantage of PA and IgG affinity.

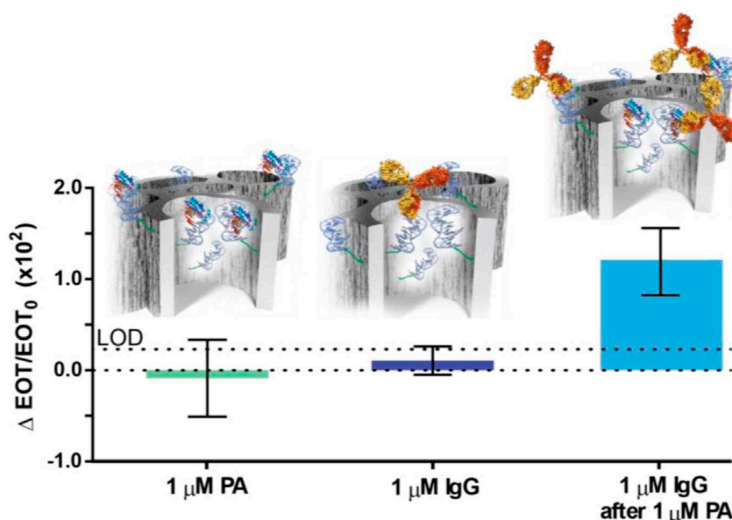


Figure 3. Sensitivity enhancement of the PAA-functionalized PSiO₂ biosensor. Averaged optical response (relative EOT) of the biosensor upon exposure to 1 M of: PA, IgG or both in a successive manner. Schematic illustration of biomolecules captured by the aptamers within the porous scaffold. Upper dashed line indicates the LoD value. Differences between both single exposures (of PA or IgG) and the sandwich assay are statistically significant ($p < 0.05$, $n \geq 3$). Reproduced with permission from [58].

3.2. Porous Silicon Aptasensor for Detection of Insulin

Diabetes mellitus is a worldwide health problem, and severe complications associated with this disease are causes of death [61]. Diabetes mellitus is a pathological state resulting from an absolute or relative deficiency of insulin in the body. Insulin is a hormone synthesized by the β cells of the pancreatic Islets of Langerhans. The carrier glucose transporter (type 4) is able to bind with insulin, allowing glucose entry to the heart, muscles, and brain cells. When the regulatory

mechanisms fail, a hyperglycemia occurs; blood glucose concentrations increase to over 7.0 millimoles per liter, and random glucose concentrations increase to over 11.1 millimoles per liter [62]. Long-term hyperglycemia may be the cause of several life-threatening complications such as cardiovascular diseases, diabetic nephropathy, neuropathy, and retinopathy. The monitoring of glucose blood levels is the first step in diagnoses of diabetes mellitus, whereby a rapid and accurate diagnosis method is necessary for the prevention of lethal complications. Standard diagnostic techniques (e.g., enzyme-linked immunosorbent assay (ELISA), radioimmunoassay (RIA), chromatography) are typically laborious, expensive, time-consuming and require sophisticated laboratory equipment. Recently, Prof. N.H. Voelker and co-workers at Monash Institute, Melbourne, Australia [63], developed two different label-free P*Si*-based optical biosensors for the detection of insulin secreted by human pancreatic islets: an antibody-modified P*Si* (Ab-modified) and an aptamer-modified P*Si* (Ap-modified). Freshly etched P*Si* single layer structures were exposed to a thermal hydrosilylation reaction with undecylenic acid, followed by reaction with carbodiimide chemistry (EDC/NHS), the immobilization of the Ab (150 kDa) or the aptamer (9.7 kDa) and, finally, (d) quenching of active NHS ester with bis-PEG-amine (BPA). Both of the prepared P*Si* devices (i.e., Ab-modified- and Ap-modified-P*Si*) were tested as optical biosensors for the detection of insulin under the same conditions in a Krebs Ringer buffer (a solution used for glucose-stimulated insulin secretion clinical assay). The devices were exposed to Krebs buffer for 20 min to establish a baseline, and no significant change in Δ EOT value was observed. The exposure of the P*Si* devices to insulin (50 μ g/mL) solution for 60 min increased Δ EOT, and finally, rinsing with Krebs buffer for 20 min was carried out. The results showed that Ap-modified P*Si* outperformed Ab-modified P*Si* devices in terms of insulin detection time and sensitivity: 19 nm EOT shift in 12 min compared to 16 nm EOT shift in 60 min. The rapid response of Ap-modified P*Si* is associated with the exclusive conformation change of the aptamer during insulin binding, highlighting the potential benefit of using aptamers rather than Abs as bioprobes in biosensor development. Ap-modified P*Si* was tested as a biosensor in a real sample detection of insulin secreted by human donor islets. Human islets (40,000 IEQ) were stimulated with 20 mM glucose for 2 h in Krebs buffer, after which the cells were centrifuged and the insulin-containing supernatant was used for the sensing experiment, following the previously-described protocol. The exposure of the Ap-biosensor to insulin (20 mM) in Krebs solution showed a gradual increase in Δ EOT with a maximum shift of \sim 17 nm over 80 min (Figure 4). After the washing step with Krebs buffer, no significant change in Δ EOT was observed. Applying the maximum Δ EOT shift to the calibration curve obtained for the Ap-modified surface, a concentration of 15.4 μ g/mL was obtained. In addition, no significant changes to Δ EOT were observed on the control surface, except for a small blue shift as a result of a slight degradation of P*Si* in the aqueous medium. For comparison, the ELISA technique was used to determine the level of insulin in the real sample, showing a result of 16.9 ± 0.2 μ g/mL, which is in agreement with the result of the Ap-P*Si* biosensor. These results demonstrated, for the first time, the great capability of the Ap-modified P*Si* surface to detect insulin secreted by human islets from a donor upon stimulation with glucose.

Recently, N.H. Voelker and co-workers [64] demonstrated the optimization of P*Si* fabrication for the development of optical insulin biosensors with high sensing performance in terms of response time and LoD. P*Si* rugate filter (P*Si*RF) were modified by thermal hydrosilylation and conjugated to an insulin binding aptamer (IBA) at different concentrations (1, 10, 20, 50 and 70 μ M) via carbodiimide chemistry. The different prepared surfaces were tested for insulin detection (50 μ g/mL) using IRS in order to verify the effect of IBA concentration on biosensing device performance. Insulin biosensing was carried out on each prepared P*Si* device with 20 min PBS baseline, 30 min 50 μ g/mL insulin flow, and 30 min PBS washing. Generally, a high bioprobe density is preferred in biosensor development in order to guarantee the highest target binding capacity. In this specific case, the obtained result showed the opposite trend, i.e., the surface obtained with a low aptamer concentration (1 μ M) performed better compared to the surface prepared using the highest aptamer concentration (70 μ M) (Figure 5).

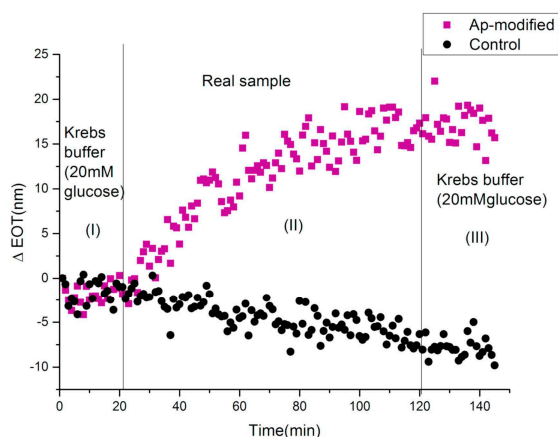


Figure 4. Sensorgram for the detection of insulin secreted by human islets upon stimulation with 20 mM glucose for 2 h in Krebs buffer using IRS. Reproduced with permission from [63].

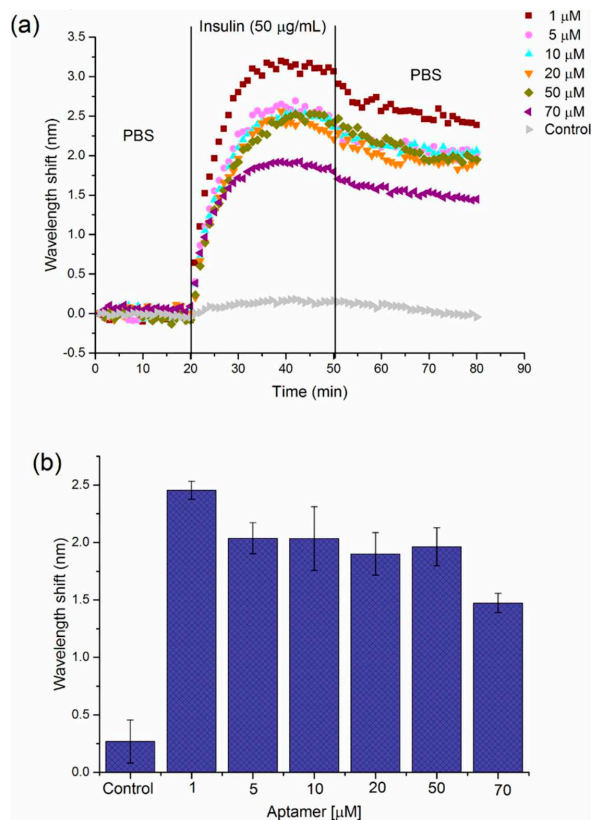


Figure 5. (a) Sensorgrams showing the effect of IBA solution concentration used for modified-PSi device on the response to 50 $\mu\text{g/mL}$ insulin. (b) Graph representing the average wavelength shift (nm) obtained for detection of 50 $\mu\text{g/mL}$ insulin by PSi-5 cycles surface, which is modified with a range of aptamer concentrations (1–70 μM). Error bars correspond to the standard deviation from three individual experiments on PSi-devices prepared with each IBA concentration. Reproduced with permission from [64].

This phenomenon might be due to a steric hindrance effect that could prevent the aptamer from folding into the correct 3D conformation required to show the highest insulin affinity [64]. The optimized PSi biosensor platform was then applied to detect insulin in a real sample. For biosensing experiments with IRS, the sensor surface was exposed to Krebs buffer flow for 20 min, followed by supernatant containing the insulin secreted by human islets (20000 IEQ), and then washed with Krebs buffer for 30 min. At first, a steady baseline was achieved in the Krebs buffer, and no shift in the peak wavelength was observed. Then, the supernatant with secreted insulin was flowed over the biosensor surface and a gradual red shift was observed, as a result of insulin/IBA binding. During the final washing step, a decrease in the maximum wavelength was observed due to the removal of unbound insulin from the biosensor surface. A shift of 0.19 nm calculated by subtracting the final wavelength value from the initial baseline value was applied to the linear regression equation from the calibration curve (data not shown) in Krebs buffer and the calculated concentration of insulin in the real sample was 1.3 $\mu\text{g/mL}$. This result was confirmed by an ELISA test validating the PSiRF sensor as a successful device for the detection of insulin secreted by human islets stimulated with glucose.

3.3. Macroporous Silica Aptasensor for Label-Free Optical Quantification of Human Thrombin

Human thrombin (MW \approx 37 kDa) is a serine protease—also known as coagulation factor II—which is able to convert soluble fibrinogen (factor I) into insoluble strands of fibrin (factor Ia), with a fundamental role in coagulation and hemostasis. The balance between its production and inhibition avoids hemorrhagic or thrombosis phenomena, which may be fatal to human health. In a healthy subject, thrombin concentration is almost absent until it passes from nM to μM levels during the coagulation process [65]. Pathological coagulation disorders, such as ischemic stroke or thromboembolism, could be induced by high levels of thrombin in the blood (beyond the normal coagulation phenomenon) [66]. Moreover, the deregulation of neuronal PAR1-activation by thrombin has been associated with many disorders of the central nervous system (SNC), including the Alzheimer and Parkinson diseases, and the role of thrombin in cancer is well known [67,68]. The important role of thrombin in different (patho)physiological processes has triggered interest in the possible discovery of novel thrombin inhibitors, as well as in the development of new devices which are capable of rapidly detecting its level in blood with high selectivity and very low LoD [69,70]. M. Terracciano et al. [71] described the fabrication of a label-free PSi optical aptasensor by in situ synthesis of a 15-mer thrombin binding aptamer (TBA) on silanized macro-PSi for the quantification of human α -thrombin levels. The high sensitivity, selectivity, and reversibility of the obtained aptasensor were also demonstrated. Macro-PSi structure (pores size $>$ 50 nm), after thermal oxidation, was functionalized by grafting aminosilane compound (APTES), and bioconjugated to a TBA probe by an in situ synthesis [72]. Figure 6 shows the reflectivity spectra (A) with the corresponding FFTs (B) of APTES-modified PSi before and after the in situ synthesis process. The calculated FFT peak shift of 36 nm confirmed the success the TBA growth on the PSi structure. This result was also confirmed by the coupling yield analysis of the 5'-dimethoxytrityl (DMT) group released into the solution after each synthesis cycle using ultraviolet (UV) spectroscopy. The PSi surface functionalization with TBA (F_{TBA}) was quantified using the Lambert-Beer law (DMT molar absorptivity $\epsilon = 71,700 \text{ M}^{-1} \text{ cm}^{-1}$, $\lambda = 500 \text{ nm}$) and UV intensity value corresponding to the last synthesized nucleotide, i.e., $I_{\text{N17}} = 0.055 \pm 0.001$. The F_{TBA} was calculated to be $(1.92 \pm 0.03) \times 10^{-5} \text{ mol/g}$ for PSi sample with a weight of 0.2 mg. The PSi surface functionalization in terms of nmol cm^{-2} evaluated using the ratio $F_{\text{TBA}}/\text{SSA}$ (specific surface area of PSi $199 \text{ m}^2 \text{ g}^{-1}$ evaluated by the Brunauer–Emmett–Teller analysis) was found to be $0.0125 \pm 0.0002 \text{ nmol cm}^{-2}$. For biosensing experiments, the aptasensor was exposed to different thrombin concentrations (13, 27, 54 and 109 nM). The TBA-thrombin interaction was monitored using spectroscopic reflectometry, demonstrating the technique's ability to recognize the analyte at different molar concentrations. The calculated affinity constant was $14 \pm 8 \text{ nM}$, with a sensitivity of $4.1 \pm 0.8 \text{ nm nM}^{-1}$ and LoD of $1.5 \pm 0.3 \text{ nM}$. The LoD value was lower than other well-known, very sensitive assays [73]. Moreover, the reversibility of the PSi-aptasensor was also proved. The PSi-aptasensor was

regenerated by treatment in water at 53 °C, corresponding to the melting temperature of TBA [74]. At this temperature, TBA lost the typical G-quadruplex structure, as well as its affinity with thrombin. However, this process was reversible: by exposing TBA-PSi to thrombin and/or monovalent cations at room temperature, the aptamer folded again into a G-quadruplex structure [75]. The device regeneration induced a decrease of optical thickness (about 14 nm) due to the release of thrombin from the PSi pores. An increase of 38 nm was observed after exposing the device to 109 nM of thrombin solution, thus proving the ability of the aptasensor to recognize the analyte. The results reported in this work endorse macro-PSi as a suitable substrate for the realization of a wide range of aptasensors using an in situ synthesis approach for surface functionalization.

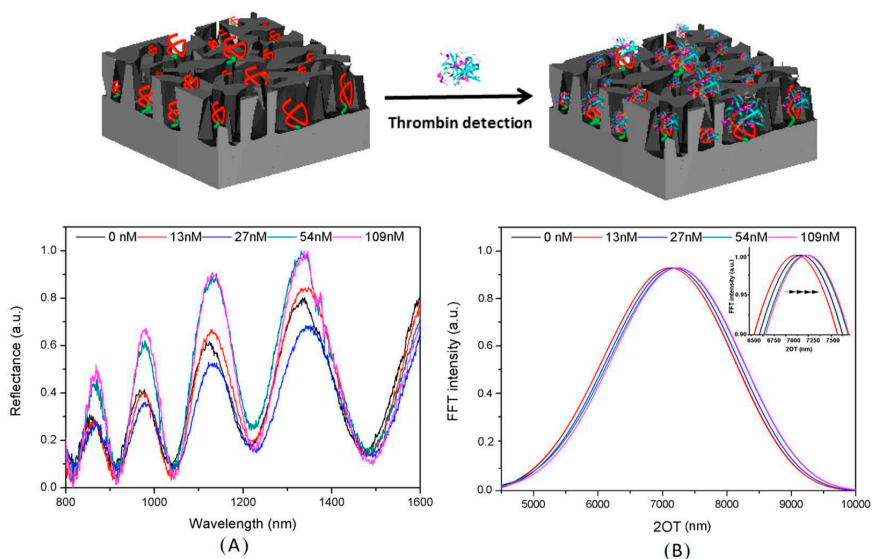


Figure 6. Reflectivity spectra (A) and corresponding Fourier transforms (B) of PSi-aptasensor after exposure to different thrombin concentrations (13, 27, 54 and 109 nM). Reproduced with permission from [71].

4. Conclusions

Label-free optical PSi biosensors using aptamers as bioprobes represent a promising class of devices in future healthcare diagnoses. Aptamers have emerged as new molecular recognition tools with great affinities and specificities. The integration and automation of aptamers are easier than conventional bioprobes, and are extremely convenient for the development of biosensors. PSi is an appealing nanostructured material which is largely used in biosensing due to the ease with which its properties, e.g., pore morphology, photonic properties, biocompatibility and surface chemistry, may be tuned.

In this review article, we summarized the recent progress in the development of label-free optical PSi-aptasensors for human diseases diagnosis such as bacterial infections, real-time monitoring of insulin and human α -thrombin. Particular attention was paid to PSi fabrication and functionalization strategies; it was shown that PSi-aptasensors demonstrate high levels of performance in terms of stability, sensitivity, early detection and reversibility. Moreover, the LoD values of the described PSi optical aptasensor were found to be comparable or below those of other well-known electrical or electrochemical aptasensors. Moreover, optical devices are preferred because opto-instruments are non-invasive and safe, even in harsh conditions such as in vivo monitoring inside a patient's body, where, for example, electrical devices could be harmful. The potential of aptasensors appears to be huge, and this exciting area is seeing exponential growth. The capacity to develop high affinity-based

detection systems with tailored characteristics offers to the biosensing field the chance to explore new and dynamic routes of biosensor development. The possibility of commercializing aptasensors in the near future can therefore be reasonably foreseen.

Funding: This research received no external funding.

Conflicts of Interest: The authors declare no conflict of interest.

References

1. Lin, V.S.Y.; Motesharei, K.; Dancil, K.P.S.; Sailor, M.J.; Ghadiri, M.R. A porous silicon-based optical interferometric biosensor. *Science* **1997**, *278*, 840–843. [[CrossRef](#)] [[PubMed](#)]
2. Jane, A.; Dronov, R.; Hodges, A.; Voelcker, N.H. Porous silicon biosensors on the advance. *Trends Biotechnol.* **2009**, *27*, 230–239. [[CrossRef](#)] [[PubMed](#)]
3. Dancil, K.P.S.; Greiner, D.P.; Sailor, M.J. A porous silicon optical biosensor: Detection of reversible binding of IgG to a protein A-modified surface. *J. Am. Chem. Soc.* **1999**, *121*, 7925–7930. [[CrossRef](#)]
4. De Stefano, L.; Rea, I.; Giardina, P.; Armenante, A.; Rendina, I. Protein-Modified Porous Silicon Nanostructures. *Adv. Mat.* **2008**, *20*, 1529–1533. [[CrossRef](#)]
5. Lehninger, A.L.; Nelson, D.L.; Cox, M.M. *The Molecular Basis of Cell Structure and Function, Biochemistry*, 2nd ed.; Worth Publishers: New York, NY, USA, 1975; pp. 71–77.
6. Byfield, M.P.; Abuknesha, R.A. Biochemical aspects of biosensors. *Biosen. Bioelectron.* **1994**, *9*, 373–399. [[CrossRef](#)]
7. Sefah, K.; Shangguan, D.; Xiong, X.; O'donoghue, M.B.; Tan, W. Development of DNA aptamers using Cell-SELEX. *Nat. Protoc.* **2010**, *5*, 1169. [[CrossRef](#)] [[PubMed](#)]
8. Jayasena, S.D. Aptamers: An emerging class of molecules that rival antibodies in diagnostics. *Clin. Chem.* **1999**, *45*, 1628–1650. [[PubMed](#)]
9. Toh, S.Y.; Citartan, M.; Gopinath, S.C.B.; Tang, T.H. Aptamers as a replacement for antibodies in enzyme-linked immunosorbent assay. *Biosens. Bioelectron.* **2015**, *64*, 392–403. [[CrossRef](#)]
10. Cho, E.J.; Lee, J.W.; Ellington, A.D. Applications of aptamers as sensors. *Annu. Rev. Anal. Chem.* **2009**, *2*, 241–264. [[CrossRef](#)]
11. Oliviero, G.; Borbone, N.; Amato, J.; D'Errico, S.; Galeone, A.; Piccialli, G.; Mayol, L. Synthesis of quadruplex-forming tetra-end-linked oligonucleotides: Effects of the linker size on quadruplex topology and stability. *Biopolymers* **2009**, *91*, 466–477. [[CrossRef](#)]
12. Meng, H.M.; Liu, H.; Kuai, H.; Peng, R.; Mo, L.; Zhang, X.B. Aptamer-integrated DNA nanostructures for biosensing, bioimaging and cancer therapy. *Chem. Soc. Rev.* **2016**, *45*, 2583–2602. [[CrossRef](#)] [[PubMed](#)]
13. Deisingh, A.K. *RNA Towards Medicine*; Springer: Berlin/Heidelberg, Germany, 2006; pp. 341–357.
14. Zhang, Y.; Sun, X. A novel fluorescent aptasensor for thrombin detection: Using poly(*m*-phenylenediamine) rods as an effective sensing platform. *Chem. Commun.* **2011**, *47*, 3927–3929. [[CrossRef](#)]
15. Rusciano, G.; De Luca, A.C.; Pesce, G.; Sasso, A.; Oliviero, G.; Amato, J.; Mayol, L. Label-free probing of G-quadruplex formation by surface-enhanced Raman scattering. *Anal. Chem.* **2011**, *83*, 6849–6855. [[CrossRef](#)] [[PubMed](#)]
16. Xu, L.; Zhao, S.; Ma, W.; Wu, X.; Li, S.; Kuang, H.; Xu, C. Multigaps embedded nanoassemblies enhance in situ Raman spectroscopy for intracellular telomerase activity sensing. *Adv. Funct. Mat.* **2016**, *26*, 1602–1608. [[CrossRef](#)]
17. Dhanekar, S.; Jain, S. Porous silicon biosensor: Current status. *Biosen. Bioelectron.* **2013**, *41*, 54–64. [[CrossRef](#)] [[PubMed](#)]
18. De Stefano, L.; Rotiroti, L.; Rea, I.; Moretti, L.; Di Francia, G.; Massera, E.; Rendina, I. Porous silicon-based optical biochips. *J. Opt.* **2006**, *8*, S540. [[CrossRef](#)]
19. De Stefano, L.; Arcari, P.; Lamberti, A.; Sanges, C.; Rotiroti, L.; Rea, I.; Rendina, I. DNA optical detection based on porous silicon technology: From biosensors to biochips. *Sensors* **2007**, *7*, 214–221. [[CrossRef](#)]
20. Wu, J.; Sailor, M.J. Chitosan hydrogel-capped porous SiO₂ as a pH responsive nanovalve for triggered release of insulin. *Adv. Funct. Mat.* **2009**, *19*, 733–741. [[CrossRef](#)]
21. Rea, I.; Sansone, L.; Terracciano, M.; De Stefano, L.; Dardano, P.; Giordano, M.; Casalino, M. Photoluminescence of graphene oxide infiltrated into mesoporous silicon. *J. Phys. Chem. C* **2014**, *118*, 27301–27307. [[CrossRef](#)]

22. Ouyang, H.; De Louise, L.A.; Miller, B.L.; Fauchet, P.M. Label-free quantitative detection of protein using macroporous silicon photonic bandgap biosensors. *Anal. Chem.* **2007**, *79*, 1502–1506. [[CrossRef](#)]
23. Terracciano, M.; Galstyan, V.; Rea, I.; Casalino, M.; De Stefano, L.; Sberveglieri, G. Chemical modification of TiO₂ nanotube arrays for label-free optical biosensing applications. *Appl. Surf. Sci.* **2017**, *419*, 235–240. [[CrossRef](#)]
24. De Stefano, L.; Rossi, M.; Staiano, M.; Mamone, G.; Parracino, A.; Rotiroti, L.; D’Auria, S. Glutamine-binding protein from *Escherichia coli* specifically binds a wheat gliadin peptide allowing the design of a new porous silicon-based optical biosensor. *J. Proteome Res.* **2006**, *5*, 1241–1245. [[CrossRef](#)]
25. De Stefano, L.; Malecki, K.; Della Corte, F.; Moretti, L.; Rea, I.; Rotiroti, L.; Rendina, I. A microsystem based on porous silicon-glass anodic bonding for gas and liquid optical sensing. *Sensors* **2006**, *6*, 680–687. [[CrossRef](#)]
26. Martucci, N.M.; Rea, I.; Ruggiero, I.; Terracciano, M.; De Stefano, L.; Migliaccio, N.; Lamberti, A. A new strategy for label-free detection of lymphoma cancer cells. *Biomed. Opt. Express* **2015**, *6*, 1353–1362. [[CrossRef](#)]
27. Bonanno, L.M.; Segal, E. Nanostructured porous silicon–polymer-based hybrids: From biosensing to drug delivery. *Nanomedicine* **2011**, *6*, 1755–1770. [[CrossRef](#)]
28. D’Auria, S.; De Champdore, M.; Aurilia, V.; Parracino, A.; Staiano, M.; Vitale, A.; Borini, S. Nanostructured silicon-based biosensors for the selective identification of analytes of social interest. *J. Phys. Condens. Matter* **2006**, *18*, S2019. [[CrossRef](#)]
29. Rea, I.; Lamberti, A.; Rendina, I.; Coppola, G.; Gioffrè, M.; Iodice, M.; De Stefano, L. Fabrication and characterization of a porous silicon based microarray for label-free optical monitoring of biomolecular interactions. *J. Appl. Phys.* **2010**, *107*, 014513. [[CrossRef](#)]
30. Korotcenkov, G.; Terracciano, M.; Politi, J.; Caliò, A.; Rea, I.; De Stefano, L. *Porous Silicon: From Formation to Application: Biomedical and Sensor Applications*; CRC Press: Boca Raton, FL, USA, 2016; pp. 82–107.
31. Smith, R.L.; Collins, S.D. Porous silicon formation mechanisms. *J. App. Phys.* **1992**, *71*, R1–R22. [[CrossRef](#)]
32. Massad-Ivanir, N.; Shtenberg, G.; Tzur, A.; Krepker, M.A.; Segal, E. Engineering nanostructured porous SiO₂ surfaces for bacteria detection via direct cell capture. *Anal. Chem.* **2011**, *83*, 3282–3289. [[CrossRef](#)]
33. Reddy, K.; Guoa, Y.; Liua, J.; Leea, W.; Khaing Ooa, M.K.; Fana, X. On-chip Fabry–Pérot interferometric sensors for micro-gas chromatography detection. *Sens. Actuators B Chem.* **2011**, *159*, 60–65. [[CrossRef](#)]
34. Casalino, M.; Coppola, G.; Gioffrè, M.; Iodice, M.; Moretti, L.; Rendina, I.; Sirleto, L. Silicon technology compatible photodetectors at 1.55 μm. *J. Lightwave Technol.* **2010**, *28*, 3266.
35. Pacholski, C.; Sartor, M.; Sailor, M.J.; Cunin, F.; Miskelly, G.M. Biosensing using porous silicon double-layer interferometers: Reflective interferometric Fourier transform spectroscopy. *J. Am. Chem. Soc.* **2005**, *127*, 11636–11645.
36. Low, S.P.; Voelcker, N.H.; Canham, L.T.; Williams, K.A. The biocompatibility of porous silicon in tissues of the eye. *Biomaterials* **2009**, *30*, 2873–2880. [[CrossRef](#)]
37. Lehmann, V.; Gösele, U. Porous silicon formation: A quantum wire effect. *Appl. Phys. Lett.* **1991**, *58*, 856–858. [[CrossRef](#)]
38. Santos, H.A. *Porous Silicon for Biomedical Applications*, 1st ed.; Elsevier: Amsterdam, The Netherlands, 2014.
39. Rendina, I.; Rea, I.; Rotiroti, L.; De Stefano, L. Porous silicon-based optical biosensors and biochips. *Phys. E Low Dimens Syst. Nanostruct.* **2007**, *38*, 188–192.
40. Harraz, F.A. Porous silicon chemical sensors and biosensors: A review. *Sens. Actuator B-Chem.* **2014**, *202*, 897–912. [[CrossRef](#)]
41. Shabir, Q.; Webb, K.; Nadarassan, D.K.; Loni, A.; Canham, L.T.; Terracciano, M.; Rea, I. Quantification and reduction of the residual chemical reactivity of passivated biodegradable porous silicon for drug delivery applications. *Silicon* **2018**, *10*, 349–359. [[CrossRef](#)]
42. Song, J.H.; Sailor, M.J. Chemical modification of crystalline porous silicon surfaces. *Comments Inorg. Chem.* **1999**, *21*, 69–84. [[CrossRef](#)]
43. Pap, A.E.; Kordás, K.; Tóth, G.; Levoska, J.; Uusimäki, A.; Vähäkangas, J.; George, T.F. Thermal oxidation of porous silicon: Study on structure. *Appl. Phys. Lett.* **2005**, *86*, 041501. [[CrossRef](#)]
44. Terracciano, M.; Rea, I.; Politi, J.; De Stefano, L. Optical characterization of aminosilane-modified silicon dioxide surface for biosensing. *JEOS* **2013**, *8*, 1–6.
45. Moretta, R.; Terracciano, M.; Dardano, P.; Casalino, M.; De Stefano, L.; Schiattarella, C.; Rea, I. Toward multi-parametric porous silicon transducers based on covalent grafting of graphene oxide for biosensing applications. *Front. Chem.* **2018**, *6*, 583. [[CrossRef](#)]

46. Moretta, R.; Terracciano, M.; Dardano, P.; Casalino, M.; Rea, I.; De Stefano, L. Covalent grafting of graphene oxide on functionalized macroporous silicon. *Open Mater. Sci.* **2018**, *4*, 15–22. [[CrossRef](#)]
47. Buriak, J.M. Silicon-Carbon Bonds on Porous Silicon Surfaces. *Adv. Mater.* **1999**, *11*, 265–267. [[CrossRef](#)]
48. Sailor, M.J. *Porous Silicon in Practice*; Wiley-VCH: Weinheim, Germany, 2007.
49. Terracciano, M.; Rea, I.; De Stefano, L.; Rendina, I.; Oliviero, G.; Nici, F.; Borbone, N. Synthesis of mixed-sequence oligonucleotides on mesoporous silicon: Chemical strategies and material stability. *Nanoscale Res. Lett.* **2014**, *9*, 317. [[CrossRef](#)] [[PubMed](#)]
50. Rea, I.; Oliviero, G.; Amato, J.; Borbone, N.; Piccialli, G.; Rendina, I.; De Stefano, L. Direct synthesis of oligonucleotides on nanostructured silica multilayers. *J. Phys. Chem. C* **2010**, *114*, 2617–2621. [[CrossRef](#)]
51. Hermann, T.; Patel, D.J. Adaptive recognition by nucleic acid aptamers. *Science* **2000**, *287*, 820–825. [[CrossRef](#)]
52. Mascini, M.; Mascini, M. *Aptamers in Bioanalysis*; Wiley: New York, NY, USA, 2009.
53. Roda, A.; Mirasoli, M.; Roda, B.; Bonvicini, F.; Colliva, C.; Reschiglian, P. Recent developments in rapid multiplexed bioanalytical methods for foodborne pathogenic bacteria detection. *Microchim. Acta* **2012**, *178*, 7–28. [[CrossRef](#)]
54. Palmieri, G.; Tatè, R.; Gogliettino, M.; Balestrieri, M.; Rea, I.; Terracciano, M.; De Stefano, L. Small synthetic peptides bioconjugated to hybrid gold nanoparticles destroy potentially deadly bacteria at submicromolar concentrations. *Bioconj. Chem.* **2018**, *29*, 3877–3885. [[CrossRef](#)]
55. Law, J.W.F.; Mutalib, N.S.; Chan, K.G.; Lee, L.H. Rapid methods for the detection of foodborne bacterial pathogens: Principles, applications, advantages and limitations. *Front. Microbiol.* **2015**, *5*, 770. [[CrossRef](#)]
56. Urmann, K.; Arshavsky-Graham, S.; Walter, J.G.; Scheper, T.; Segal, E. Whole-cell detection of live lactobacillus acidophilus on aptamer-decorated porous silicon biosensors. *Analyst* **2016**, *141*, 5432–5440. [[CrossRef](#)]
57. Foster, T.J.; Geoghegan, J.A.; Ganesh, V.K.; Höök, M. Adhesion, invasion and evasion: The many functions of the surface proteins of *Staphylococcus aureus*. *Nat. Rev. Microbiol.* **2014**, *12*, 49. [[CrossRef](#)]
58. Urmann, K.; Reich, P.; Walter, J.G.; Beckmann, D.; Segal, E.; Scheper, T. Rapid and label-free detection of protein A by aptamer-tethered porous silicon nanostructures. *J. Biotechnol.* **2017**, *257*, 171–177. [[CrossRef](#)] [[PubMed](#)]
59. Terracciano, M.; Shahbazi, M.A.; Correia, A.; Rea, I.; Lamberti, A.; De Stefano, L.; Santos, H.A. Surface bioengineering of diatomite based nanovectors for efficient intracellular uptake and drug delivery. *Nanoscale* **2015**, *7*, 20063–20074. [[CrossRef](#)] [[PubMed](#)]
60. Williams, A.; Ibrahim, I.T. Carbodiimide chemistry: Recent advances. *Chem. Rev.* **1981**, *81*, 589–636. [[CrossRef](#)]
61. World Health Organization. Diabetes. Available online: <https://www.who.int/health-topics/diabetes> (accessed on 29 April 2019).
62. Umpierrez, G.E.; Isaacs, S.D.; Bazargan, N.; You, X.; Thaler, L.M.; Kitabchi, A.E. Hyperglycemia: An independent marker of in-hospital mortality in patients with undiagnosed diabetes. *J. Clin. Endocrinol. Metab.* **2002**, *87*, 978–982. [[CrossRef](#)] [[PubMed](#)]
63. Chhasatia, R.; Sweetman, M.J.; Harding, F.J.; Waibel, M.; Kay, T.; Thomas, H.; Voelcker, N.H. Non-invasive, in vitro analysis of islet insulin production enabled by an optical porous silicon biosensor. *Biosens. Bioelectron.* **2017**, *91*, 515–522. [[CrossRef](#)] [[PubMed](#)]
64. Chhasatia, R.; Sweetman, M.J.; Prieto-Simon, B.; Voelcker, N.H. Performance optimisation of porous silicon rugate filter biosensor for the detection of insulin. *Sens. Actuators B Chem.* **2018**, *273*, 1313–1322. [[CrossRef](#)]
65. Lisman, T.; Bakhtiari, K.; Pereboom, T.; Hendriks, H.G.; Meijers, J.C.; Porte, R.J. Normal to increased thrombin generation in patients undergoing liver transplantation despite prolonged conventional coagulation tests. *J. Hepatol.* **2010**, *52*, 355–361. [[CrossRef](#)]
66. Tanaka, K.A.; Key, N.S.; Levy, J.H. Blood coagulation: Hemostasis and thrombin regulation. *Anesth. Analg.* **2009**, *108*, 1433–1446. [[CrossRef](#)]
67. Ben Shimon, M.; Lenz, M.; Ikenberg, B.; Becker, D.; Shavit Stein, E.; Chapman, J.; Vlachos, A. Thrombin regulation of synaptic transmission and plasticity: Implications for health and disease. *Front. Cell Neurosci.* **2015**, *9*, 151. [[CrossRef](#)]
68. Danckwardt, S.; Hentze, M.W.; Kulozik, A.E. Pathologies at the nexus of blood coagulation and inflammation: Thrombin in hemostasis, cancer, and beyond. *J. Mol. Med.* **2013**, *91*, 1257–1271. [[CrossRef](#)] [[PubMed](#)]

69. Borbone, N.; Bucci, M.; Oliviero, G.; Morelli, E.; Amato, J.; D'Atri, V.; Fattorusso, C. Investigating the role of T7 and T12 residues on the biological properties of thrombin-binding aptamer: Enhancement of anticoagulant activity by a single nucleobase modification. *J. Med. Chem.* **2012**, *55*, 10716–10728. [[CrossRef](#)] [[PubMed](#)]
70. Scuto, M.; Persico, M.; Bucci, M.; Vellecco, V.; Borbone, N.; Morelli, E.; Varra, M. Outstanding effects on antithrombin activity of modified TBA diastereomers containing an optically pure acyclic nucleotide analogue. *Org. Biomol. Chem.* **2014**, *12*, 5235–5242. [[CrossRef](#)] [[PubMed](#)]
71. Terracciano, M.; De Stefano, L.; Borbone, N.; Politi, J.; Oliviero, G.; Rea, I. Solid phase synthesis of a thrombin binding aptamer on macroporous silica for label free optical quantification of thrombin. *RSC Adv.* **2016**, *6*, 86762–86769. [[CrossRef](#)]
72. De Stefano, L.; Oliviero, G.; Amato, J.; Borbone, N.; Piccialli, G.; Mayol, L.; Rea, I. Aminosilane functionalizations of mesoporous oxidized silicon for oligonucleotide synthesis and detection. *J. R. Soc. Interface* **2013**, *10*, 20130160. [[CrossRef](#)] [[PubMed](#)]
73. Gu, M.B.; Kim, H.S. *Biosensors Based on Aptamers and Enzymes*; Springer: New York, NY, USA, 2014.
74. Lehman, G.W.; McTague, J.P. Melting of DNA. *J. Chem. Phys.* **1968**, *49*, 3170–3179. [[CrossRef](#)] [[PubMed](#)]
75. Smirnov, I.; Shafer, R.H. Effect of loop sequence and size on DNA aptamer stability. *Biochemistry* **2000**, *39*, 1462–1468. [[CrossRef](#)]



© 2019 by the authors. Licensee MDPI, Basel, Switzerland. This article is an open access article distributed under the terms and conditions of the Creative Commons Attribution (CC BY) license (<http://creativecommons.org/licenses/by/4.0/>).



Extending the Shelf-Life of Meat and Dairy Products via PET-Modified Packaging Activated With the Antimicrobial Peptide MTP1

Marta Gogliettino^{1†}, Marco Balestrieri^{1†}, Rosa Luisa Ambrosio², Aniello Anastasio², Giorgio Smaldone³, Yolande T. R. Proroga⁴, Rosalba Moretta⁵, Ilaria Rea⁵, Luca De Stefano⁵, Bruna Agrillo^{1,6} and Gianna Palmieri^{1,6*}

¹ Institute of Biosciences and Bioresources, National Research Council (IBBR-CNR), Naples, Italy, ² Department of Veterinary Medicine and Animal Production, University of Naples Federico II, Naples, Italy, ³ Department of Agricultural Science, University of Naples Federico II, Naples, Italy, ⁴ Department of Food Microbiology, Istituto Zooprofilattico Sperimentale del Mezzogiorno, Portici, Italy, ⁵ Institute for Microelectronics and Microsystems, National Research Council (IMM-CNR), Naples, Italy, ⁶ Materias Srl, Naples, Italy

OPEN ACCESS

Edited by:

Nadia Oulahal,
Université Claude Bernard Lyon 1,
France

Reviewed by:

Pascal Degraeve,
Université Claude Bernard Lyon 1,
France
Xinglian Xu,
Nanjing Agricultural University, China

*Correspondence:

Gianna Palmieri
gianna.palmieri@ibbr.cnr.it

[†]These authors have contributed
equally to this work

Specialty section:

This article was submitted to
Food Microbiology,
a section of the journal
Frontiers in Microbiology

Received: 25 July 2019

Accepted: 09 December 2019

Published: 09 January 2020

Citation:

Gogliettino M, Balestrieri M,
Ambrosio RL, Anastasio A,
Smaldone G, Proroga YTR,
Moretta R, Rea I, De Stefano L,
Agrillo B and Palmieri G (2020)
Extending the Shelf-Life of Meat
and Dairy Products via PET-Modified
Packaging Activated With
the Antimicrobial Peptide MTP1.
Front. Microbiol. 10:2963.
doi: 10.3389/fmicb.2019.02963

Fresh products are characterized by reduced shelf-life because they are an excellent growth medium for a lot of microorganisms. Therefore, the microbial spoilage causing significant food supply losses has become an enormous economic and ethical problem worldwide. The antimicrobial packaging is offering a viable solution to tackle this economic and safety issue by extending the shelf-life and improving the quality and safety of fresh products. The goal of this study was to investigate the effects of a food contact surface of polyethylene terephthalate (PET) functionalized with the previously characterized antimicrobial peptide mitochondrial-targeted peptide 1 (MTP1), in reducing the microbial population related to spoilage and in providing the shelf-life stability of different types of fresh foods such as ricotta cheese and buffalo meat. Modified polymers were characterized concerning the procedure of plasma-activation by water contact angle measurements and Fourier transform infrared spectroscopy measurements in attenuated total reflection mode (ATR-FTIR). Results showed that the MTP1-PETs provided a strong antimicrobial effect for spoilage microorganisms with no cytotoxicity on a human colon cancer cell line. Finally, the activated polymers revealed high storage stability and good reusability. This study provided valuable information to develop alternative antimicrobial packaging for enhancing and extending the microbial quality and safety of perishable foods during storage.

Keywords: antimicrobial packaging, antimicrobial peptide, shelf-life, spoilage microorganism, cytotoxicity

INTRODUCTION

Short shelf-life of fresh foods represents one of the main limitations for the commercialization of this class of products, mainly due to their high content in nutrients and superficial moisture which leads to the fast growth of spoilage and pathogenic microorganisms (Aymerich et al., 2008; Patsias et al., 2008; Zhou et al., 2010). Indeed, it is well-known that microbial growth on the surface of a product is often responsible for the undesirable changes in flavor, aroma, and other organoleptic

characteristics of fresh foods, which lower their quality and shorten their commercial life (Mead, 2004; Samelis, 2006; Petrou et al., 2012). Although the exact figure of the total economic loss due to food spoilage is hardly to estimate, it is clear that it constitutes an enormous financial burden (Blackburn, 2006) accounting for 1.3 billion tons per year by FAO (Cichello, 2015; Bondi et al., 2017). Therefore, even a reduction in food waste of 20–25% could save between \$120 and \$300 billion per year according to a recent report by the UK Waste & Resources Action Programme (WRAP). As a preservation technique, the refrigeration is necessary to maintain the microbial quality of fresh products, but it does not guarantee by itself a long shelf-life, which in the case of some foods amounts to a time period of about 4–5 days. Therefore, demand for safe fresh products presents major challenges to the food industry to develop innovative strategies for improving the preservation process and prolonging the storage time maintaining both the natural appearance and safety of foods by reducing or eliminating spoilage bacteria. A significant support in this field derives from the use of packages, which not only act as a barrier against moisture, water vapor, and gases, but they may also serve as a carrier of active substances in the “active packaging,” thus increasing the shelf-life and assuring the safety and/or quality of food products (Suppakul et al., 2003). Active packaging is the most relevant innovative idea applied for consumer satisfaction. It can be defined as a mode of packaging in which product, package, and the environment interact in a positive way to extend shelf-life of products and/or to enhance safety or sensory properties while maintaining the quality of the foods (Suppakul et al., 2003). Among the active packaging technologies, antimicrobial packaging is considered one of the most promising. These systems are based on the immobilization of antimicrobial agents on the surface of polymers, whose usage has strongly increased due to their large variety and the different compositions available, which make possible to adopt the most convenient packaging solutions, focusing on the specific needs of each product. One of the most common support that has found increasing applications within the packaging field is the polyethylene terephthalate (PET), a simple long-chain polymer, whose chemical inertness and physical properties have made it particularly suitable for different food applications. However, the chemical inertness of PET makes necessary to activate and functionalize its surface with specific treatments as the cold plasma before proceeding with the subsequent immobilization of bioactive compounds such as essential oils, plant extracts, bacteriocins, or enzymes (Jordá-Vilaplana et al., 2014; Malhotra et al., 2015). Some antimicrobial packages use immobilized antimicrobial peptides (AMP) to suppress the growth of microbes (Malhotra et al., 2015). AMPs are part of the innate immune system of all multicellular organisms (Andreu and Rivas, 1998; De Smet and Contreras, 2005; Guaní-Guerra et al., 2010) and include a chemically and structurally heterogeneous family, whose members have been isolated from a wide variety of animals, plants, bacteria, fungi, and viruses (Andreu and Rivas, 1998; Reddy et al., 2004). Nevertheless, three main characteristics that are shared by almost all known AMPs, can be distinguished: small size, highly cationic character, and tendency to adopt amphipathic

structures (Nakatsuji and Gallo, 2012). These physicochemical properties make AMPs able to interact with the negatively charged microbial membranes. However, to serve as effective coating agents, the AMPs must meet several prerequisites, which include the retention of broad-spectrum antimicrobial activity once bound to packaging materials. As many naturally occurring peptides lack the ability to retain these properties, there is a need to develop new and more effective AMPs, with the aim to increase safety and shelf-life of food products. Recently, starting from the human source sequence of CPT-1a (McGarry and Brown, 1997), a new AMP, named mitochondrial-targeted peptide 1 (MTP1), was designed as already stated in Palmieri et al. (2016) and characterized. Specifically, the 15-mer peptide was revealed to be highly stable in a broad range of pH (2–10) and temperature (15–90°C) for prolonged incubation times. Moreover, MTP1 assumed α -helix/ β -sheet structures in mimicked cell membrane solutions, as revealed by CD analyses. Finally, the compound exhibited significant bactericidal activity against *Listeria monocytogenes*, one of the most important foodborne pathogens.

The aim of the present study was to develop a new class of packaging materials, functionalized with the bactericidal peptide MTP1 and to evaluate both the usefulness and effectiveness of the aforementioned active coatings on the microbial quality and safety of fresh perishable products and the potential extension of their shelf-life.

MATERIALS AND METHODS

Plasma Treatment

For plasma treatment and further peptide immobilization, the PET films were cut into disk-shaped pieces. Etching of PET disks was carried out using the PlasmaLab 80 Plus Reactive Ion Etching (RIE) system (Oxford Instruments, Abingdon, Oxfordshire, United Kingdom). The following parameters were modified to identify the best operative conditions: exposure time (T) (10–20–30–50–100–300 s); molecular oxygen concentration (O_2) (10–50–100 sccm); partial gas pressure (P) (0.1–0.5 atm); and power of radiofrequency generator (RF) (50–100–300 W).

Water Contact Angle Measurements

Water contact angles (WCA) were measured under static conditions by sessile drop method using an OCA 15EC system (DataPhysics Instruments GmbH, Filderstadt, Germany) coupled with a drop shape analysis software (SCA 20, DataPhysics Instruments GmbH, Filderstadt, Germany). A 1- μ L drop was placed on the functionalized polymer surfaces, recording the images after 10 s. The WCA values are expressed as mean \pm standard deviation (s.d.) of at least three measurements on the same sample in two independent experiments (i.e., at least six measurements for each result).

Fourier Transform Infrared Spectroscopy

Fourier transform infrared spectroscopy measurements in attenuated total reflection mode (ATR-FTIR) were carried out in the 4000–650 cm^{-1} spectral range with a resolution of 4 cm^{-1} , using a Thermo-Nicolet Continuum XL spectrometer

(Thermo Scientific, United States). The FTIR measurements were performed under inert (N₂) atmosphere. Spectra have been automatically corrected from the background using Omnic software (Thermo Scientific, United States).

MTP1 Immobilization Procedure

After oxygen plasma exposure, the pre-activated PET films were incubated into a MTP1 solution of 50 μM concentration prepared in sodium phosphate buffer (PB; 10 mM), pH = 7.0 for 24 h at 25°C. After incubation, the liquid solution of unbound peptide was removed manually and the functionalized PETs were extensively rinsed in water and DMSO in order to remove the traces of non-covalently bound peptide before performing all the surface characterizations. The PET containers used in all the analyses were kindly provided by the dairy “Mini Caseificio Costanzo s.r.l.” located in Lusciano (Caserta, Italy).

Immobilization Yield Analysis of PET Polymers

Immobilization yield analysis of MTP1 on pre-activated PETs was performed by using a reverse-phase high-performance liquid chromatography (RP-HPLC) system (Shimadzu, Milan, Italy). Once immobilization was completed, the supernatant solutions were recovered after 24 h incubation and chromatographically analyzed to indirectly estimate the amount of the peptide attached to the polymeric surfaces. For these analyses, 200 μL of the samples was injected over a μBondapak C18 reverse-phase column (3.9 mm × 300 mm, Waters Corp., Milford, MA, United States) connected to an HPLC system, using a linear gradient of 0.1% TFA in acetonitrile from 5 to 95%. A reference solution was prepared with the initial peptide concentration used for the functionalization procedure under the same reaction conditions and run in parallel. Therefore, by knowing the added peptide (reference solution), the amount of peptide not bound to the polymers (expressed as a percentage) was determined by comparing the peak area. A calibration curve of the C18 column using different MTP1 concentrations was built. All measurements were performed in triplicate on three different preparations.

Release Test

The quantity of MTP1 released from the pre-activated PET disks was assayed by RP-HPLC following the same procedure previously described. Peptide-immobilized PET slides were immersed in pure water or mozzarella cheese brine (1 mL) for 24 h at 4°C and then the recovered solutions were analyzed by RP-HPLC. The solutions in contact with the functionalized polymers at time $t = 0$ were used as control samples and run in parallel. All measurements were performed in triplicate on three different preparations.

Shelf-Life Testing on Dairy Products

A total of three random samples of buffalo ricotta cheese (200 g) were collected from a dairy factory. MTP1-PETs disks of 2.5 cm diameter (surface of 4.91 cm²) were placed on the base of two Petri dishes. Non-functionalized PETs were used as control.

From each package, 30 g of ricotta cheese was weighted and laid aseptically on disks inside Petri dishes and storage at 4°C. Microbiological analyses were performed at t_0 (beginning), t_1 (4 days), and t_2 (10 days) in contact with the MTP1-PETs. After incubation, 10 g of ricotta samples was added to 90 mL of buffered Peptone Water in sterile stomacher bag and homogenized for 3 min at 230 rpm using a peristaltic homogenizer (BagMixer®400 P, Interscience, Saint Nom, France). Further 10-fold dilutions of the homogenates were made. Aerobic Plate Count (APC) and yeasts and molds were enumerated by spread plating on PCA incubated at 30°C for 48–72 h (ISO 4833-2:2013) and DRBC Agar plates incubated at 25 ± 1°C for 5 days for the colony count (21527-1:2008), respectively. The functionalized disks were washed three times by a sanitizing solution (Pursept-A Xpress, Schülke & Mayr GmbH, Germany) and exposed 2 h to UV radiations, before reusing.

Shelf-Life Testing on Buffalo Meat

Water Buffalo (n.5), slaughtered in an EU authorized slaughterhouse at 34 months and live weight of approximately 470 kg was chosen. The half-carcasses were cold-stored (0 ± 3°C) for 5 days and then the sirloin steak muscles (SSM) from both sides of the animal were removed. Subsequently, SSM were placed, for prolonged dry aging, in a forced ventilation patented cell named “Maturmeat” (ARREDO INOX S.r.l.) with an automatic extraction system set at a temperature of 0°C and at HR values ranging between 68 and 70% at microbiological lab of Department of Veterinary Medicine and Animal Productions (University of Naples Federico II). At 90 days of the aging period, three sirloin steaks (SS) were chosen. This aging time was selected due to the best palatability of the meat increasing tenderness, flavor, and/or juiciness. Aseptically 50 g from steaks was cut and placed on plastic disk functionalized with MTP1 (9 cm diameter, surface of 64 cm²) inside Petri dishes and stored at 4°C. Analytical determinations were performed at t_0 (beginning) and t_1 (4 days) after contact with the peptide. APC was detected according to following procedures: 10 g of each sample and 90 mL of sterilized Peptone Water were placed in sterile stomacher bag and homogenized for 3 min at 230 rpm using a peristaltic homogenizer (BagMixer®400 P, Interscience, Saint Nom, France). Afterward, 10-fold serial dilutions of each homogenate were prepared in Peptone Water, followed by streaking in duplicate for APC performed according to ISO 4833-2:2013 on Plate Count Agar incubated at 30°C for 48–72 h and for yeasts and molds performed according to ISO 21527-1:2008 on DRBC plates incubated at 25 ± 1°C for 5 days. The functionalized disks were washed three times by a sanitizing solution (Pursept-A Xpress, Schülke & Mayr GmbH, Germany) and exposed 2 h to UV radiations, before reusing.

Physicochemical Analyses

The pH of samples was measured using a digital pH-meter (Crison-Micro TT 2022, Crison Instruments, Barcelona, Spain). The a_w (activity water) (Aqualab 4 TE – Decagon Devices Inc., United States) was determined by oven drying for 24-h at 105°C (AOAC, 1990). The 2-thiobarbituric acid (TBA) test

(AOAC, 2000) was used to measure the lipid oxidation for each sample.

Rheological Analysis

On buffalo meat samples was performed: (a) Texture profile analysis (TPA), a compression test for determining the textural properties of meat pieces (Ruiz de Huidobro et al., 2005) by measuring the compression force developed by the texturometer (Shimadzu EZ test); (b) Colorimetric measurement using a Konica Minolta CR300 colorimeter (Minolta, Osaka, Japan). CIE L^* (lightness), a^* (redness), and b^* (yellowness) values were recorded for each sample. For all rheological analyses, the steak cores were collected in parallel to the muscle fibers, using a hand-held steel cork borer. A cylindrical 10 mm-diameter probe of ebonite was used for the TPA tests.

Sensory Evaluation

The sensory attributes of buffalo meat and ricotta buffalo cheese were estimated by a panel of five panelists (Altieri et al., 2005), which evaluated the following parameters: color, odor, taste, chewiness, and general appearance. The samples treated with not-functionalized PETs were used as control. Panelists scored each sample with a point scale, ranging from 0 (attributes most disliked) to 5 (attributed most liked). After storage period, the meat was cooked at 80°C for 10 min (to simulate the mode of administration in restaurant) for taste and chewiness evaluation. Two pieces of each sample, buffalo meat and ricotta cheese, were served to panelists at each sample time.

Cytotoxicity Assay

The cytotoxicity of the immobilized MTP1 was tested against HT-29 cells, a human colon cancer cell line used extensively to study the effects of different food products on human health (Martínez-Maqueda et al., 2015). HT-29 cells (kindly donated by Dr. Rosanna Palumbo CNR-IBB, Naples, Italy) were grown in Dulbecco's Modified Eagle Medium (DMEM) supplemented with 10% (v/v) fetal bovine serum (FBS) and 10 mM L-glutamine. After reaching log phase, cells were transferred into 24-well plates (1×10^5 /mL) and incubated for 24 h at 37°C. Therefore, MTP1-functionalized PET disks (surface of 80 mm²) were added in each well and incubated for 24, 48, and 72 h at 37°C. Experiments were performed in quadruplicate. After incubation, the medium was removed and the remaining adherent cells were washed with PBS, fixated with 10% formaldehyde solution for 15 min at room temperature. Samples were subsequently washed with water and stained with 10% crystal violet solution for 30 min. Cell viability was quantified by eluting the dye from the stained cells with 10% acetic acid. Absorbance was measured spectrophotometrically at 595 nm (Multiskan FC; THERMO). Cells with the addition of not-functionalized PETs were set as negative control.

Statistical Analysis

All experiments were performed at least five times. Data were analyzed using GraphPad Prism 5.0 (GraphPad Software Inc., San Diego, CA, United States). Statistical analysis of microbial counts was performed by using Student's *t*-test for independent

data. Sensory evaluations, TBA, a_w , and pH data were analyzed by Student's *t*-test for independent data. $p < 0.05$ was considered to be statistically significant.

RESULTS AND DISCUSSION

Activation and Functionalization of PET Polymer by Cold Plasma and MTP1

Packaging has a fundamental role in ensuring the safe delivery of goods throughout supply chains to the end consumer (Lindh et al., 2016). In this context, polymeric materials cover a large section of requirements in the field of the food industry and provide support surfaces for the immobilization of biologically active molecules. Specifically, PET is actually one of the most common polymers used in the food packaging, because of its physicochemical and mechanical properties and it is also relatively inexpensive to produce (Siracusa, 2012). However, surface properties of PET are usually inadequate in terms of wettability and adhesion properties, so it should be modified in order to improve its desired surface features and enhance its suitability, prior to any further processing, such as functionalization with biologically active molecules. In recent years, one of the most interesting procedures that have been employed to overcome these disadvantages is gaseous plasma treatment (Jordá-Vilaplana et al., 2014; Pankaj et al., 2014). Because of this procedure, the PET wettability is enhanced, and a more hydrophilic surface is created, rendering the polymer suitable for the preparation of new materials. Indeed, the versatility of PET is based on the development of metastable reactive groups ($-\text{COOH}^*$, $-\text{OH}^*$) (Pankaj et al., 2014), which allow the covalent surface derivatization with the available chemical groups of biomolecules.

In this study, an immobilization platform on PET surfaces by using the previously characterized AMP MTP1 (Palmieri et al., 2016) was developed, exposing PET disks to a radiofrequency cold plasma by changing the main parameters of the process including the O₂ exposure time (*T*), RF power, and the concentration/the partial pressure (*P*) of molecular oxygen O₂. To assess the surface hydrophilicity of the PET slides after treatments, water contact angle (WCA) measurements were performed (Figure 1). Prior to activation, WCA was found to be $89 \pm 3^\circ$ (Figure 1A), confirming the hydrophobic nature of PET surface, whereas after plasma treatment carried out at the optimal experimental conditions (50 W and 10 s of exposure

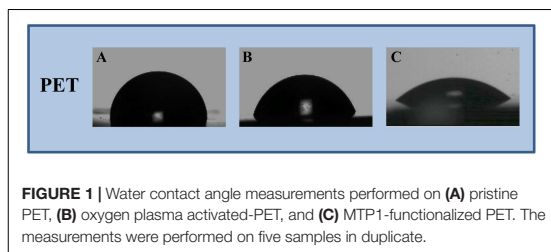


FIGURE 1 | Water contact angle measurements performed on (A) pristine PET, (B) oxygen plasma activated-PET, and (C) MTP1-functionalized PET. The measurements were performed on five samples in duplicate.

time), the contact angle was reduced to $76 \pm 2^\circ$, demonstrating that the plasma process significantly increased the hydrophilicity of the surface (**Figure 1B**). It is important to note that when higher values of RF power (RF = 300 W) and long exposure times ($T = 100\text{--}300$ s) were applied, a macroscopic change in the roughness of the PET surface was detectable, indicative of a material degradation process. Subsequently to the plasma procedure, PET samples were incubated for 24 h in MTP1 buffer solution. As shown in **Figure 1C**, the efficiency of the coupling reaction with MTP1 was confirmed by a strong increase in the surface hydrophilicity, as indicated by the pronounced decrease of WCA value ($36 \pm 3^\circ$). This phenomenon was due to the reaction of the peptide free chemical groups (typically $-\text{COOH}$ and $-\text{NH}_2$) with the reactive groups ($-\text{COOH}^*$, $-\text{OH}^*$) generated on PET surface by plasma activation (De Stefano et al., 2009). On the other hand, PET samples not pre-treated by radiofrequency cold plasma and incubated in same conditions in the presence of MTP1 showed the same value of WCA ($75 \pm 1^\circ$) of the pre-activated polymer, corresponding to negligible non-specific adsorption of the peptide on the PET surface. FTIR was also employed to confirm the success of bio-conjugation of MTP1 on PET disks. The ATR-FTIR spectrum of the not pre-activated PET (**Figure 2A**) displayed different main peaks corresponding to the C–C, C–H, and C–O bond stretching. After plasma treatment, the presence of the $-\text{OH}$ group peaks in the FTIR spectra was detected (**Figure 2B**), consistently with the increase of the surface wettability quantified by WCA measurements (Socrates, 1994; De Stefano et al., 2013). The appearance of the characteristic absorption signals of the peptide, including the Amide I and Amide II bands, which arise from the peptide bonds that link the amino acids ($\text{O}=\text{C}-\text{NH}$) residues in the MTP1 sequence, confirmed the covalent bonding of the peptide on the PET surface (**Figure 2C**). Specifically, the Amide I band located between $1650\text{--}1560\text{ cm}^{-1}$ is produced mainly by the $\text{C}=\text{O}$ stretching vibration of the peptide bond, while the absorption associated with the Amide II band at higher frequencies in the $1580\text{--}1490\text{ cm}^{-1}$ interval led primarily to bending vibrations of the N–H bond (**Figure 2C**). The main absorption peaks observed in ATR-FTIR spectra of PET samples are listed in the table reported in **Figure 2D**. Control samples not subjected to radiofrequency cold plasma treatment and incubated in aqueous peptide solution displayed an FTIR spectrum almost identical to that of **Figures 2A,B** (data not shown) (Edge et al., 1996; Silverstein and Webster, 1998; Chen et al., 2013).

Coupling Yield and Stability of MTP1-Immobilized PET Disks

In order to consider PET materials as promising candidates for applications in the food industry as antimicrobial packaging that are able to efficiently increase the food quality and safety, the AMPs used as coating agents must retain several prerequisites, including the broad activity spectrum and the biocompatibility. Nevertheless, the immobilization of AMPs is still challenged by suboptimal coating strategies leading to (i) inadequate surface concentrations and (ii) loss of antimicrobial activities with non-specific binding chemistry culminating in changed orientations

of the peptide molecules and/or associated cell toxicities. Therefore, it is firstly important to develop an effective surface tethering strategy that would impart the desired antimicrobial characteristics of the targeted biomaterial. This challenge strongly depends on the appropriate peptide concentration required to ensure a high efficiency of the immobilization procedure used and a great surface coating.

In this work, RP-HPLC analysis was employed to quantitatively measure the surface-immobilized yield starting from different MTP1 concentrations. Using this method, the amount of the PET-tethered peptide was indirectly evaluated by comparing the peak area (in the RP-HPLC-chromatograms) of the peptide not bound to the polymer after the bio-conjugation, with that of the initial peptide concentration used (at $t = 0$). The data obtained from these analyses demonstrated that the immobilization efficiency was concentration-dependent, reaching the highest yield (53%) using $50\text{ }\mu\text{M}$, corresponding to a surface coverage of 11.2 nmol/cm^2 of PET. The chromatographic profile obtained for the MTP1 $50\text{ }\mu\text{M}$ concentration and used to calculate the immobilization yield is reported in **Supplementary Figure 1**. The coupling yield was further confirmed by interpolation using a six-point calibration curve, which was generated utilizing known MTP1 concentrations (measured using an analytical balance) (**Supplementary Figure 1 insert**).

An important pre-requisite for AMP-coated packaging is the stability of the immobilized peptides. Therefore, the functionalized PET disks were incubated under different physiological conditions (i.e., immersion in pure water or in a representative liquid food matrix such as mozzarella cheese brine) up to 24 h, and the peptide-release was analyzed by RP-HPLC. As shown in the chromatograms reported in **Supplementary Figure 2**, both pure water and mozzarella brine did not cause MTP1 leakage from the PET polymers after 24 h incubation either at 4 or 25°C . In addition, no peptide-release was detectable even after prolonged incubation times (until to 72 h) in all the conditions analyzed (data not shown), thus highlighting the high stability of our system, that makes it an appropriate candidate for food applications.

Effect of MTP1-PETs on the Microbiological Quality of Dairy Products and Meat

Fresh food such as dairy products and meat because of their specific composition represent good support for a rapid growth of spoilage microorganisms that strongly influence the storage life of this class of products. In the case of cheese and meat, parameters such as water activity, pH, temperature, types, and viability of contaminating microorganisms are reported as some of the key factors that affect their rate of spoilage. Therefore, it is not surprising that these foods differ widely in spoilage characteristics. Among the troublesome microorganisms, yeasts and aerobic psychrotrophic Gram-negative bacteria can be considered the main causative agents of microbial spoilage and therefore they are recognized indicators of the hygienic quality of the foods. Indeed, psychrotrophic bacteria can produce

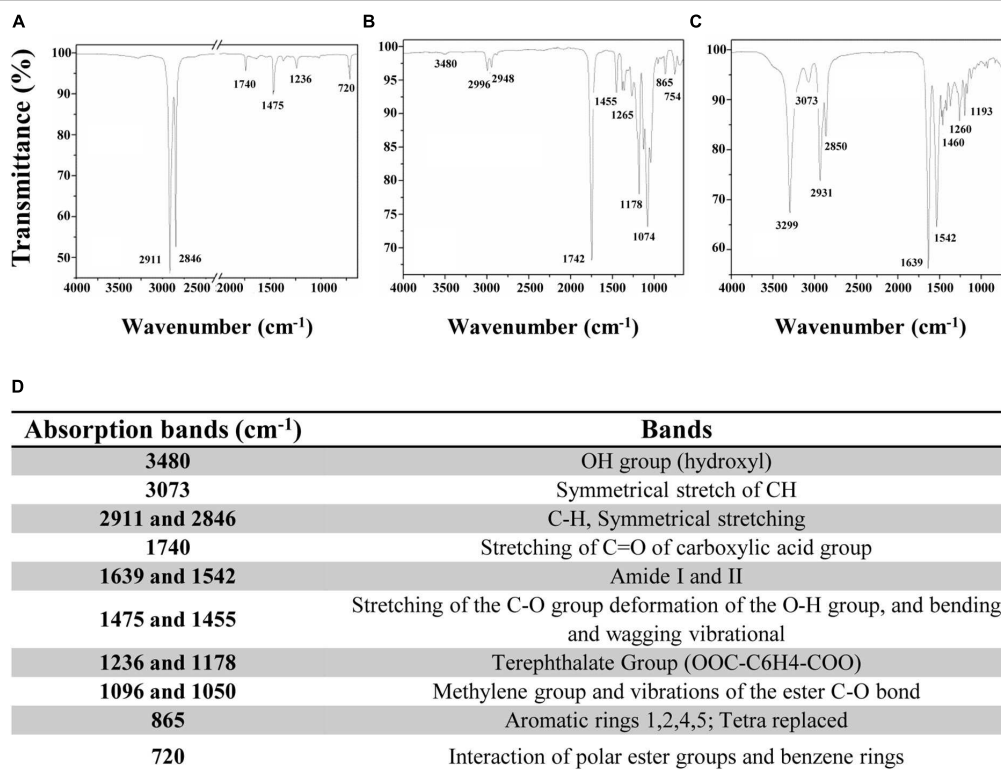
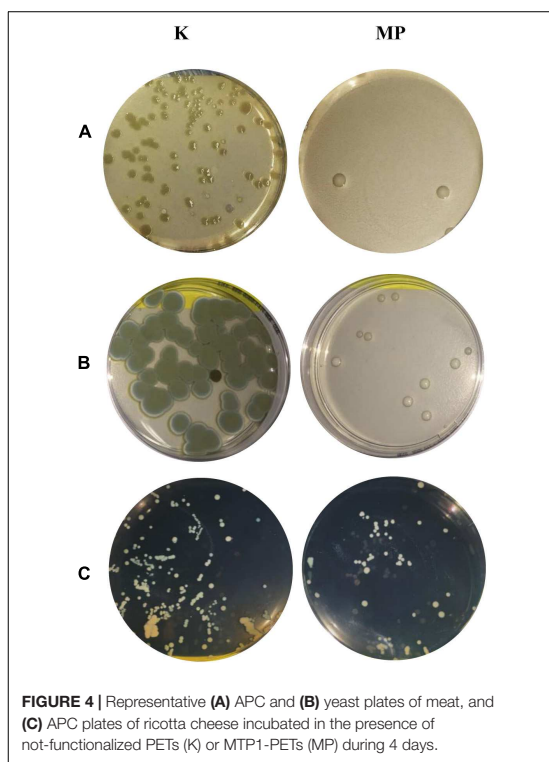
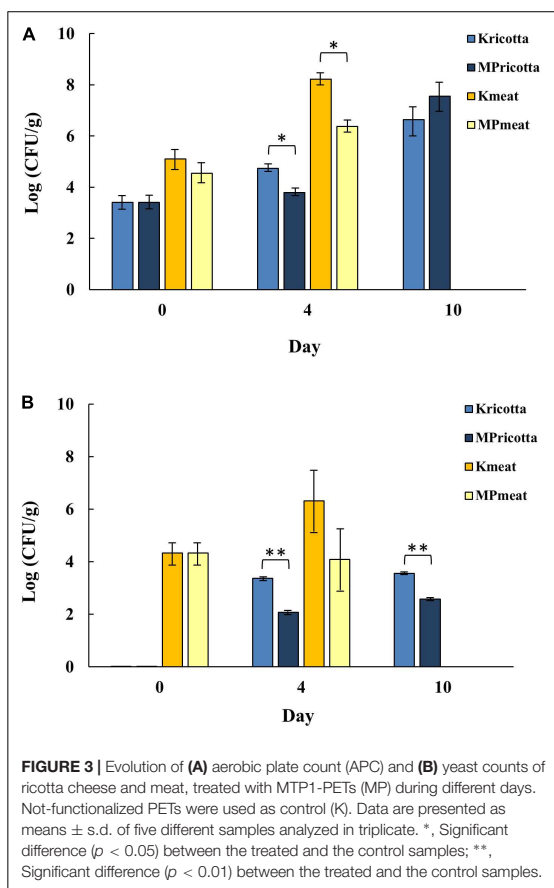


FIGURE 2 | ATR-FTIR spectra of PET samples **(A)** before radiofrequency cold plasma treatment, **(B)** after plasma treatment, and **(C)** after MTP1 bio-conjugation. **(D)** The table reporting the main absorption peaks observed in ATR-FTIR spectra of PET samples.

large amounts of extracellular hydrolytic enzymes, and the recontamination of food products with these bacteria is determinant for their shelf-life, while yeasts are responsible of the main food degradations. These microorganisms are able to grow under a great variety of conditions and to survive in different environments resulting in unwanted physical and chemical changes, altering texture, smell, taste, or appearance of fresh products and rendering them not feasible for human consumption anymore. Therefore, extending the shelf-life of meats and dairy products represents the main challenge for food companies, and it is vital because, in the real world, these products do have fixed lifetimes after which they will perish.

In this context, the effectiveness of MTP1-PETs was evaluated through a comparison of the development of total aerobic mesophilic bacteria (APC) and yeasts on ricotta cheese and meat samples, stored under refrigeration (4°C) 1 day more than the normal shelf-life set by the company and analyzed in order to simulate a commercial storage time interval. With the aim to determine the possible influence of MTP1-PETs on the microbial growth in the products under investigation, the

evolution of APC and yeast counts of samples treated with not-functionalized PETs (control) was assessed (**Figure 3**). Firstly, the initial values of the microbial counts were approximately in the range usually found for this variety of foods (4–5 Log CFU/g). As expected, bacterial microorganisms were able to proliferate in the control samples, with APC values ranging from 4–8 Log CFU/g during the period of monitoring (**Figure 3A**). On day 4 of treatment, meat samples in contact with MTP1-PETs were characterized by a significant ($p < 0.05$) bacteria growth inhibition (2.0 ± 0.2 Log CFU/g) respect to those exposed to the control PETs. It is worth to note that the microbiological acceptability limit of 7 Log CFU/g, as defined by the International Commission on Microbiological Specifications for Food (ICMSF) (1986), was reached in the control samples in the 4 days of storage, while this microbial count was observed in the treated samples after 6 days of storage with a concomitant worsening of the sensorial characteristics of the meat. These results indicated that MTP1-PET films might be an effective coating to extend the fresh meat shelf-life, which is generally estimated to be 2–3 days beyond a sell-by date.



Concerning ricotta cheese samples, as reported in **Figure 3A**, a statistically significant 1 Log reduction ($p < 0.05$) of APC in the MTP1-PET samples was observed respect to control after 4 days of storage. Besides, no significant differences in APC values were detected between samples of ricotta cheese stored on the PETs activated or not at day 10 of treatment, probably indicating the limited effect of long storage time on ricotta cheese preservation of the functionalized polymers (**Figure 3A**).

Similar results were obtained by evaluating yeasts growth (**Figure 3B**). After 4 days of storage 1 Log CFU/g increasing was revealed in meat products on control PETs in contrast to values of yeast counts equivalent to those determined at t_0 and measured for MTP1-PET meat samples. As far as ricotta cheese is concerned, both at 4 and 10 days of treatment, it was observed the same significant ($p < 0.01$) trend of yeasts count reduction (1 Log CFU/g) confirming the possible effectiveness of the active PET to prolong the shelf-life of this kind of products. Interestingly, the results obtained for ricotta cheese samples are very notable considering that the yeasts constitute the most representative microbiological typology that strongly affects the

shelf-life of this class of products, although no limits were fixed by European rules. However, Argentinian food regulations set up a maximum limit at no >3.5 Log CFU/g yeasts for cheeses with water content $>55\%$, such as ricotta. As shown in **Figure 3B**, PET-coated ricotta samples did exceeded this limit until the end of storage (10 days) while the control samples reached the limit already after 4th day.

Remarkably, the same results in terms of APC and yeast counts were determined even after three times of reuse of MTP1-PETs. Representative APC and yeast plates were reported in **Figure 4**.

Effect of MTP1-PETs on Physicochemical, Rheological, and Sensory Quality of Dairy Products and Meat

During storage, food products undergo physicochemical, rheological, and sensory changes that may affect their organoleptic qualities and in turn, discourage their consumption. In this context, it is essential for a packaging to preserve also the inherent qualities of a product during storage beyond the microbiological safety. Therefore, a detailed analysis concerning the aforementioned parameters was performed on the buffalo meat and ricotta cheese samples treated or not with MTP1-PETs at the investigation times. All data are reported in **Tables 1, 2**.

TABLE 1 | Effects of MTP1-PETs on physical–chemical (pH, a_w , and TBA test), rheological parameters (color and texture), and sensory evaluation of buffalo meat samples.

	Day 0	Day 4				
		Control		MTP1-PETs		t-test
		M	SD	M	SD	
pH	5.630	5.700	–	5.810	–	–3.024*
a_w	0.983	0.978	–	0.980	–	–2.450
TBA test	0.673	0.768	–	0.722	–	–5.489**
Lightness	28.270	32.643	10.570	31.143	16.910	0.701
Redness	10.753	7.700	2.460	10.863	2.390	3.398*
Yellowness	5.583	3.180	9.880	5.913	3.320	–1.843
Chroma	16.337	10.880	18.460	16.777	8.450	–2.785*
Hue angle	0.479	0.392	0.090	0.499	0.010	–0.976
Adhesiveness	–35.643	–29.420	–	–22.187	0.080	–6.320**
Cohesion	39.178	31.583	1.470	32.345	0.130	0.080
Hardness	343.142	336.928	2.320	331.237	2.010	0.223
Cohesiveness	0.384	0.365	0.020	0.357	0.010	–0.452
Friability	121.750	128.428	1.900	127.654	0.980	–0.541
Elasticity	0.781	0.784	0.010	0.779	0.060	–0.014
Gumminess	137.002	126.784	1.410	121.350	2.010	0.418
Chewiness	104.887	99.949	1.620	101.279	6.820	–0.385
Resilience	0.215	0.196	0.010	0.192	0.020	–0.260
Color	4.200	2.800	0.800	3.400	1.200	–189.737
Taste	4.400	3.600	1.200	3.800	0.800	–0.632
Odor	3.600	2.800	0.800	3.200	0.800	–141.421
Chewiness	4.400	3.400	1.200	3.800	0.800	–126.491
Overall acceptance	4.400	2.800	0.800	3.800	0.800	–3.536*

Levels of significance of treatments: ** $p \leq 0.01$; * $p \leq 0.05$. M, means; SD, standard deviations.

TABLE 2 | Effects of MTP1-PETs on physical–chemical (pH, a_w , and TBA test) and sensory evaluation of buffalo ricotta cheese samples.

	Day 0	Day 4					Day 10				
		Control		MTP1-PETs		t-test	Control		MTP1-PETs		t-test
		M	SD	M	SD		M	SD	M	SD	
pH	6.770	6.900	0.010	6.860	–	0.894	6.950	–	6.950	–	–0.229
a_w	0.983	0.989	–	0.991	–	–0.695	0.989	–	0.991	–	–118.695
TBA test	0.009	0.010	–	0.012	–	–0.133	0.015	–	0.012	–	1.270
Color	4.800	4.400	1.200	4.800	0.800	–126.491	3.000	2.000	3.600	1.200	–1.500
Taste	4.200	4.000	–	4.200	0.800	–1.000	2.600	1.200	3.000	2.000	–1.000
Odor	4.800	2.800	0.800	3.600	1.200	–2.529*	1.800	0.800	2.600	1.200	–2.529*
Chewiness	5.000	3.800	0.800	4.200	0.800	–141.421	2.200	0.800	3.200	0.800	–3.535*
Overall acceptance	4.800	3.600	1.200	4.400	1.200	–2.309*	2.400	1.200	3.400	1.200	–2.887*

Levels of significance of treatments: * $p \leq 0.05$. M, means; SD, standard deviations.

Interestingly, a significant increase ($p < 0.05$) in the overall acceptance parameter was measured in the MTP1-PETs respect to the controls at each investigation time both for buffalo meat and ricotta buffalo cheese. On the contrary, the findings showed that the meat products had little differences in terms of color, taste, odor, and chewiness along the storage, but they were not statistically meaningful ($p > 0.05$). However, panelists indicated that the odor intensity in the MTP1-PETs ricotta cheese sample

was more desirable than the control ($p < 0.05$) after 4 and 10 days of storage.

As far as the physicochemical parameters is concerned, there were no substantial changes in the pH and a_w values and in general no significant differences were found across all groups of meat and the dairy product following the MTP1-PET treatment during storage (Tables 1, 2). In addition, the levels of oxidative deterioration (TBA) did not change in any meaningful way

between the MTP1-PETs samples and the controls but for buffalo meat samples after 4 days of contact ($p < 0.01$), suggesting that MTP1 had a slight effect on the lipid oxidation of meat products.

Color of foods is another important parameter to evaluate their quality, since the consumers associate it with freshness. As reported in **Table 1**, the not treated samples suffered a gradual lean browning during the retail period, reflecting in terms of an increase of L^* and a decrease in a^* and C^* values respect to t_0 . Conversely, lower L^* and greater redness (resulting in higher a^* and C^* , $p < 0.05$) were found in the MTP1-PET meats compared with the controls at 4 days. Finally, the rheological analysis evidenced no significant change in the textural qualities of the buffalo meat samples following the MTP1-PET treatments.

Cytotoxicity Testing of Immobilized MTP1

In addition to antibacterial activity, cytotoxicity is another important parameter influencing the application of any material for industrial and medical purposes. Therefore, in order to ascertain the non-toxic behavior of MTP1-modified PETs, cell viability assay was carried out on the human colon cancer cell line HT-29, that is receiving special interest in studies focused on the effects of food products on human health (Martínez-Maqueada et al., 2015). To this aim, cell viability was determined by exposing these cells to functionalized polymers for different time intervals, using the non-conjugated PET disks as control. As reported in **Figure 5**, the mammalian cells remained viable up to 72 h of incubation with the functionalized PET, with no significant difference in cell viability in terms of absorbance between the controls and the MTP1-PET disks. These results indicated that the amount of peptide immobilized on PETs was not toxic to mammalian cells, thus suggesting that the projected polymers could be considered safe to be applied as antimicrobial packages in the food industry.

CONCLUSION

In the field of food technology, innovative packaging represents an emerging solution that can confer many preservation profits on many food products. This study revealed that a 15-mer AMP could be covalently bound to the surface of PET materials, to produce highly stable antimicrobial packaging, which could be successfully used to improve the quality and safety of fresh products, maintaining the nutritional values during storage. The results obtained demonstrated the potential applicability of the MTP1-PET materials as not cytotoxic and safe active antimicrobial packaging through inhibition of the growth of spoilage microorganisms in relevant food model systems, such as the easily perishable ricotta cheese and fresh meat. The significant effects against bacteria in meat samples and yeast in ricotta cheese suggest a possible increase over the expiration date compared to the samples in contact with the control PETs. Although no significant variation was observed against yeast in meat samples and bacteria in ricotta cheese, we considered notable to underline the constant bacteria/yeast decrease in all samples stored on the PETs activated. Thus, the presented

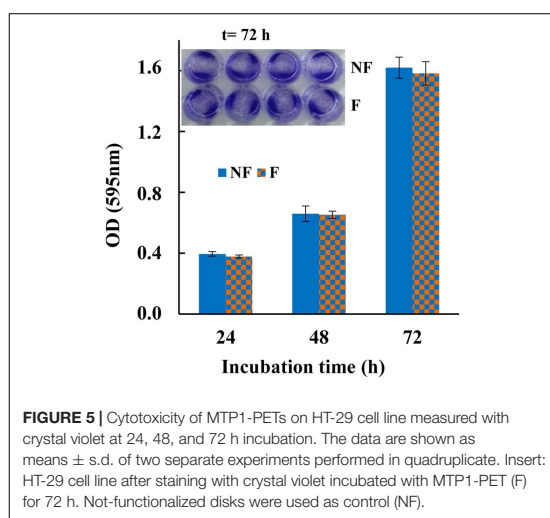


FIGURE 5 | Cytotoxicity of MTP1-PETs on HT-29 cell line measured with crystal violet at 24, 48, and 72 h incubation. The data are shown as means \pm s.d. of two separate experiments performed in quadruplicate. Insert: HT-29 cell line after staining with crystal violet incubated with MTP1-PET (F) for 72 h. Not-functionalized disks were used as control (NF).

technology holds a great prospective for the development of highly effective bio-active and appealing packaging for food, preserving the microbiology quality and improving the safety of fresh products, with a concomitant extension of their shelf-life without adversely affect the organoleptic properties. However, long-term stability studies will be necessary in order to assure that the developed MTP1-PETs maintain stable performances over longer storage periods, which constitute an essential requirement for an innovative food packaging.

This work represents a pilot study, which provides a starting point to evaluate further the real potential application of MTP1-PETs as antimicrobial packaging in the food market.

DATA AVAILABILITY STATEMENT

All datasets generated for this study are included in the article/**Supplementary Material**.

ETHICS STATEMENT

All experimental designs and animal care protocols were approved by the Animal Ethics Committee of the Buffalo Research Institute, Chinese Academy of Agricultural Sciences (BRI-CAAS) and Huazhong Agricultural University.

AUTHOR CONTRIBUTIONS

GP, LD, AA, YP, MG, and MB conceived and designed the experiments. BA, RA, GS, and RM performed the experiments. IR, MB, LD, and YP generated and analyzed the data. MG, GP, and AA wrote the manuscript. All authors contributed to the manuscript revision, read, and approved its submitted version.

FUNDING

This research was supported by the “Packaging innovativi a base di peptidi antimicrobici per la Sicurezza Alimentare” (PERSIA) project, grant number POR FESR CAMPANIA 2014/2020 n. B63D18000530007; the “Sviluppo di metodologie innovative per ridurre il rischio di malattie trasmesse da alimenti in prodotti della filiera ittica”-Ricerca Corrente 2016 project, grant number IZS ME 01/16 RC; the “Attività battericida ed anti-biofilm di nano-sistemi ibridi coniugati con peptidi antimicrobici: una nuova strategia per la formulazione di bio-sanitizzanti contro ceppi patogeni resistenti”-Ricerca Corrente 2017 project, grant number IZS ME 06/18 RC; the “Miglioramento delle caratteristiche funzionali e della shelf life degli alimenti derivanti da tecniche innovative di allevamento della bufala” (RAZIONALE) project, PON

REFERENCES

- Altieri, C., Speranza, B., Del Nobile, M. A., and Sinigaglia, M. (2005). Suitability of bifidobacteria and thymol as biopreservatives in extending the shelf life of fresh packed plaice filets. *J. Appl. Microbiol.* 99, 1294–1302. doi: 10.1111/j.1365-2672.2005.02740.x
- Andreu, D., and Rivas, L. (1998). Animal antimicrobial peptides: an overview. *Biopolymers* 47, 415–433. doi: 10.1002/(sici)1097-0282(1998)47:6<415::aid-bip2>3.0.co;2-d
- AOAC (1990). *Official Methods of Analysis*, 15th Edn, Method 950.46, Vol. 11, Arlington, VA: Association of Official Analytical Chemists.
- AOAC (2000). *Official Methods of Analysis*, 17th Edn, Method 976.18, Gaithersburg, MD: Association of Official Analytical Chemists.
- Aymerich, T., Picouet, P. A., and Monfort, J. M. (2008). Decontamination technologies for meat products. *Meat Sci.* 78, 114–129. doi: 10.1016/j.meatsci.2007.07.007
- Blackburn, C. deW. ed (2006). “Introduction,” in *Food Spoilage Microorganisms*, ed. C. deW Blackburn, (Cambridge: Woodhead), xvii–xxiii.
- Bondi, M., Lauková, A., de Niederhauser, S., Messi, P., and Papadopoulou, C. (2017). Natural preservatives to improve food quality and safety. *J. Food Qual.* 2017:3. doi: 10.1155/2017/1090932
- Chen, Z., Hay, J. N., and Jenkins, M. J. (2013). The thermal analysis of poly(ethylene terephthalate) by FTIR spectroscopy. *Thermochim. Acta* 552, 123–130. doi: 10.1016/j.tca.2012.11.002
- Cichello, S. A. (2015). Oxygen absorbers in food preservation: a review. *J. Food Sci. Technol.* 52, 1889–1895. doi: 10.1007/s13197-014-1265-2
- De Smet, K., and Contreras, R. (2005). Human antimicrobial peptides: defensins, cathelicidins and histatins. *Biotechnol. Lett.* 27, 1337–1347. doi: 10.1007/s10529-005-0936-5
- De Stefano, L., Oliviero, G., Amato, J., Borbone, N., Piccialli, G., Mayol, L., et al. (2013). Aminosilane functionalizations of mesoporous oxidized silicon for oligonucleotide synthesis and detection. *J. R. Soc. Interface* 10:20130160. doi: 10.1098/rsif.2013.0160
- De Stefano, L., Rotiroli, L., De Tommasi, E., Rea, I., Rendina, I., Canciello, M., et al. (2009). Hybrid polymer-porous silicon photonic crystals for optical sensing. *J. Appl. Phys.* 106:023109. doi: 10.1063/1.3177344
- Edge, M., Wiles, R., Allen, N. S., McDonald, W. A., and Mottock, S. V. (1996). Characterization of the species responsible for yellowing in melt degraded aromatic polyesters-I: yellowing of poly (ethylene terephthalate). *Polym. Degrad. Stab.* 53, 141–151. doi: 10.1016/0141-3910(96)00081-x
- Guaní-Guerra, E., Santos-Mendoza, T., Lugo-Reyes, S. O., and Terán, L. M. (2010). Antimicrobial peptides: general overview and clinical implications in human health and disease. *Clin. Immunol.* 135, 1–11. doi: 10.1016/j.clim.2009.12.004
- F/050129/01-03//X32. All funders had no role in study design, data collection and analysis, decision to publish, or preparation of the manuscript.

ACKNOWLEDGMENTS

The authors would like to thank Dr. Rosanna Palumbo for help in optimization of the cytotoxicity assays.

SUPPLEMENTARY MATERIAL

The Supplementary Material for this article can be found online at: <https://www.frontiersin.org/articles/10.3389/fmicb.2019.02963/full#supplementary-material>

- International Commission on Microbiological Specifications for Food (ICMSF) (1986). *Microorganisms in Foods. 2. Sampling for Microbiological Analysis: Principles and Specific.* Hoboken, NJ: Blackwell Scientific Publications.
- Jordá-Vilaplana, A., Fombuena, V., García-García, D., Samper, M. D., and Sánchez-Nácher, L. (2014). Surface modification of polylactic acid (PLA) by air atmospheric plasma treatment. *Eur. Polym. J.* 58, 23–33. doi: 10.1016/j.eurpolymj.2014.06.002
- Lindh, H., Olsson, A., and Williams, H. (2016). Consumer perceptions of food packaging: contributing to or counteracting environmentally sustainable development? *Packag. Technol. Sci.* 29, 3–23. doi: 10.1002/pts.2184
- Malhotra, B., Keshwani, A., and Kharkwal, H. (2015). Antimicrobial food packaging: potential and pitfalls. *Front. Microbiol.* 6:611. doi: 10.3389/fmicb.2015.00611
- Martínez-Maqueda, D., Miralles, B., and Recio, I. (2015). “HT29 cell line,” in *The Impact of Food Bioactives on Health: in vivo and ex vivo Models*, ed. K. Verhoeckx, (Berlin: Springer).
- McGarry, J. D., and Brown, N. F. (1997). The mitochondrial carnitine palmitoyltransferase system. from concept to molecular analysis. *Eur. J. Biochem.* 244, 1–14. doi: 10.1111/j.1432-1033.1997.00001.x
- Mead, G. C. (2004). “Shelf-life and spoilage of poultry meat,” in *Poultry Meat Processing and Quality*, ed. G. C. Mead, (Cambridge: CRC Press), 283–303. doi: 10.1533/9781855739031.283
- Nakatsuji, T., and Gallo, R. L. (2012). Antimicrobial peptides: old molecules with new ideas. *J. Invest. Dermatol.* 132, 887–895. doi: 10.1038/jid.2011.387
- Palmieri, G., Balestrieri, M., Proroga, Y. T., Falcigno, L., Facchiano, A., Riccio, A., et al. (2016). New antimicrobial peptides against foodborne pathogens: from in silico design to experimental evidence. *Food Chem.* 211, 546–554. doi: 10.1016/j.foodchem.2016.05.100
- Pankaj, S. K., Bueno-Ferrer, C., Misra, N. N., Milosavljevic, V., O’Donnel, C. P., Bourke, P., et al. (2014). Applications of cold plasma technology in food packaging. *Trends Food Sci. Technol.* 35, 5–17. doi: 10.1016/j.tifs.2013.10.009
- Patsias, A., Badeka, A. V., Savvaidis, I. N., and Kontominas, M. G. (2008). Combined effect of freeze chilling and MAP on quality parameters of raw chicken filets. *Food Microbiol.* 25, 575–581. doi: 10.1016/j.fm.2008.02.008
- Petrou, S., Tsiraki, M., Giatrakou, V., and Savvaidis, I. N. (2012). Chitosan dipping or oregano oil treatments, singly or combined on modified atmosphere packaged chicken breast meat. *Int. J. Food Microbiol.* 156, 264–271. doi: 10.1016/j.ijfoodmicro.2012.04.002
- Reddy, K. V., Yedery, R. D., and Aranha, C. (2004). Antimicrobial peptides: premises and promises. *Int. J. Antimicrob. Agents* 24, 536–547. doi: 10.1016/j.ijantimicag.2004.09.005
- Ruiz, de Huidobro, F., Miguel, E., Blázquez, B., and Onega, E. (2005). A comparison between two methods (Warner-Bratzelz and texture profile analysis) for testing

- either raw or cooked meat. *Meat Sci.* 69, 527–536. doi: 10.1016/j.meatsci.2004.09.008
- Samelis, J. (2006). “Managing microbial spoilage in the meat industry,” in *Food Spoilage Microorganisms*, ed. W. Blackburn, (Boca Raton, FL: CRC Press LLC).
- Silverstein, R. M., and Webster, F. X. (1998). *Spectrometric Identification of Organic Compounds*. New York, NY: Wiley.
- Siracusa, V. (2012). Food packaging permeability behaviour: a report. *Int. J. Polym. Sci.* 2012:11. doi: 10.1155/2012/302029
- Socrates, G. (1994). *Infrared and Raman Characteristic Group Frequencies*, 3rd Edn. New York, NY: Wiley & Sons Ltd.
- Suppakul, P., Miltz, J., Sonneveld, K., and Bigger, S. W. (2003). Active packaging technologies with an emphasis on antimicrobial packaging and its application. *J. Food Sci.* 68, 408–420. doi: 10.1111/j.1365-2621.2003.tb05687.x
- Zhou, G. H., Xu, X. L., and Liu, Y. (2010). Preservation technologies for fresh meat e a review. *Meat Sci.* 86, 119–128. doi: 10.1016/j.meatsci.2010.04.033
- Conflict of Interest:** BA was employed by Materias Srl. GP was employed by the government National Research Council (IBBR-CNR) and she was associated with the company Materias Srl.
- The remaining authors declare that the research was conducted in the absence of any commercial or financial relationships that could be construed as a potential conflict of interest.

Copyright © 2020 Gogliettino, Balestrieri, Ambrosio, Anastasio, Smaldone, Proroga, Moretta, Rea, De Stefano, Agrillo and Palmieri. This is an open-access article distributed under the terms of the Creative Commons Attribution License (CC BY). The use, distribution or reproduction in other forums is permitted, provided the original author(s) and the copyright owner(s) are credited and that the original publication in this journal is cited, in accordance with accepted academic practice. No use, distribution or reproduction is permitted which does not comply with these terms.